EPFL

Thèse n° 7790

Advanced design methods and non-ideal gas lubrication applied to aerodynamic bearings

Présentée le 13 mars 2020

à la Faculté des sciences et techniques de l'ingénieur
Laboratoire de conception mécanique appliquée
Programme doctoral en énergie

pour l'obtention du grade de Docteur ès Sciences

par

Eliott Philippe GUENAT

Acceptée sur proposition du jury

Prof. K. A. J. Mulleners, présidente du jury
Prof. J. A. Schiffmann, directeur de thèse
Prof. I. Santos, rapporteur
Prof. M. Arghir, rapporteur
Prof. F. Gallaire, rapporteur

École
polytechnique
fédérale
de Lausanne

2020

The fact that we live at the bottom of a deep gravity well, on the surface of a gas covered planet going around a nuclear fireball 90 million miles away and think this to be normal is obviously some indication of how skewed our perspective tends to be.

Douglas Adams

Acknowledgements

I would like to thank Prof. Jürg Schiffmann for having been a much enjoyed supervisor, providing the necessary guidance when needed while granting me a large research freedom. His smooth management was very much appreciated and contributed significantly to my output. I thank my friend Dr[*]. Cyril Picard, who joined me at the Laboratory for Applied Mechanical Design soon after the beginning of my work. Without mentioning the usefulness of his expertise in so many diverse topics (ranging from Model Predictive Control to classic Opera), sharing the same lab for our doctoral studies was a driving experience. It helped me to carry this project past many obstacles. I thank my friend Dr. Karim Shalash for the inspiring debates and discussions we had and for challenging me down to the roots of what I think I know. This has been a very interesting epistemic journey that made me a more cautious researcher and person. I thank Dr. Julie Lenoble –the spine of the laboratory– for the intense care she takes of it and for her friendliness. The professional yet friendly team of engineers contributed greatly to make the lab a nice working place. I therefore thank Antonio Lopez, Christophe Darioli, Christophe Pham, Nicolas Huguelet, Nathaniel Mutrux and Thierry Mesot, with a special mention to Christophe Pham for his help in building up the test rig and to Antonio Lopez for his contagious good mood. I thank Dr. Violette Mounier and Dr[*]. Kévin Rosset for having been such nice supervisors during my early semester projects in the laboratory and for their company during my studies. I thank the current and former lab members for helping me during my stay: Eric, Chris, Partick, Philipp, Soheyl, Robin, Suresh, Markus, Lili, Wanhui, Sajjad, Tomohiro, Ansgar, Victoria, Ceyhun, Luis, and Kossi. I thank Mr. Clottu of Micromécanique MSA for providing sub-micrometric precision to some of the mechanical parts used in this thesis.

I could count during my research on the cheering presence of friends outside of my close PhD environment, including the famous *Nuages* acting as a much needed release valve, my friends met while studying at EPFL –for the sake on conciseness, citing here only Dr[*]. Guillaume Jeanmonod and Dr[*]. Sarah van Rooij, who co-represented with me the PhD students of the Doctoral Program of Energy–, my many former flatmates of *Couvaswag* who supported me during the two most critical years of my PhD with many dinners and much friendship. I thank them all for their help in gaining altitude over the daily problems.

---

[*] Anticipated doctoral title

I thank my parents, Martine and Alain for the continuous support they provided over the past 29 years. I thank them for having cultivated my interest for science during my childhood and for having shown a genuine interest in what drives me, even when it sometimes implied to spend hours in freezing nights waiting for Saturn to appear in my telescope. Furthermore, their generous material support allowed me to fully enjoy my 10-year stay at EPFL and was undoubtedly a critical contribution to its success. Many thanks to my brother Valentin and my grand-parents Danielle, Pipo and Trudy for their love and support. I am glad to complete my PhD thesis with them as witnesses.

I bow down to Maud Oïhénart for her fundamental contribution to this thesis. The last four years saw some moments of discouragement, overwhelming uncertainties and doubts. Maud endured my worst moods and helped me emerge and change my perspective until better times came. She listened patiently when I was complaining about my unstable gas bearings, cheered when I finally got them running and pulled me out of my bubble when I was getting lost in my thoughts. She made genuine effort to understand my work, to the point where she now grasps the basics of gas lubrication[*]. Maud made this thesis possible by enlightening the outside world with her ever-surprising creativity and her endless resources. Thank you.

Finally, I thank Prof. François Gallaire, Prof. Mihai Arghir, Prof. Ilmar Santos and Prof. Karen Mulleners for having taken part to my thesis jury, providing a helpful feedback. The Swiss National Science Foundation is acknowledged for its support.

Neuchâtel, February 5th 2020
Eliott Guenat

---

[*] Jürg, are you still looking for promising candidates?

Abstract

Clean and energy-efficient turbomachinery are playing an increasingly important role in the decarbonization of heating systems, waste heat recovery and transportation, as the use of small-scale heat pumping and fuel cells spreads. Such machines typically employ aerodynamic bearings because of their oilfreeness and very large lifespan. In particular, grooved bearings enjoy a high stiffness and repeatable performance under similar manufacturing conditions and are particularly well suited for small-scale rotors. However, such gas bearings are usually modeled under the assumption that the lubricant follows the ideal gas law, which may not be valid in conditions met in heat pumping (high pressure condensable gases) and ambient air compression (condensation of moisture). In addition, a strict separation between grooved and compliant bearings exist without justification and optimization methods used for the design of such elements ignore the concept of robustness. This thesis explores these shortcomings.

First, the classical modeling theory for grooved bearings, the Narrow-Groove Theory (NGT), is experimentally validated in dynamic conditions. A test rig is built, consisting of a 16 mm rotor rotating at 100 krpm on two herringbone grooved journal bearings (HGJBs) driven by an impulse turbine. The bearing bushings are excited in two orthogonal directions using piezo-electric shakers, allowing the deduction of the frequency-dependent force coefficients. The measurements are in good qualitative agreement with the theory, although stiffness and damping coefficients were observed 23 and 29% lower than the predicted values, respectively.

The influence of real-gas effects and humid air on the static and dynamic performance of plain bearings and HGJBs is theoretically and numerically investigated on a wide range of operating conditions. Real-gas effects were found to negatively affect the load capacity and either have a positive or negative influence on the stability depending on the operating conditions. Humid air effects have a negligible yet negative influence on the static performance and can decrease the critical mass of HGJBs by 25%. The effects of pure-fluid condensation are theoretically assessed using a 1D slider bearing. Further, an experimental setup consisting of a 20 mm three-pad Rayleigh step journal bearing operating at 30 krpm in pressurized R245fa is built to experimentally validate the proposed model by measuring and comparing the pressure in the thin gas film. Theoretically-predicted characteristic features of a condensing gas film are observed experimentally, suggesting sustained operation of a gas lubricated bearing with local condensation.

The path toward hybrid foil and grooved bearings is explored, as a tentative to combine the best of the two worlds. A model based on the simple foundation approach is proposed and the improvement potential of spiral grooves applied on foil thrust bearings is numerically assessed using multi-objective optimization of the grooved pattern. Results suggest that the load capacity can be improved while reducing the drag torque. However, the ultimate load capacity does not systematically benefit from the presence of spiral grooves. Finally, a novel design procedure maximizing the robustness of aerodynamic bearings against manufacturing deviation is proposed and applied to HGJBs. Based on an unique pre-computed look-up table of critical mass, the hyperspace is dimensionalized for a case-specific rotor and is scanned to find the largest admissible deviation on the groove depth and radial clearance simultaneously. It yields a Pareto front of the best possible allocation of manufacturing tolerances on the two design parameters.

Keywords: Energy, Aerodynamic bearing, Real gas, Modeling, System identification, Experiment, Design, Optimization

Résumé

Les turbomachines efficientes et sans huile jouent un rôle de plus an plus important dans la décarbonisation les installations énergétiques pour le chauffage et le transport, à mesure que l'usage de piles à combustibles et des de pompes à chaleur s'accroît. De telles machines utilisent typiquement des paliers aérodynamiques pour leurs qualités non-contaminantes et de très longue durée de vie. En particuliers, les paliers aérodynamique rainurés bénéficient d'une grande rigidité, d'un comportement répétable lorsque les conditions de fabrications sont similaires et sont bien adaptés aux machines tournantes de petites dimensions. Cependant, de tels paliers aérodynamiques sont en général modelisés sous l'hypothèse que le lubrifiant suit la loi des gaz parfaits, ce qui n'est pas forcément valide dans des environnement rencontrés dans les pompes à chaleur (gaz condensable à haute pression) et dans la compression d'air ambiant (condensation de l'eau atmosphérique). De plus, les paliers à feuillets et les paliers rainurés demeurent deux familles strictement séparées et les méthodes d'optimisation habituellement appliquées pour la conception de telles machines ne tiennent pas en compte de la robustesse. Cette thèse explore ces manquements.

Premièrement, la théorie classique de modélisation des paliers à rainures, la *Narrow Groove Theory* (NGT), est validée expérimentalement en conditions dynamiques. Un banc d'essai est construit, consistant en un arbre de 16 mm tournant à 100'000 tours par minute sur deux paliers radiaux arodynamiques à chevrons (HGJBs) mû par une turbine à impulsion. The douilles des paliers sont excitées par des vibreurs piezo-éléctriques dans deux directions orthogonales, ce qui permet de déduire les impédances dynamiques des paliers. Les mesures sont en bon accord qualitatif avec la théorie, bien que les paramètres de raideur et d'amortissement des paliers sont mesurés 23 et 29% plus faibles que prédits, respectivement.

L'influence de l'air humide et des effets gaz réels sur les paliers lisses et des HGJBs est étudié théoriquement et numériquement dans un large domaines de conditions d'utilisation. Les effets gaz réels révèlent avoir un effet négatif la capacité de charge et peuvent avoir un effet soit positif soit négatif sur la stabilité, dépendamment des conditions. L'air humide a un effet négligeable sur la capacité de charge tandis que la stabilité des HGJBs peut être diminuée de 25%. Les effets de la condenation d'un fluid pur sont évalués sur un palier linéaire monodimensionel. Un setup expérimental, consistant en un palier radial de Rayleigh de 20 mm tournant à 30'000 tours par minute dans du réfrigérant R245fa pressurisé, est construit pour valider expérimentalement le modèle proposé en mesurant la pression à l'intérieur du film de gaz. Les charactéristiques théoriques d'un film de gaz

en état de condensation sont observées expérimentalement, ce qui suggère l'appartition de condensation dans les paliers aerodynamiques.
L'hybridation de paliers à feuillets avec les paliers rainurés est explorée, motivée par la volonté de combiner le meilleur des deux mondes. Un modèle, basé sur l'approche des fondations simples, est porposé et le potentiel d'amélioration de rainures spirales appliquées sur un palier axial à feuillets est évalué numériquement en utilisant une optimisation multi-objectifs sur la géométrie des rainures. Les résultats suggèrent que la capacité de charge peut être améliorée tout en réduisant les pertes visqueuses. Cependant, la capacité de charge ultime ne bénéficie pas systématiquement de la présence des rainures. Finalement, une nouvelle procédure de conception maximisant la robustesse de paliers aérodynamiques face aux erreurs de fabrications est proposées et appliquées aux HGJBs. Basée sur un unique tableau pré-calculé de mass critique adimensionelle, cet hyper espace est dimensionalisé pour un rotor spécifique et est scanné pour determiner les zones permettant la plus grande déviations de la profondeur des rainures et du jeu radial simulatanément. La procédure aboutit à un front de Pareto des meilleures tolérances de fabrication attribuables à chacun des paramètres.

Mots clés : Energie, Palier aérodynamique, Gaz Réels, Modelisation, Identification de Système, Experimentation, Conception, Optimisation

Zusammenfassung

Effiziente und ölfreie Turbomaschinen werden voraussichtlich eine wichtige Rolle bei der Transition von Energieanlagen von fossilen zu erneuerbaren Energieträgern spielen, da der Einsatz von Brennstoffzellen und Wärmepumpen zunimmt. Solche Maschinen verwenden typischerweise aerodynamische Lager aufgrund ihrer kontaminationsfreien Eigenschaften und ihrer sehr hohen Lebensdauer. Insbesondere aerodynamische Lager mit Nuten profitieren von einer hohen Steifigkeit und einem reproduzierbaren Verhalten unter Einhlatung von ähnlichen Fertigungsbedingungen, weswegen sich diese gut für kleine rotierende Maschinen eignen. Solche aerodynamischen Lager werden jedoch meistens unter der Annahme eines idealen Gases modelliert, welche nicht immer zulässig ist; zum Beispiel in Wärmepumpen (kondensierbares Gas bei hohem Druck) und in der feuchten Umgebungsluft (atmosphärische Wasserkondensation). Darüber hinaus bleiben Folien- und Spiralrillenlager zwei streng getrennte Familien. Die üblicherweise bei der Konstruktion solcher Maschinen angewandten Optimierungsmethoden berücksichtigen die Robustheit nicht. Diese Arbeit untersucht diese Probleme. Die klassische Theorie der aerodynamischen Lager basierend auf Nuten, die Narrow Groove Theory, wird experimentell unter dynamischen Bedingungen validiert. Hierzu dient ein Versuchsaufbau, bestehend aus einer Impulsturbine, welche eine bis zu 100 000 U/min rotierenden 16 mm Welle auf zwei aerodynamischen Radiallagern mit pfeilförmigen Nuten (HGJBs) antreibt. Die Lagerhülsen werden von piezoelektrischen Vibratoren in zwei orthogonalen Richtungen angeregt, wodurch die dynamischen Impedanzen der Lager abgeleitet werden können. Die Messungen sind in guter qualitativer Übereinstimmung mit der Theorie, obwohl die berechneten Steifigkeits- und Dämpfungsparameter der Lager 23%, und 29% niedriger als die Messwerte sind. Der Einfluss von feuchter Luft und realer Gaseigenschaften auf zylindrischen Luftlagern und HGJBs wird theoretisch und numerisch unter variablen Betriebsbedingungen untersucht. Die Realgaseffekte zeigen einen negativen Einfluss auf die Tragfähigkeit und können je nach Bedingungen einen positiven oder negativen Einfluss auf die Stabilität haben. Feuchte Luft hat einen vernachlässigbaren Einfluss auf die Tragfähigkeit, während die Stabilität von HGJBs um bis zu 25% reduziert werden kann. Die Auswirkungen der Kondensation eines reinen Fluids werden an einem eindimensionalen Linearlager bewertet. Ein Versuchsaufbau, bestehend aus einem radialen Rayleigh-Lager mit 20 mm Durchmesser, das sich mit bis zu 30 000 U/min in druckbeaufschlagtem R245fa-Kältemittel dreht, erlaubt es, dass vorgeschlagene Modell experimentell zu validieren, indem der Druck innerhalb des Gasfilms gemessen wird. Die theoretischen Eigenschaften eines Gasfilms im verdichteten

Zustand werden experimentell beschrieben.
Die Hybridisierung von Folienlagern mit aerodynamischen Axiallagern mit sprialförmigen Nuten wird untersucht, um die besten Eigenschaften beider Technologien zu kombinieren. Ein Modell, das auf der simple foundation Methode basiert, erlaubt es die Nutgeometrie dieser Hybridlager nach mehrerern Kirterien zu optimieren. Die Ergebnisse deuten darauf hin, dass die Tragfähigkeit verbessert und gleichzeitig die viskosen Verluste reduziert werden können. Die Tragfähigkeit profitiert jedoch nicht immer von den zusätzlichen Rillen. Letzendlich wird ein neues Konstruktionsverfahren vorgeschlagen, das die Robustheit der aerodynamischen Lager gegenüber Herstellungsfehlern maximiert und auf HGJBs angewendet wird. Basierend auf einer berechneten Tabelle mit dimensionsloser kritischer Masse wird dieser Hyperraum für einen bestimmten Rotor dimensioniert und gescannt. Dies ermöglicht die Bestimmung der Bereiche, welche die grössten Abweichungen, sowohl in der Nuttiefe, als auch im im Radialspiel, zulassen. Das Verfahren führt zu einer Paretofront der besten Fertigungstoleranzen, basierend auf den optimierten Lagerparameter.

Schlagworte: Energie, Aerodynamisches Lager, Reales Gas, Modellierung, Systemidentifikation, Experiment, Design, Optimierung

Contents

Acknowledgements i

Abstract (English/Français/Deutsch) iii

Contents ix

List of Publications xiii

List of Figures xv

List of Tables xxv

List of Acronyms xxvii

List of Symbols xxix

1 Introduction 1
- 1.1 Motivation 1
- 1.2 The grooved gas bearings 3
- 1.3 Goal and objectives 7
- 1.4 Thesis outline 8
- 1.5 Aspects of novelty 9

2 Theory 13
- 2.1 Narrow Groove Theory 15
- 2.2 Perturbation 22
- 2.3 Numerical implementation 28
  - 2.3.1 Discretization and resolution scheme 28
  - 2.3.2 Output and comparison 29
- 2.4 Experimental validation 36
  - 2.4.1 Test rig selection 40
  - 2.4.2 Theoretical force coefficients identification 43
  - 2.4.3 Test rig description 47
  - 2.4.4 Results 59
- 2.5 Chapter conclusion 67

3 Non-ideal gas lubrication 77
3.1 Real gas effects . . . 79
3.1.1 Introduction . . . 79
3.1.2 Theory . . . 80
3.1.3 Results and discussion . . . 82
3.1.4 Conclusion . . . 103
3.2 Humid air effects . . . 106
3.2.1 Introduction . . . 106
3.2.2 Theory . . . 108
3.2.3 Numerical computations and results . . . 111
3.2.4 Conclusions . . . 118
3.3 Thin film gas condensation in gas bearings . . . 122
3.3.1 Introduction . . . 122
3.3.2 Theory . . . 124
3.3.3 Numerical computations and results . . . 126
3.3.4 Experimental validation . . . 131
3.3.5 Conclusions . . . 148
3.4 Chapter conclusion . . . 151

4 Advanced bearing design 155
4.1 Gas Foil Spiral Groove Thrust Bearing . . . 157
4.1.1 Introduction . . . 157
4.1.2 Theory . . . 158
4.1.3 Numerical computations and results . . . 161
4.1.4 Conclusions . . . 169
4.2 Improvement of manufacturing through optimal tolerancing of HGJB . . . 173
4.2.1 Introduction . . . 173
4.2.2 Theory . . . 174
4.2.3 Numerical computations and results . . . 177
4.2.4 Conclusions . . . 186
4.3 Chapter conclusion . . . 188

5 Epilogue 191
5.1 Summary . . . 191
5.2 Future work . . . 193

A Reynolds equation 195

B Matrix coefficient of bearing impedance identification 199

C HGJB groove parameters measurements 201

D Parameters and displacement uncertainties **205**
- D.1 Rotor mass . . . 205
- D.2 Rotor transverse inertia . . . 205
- D.3 Rotor axial inertia . . . 206
- D.4 Center of mass position . . . 206
- D.5 Displacement probes . . . 207
  - D.5.1 Random error . . . 207
  - D.5.2 Linearity error . . . 208
  - D.5.3 Roundness error . . . 210
  - D.5.4 Filter and fit error . . . 212
- D.6 Temperature measurements . . . 214
  - D.6.1 Infra-red temperature sensors . . . 214
  - D.6.2 PT100 temperature sensors . . . 215

E Results of force coefficients identification is ambient air **217**

F Nucleation in saturated thin gas films **223**

Curriculum Vitae **227**

List of Publications

Journal articles as first author

The following articles were published as first author in peer-reviewed journals. They result directly from the work presented in this thesis.

1. **Guenat, E.**, Schiffmann, J., 2018. **Real-gas effects on aerodynamic bearings**. Tribology International 120, 358–368. doi:10.1016/j.triboint.2018.01.008
2. **Guenat, E.**, Schiffmann, J., 2018. **Effects of humid air on aerodynamic journal bearings**. Tribology International 127, 333–340. doi:10.1016/j.triboint.2018.06.002
3. **Guenat, E.**, Schiffmann, J., 2019. **Performance potential of gas foil thrust bearings enhanced with spiral grooves**. Tribology International 131, 438–445. doi:10.1016/j.triboint.2018.11.003
4. **Guenat, E.**, Schiffmann, J., 2019. **Multi-Objective Optimization of Grooved Gas Journal Bearings for Robustness in Manufacturing Tolerances**. Tribology transaction 61 (6), 1041-1050. doi:10.1080/10402004.2019.1642547
5. **Guenat, E.**, Schiffmann, J., 2019. **Thin gas film isothermal condensation in aerodynamic bearings**. Journal of Tribology 141 (11). doi:10.1115/1.4044447
6. **Guenat, E.**, Schiffmann, J., 2020. **Dynamic force coefficients identification of air-lubricated Herringbone Grooved Journal Bearing**. Mechanical Systems and Signal Processing 136, 106498. doi:10.1016/j.ymssp.2019.106498

Journal articles as co-author

The following articles were published as co-author in peer-reviewed journals. They do not take place in the scope of the dissertation but are the result of academic cooperation within the Laboratory for Applied Mechanical Design of EPFL.

1. Shalash, K., **Guenat, E.**, Schiffmann, J., 2018. **Spatially Sampled Pressure Profile Measurements in Externally Pressurized Gas Journal Bearings**. Tribology Transactions 61:6, 1094-1106. doi:10.1080/10402004.2018.1480078
2. Rosset, K., Mounier, V., **Guenat, E.**, Schiffmann, J., 2018. **Multi-objective optimization of turbo-ORC systems for waste heat recovery on passenger car engines**. Energy 159, 751–765. doi:10.1016/j.energy.2018.06.193

3. Gu, L., **Guenat, E.**, Schiffmann, J., 2020. **A Review on Grooved Gas Bearings.** Applied Mechanics Reviews 72 (1),010802. doi:10.1115/1.4044191
4. Isali, E., **Guenat, E.**, Schiffmann, J., 2020. **Analysis of spiral-grooved gas journal bearings by the narrow-groove theory and the finite element method at large eccentricities**, Journal of Tribology 142 (4), 041802. do:10.1115/1.4045636

List of Figures

1.1 Schematic principle of an heat pump cycle and a pressurized fuel cell . . . 2
1.2 Saturation curve in a temperature-entropy diagram, schematically showing the path of two isothermal compressions occurring in gas bearings: a compression subjected to a phase change of the lubricant, and a compression subjected to real-gas effects triggered by the proximity of the critical point 3
1.3 Illustration of a spectrum waterfall plot (frequency-time-amplitude) of an accelerating airborne rotor (of synchronous frequency Ω) experiencing a sudden sub-synchronous instability emerging at the rotor frequency Ω_c with a whirl frequency ω_c 4
1.4 Journal and axial thrust spiral groove bearings 5
1.5 Journal and axial thrust foil bearings 6
1.6 Comparison of a typical gas bearing clearance with other small-scale corpora 7

2.1 Approaches for the modelling of grooved gas bearings 15
2.2 Pressure fields for a large yet finite number of grooves N and an infinite number of grooves, resulting in the smooth profile 16
2.3 Control volume employed for the derivation of the smoothed pressure field 16
2.4 Schematic representation of a journal bearing 19
2.5 Schematic representation of perturbed bearing 23
2.6 Illustration of the evolution of the imaginary part of the equivalent impedance and the equivalent mass as a function the excitation frequency ω_{ex} and the eigenfrequency ω_0 respectively 27
2.7 Schematic representation of the discretization grid 28
2.8 5×5 grid of a bearing domain. P: Periodicity boundary condition, A: ambient boundary condition, C: mass continuity condition 30
2.9 Disposition of the terms in the matrices A for a 5×5 grid, in case of a HGJB with $\gamma = 1$. P: Periodicity boundary condition, A: ambient boundary condition, C: mass continuity condition 30
2.10 Process of iteratively solving the static pressure field to then compute the perturbed pressure field for each considered excitation frequency ω_{ex} . . . 31
2.11 Nomenclature of a HGJB 32
2.12 Computed pressure fields for the test bearing at two different relative eccentricities 33

2.13 Relative error made on the total load capacity at different grid sizes. The error is computed with the value evaluated at ($N_\theta = N_{\bar{z}} = 150$) as reference 34
2.14 Comparison of the computed reaction force in the radial direction with the output of the FEM model of Bonneau and Absi with 12 grooves. The original figure, assumed to have its vertical coordinate reported wrong, was rescaled using Fig. 3 of the reference, which corresponds well to Vohr and Chow [2] . . . 34
2.15 Comparison of the computed minimum critical mass with the results from Fleming and Hamrock [15] . . . 35
2.16 Predicted critical mass against non-dimensional mass or rotors at their onset on instability, with the data of Cunningham [17] . . . 37
2.17 Schematic of typical test rig for force coefficients identification, with the test bearing floating on a rigidly-mounted shaft, with shaker-induced excitations on the bushing, similarly to the rig of San Andres and Chirathadam [27] . 39
2.18 Schematic of typical test rig for force coefficients identification, with the test bearing fixed, supporting a floating rotor, with an impact hammer exciting the journal, as investigated by Le Rouzic and Arghir [28] 39
2.19 Nomenclature and coordinates of the rotating shaft supported on two gas bearings . . . 44
2.20 Principal lengths of the considered test rotor . . . 47
2.21 Picture of the investigated rotor, with the two HGJBs and the impulse turbine visible . . . 48
2.22 Evaluation of the first bending mode at rest and without journal bearings 48
2.23 Spectrum of the rotor free response (acceleration) after impulse from a soft hammer . . . 48
2.24 Representation of the excitation-measurement setup in one plane. The same setup is repeated in the orthogonal plane. . . . 49
2.25 Pareto front resulting from the two-objective optimization, showing the nominal clearance against the minimum logarithmic decrement Γ. 49
2.26 Stable domain of the bearing and chosen manufacturing tolerances around a nominal point . . . 50
2.27 Simplified rotor model assessing the relative influence of tilting stiffness on restoring torque . . . 51
2.28 Ratio of tilting stiffness over translational stiffness in the shaft restoring torque . . . 51
2.29 View of one of HGJB and its bushing . . . 52
2.30 Front view of a monolithic flexible bushing support . . . 52
2.31 Projected views of the flexible bearing support . . . 53
2.32 Cut view of the flexible bearing support showing the location of the PT100 probe . . . 54

2.33 Partial assembly showing the rotor mounted in the flexible supports equipped with piezo-shakers and the 8 capacitive sensors, denoted W_1 to W_8 54
2.34 Cut-view of the experimental apparatus showing the main components : capacitive sensors, piezo-shakers, rotor, turbine. The axial bearings are not represented on this view 55
2.35 Near-complete assembly, with the steel frame accommodating the different organs. The turbine distributor around the impulse turbine is missing for presentation purpose 55
2.36 Cut-view of the turbine distributor. Compressed air enters via two inlets, is equalized in an annular volume and expanded in 9 circumferential nozzles 56
2.37 Clearances of the two HGJBs measured on three angular location at each of 6 axial locations. Upper and lower values indicate the maximum and minimum values measures. The bold value indicate the mean of the three measures 56
2.38 Example of groove-ridge profile used to determine the groove depth 57
2.39 Radial centrifugal growth against rotor speed 57
2.40 Schematic cut-view representation of the aerostatic axial bearing 57
2.41 Experimental apparatus in vertical position 58
2.42 Speed over time for a test run at 100 krpm 61
2.43 Bushings and rotor temperature during the run at 100 krpm 61
2.44 Waterfall plot of the test run spectrum, with excitation signatures, synchronous vibration and turbine sub-synchronous noise visible 62
2.45 Amplitude of identified signals on the 8 proximity probes at different excitation frequencies, for the two orthogonal excitation runs 62
2.46 Peak-to-peak amplitude (diameter of the orbits of the bearings as different rotational speeds 63
2.47 Isovalue lines for the change in radial clearance (in µm) due to the change of temperature of the rotor and bushing from the reference temperature T_{ref} =21 °C 63
2.48 Change of radial clearance due to thermal expansion as a function of time for the test run at 100krpm, computed from Fig.2.47 the temperature profile of Fig.2.43 64
2.49 Parametric contribution of uncertainties on K_{xx} and K_{xy} for 100 krpm at an excitation frequency of 700 Hz 64
2.50 Parametric contribution of uncertainties on C_{xx} and C_{xy} for 100 krpm at an excitation frequency of 700 Hz 65
2.51 Results of identified force coefficient of bearing A for 100krpm in ambient air 68
2.52 Results of identified force coefficient of bearing B for 100krpm in ambient air 69
2.53 Results of identified force coefficient of bearing A for 70 krpm in ambient air at two relative excitation frequencies and different excitation amplitude 70
2.54 Effect of orientation on the measured performance at 100 krpm 70

2.55 Effect of orientation on the measured performance at 50 krpm 71

3.1 Illustration of the three situations studied in this Chapter: the real-gas effects leading to an increases gas compressibility (a), the humid air effect resulting from the partial condensation of water contained in air (b) and the partial condensation of a pure fluid (c) 78
3.2 Schematic representation in a temperature-entropy diagram of an isothermal compression starting from ambient pressure P_a to the saturation pressure P_{max}, close to the critical point 79
3.3 Geometry of the studied step bearing 83
3.4 Comparison of pressure distribution in a step slider bearing for two compressibility numbers, with R134a at $T_r = 1$, $P_r = 0.5$ 84
3.5 Evolution of the non-dimensional load capacity of an infinitely wide Rayleigh step bearing as a function of Λ for R134a. The dots indicate the points of a 10%-deviation from the incompressible solution 85
3.6 Isolines of W_r for a step slider bearing at $\Lambda = 1$ with R134a 85
3.7 Isolines of W_r for a step slider bearing at $\Lambda = 10$ with R134a 86
3.8 Isolines of maximum deviation of W_r between 10 different fluids for a step slider bearing at $\Lambda = 10$ as a function of reduced pressure and temperature 86
3.9 Isolines of compressibility factor Z (R134a) in the $T_r - P_r$ space 87
3.10 Isolines of parameter $(\partial_{\overline{\rho}}\overline{P})_T$ (R134a) in the $T_r - P_r$ space 87
3.11 Value of W_r along three different isolines of Z in the $T_r - P_r$ domain, for a step slider bearing ($\Lambda = 10$, R134a). The relative difference is indicated for each value of Z between the saturation point and $T_r = 1.1$ 88
3.12 Value of W_r along the isoline of $Z = 0.8$ in the $T_r - P_r$ domain, for a step slider bearing at three different values of Λ (R134a) 88
3.13 Maximum deviation on W_r over 10 different fluids along the isoline of $Z = 0.8$ in the $T_r - P_r$ domain, for a step slider bearing at $\Lambda = 10$. The relative difference is indicated for each value of Z between the saturation point and $T_r = 1.1$ 89
3.14 Isolines of W_r for a PJB (ϵ_x=0.2, $\epsilon_y = 0$, R134a) at $\Lambda = 1$ 90
3.15 Isolines of W_r for a PJB (ϵ_x=0.2, ϵ_y=0, R134a) at $\Lambda = 10$ 90
3.16 Evolution of W_r with Λ for a PJB (ϵ_x=0.2, ϵ_y=0, R134a) 90
3.17 Mid-span pressure profiles of a PJB (ϵ_x=0.6, ϵ_y=0) at $\Lambda = 1$ with R134a at $P_r = 0.75$ and $T_r = 1$ 91
3.18 Static locus of a PJB lubricated with R134a at $\Lambda = 1$ and $T_r = 1$ with a force acting along the x-axis. The angle ϕ designates the tilt angle of an arbitrary point 91
3.19 Isolines of M_r for a PJB (ϵ_x=0.2, $\epsilon_y = 0$, R134a) at $\Lambda = 1$ 92
3.20 Isolines of M_r for a PJB (ϵ_x=0.2, $\epsilon_y = 0$, R134a) at $\Lambda = 10$ 92
3.21 Evolution of the critical mass ratio with the compressibility number for a PJB (R134a, ϵ_x=0.2, $\epsilon_y = 0$) 93

3.22 Isolines of maximum deviation of W_r between 10 fluids for a PJB (ϵ_x=0.2, ϵ_y=0) at $\Lambda = 10$ 93
3.23 Isolines of maximum deviation of M_r between 10 fluids for a PJB (ϵ_x=0.2, ϵ_y=0) at $\Lambda = 10$ 94
3.24 Value of W_r along three different isolines of Z in the $T_r - P_r$ domain, for a PJB operated at $\epsilon_x = 0.5$ in R134a 94
3.25 Value of M_r along three different isolines of Z in the $T_r - P_r$ domain, for a PJB operated at $\epsilon_x = 0.5$ in R134a 95
3.26 Isolines of M_r for a HGJB (ϵ=0, R134a) at $\Lambda = 1$ 95
3.27 Evolution of M_r with T_r at $P_r = 0.5$ (R134a, $\epsilon = 0$) 96
3.28 Different domains of value of M_r for a HGJB (ϵ=0, R134a) at $\Lambda = 10$ . . 96
3.29 Position of the lines of maximum stability for a HGJB (ϵ=0, R134a) . . . 96
3.30 Position of the lines of maximum M_r for HGJB lubricated with 10 different fluids at $\Lambda = 10$ 97
3.31 Variation of W_r for a HGJB along three different isolines of Z in the $T_r - P_r$ domain (R134a, $\epsilon = 0.2$) 98
3.32 Variation of M_r for a HGJB along three different isolines of Z in the $T_r - P_r$ domain (R134a, $\epsilon = 0$, $\Lambda = 10$) 98
3.33 Isolines of Z in the $T_r - P_r$ domain together with the line of maximum stability of a HGJB operating in R134a at $\epsilon = 0$ and $\Lambda = 10$ 99
3.34 Evolution of the minimum critical mass with the compressibility number for different ambient reduced pressures (R134a) 99
3.35 Evolution of the ratio of minimum critical mass with the compressibility number for different ambient reduced pressures (R134a) 100
3.36 Evolution of W_r with Λ for HGJB at $\epsilon_x = 0.2$, $\epsilon_y = 0$ (R134a) 101
3.37 Evolution of W_r for PJB at $\epsilon_x = 0.2$ with turbulent flow ($P_r = 0.5$, $T_r = 1$, R134a) 101
3.38 Evolution of M_r for PJB at $\epsilon_x = 0.2$ with turbulent flow ($P_r = 0.5$, $T_r = 1$, R134a) 102
3.39 Evolution of M_r for HGJB at $\epsilon = 0$ with different values of Re_a ($P_r = 0.2$, $\Lambda = 5$, R134a) 102
3.40 Qualitative illustration of the evolution of the maximum stability line as the ambient Reynolds number increases for a given Λ 103
3.41 Dew lines in a Pressure-Temperature diagram, with the black dot as reference point. Starting from the point and following the dashed isothermal line, condensation can be reached at higher pressure depending on the ambient relative humidity (ϕ_a), when the corresponding dew line is crossed 107
3.42 Relative pressure and deviation along the circumference of a PJB at $\bar{z} = 0$, $\epsilon_x = 0.5$, $\phi_a = 0.8$ and $\Lambda = 30$. The pressure profile under condensable conditions is not represented, as it is indistinguishable from the non-condensable case 112
3.43 Isolines of W_r for PJB at $\epsilon_x = 0.5$ ($T_a = 308$ K) 113

3.44 Isolines of M_r for PJB at $\epsilon_x = 0.5$ ($T_a = 308$ K) . . . 113

3.45 Isolines of W_r for HGJB at $\epsilon_x = 0.05$ ($T_a = 308$ K) . . . 114

3.46 Isolines of M_r for HGJB at $\epsilon_x = 0.05$ ($T_a = 308$ K) . . . 114

3.47 Critical mass for HGJB at $\epsilon_x = 0.05$ ($T_a = 308$ K, $\phi_a = 1$) as a function of Λ with and without vapor condensation . . . 115

3.48 M_r and $M_{r,min}$ for HGJB at $\epsilon_x = 0.05$ ($T_a = 308$ K, $\phi_a = 1$) as a function of Λ . . . 115

3.49 Evolution of total stiffness and damping ratio for PJB and HGJB ($T_a = 308$ K, $\phi_a = 1$) as a function of Λ . . . 116

3.50 Evolution of W_r and M_r for HGJB and PJB with the eccentricity ratio (T_a= 308 K. Λ=5, ϕ_a=0.9) . . . 116

3.51 Evolution of the minimum value of $M_{r,min}$ for $\Lambda^* = 50$ with the eccentricity ratio for HGJB (T_a= 308 K, ϕ_a=1) . . . 117

3.52 Evolution of W_r and M_r for HGJB and PJB with the ambient temperature ($\Lambda = 5$, ϕ_a=0.9), together with the evolution of the minimum value of $M_{r,min}$ for ϕ_a=1 . . . 118

3.53 Void fraction as a function of temperature in the limit case where all the water content condenses (ϕ_a=1) . . . 118

3.54 Schematic representation in a temperature-entropy diagram of an isothermal compression starting from ambient pressure P_a to the saturation pressure P_{sat} corresponding to the ambient temperature T_a . . . 122

3.55 Description of the three evaluated 1D bearing geometries: Parabolic, Rayleigh step and wedge . . . 127

3.56 Pressure and density profiles in Case A for different saturation densities at $\Lambda = 20$ . . . 127

3.57 Density profiles in Case A for different compressibility numbers and $\bar{\rho}_{sat} = 1.3$ . . . 128

3.58 Pressure and density profiles in Case B for different saturation densities and $\Lambda = 20$ . . . 128

3.59 Density profiles in Case B for different compressibility numbers and $\bar{\rho}_{sat} = 1.3$128

3.60 Density profiles in Case C for different saturation densities and $\Lambda = 20$. 129

3.61 Density profiles in Case C for different compressibility numbers and $\bar{\rho}_{sat} = 1.3$129

3.62 Load capacity ratio in Case A for different saturation densities . . . 131

3.63 Load capacity ratio in Case B for different saturation densities . . . 131

3.64 Load capacity ratio in Case C for different saturation densities . . . 131

3.65 Local increase in the pressure profile leading to a net gain in load capacity. Case B, $\Lambda = 2$ . . . 132

3.66 Saturation pressure of R245fa . . . 132

3.67 Cut-view of Kingburry's gas bearing apparatus presented in 1897 . . . 133

3.68 Illustration of the geometry numerically simulated, with only one pocket represented . . . 134

3.69 Computed static pressure field of the Rayleigh step bearing for 70krpm, h_0 =6 µm and δ =10 µm, in air (1 bar, 305 K). 135
3.70 Critical mass, maximum relative pressure and drag torque in R245fa (1.4 bar, 305 K) for different step depths and clearances. The dots indicate the selected nominal values of h_0 and δ 135
3.71 Critical mass, maximum relative pressure and drag torque in air (1 bar, 305 K) for different step depths and clearances. The dots indicate the selected nominal values of h_0 and δ 136
3.72 Close-view on one of the pressure taps on the external surface of the bearing 136
3.73 Shape of the step resulting from the EDM process wire real-size wire diameter 137
3.74 Interface between the second pressure tap and the inner diameter of the bearing. The straight line is the delimitation of the step manufactured with EDM 137
3.75 Geometry of the Rayleigh step journal bearing in the circumferential direction (a) and Cut of the motor-rotor-bearing system perpendicular to the rotor axis (b) 138
3.76 Axial cut of the motor-rotor-bearing system: 1) Motor 2) Bearing 3) Rotor 4) Coupling 5) Pressure tap 138
3.77 Representation of the capillary system with gas reservoir 139
3.78 Pressure settling time in the taps against capillary diameter. Dashed lines indicated the selected diameter and the corresponding settling time 139
3.79 Rotor-Bearing assembly, with marks of balancing visible 140
3.80 Test apparatus: 1.MRBS 2.Cooling circuit 3.Circulation pump 4.Water reservoir 5.High-precision thermometer probe 6.Thermometer reader 7.Thermocouples 8.Thermocouple reader 9.Pressure scanner 10.Pressure pipe heater 11.DC source 12.Vessel 13.Motor drive 140
3.81 The pressure chamber (red, right) and the pressure scanner (left) of the test apparatus. The cooling water reservoir is visible behind the tank . . . 141
3.82 Location of the bearing thermocouple 141
3.83 Measured gauge pressure in time for different steps in speed toward 40 krpm 142
3.84 Predicted and measured pressure fields in air at three different speeds. Bearing temperatures are 31.0, 34.2 and 42.1 °C respectively 143
3.85 Comparison 1D and 2D model-measurements in ambient air at 40 krpm. Measurements uncertainty bounds are smaller that the diameter of the dots 144
3.86 Measured pressures against time in R245fa, $T_{bearing} = 23.4$°C $P_a = 96.0$ kPa, accelerating from 3.6 to 30 krpm 144
3.87 Comparison model-measurements in ambient air in non-saturated R245fa at 30 krpm, corresponding to $t = 100s$ in Fig. 3.86. Measurements uncertainty bounds are smaller that the diameter of the dots 145
3.88 Measured pressures and computed saturation pressures against time . . . 146
3.89 Influence of the opening and closing of the taps 2 to 5 on the pressure $\overline{P}_1$ 147
3.90 Model-experimental comparison of $\overline{P}_1$ and $\overline{P}_2$ over time 148

3.91 Model-experimental comparison of $\overline{P}_3$, $\overline{P}_4$ and $\overline{P}_5$ over time 149

3.92 Spectrum between start and touch-down of the rotor in R245fa, $P_a = 117\,\mathrm{kPa}$150

4.1 Geometry and nomenclature of GFSGTB 159

4.2 Geometry and nomenclature of inward-pumping GFSGTB 160

4.3 Comparison of the present model with reference [1] 162

4.4 Pareto fronts for $\Lambda = 0.1$ and different ramp depth ratios. 163

4.5 Solutions of maximum W_r for a compliance $\alpha_F = 1$ 164

4.6 Values of T_r for solutions with $W_r = 1$ for a compliance $\alpha_F = 1$ 164

4.7 Groove parameters corresponding to solutions in Figure 4.5 165

4.8 Contour of $100 \cdot (\overline{P} - 1)$ for the geometries maximizing the load capacity at $\Lambda = 5$ and different ramp depths 166

4.9 Evolution of the load capacity ratio against the bearing compliance at $\Lambda = 500$ and $\bar{h}_R = 1$ 167

4.10 Off-design performance ($\bar{h}_R = 20$) in terms of W_r of geometries optimized for $\Lambda = 0.1$ and 50 167

4.11 Off-design performance in terms of W_r of the geometry optimized for $\Lambda = 0.1$ and $\bar{h}_R = 20$ 168

4.12 Off-design performance in terms of W_r of the geometry optimized for $\Lambda = 50$ and $\bar{h}_R = 20$ 168

4.13 Off-design performance in terms of W_r of the geometry optimized for $\Lambda = 1$ and $\Lambda = 100$ 169

4.14 Case-specific dimensionalization of the universal stability look-up table . . 175

4.15 Location of the rectangle stability check points to verify that the rectangle covers no unstable points. Check points are either on a grid (black points) or randomly positioned (grey points). 176

4.16 Simplified representation of a stable domain on a slice (a), random generation rectangles in the stable domain (b) and determination of the particular Pareto front (c). The purple rectangle, falling outside of the feasibility domain, is discarded 177

4.17 Particular Pareto fronts projected to obtain the global front 178

4.18 Examples of stability limits for the considered rotor and α=0.6. The arrows indicate the orientation of the stable domain. 179

4.19 Global Pareto front for the nominal rotor-bearing system 180

4.20 Values of α and $\hat{\beta}$ resulting in the points shown in the Pareto front of Figure 4.19. 181

4.21 Values of $h_{0,\square}$ and $\delta_\square$ resulting in the points shown in the Pareto front of Figure 4.19. 182

4.22 Output parameters from the optimization maximizing the critical mass for different values of h_0. 183

4.23 Effect of the ambient pressure on the global Pareto front 183

4.24 Effect of the gas viscosity on the global Pareto front 184

4.25 Effect of the rotor radius on the global Pareto front 184
4.26 Effect of the rotor mass on the global Pareto front 184
4.27 Effect of the rotor maximum speed on the global Pareto front 185
4.28 Effect of parametric variation on the maximum clearance tolerance 185
4.29 Effect of parametric variation on the maximum groove depth tolerance . . 185
4.30 Effect of the centrifugal rotor radial growth on the tolerance Pareto Front 186

A.1 Surfaces in motion in a lubricant 195

C.1 Optical measurement of the groove angle using a digital microscope 201
C.2 Optical measurement of the groove aspect ratio using a digital microscope 202
C.3 Measurement of the groove depth using a rugosimeter 203

D.1 Close view of the annular mass removal scenario for estimation of the uncertainty on transverse inertia 206
D.2 Distribution of the recorded data from W_1 in static conditions around its mean value 207
D.3 Standard deviation due to random error of each of the 8 displacement channels 208
D.4 Uncertainty on the amplitude of the fitted sine from $2 \cdot 10^5$ data points . . 208
D.5 Uncertainty on the phase of the fitted sine from $2 \cdot 10^5$ data points, assuming a sine amplitude of 0.2 µm 209
D.6 Relative linearity error on the voltage, scaled on the full scale range of the sensor 209
D.7 Relative error on small relative displacements against the absolute position 210
D.8 Calibration apparatus assessing the measurement error due to curvature of the target 211
D.9 Absolute error on the position against target distance 211
D.10 Error on the local sensitivity of the probe 212
D.11 Distribution of relative amplitude error on the isolated signal for a noise ratio of 5 213
D.12 Distribution of absolute phase error on the isolated signal for a noise ratio of 5 213
D.13 Standard deviation of relative amplitude error on the isolated signal for different noise ratio 214
D.14 Standard deviation of absolute phase error on the isolated signal for different noise ratio 214
D.15 Setup for the calibration of the two IR probes 215
D.16 Results of the calibration, with the two sets of data and the corresponding regression 215
D.17 Setup for the calibration of the PT100 probes 216
D.18 Results of the PT100 calibration, with the two sets of data and the corresponding regression 216

(E.2) Bearing B, Direct stiffness 218
(E.3) Bearing B, Direct damping 218
E.3 Results of identified force coefficient for 50 krpm in ambient air 218
E.4 Results of identified force coefficient for 60 krpm in ambient air 219
E.5 Results of identified force coefficient for 70 krpm in ambient air 220
E.6 Results of identified force coefficient for 80 krpm in ambient air 221
E.7 Results of identified force coefficient of bearing A for 90 krpm in ambient air 222

F.1 Ratio of nucleation time over residence time against saturation pressure ratio for CO_2 224
F.2 Ratio of nucleation time over residence time against saturation pressure ratio for R134a, $T_r = 0.85$ 225

List of Tables

2.1 HGJB parameters employed for the examples of pressure fields 31
2.2 HGJB geometries corresponding to the maximization of $M_{c,min}$ according to [15], for rotating grooves and $L_z/D = 1$ 34
2.3 List of published experimental investigations of HGJB 38
2.4 List of published experimental investigations of HGJB 41
2.5 Qualitative comparison between the floating rotor and floating bearing configurations for the test rig 42
2.6 Qualitative comparison between the excitation methods 43
2.7 HGJB geometrical parameters 49
2.8 Summary of the average, mean minimum, mean maximum and extreme values of measured clearances 53
2.9 Fixed and variable rotordynamic model parameters nominal value and associated uncertainties as estimated in Appendix D 59

4.1 Parameters of the studied rotor 178

Nomenclature

Acronyms

CO_2	Carbon dioxide
COP	Coefficient of performance
DOF	Degree Of Freedom
EDM	Electrical discharge machining
EU	European Union
FDM	Finite difference method
FEM	Finite element method
FJB	Foil journal bearing
FTB	Foil thrust bearing
FVM	Finite volume method
GFSGTB	Gas foil spiral groove thrust bearings
HA	Humid air
HC	Hydrocarbons
HCFC	Hydrochlorofluorocarbons
HFC	Hydrofluorocarbons
HGJB	Herringbone groove journal bearing
JFO	Jakobson-Floberg-Olsson
MRBS	Motor-rotor-bearing system
NGT	Narrow groove theory
PDE	Partial Differential Equation

PEM	Proton exchange membrane
PJB	Plain journal bearing
SGTB	Spiral groove thrust bearing

Greek Symbols

α	Groove aspect ratio $\alpha = \frac{a}{a+b}$, rotor tilt angle in direction y
α_R	Foil compliance
β	Groove angle, bulk modulus, rotor tilt angle in direction x
$\Delta\delta$	Tolerance on the groove depth
δ	Groove depth, void fraction
$\delta_{\square}$	Nominal groove depth
ϵ	Eccentricity ratio
γ	Bearing groove ratio
κ	Relaxation coefficient
Λ	Compressiblity number
Λ_l	Local compressibility number
ρ	FDM density vector
μ	Dynamic viscosity
ν	Poisson ratio
Ω	Angular velocity
ω	Excitation frequency
ϕ	Relative humidity
Φ_{av}, Φ_{va}	Humid air viscosity coefficients
Ψ	Generic variable
ψ	Mass flux
ρ	Density
σ	Uncertainty, Squeeze number, Surface tension
θ	Angular coordinate

θ	Rotor tilt angle, fluid contact angle
E	Young's modulus

Roman Symbols

G	Gibbs free energy
J	Nucleation rate
k	Boltzmann's constant
S	Contact area
$\mathbf{A}$	FDM Matrix
$\mathbf{A}$	Matrix of relative displacement
a	Groove width, arbitrary coordinate
A	Integration variable
$\mathbf{b}$	FDM vector
$\mathbf{b}$	Vector of accelerations
b	Ridge width
B	Integration variable
$\tilde{c}_{vap}$	Molar concentration of water vapor
C	Damping coefficient
c_i	Saturation humidity ratio coefficients, $i = \{1, 2, 3\}$
c_s	NGT coefficient
C	Integration variable
$C_{x,r}$	Damping ratio
D	Diameter
D	Integration variable
$\mathbf{e}_x$	Unit vector in direction x
$\mathbf{e}_y$	Unit vector in direction y
$\mathbf{e}_z$	Unit vector in direction z
f	NGT coefficients

g	Elrod's switch function, Specific Gibbs free energy
g	NGT coefficients
$G_{\parallel}$	Turbulence correction factor along the displacement
$G_{\perp}$	Turbulence correction factor perpendicular to the displacement
Δh_0	Tolerance on the nominal clearance
Δh_{growth}	Radial centrifugal growth
h	Clearance
$h_{0,\square}$	Nominal clearance
i	Imaginary number
I_P	Moment of inertia along the axial direction
I_T	Transverse moment of inertia
K	Stiffness coefficient
K_f	Foil stiffness
$K_{x,r}$	Stiffness ratio
K_{θ}	Tilting stiffness
K_y	Radial stiffness
L	Length
L_A	Distance between bearing A and the center of mass
L_B	Distance between bearing B and the center of mass
L_W	Sensor-center of mass distance
$\dot{m}$	Mass flow rate, specific mass flow rate
$\tilde{m}$	Molar mass
m	Mass
M_c	Non-dimensional critical mass
m_c	Critical mass
M_r	Ratio of critical mass
m_R	Rotor mass

$M_{r,min}$	Ratio of minimum critical mass
N	Number of elements
N_{max}	Maximum rotor speed
P	Overall pressure
p	Pressure
P_r	Reduced pressure
P_V	Cavity pressure
$P{*}_{vap}$	Saturation vapor pressure
R	Radius
r	Specific gas constant, radial coordinate
r	Specific ideal gas constant
r_a	Specific gas constant in ambient conditions
Re	Reynolds number
T	Drag torque
T	FDM Matrix
t	Time
T_r	Ratio of restoring torques
T_r	Reduced temperature
T_θ	Restoring torque from bearing rotation
T_y	Restoring torque from bearing radial displacement
U	Tangential velocity
U	Velocity
u	Velocity
V	Velocity
v	Velocity
W	Load carrying capacity
w	Humidity ratio

$w*$	Saturation humidity ratio
W_i	Displacement sensor, $i = \{1, 2, 3, 4, 5, 6, 7, 8\}$
W_r	ratio of load capacity
w	Velocity
x_A	Position along x of bearing A
x_B	Position along x of bearing B
x	Cartesian coordinate, input variable of the impedance model
y_B	Position along y of bearing A
y_B	Position along y of bearing B
y	Cartesian coordinate
$\mathbf{z}$	Vector of impedances
Z	Impedance, compressibility factor
z	Cartesian coordinate

Superscripts

$\bar{}$	Non-dimensional
$\hat{}$	Complex norm

Subscripts

$\ominus$	Left-hand side of a boundary
$\oplus$	Right-hand side of a boundary
θ	Direction θ, circumferential direction
g	Groove
$hetero$	Heterogeneous nucleation
$homo$	Homogeneous nucleation
l	Liquid phase
$land$	Land region
nom	Nominal
r	Ridge

s	Normal to groove
v	Vapor phase
0	Static, nominal
1	Perturbed
A	Relative to bearing A
a	Ambient
air	Dry air
B	Relative to bearing B
c	Critical
$cond$	Condensable
eq	Equivalent
ig	Ideal gas
min	Minimum
$non-cond$	Non-condensable
rg	Real gas
sat	Saturation
vap	Water vapor
w	Liquid water
x	Direction x, variables
y	Direction y
y	Direction z, axial direction
A	Surface A
B	Surface B
el	electrical
th	thermal

1 Introduction

1.1 Motivation

The Paris agreement [1] is seen as the response of most nations to the threat of climate change, enforcing a decarbonization of all activity sectors, with an objective for the European Union (EU) to reach net 0 carbon dioxide emissions in the second half of the 21^{st} century. In 2016, 20% of EU's CO_2 emissions resulted from road transport [2], while the residential sector contributed to half as much [3], mostly for heating purposes. In both sectors, the pathway for decarbonization consist in a major shift toward electrification [4], switching from direct use of fossil fuel to the EU's electricity mix, which is called to switch massively from fossil to renewable sources. The generalized use of heat pumps for households heating has a great potential of lower net CO_2 emissions only if the coefficient of performance (COP) compensates for the overall conversion/transport efficiency of fossil fuel fired thermal power plants, a condition that is not always met. An efficient and compact compressor technology is paramount to achieve both high COP while being economically advantageous [5]. In the transportation sector, fuel cells (FC) and batteries are both being extensively investigated by the automotive industry as mean of embedded energy storage. Efficiency and compactness are key characteristics to achieve mass penetration. Typically, the Proton Exchange Membrane (PEM) is the leading technology for fuel cells in the automotive industry because of its high power density, which can be further increased together with the electrical efficiency if pressurized air is forced into the stack [6], typically by the mean of a centrifugal compressor. Figure 3.75 illustrates these two applications, heap pumping and PEM-FC pressurization, employing a centrifugal compressor.

Both heat pump cycles and PEM fuel cells are sensitive to pollutants: lubricant oil transported from the compressor in the refrigerant loop lowers the heat transfer coefficient in heat pumps [7]. In PEM, oil-polluted air fatally poisons the stack. Oil-free turbocompressors can fulfill all the requirements of cleanliness, high power density and efficiency. A dynamic compression allows a wide operating range in both pressure ratio and mass flow

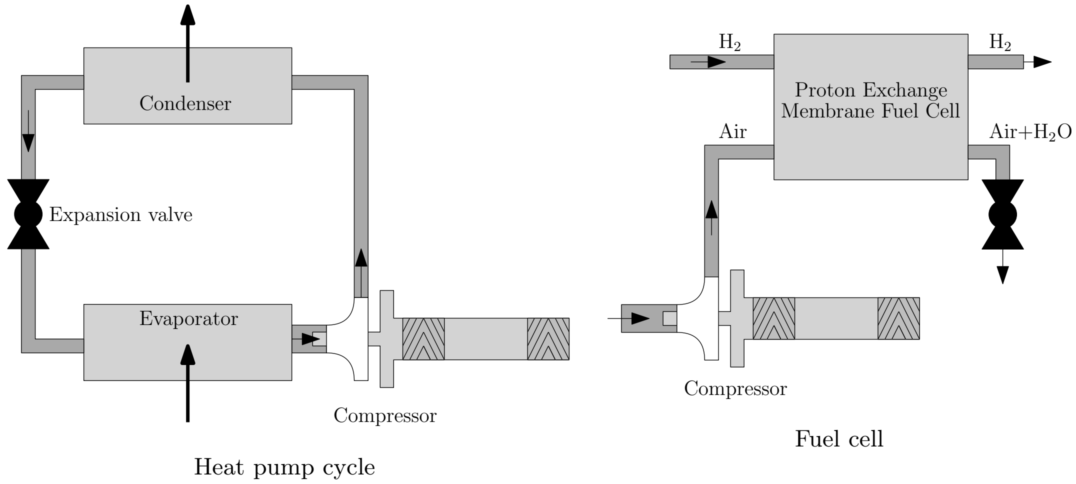

Figure 1.1 – Schematic principle of an heat pump cycle and a pressurized fuel cell

rate, as well as a potential for high isentropic efficiency. The use of aerodynamic bearings enables high speed rotors (and therefore reduced dimensions) thanks to very low friction coefficients, cleanliness by the absence of secondary lubricant and a high lifespan compared to other bearing technologies due to absence of physical contact between mechanical parts.

The use of the ideal gas law for the modelling of bearings have been the state of the art for decades, since most applications have been actually operating in low-pressure, high-temperature conditions with a low risk of phase transition. Because aerodynamic bearing typically operate with a near-isothermal behavior, a local increase in gas film pressure can lead to the saturation of the lubricant and subsequent phase change, a problem which can occur not only in pure condensable fluids (refrigerants), but also in humid air, as the water content can condensate if the dew pressure is reached. In case of refrigerant-lubricated bearings operating close to the critical point, the compressibility of the gas increases and deviates from the ideal gas law. The path leading to the two phenomenon is represented in en temperature-entropy diagram in Figure 1.2. The further development of gas bearing in (inverse) organic Rankine cycles and PEM-FC pressurization is limited by the understanding of gas lubrication in conditions of high pressure gases subject to real gas and two-phase flow effects. These effects have been insufficiently explored in the literature, both experimentally and theoretically. The available literature is at best extremely case-specific, making no use of non-dimensional numbers and provide a poor understanding of the mechanism playing a role in the relevant phenomenon, as it will later developed in dedicated sections.

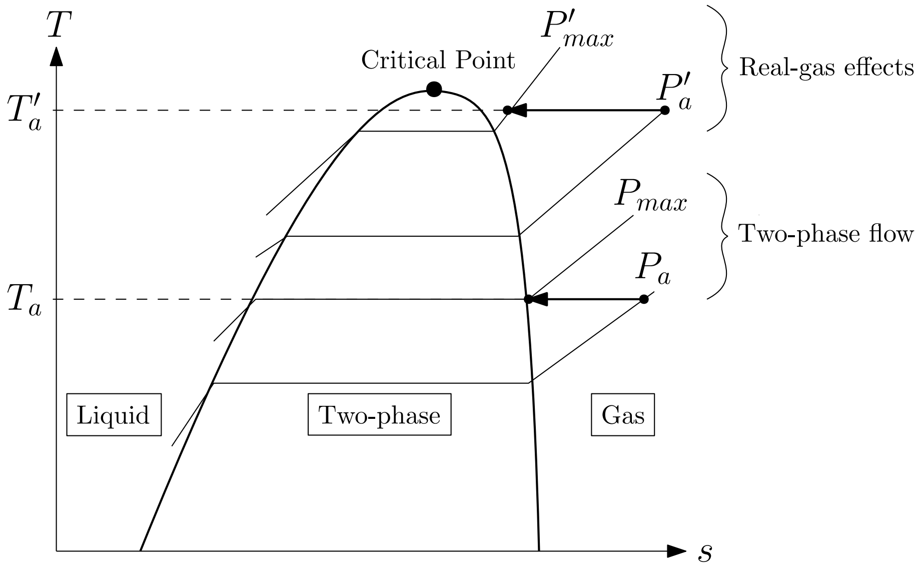

Figure 1.2 – Saturation curve in a temperature-entropy diagram, schematically showing the path of two isothermal compressions occurring in gas bearings: a compression subjected to a phase change of the lubricant, and a compression subjected to real-gas effects triggered by the proximity of the critical point

1.2 The grooved gas bearings

The gas bearing technology has been a research topic for the last six decades and accompanied the rapid development of aerospace and nuclear industry in the mid-20th century [8]. During the past two decades, gas bearing made their way to small-scale centrifugal compressors of vapor compression (heat pump) cycles and as multi-purpose gas compressors, including the fuel cell pressurization for embedded applications. Among the gas bearing technologies applied to turbomachinery, compliant foil bearings (Figure 1.5) and spiral groove bearings (Figure 1.4) are notorious, with former occupying the larger scale (typically above a rotor diameter of 30 mm) and latter the smaller scale. Aerodynamic bearings are prone to sub-synchronous whirl because of the compressible nature of the lubricant, which induces a frequency-dependency of the bearing impedance on top of high cross-coupled stiffnesses and low damping coefficients. First described as a "half-speed whirl" because it appears, for simple plain cylindrical bearings, in the form of a growing orbit whirling at approximately half the synchronous frequency, as illustrated in Figure 1.3). This instability has been the major issue in the development of this technology in the early 1960's [8]. Grooved bearings mitigate this stability issue with the pumping effect of the grooves in order to reduce the cross-coupled stiffness while improving the damping of the gas film. In order to guarantee a stable operation, a very tight clearance is required as illustrated in Figure 1.6, which has very stringent manufacturing tolerances typically ranging in 10% of the clearance. This tight range of feasibility is a bottleneck for cost-effective mass production of high-speed rotors with HGJBs and motivate a significant research effort for means of improving the stability threshold of gas lubricated bearings, which would result in a relaxation of the manufacturing constraints and thus lead to reduced costs. Such methods include the use of flexibly supported bushings [9], external magnetic dampers [10] or enhanced bearing geometries [11]. However, typical design strategy aim at maximizing the nominal stability of a rotor-bearing system with little attention paid to the actual sensitivity of the stability against manufacturing deviations on critical parameters such as the bearing clearance. When accordingly designed, grooved bearings generally enjoy a large stiffness and stability, but they do not tolerate any touch-down at high speed and have a limited load capacity at high eccentricity. Foil bearings deal with the sub-synchronous instability problem with a compliant surface, which provides a taylorable clearance distribution and additional damping thanks to the rubbing between layers of foils. This also allows a tolerance against a rupture of lubricant film at high speed (leading to a direct mechanical contact between moving parts) and can comply with thermal and centrifugal growth of the rotor. However, this technology suffers from a high sensitivity on geometrical properties of the compliant structure for both their static and dynamic properties [12], which cannot always be repeated. Finally, they typically provide a lower stiffness because of the compliant structure added in series with the gas film. The two families of gas bearings have remained surprisingly segregated during the past decades, with very limited attempts to combine grooved and foil bearing in a quest to combine the best of the two worlds.

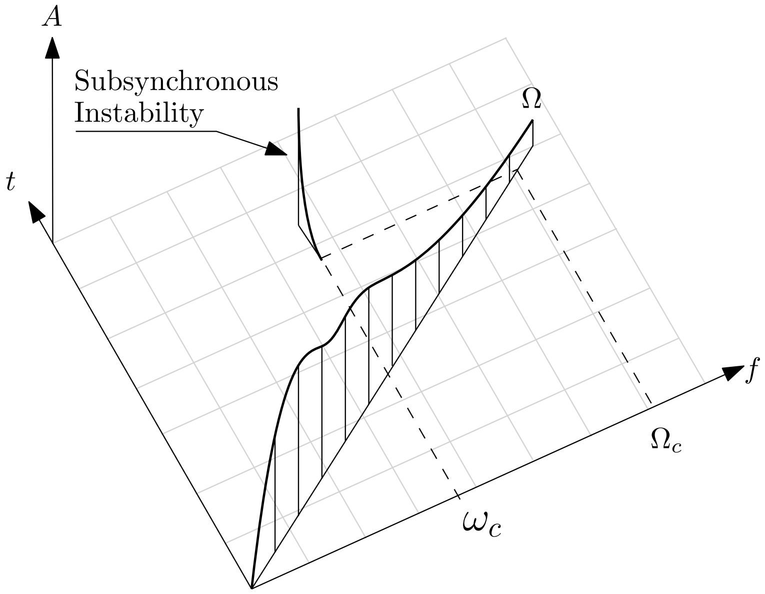

Figure 1.3 – Illustration of a spectrum waterfall plot (frequency-time-amplitude) of an accelerating airborne rotor (of synchronous frequency Ω) experiencing a sudden sub-synchronous instability emerging at the rotor frequency Ω_c with a whirl frequency ω_c

The further development and improvement of aerodynamic bearing in the scope of high-speed turbomachinery for the mentioned applications follows three key pathways:

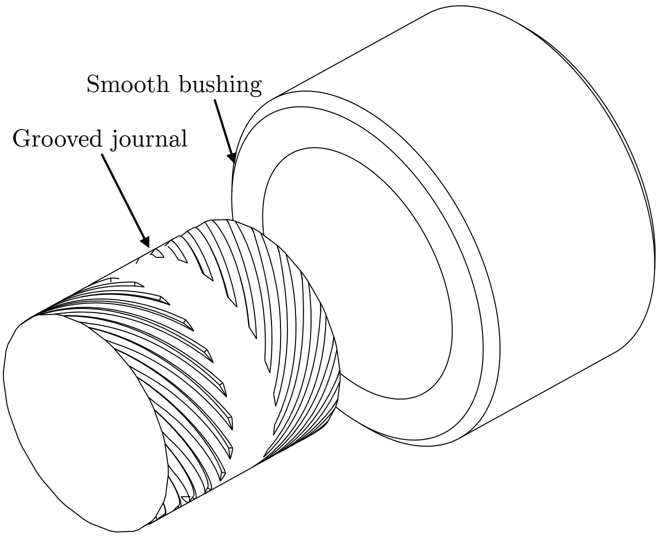
Smooth bushing
Grooved journal

a) Herringbone grooved journal bearing

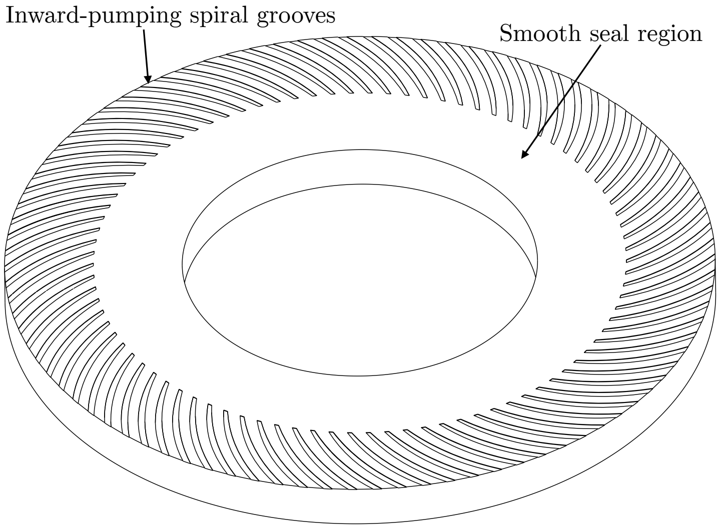
Inward-pumping spiral grooves
Smooth seal region

b) Inward-pumping spiral groove thrust bearing

Figure 1.4 – Journal and axial thrust spiral groove bearings

1) An in-depth understanding of phenomena likely to appear in actual gas lubricant, due to the proximity to the critical point (real gas effects), to a phase change of the lubricant (condensation) or to the dew point of moist air (humid air effects). These effects on gas lubrication and on bearing performance are, at best, barely investigated in the literature, although applications of aerodynamic bearing are prone to meet conditions where such

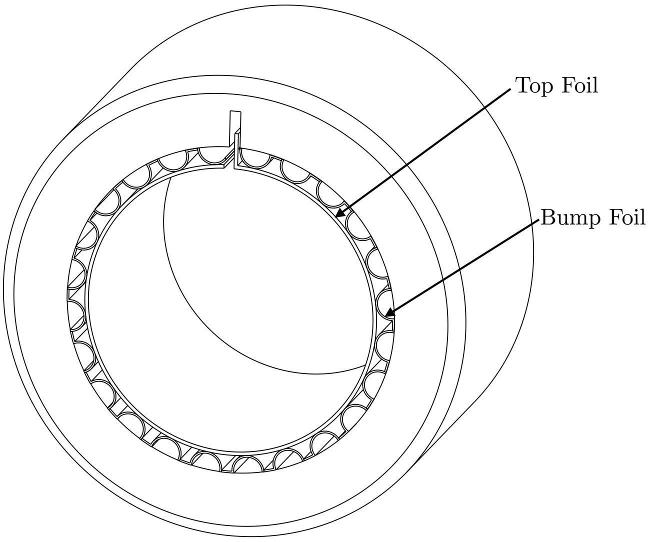

a) Foil journal bearing

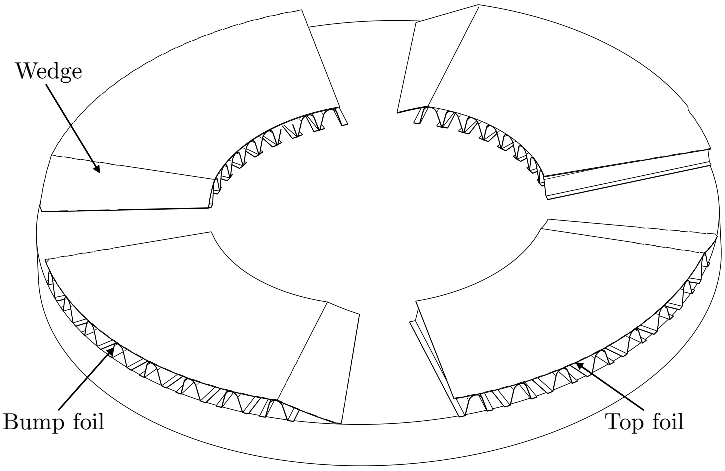

b) Axial thrust foil bearing

Figure 1.5 – Journal and axial thrust foil bearings

effect may have a significant influence.

2) The identification of the relevant optimization procedure for the design issue of gas bearing, especially regarding the constraint on stability and the tight manufacturing tolerances. The quest for cost-effective and mass-oriented manufacturing would benefit from new optimization approaches.

3) A exploration of new gas bearing layouts at the interface between foil and grooved gas bearing families, in an attempt to combine the best of the two worlds in the form of foil

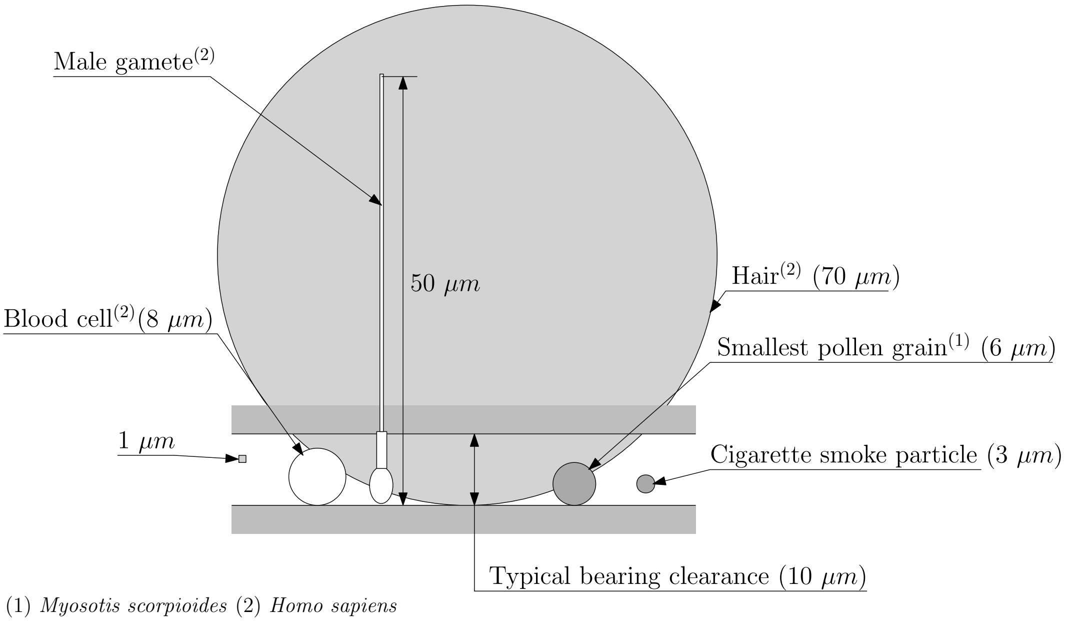
Male gamete$^{(2)}$
50 μm
Hair$^{(2)}$ (70 μm)
Blood cell$^{(2)}$(8 μm)
Smallest pollen grain$^{(1)}$ (6 μm)
1 μm
Cigarette smoke particle (3 μm)
Typical bearing clearance (10 μm)
(1) *Myosotis scorpioides* (2) *Homo sapiens*

Figure 1.6 – Comparison of a typical gas bearing clearance with other small-scale corpora

bearings enhanced with spiral grooves.

1.3 Goal and objectives

The goal of the thesis is to explore the three mentioned approaches to improve the understanding of non-ideal gas effects occurring on aerodynamic bearings, improve the design methodology of such mechanical systems and propose new layouts. In order to reach this goal, the objectives are listed as follows:

1. Implementation of a numerical model of rigid gas journal bearing based on the theory of lubrication able to accommodate diverse non-ideal gas effects
2. Validation of the model by the mean of a novel test rig able to experimentally measure the dynamic impedance of HGJBs in ambient air
3. Theoretical and numerical assessment of the effects of real gas, humid air and condensation on various geometries of aerodynamic bearings
4. Validation of the model in saturation condition by the mean of a dedicated test rig operating in refrigerant
5. Development of new optimization techniques suitable of the maximization of robustness in aerodynamic bearings
6. Assessment of the potential of foil gas bearings enhanced with spiral grooves

1.4 Thesis outline

The thesis is articulated around three chapters.

Chapter 2 introduces the theory and numerical tools for the modelling of aerodynamic bearings. The Narrow Groove Theory (NGT) is derived. The perturbation method and the procedure for the estimation of linear dynamic force coefficients (stiffness and damping) are presented. The output of the numerical tool is compared to published numerical results for sanity check. A test rig for the experimental evaluation of dynamic force coefficients of 16 mm air-lubricated HGJBs is presented. Results at different rotor speed, excitation frequency and static eccentricities are presented and compared to the numerical predictions, with good agreement. This chapter led to one published journal paper.

Chapter 3 investigates different aspects of non-ideal gas lubrication on aerodynamic bearings, with a focus on grooved bearings. The real-gas effects are investigated with non-dimensional numbers on three different bearing types with the load capacity and stability (critical mass) as comparison metrics. The effects of humid air are also studied, with the development of a modified Reynolds equation and the NGT able to account for partial condensation of moisture in the lubricant. The model is employed to address these effects on load capacity and stability. Finally, the theory for the modelling of bearings with a saturated gas lubricant prone to condensation is proposed. The numerical model is applied on three linear bearing geometries and general effects on the pressure field are investigated. A test rig, consisting of a short rotor on a Rayleigh step bearing, is presented. The apparatus, that is able to measure the pressure of the bearing gas film in several locations, is ran in refrigerant and experimentally validates the numerical model and the underlying theory. This chapter led to three published journal papers, one for each section.

Chapter 4 explores new possibilities in bearing layouts and design procedure. A new design of axial thrust gas bearing is proposed, which consists of a compliant foil bearing enhanced with spiral grooves manufactured on its top foil. A numerical model is developed and implemented, associating the NGT with a compliant bearing structure. Multi-objective optimization of the groove pattern allows to find Pareto-optimum geometries with the load capacity and the drag losses as objectives. It is found that the spiral grooves can improve the load capacity and/or the drag losses of such thrust bearings. Finally, a new optimization method for grooved journal bearing is proposed, allowing to design gas bearings maximizing the robustness against manufacturing errors rather than sole stability metric. The method is applied on a case study to appreciate the dominant parameters allowing a large manufacturing tolerance of grooved bearings. This chapter led to two published journal papers, one for each section.

1.5 Aspects of novelty

The presented thesis contains several aspects of novelty, which are summarized below:

1. Experimental validation of the modelling theory of grooved bearing by the measurement of dynamic force coefficients of herringbone-grooved journal bearings in air
2. Non-dimensional investigation of real-gas effects on lubrication and gas bearing performance (load capacity and stability of plain and herringbone-grooved journal bearing)
3. Adaptation of the Reynolds equation to account for partial condensation in humid air lubricated bearings. Non-dimensional investigation of humid air effects on lubrication and gas bearing performance (load capacity and stability of plain and herringbone-grooved journal bearing).
4. Formulation of a physically consistent model to predict pressure fields of saturated gas bearing experimentally validated on a refrigerant-lubricated Rayleigh-step journal bearing
5. Theoretical investigation of axial thrust foil bearings enhanced with spiral grooves improving the load capacity and/or reducing the drag torque
6. New optimization strategy and tolerancing technique allowing a cost-oriented design of herringbone-grooved journal bearings maximizing the robustness against manufacturing errors

Bibliography

[1] UNFCCC, Adoption of the Paris Agreement, Tech. Rep. FCCC/CP/2015/L.9/Rev.1, (2015).

[2] European Commission, Road transport: Reducing CO2 emissions from vehicles (Nov. 2016).
URL https://ec.europa.eu/clima/policies/transport/vehicles_en

[3] Europan Environment Agency, Sectoral greenhouse gas emissions by IPCC sector.
URL https://eea.europa.eu/data-and-maps/daviz/change-of-co2-eq-emissions-2

[4] A. Hoen, A. v. Grinsven, B. Kampman, J. Faber, H. v. Essen, I. Skinner, European Parliament, Directorate-General for Internal Policies, Policy Department B. : Structural and Cohesion Policies, European Parliament, Committee on Transport and Tourism, Research for TRAN Committee–Decarbonisation of EU transport: study, 2017, oCLC: 1003585333.

[5] F. C. Possamai, M. L. Todescat, A Review of Household Compressor Energy Performance, 2004, p. 9.

[6] J. M. Cunningham, M. A. Hoffman, D. J. Friedman, A Comparison of High-Pressure and Low-Pressure Operation of PEM Fuel Cell Systems, SAE Transactions 110 (2001) 464–470.

[7] K. Hambraeus, Heat transfer of oil-contaminated HFC134a in a horizontal evaporator, International Journal of Refrigeration 18 (2) (1995) 87–99. `doi:10.1016/0140-7007(94)00004-H`.

[8] D. D. Fuller, A Review of the State-of-the-Art for the Design of Self-Acting Gas-Lubricated Bearings, Journal of Lubrication Technology 91 (1) (1969) 1–16. `doi:10.1115/1.3554857`.

[9] T. Waumans, J. Peirs, F. Al-Bender, D. Reynaerts, Aerodynamic journal bearing with a flexible, damped support operating at 7.2 million DN, Journal of Micromechanics and Microengineering 21 (10) (2011) 104014. `doi:10.1088/0960-1317/21/10/104014`.

[10] A. Looser, J. W. Kolar, An Active Magnetic Damper Concept for Stabilization of Gas Bearings in High-Speed Permanent-Magnet Machines, IEEE Transactions on Industrial Electronics 61 (6) (2014) 3089–3098. `doi:10.1109/TIE.2013.2284152`.

[11] J. Schiffmann, Enhanced Groove Geometry for Herringbone Grooved Journal Bearings, Journal of Engineering for Gas Turbines and Power 135 (10) (2013) 102501. `doi:10.1115/1.4025035`.

[12] K. Shalash, J. Schiffmann, Comparative Evaluation of Foil Bearings With Different Compliant Structures for Improved Manufacturability, in: Volume 7A: Structures and Dynamics, ASME, Charlotte, North Carolina, USA, 2017, p. V07AT34A014. `doi:10.1115/GT2017-63615`.

2 Theory

The modelling of fluid bearings began with the classic article of Reynolds in the 19^{th} century. Starting from the Navier-Stokes equations and making a number of assumptions regarding the dominant forces in the fluid film, a comprehensive differential equation, the Reynolds equation, is obtained. Under the assumption of thin viscous Newtonian fluid, it is valid for both compressible and incompressible lubricants. This theory has long proven its reliability as a design and investigation tool in a very broad range of bearing layout and operating conditions. Analytic solutions to the Reynolds equation were first developed for simplistic conditions such as infinitely long, centered plain bearings. With the advancement of computational resources, numerical methods such as the Finite Difference Method (FDM) emerged to approach solutions of less restrictive cases, including bearing of finite length, eccentric and with a more complex geometry than smooth coaxial cylinders. However, the use of textured bearings was too demanding in term of computational resources, as discretization needs to resolve the texturing pattern to approach a solution. In particular, the use of spiral grooves to pump the lubricant toward the center of the bearing was beyond the grasp of direct numerical methods.

Whipple [1] introduced a generalization of the Reynolds equation able to account for the effect of infinitesimal spiral grooves manufactured on the bearing, without having to resolve the individual grooves one by one. This tool, the Narrow Groove Theory (NGT), add the assumption of infinitely narrow grooves. A consequence of this assumption is that the pressure follows a linear profile between each groove-ridge pair, and therefore the fluid can be considered locally incompressible, regardless of its macroscopic compressibility. The groove-ridge pressure fluctuations become insignificant at macroscopic scale, yielding a smooth pressure field. Practically, the NGT is a Reynolds equation with additional terms accounting for the presence of grooves.

The NGT being a modified Reynolds equation, any numerical method suited for the Reynolds equation should fit the NGT. Historically, it was first solved using a perturbation method around the centered position [2], leading to a static pressure field (generating the static load capacity) and a perturbed pressure field (generating the dynamic impedance). The NGT can be simplified to the point where the static field of a radial bearing can be analytically integrated. The perturbed pressure field, result of the solution of a linear differential equation, therefore leads to a solution valid only in the vicinity of the bearing center. This initial approach propagated a misconception over the years on the validity domain of the NGT, with authors such as Bonneau and Absi [3] and Zirckelback and San Andres [4] comparing the centered NGT against their own eccentric Finite-Element simulations of grooved journal bearing, unfairly concluding that NGT is not valid at high eccentricity. However, the NGT remains valid in eccentric solution, as shown by Castelli and Vohr [5], who validated the eccentric NGT with experimental data. They used a Finite Difference scheme to solve the static pressure field of a HGJB. Authors have used this method to either solve the NGT in a time-wise integration [6] or after performing a perturbation method [2], which holds the advantage of directly providing the linear frequency-dependent force coefficients (stiffness and damping coefficients). No reference used a Finite Element and Finite Volume methods to solve it, although nothing prevents it *a priori*.

With the increasing computational power of the late 20th century, authors have solved the Reynolds equation on bearing with grooves of finite length, either with the Finite Element Method (FEM) (Bonneau and Absi [3], Zirckelback and San André [4], Faria and San Andrés [7]), FDM (Constantinescu and Castelli [8]) or Finite Volume Method (FVM) (Yu et al. [9]). An overview of the different modeling approaches is summarized in Figure 2.1. However, a bearing with a finite number of rotating grooves is excessively difficult to analyze, since the pressure field never reaches a steady state, making the Reynolds much more difficult to treat numerically. Additionally, the necessity to discretize the fluid domain in such a way that it resolves well the individual grooves and ridges leads to a very large number of discretization points, and therefore a large computational cost.

Overall, its computational simplicity makes the NGT a good candidate not only as design tool, but also as a bearing analysis framework since it can inexpensively capture the overall effect of rotating grooves, while methods resolving the Reynolds equation struggle to obtain a solution and extract useful information out of it. Therefore, the NGT is chosen as the modelling tool for grooved gas bearings, using the perturbation method to distinguish between static and dynamic pressure fields. The Reynolds equation is used to model the other type of gas bearings investigated in this work. The FDM is selected to solve the constitutive equations, as it is a versatile method, robust against modifications that might be brought to the Reynolds equation to capture non-ideal gas lubrication.

The present chapter presents the development of basic lubrication equations as well as the adopted numerical method to solve them and extract bearing properties. This theory is common to all chapters, however, each chapter will provide its complementary theoretical background, specific to each problem.

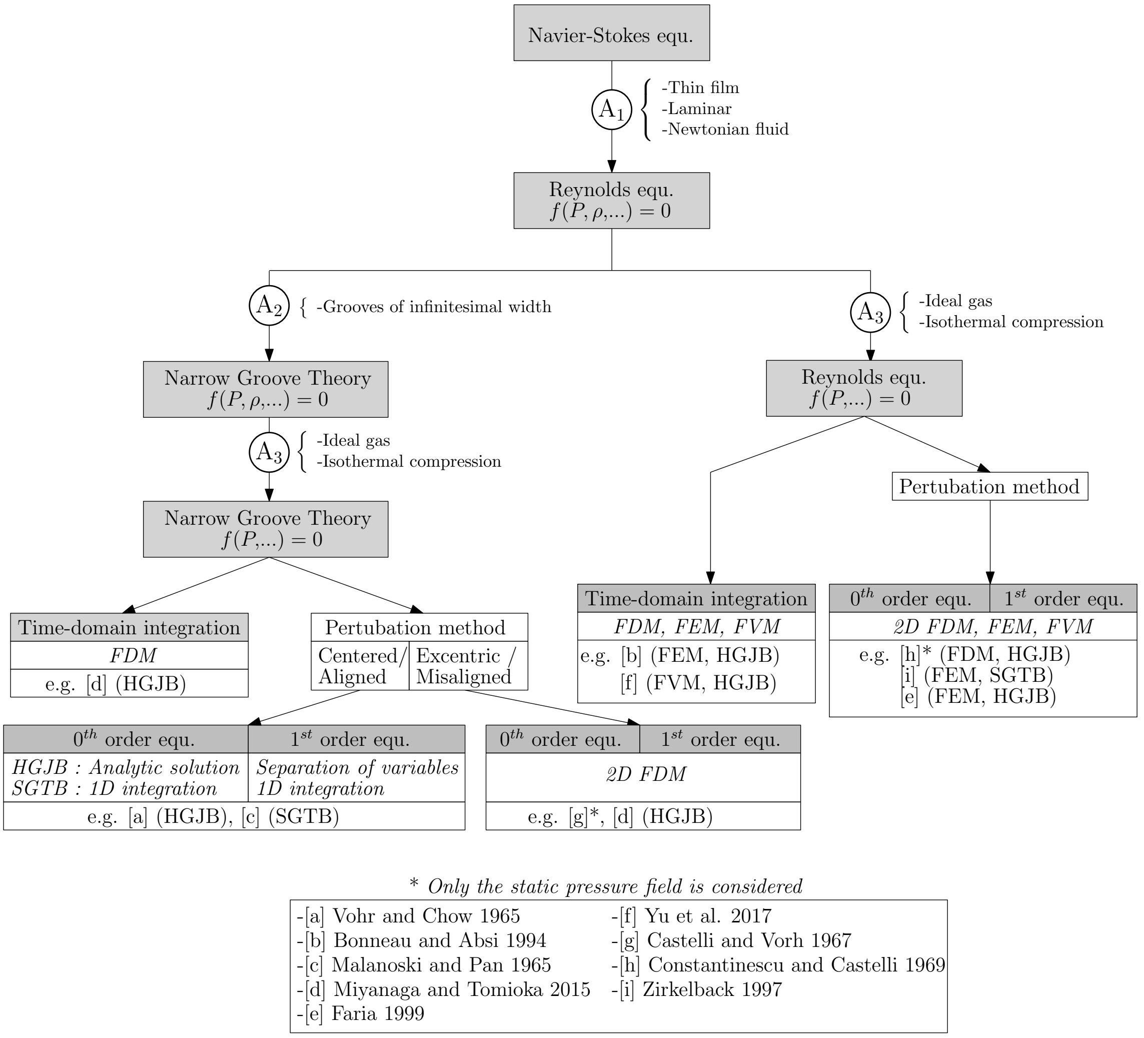
Navier-Stokes equ.
A1
-Thin film
-Laminar
-Newtonian fluid
Reynolds equ.
f(P, ρ,...) = 0
A2
-Grooves of infinitesimal width
A3
-Ideal gas
-Isothermal compression
Narrow Groove Theory
f(P, ρ,...) = 0
A3
-Ideal gas
-Isothermal compression
Narrow Groove Theory
f(P,...) = 0
Reynolds equ.
f(P,...) = 0
Pertubation method
Time-domain integration
FDM
e.g. [d] (HGJB)
Pertubation method
Centered/ Aligned
Excentric / Misaligned
Time-domain integration
FDM, FEM, FVM
e.g. [b] (FEM, HGJB)
[f] (FVM, HGJB)
0th order equ.
1st order equ.
2D FDM, FEM, FVM
e.g. [h]* (FDM, HGJB)
[i] (FEM, SGTB)
[e] (FEM, HGJB)
0th order equ.
1st order equ.
HGJB : Analytic solution
SGTB : 1D integration
Separation of variables
1D integration
e.g. [a] (HGJB), [c] (SGTB)
0th order equ.
1st order equ.
2D FDM
e.g. [g]*, [d] (HGJB)
* Only the static pressure field is considered
-[a] Vohr and Chow 1965
-[b] Bonneau and Absi 1994
-[c] Malanoski and Pan 1965
-[d] Miyanaga and Tomioka 2015
-[e] Faria 1999
-[f] Yu et al. 2017
-[g] Castelli and Vorh 1967
-[h] Constantinescu and Castelli 1969
-[i] Zirkelback 1997

Figure 2.1 – Approaches for the modelling of grooved gas bearings

2.1 Narrow Groove Theory

The NGT aims to describe the overall effect of grooves manufactured on either the rotating or the static side of a gas bearing, without resolving the individual effect of a groove. It is based on the same hypothesis as the Reynolds equation (developed in Appendix A):

- The lubricant is a Newtonian fluid
- The film thickness is much smaller than the two other orthogonal directions
- The fluid characteristics (viscosity, pressure, density) are constant across the film thickness
- Viscous forces dominate the inertia and the flow is laminar

On top of the classic assumptions of lubrication, the NGT assumes that the grooves are of infinitesimal width, which would be approached by a bearing having a infinite number of grooves, as pictured in Figure 2.2. The result is a global modified Reynolds equation, which can be solved conveniently without the use of fine meshes to resolve each groove. The theory was pioneered by Whipple and Vohr and Pan for arbitrary geometries. Vohr and Chow applied the theory on journal bearing and to investigate the performance of Herringbone Grooved Journal Bearings (HGJBs), and Malanoski used it to evaluate the performance of Spiral Groove Thrust Bearings (SGTBs). Hsing derived the theory adding correction terms accounting for rarefied gas and turbulence, by modification of the viscosity term. Following the work of Vohr and Chow [2] and Hsing [10], the classical NGT is derived here.

Consider the control volume described in Figure 2.3. The grooved and smooth members move at a linear velocity u_a and u_b respectively. The same four assumptions as for the Reynolds equation are made for the following development.

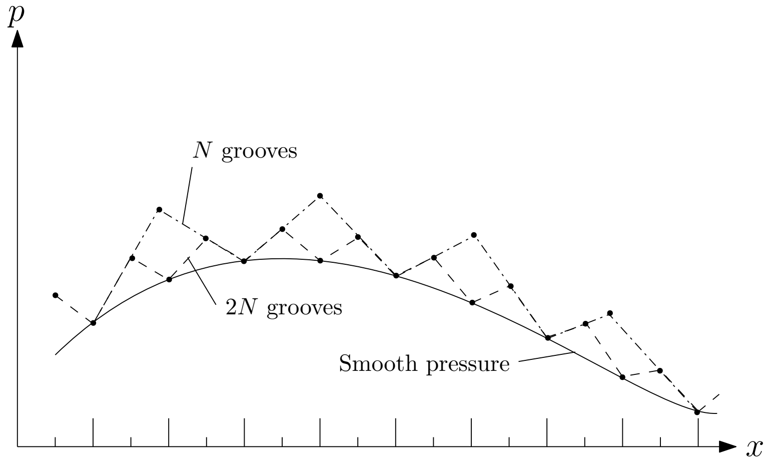

Figure 2.2 – Pressure fields for a large yet finite number of grooves N and an infinite number of grooves, resulting in the smooth profile

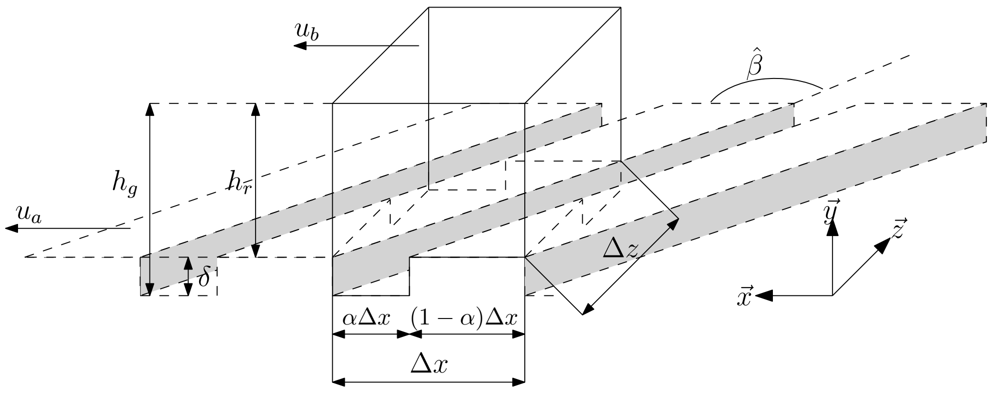

Figure 2.3 – Control volume employed for the derivation of the smoothed pressure field

The continuity equation requires that:

$$\Delta z \frac{\partial}{\partial z}\left(\Delta \psi_z\right) + \Delta x \frac{\partial}{\partial x}\left(\Delta \psi_x\right) + \frac{\partial}{\partial t}\left[\alpha h_g + (1-\alpha) h_r\right] \rho \Delta \theta \Delta z = 0 \tag{2.1}$$

The general mass fluxes in directions x and z are expressed as follows:

$$\psi_x = -\frac{\rho h^3}{12\mu}\left(\frac{\partial p}{\partial x}\right) + \frac{u_a + u_b}{2}\rho h \tag{2.2}$$

$$\psi_z = -\frac{\rho h^3}{12\mu}\left(\frac{\partial p}{\partial z}\right) \tag{2.3}$$

The general mass flux orthogonal to the direction of the groove is :

$$\begin{aligned}\psi_n = \psi_x \sin\hat{\beta} - \psi_z \cos\hat{\beta} = -\frac{\rho h^3}{12\mu_\theta}\left(\frac{\partial p}{\partial x}\right)\sin\hat{\beta} \\ + \frac{u_a + u_b}{2}\rho h \sin\hat{\beta} + \frac{\rho h^3}{12\mu_0}\frac{\partial p}{\partial z}\cos\hat{\beta}\end{aligned} \tag{2.4}$$

The mass flow continuity across the step requires that:

$$\psi_{ng} = \psi_{nr} + u_a \rho \delta \sin\hat{\beta} \tag{2.5}$$

Combining equations 2.5 and 2.4 leads to the following expression:

$$\frac{h_g^3}{\mu}\left(\frac{\partial p}{\partial z}\right)_g \frac{1}{\tan\hat{\beta}} - \frac{h_g^3}{\mu}\left(\frac{\partial p}{\partial x}\right) - \frac{h_r^3}{\mu}\left(\frac{\partial p}{\partial z}\right)_r \frac{1}{\tan\hat{\beta}} + \frac{h_r^3}{\mu}\left(\frac{\partial p}{\partial x}\right)_r = -6\mu\left(u_b - u_a\right)\delta \tag{2.6}$$

A smoothed pressure P is defined:

$$P(z+\Delta z, \theta) - P(z, \theta) = \int_z^{z+\Delta z} \frac{\partial p}{\partial z} \mathrm{d}z \tag{2.7}$$

$$P(z, x+\Delta x) - P(z, x) = \int_x^{x+\Delta x} \frac{\partial p}{\partial x} \mathrm{d}x \tag{2.8}$$

Assuming an infinite number of grooves, the terms Δz and Δx tend to 0, resulting in the following expressions:

$$\frac{\partial P}{\partial z} = \alpha \left(\frac{\partial p}{\partial z}\right)_g + (1-\alpha)\left(\frac{\partial p}{\partial z}\right)_r \tag{2.9}$$

$$\frac{\partial P}{\partial x} = \alpha \left(\frac{1}{r}\frac{\partial p}{\partial x}\right)_0 + (1-\alpha)\left(\frac{\partial p}{\partial x}\right) \tag{2.10}$$

The continuity of the local pressure gradient in the groove direction imposes:

$$\left(\frac{\partial p}{\partial z}\right)_g + \left(\frac{\partial p}{\partial x}\right)_g \frac{1}{\tan\hat{\beta}} - \left(\frac{\partial p}{\partial z}\right)_r - \left(\frac{\partial p}{\partial x}\right)_r \frac{1}{\tan\hat{\beta}} = 0 \tag{2.11}$$

From Eq. 2.6, 2.9, 2.10 and 2.11, a system of 4 equations with 4 unknown is built and solved to obtains expressions for the local pressure gradients in function of the smooth pressure gradient in x and z directions. The mass flows result from an integration of the mass fluxes over the ridge and the groove:

$$\Delta\psi_z = \int_0^{\alpha\Delta x} \psi_{zg}\mathrm{d}x + \int_{\alpha\Delta x}^{\Delta x} \psi_{zr}\mathrm{d}x \tag{2.12}$$

$$\Delta\psi_x = \int_0^{\alpha\Delta z} \psi_{xg}\mathrm{d}z + \int_{\alpha\Delta z}^{\Delta z} \psi_{xr}\mathrm{d}z \tag{2.13}$$

Taking the limits $\Delta x \to 0$ and $\Delta z \to 0$, the mass fluxes ψ_{ij} $(i = z, x\ ;\ j = r, g)$ can be considered constant within the integrated domain. Therefore:

$$\begin{aligned} \Delta\psi_z &= \psi_{zg}\alpha\Delta x + \psi_{zr}(1-\alpha)\Delta x \\ \Delta\psi_x &= \psi_{xg}\alpha\Delta z + \psi_{xr}(1-\alpha)\Delta z \end{aligned} \tag{2.14}$$

The mass flows are expressed as follows:

$$\Delta\psi_z = -\frac{\rho\Delta x}{12\mu\left[(1-\alpha)h_g^3 + \alpha h_r^3\right]} \left[\begin{array}{c} -\alpha(1-\alpha)6\mu(u_b-u_a)\delta\left(h_g^3-h_r^3\right)\sin\hat{\beta}\cos\hat{\beta} \\ +\left[\alpha(1-\alpha)\left(h_g^3-h_r^3\right)^2\sin^2\hat{\beta} + h_g^3h_r^3\right]\partial_z P \\ +\left(h_g^3-h_r^3\right)\alpha(1-\alpha)\sin\hat{\beta}\cos\hat{\beta}\partial_x P \end{array}\right] \tag{2.15}$$

$$\Delta\psi_x = -\frac{\rho\Delta z}{12\mu\left[(1-\alpha)h_g^3+\alpha h_r^3\right]}\left[\begin{array}{c} 6\mu(u_b-u_a)[\alpha(1-\alpha)(h_g^3-h_r^3)\sin^2\hat{\beta}\delta] \\ -6\mu(u_b+u_a)\left[(1-\alpha)h_g^3+\alpha h_r^3\right](\alpha h_g+(1-\alpha)h_r) \\ +\alpha(1-\alpha)(h_g^3-h_r^3)^2\sin\hat{\beta}\cos\hat{\beta}\partial_z P \\ +\left[\alpha(1-\alpha)(h_g^3-h_r^3)^2\cos^2\hat{\beta}+h_g^3h_r^3\right]\partial_x P \end{array}\right] \tag{2.16}$$

Applying the continuity (Eq. 2.1) and non-dimensionalization, the following expression is obtained in cylindrical coordinates, suited for journal bearings, as illustrated in Figure 2.4:

$$\begin{gathered} \partial_\theta\left[\frac{\bar{\rho}}{\bar{\mu}}\left(f_1\partial_\theta\bar{P}+f_2\partial_{\bar{z}}\bar{P}+c_s\sin\hat{\beta}f_4\right)\right] \\ +\partial_{\bar{z}}\left[\frac{\bar{\rho}}{\bar{\mu}}\left(f_2\partial_\theta\bar{P}+f_3\partial_{\bar{z}}\bar{P}-c_s\cos\hat{\beta}f_4\right)\right] \\ =\Lambda\partial_\theta\left(\bar{\rho}f_5\right)+\sigma\partial_t\left(\bar{\rho}f_5\right) \end{gathered} \tag{2.17}$$

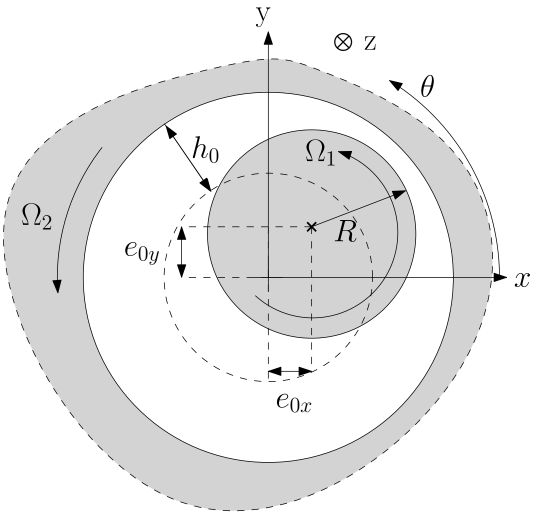

Figure 2.4 – Schematic representation of a journal bearing

With $\partial_\bullet = \dfrac{\partial}{\partial\bullet}$ and following the nomenclature developed in Eq. 2.18 and 2.19.

$$\begin{aligned}
\theta =& x/R \\
\bar{z} =& z/R \\
\bar{P} =& P/P_a \\
\bar{\rho} =& \rho/\rho_a \\
\bar{\mu} =& \mu \ \mu_a \\
\Lambda =& \frac{6\mu(\Omega_1+\Omega_2)R^2}{P_a h_0^2} \\
\sigma =& 2\frac{\omega_{ex}}{\Omega_1+\Omega_2}\Lambda \\
\bar{t} =& t\omega_{ex} \\
\Omega_1 =& u_a/R \\
\Omega_2 =& u_b/R
\end{aligned} \tag{2.18}$$

$$\begin{aligned}
\bar{h}_r =& \frac{h_r}{h_0} \\
\bar{h}_g =& \frac{h_g}{h_0} \\
\delta =& \frac{\delta}{h_0} \\
g_1 =& \bar{h}_g^3\bar{h}_r^3 \\
g_2 =& (\bar{h}_g^3-\bar{h}_r^3)^2\alpha(1-\alpha) \\
g_3 =& (1-\alpha)\bar{h}_g^3+\alpha\bar{h}_r^3 \\
c_s =& \frac{6\mu(\Omega_2-\Omega_1)R^2}{P_a h_0^2}\alpha(1-\alpha)\bar{\delta}\sin\hat{\beta} \\
f_1 =& \frac{g_1+g_2\sin^2\hat{\beta}}{g_3} \\
f_2 =& \frac{g_2\sin\hat{\beta}\cos\hat{\beta}}{g_3} \\
f_3 =& \frac{g_1+g_2\cos^2\hat{\beta}}{g_3} \\
f_4 =& \frac{\bar{h}_g^3-\bar{h}_r^3}{g_3} \\
f_5 =& \alpha\bar{h}_g+(1-\alpha)\bar{h}_r
\end{aligned} \tag{2.19}$$

If the groove parameters α, $\hat{\beta}$, δ are constant, the equation takes the following form:

$$\begin{aligned}\partial_\theta \left[\frac{\bar{\rho}}{\bar{\mu}}\left(f_1\partial_\theta\bar{P} + f_2\partial_{\bar{z}}\bar{P}\right)\right] + \partial_{\bar{z}}\left[\frac{\bar{\rho}}{\bar{\mu}}\left(f_2\partial_\theta\bar{P} + f_3\partial_{\bar{z}}\bar{P}\right)\right] + \\ c_s\left[\sin\hat{\beta}\partial_\theta\left(\frac{\bar{\rho}}{\bar{\mu}}f_4\right) - \cos\hat{\beta}\partial_{\bar{z}}\left(\frac{\bar{\rho}}{\bar{\mu}}f_4\right)\right] = \\ \Lambda\partial_\theta\left(\bar{\rho}f_5\right) + \sigma\partial_{\bar{t}}\left(\bar{\rho}f_5\right)\end{aligned} \quad 2.20$$

The NGT requires only one additional assumption on top of the Reynolds equation: that the grooves are on infinitesimal width. The pressure profile between a groove and a ridge is therefore linear in a first-order Taylor development. The consequence of this assumption is that the fluid is considered locally incompressible. Unmodelled effects might appear with an actual gas bearing having a finite number of grooves:

- Local compressibility effect: as the groove width is finite, groove-ridge pressure profiles deviate from linearity. As a consequence, the prediction of the overall smooth pressure is not physically justified. The local compressibility arises with a low number of grooves, groove angle close to $\pi/2$ and high compressibility numbers [8].

- Edge effect: close to the edges of the bearing in contact with the ambient, the saw-toothed pressure profile is of non-infinitesimal amplitude and cannot meet the boundary condition imposing the ambient pressure. This is generally mentioned as *end leakage*, because it provokes an increased axial mass flow at the edges. The phenomenon becomes significant for bearing of short axial length with a low number of grooves [10].

If the grooves vanish ($h_g = h_r = h$), the NGT boils down to the classical Reynolds equation:

$$f_1 = f_3 = \bar{h}^3 \quad 2.21$$

$$f_2 = f_4 = c_s = 0 \quad 2.22$$

$$f_5 = \bar{h} \quad 2.23$$

2.2 Perturbation

The following section, which deals with the mathematical and numerical manipulation, is based on the NGT but remains otherwise valid for the Reynolds equation.

The NGT expressed in Eq. 2.20 contains both pressure and density terms. In the vast majority of the gas bearing literature, the two terms are linked together using the ideal gas law and the assumption of isothermal compression, justified by the aspect ratio of the gas film, which has large heat exchange areas compared to its bulk [11]. Following these two assumptions, density terms can be substituted by pressure terms directly, easing the treatment of the equation. However, another change of variable is chosen, in order to maintain some versatility in the assumptions under which a particular bearing may operate (such as non-ideal gas behavior). This change of variable, under the isothermal assumption, is as follows:

$$\frac{\partial P}{\partial Y} = \left(\frac{\partial P}{\partial \rho}\right)_T \cdot \frac{\partial \rho}{\partial Y} \qquad 2.24$$

Where Y denotes indifferently θ or $\bar{z}$. Moreover, the bulk modulus, β, is introduced following the equation:

$$\rho \left(\frac{\partial P}{\partial \rho}\right)_T = \beta \qquad 2.25$$

Under the common ideal gas assumption, the expression of $\left(\frac{\partial P}{\partial \rho}\right)_T$ is simplified as follows:

$$\left(\frac{\partial P}{\partial \rho}\right)_T = rT \qquad 2.26$$

The bulk modulus is non-dimensionalized by the ambient pressure to obtain $\bar{\beta}$. Furthermore, if the fluid is assumed to be isoviscous (as viscosity mostly depends on the temperature), the resulting form of the NGT is:

$$\begin{gathered}\partial_\theta \left[\bar{\beta}\left(f_1 \partial_\theta \bar{\rho} + f_2 \partial_{\bar{z}} \bar{\rho}\right)\right] + \partial_{\bar{z}} \left[\bar{\beta}\left(f_2 \partial_\theta \bar{\rho} + f_3 \partial_{\bar{z}} \bar{\rho}\right)\right] \\ + c_s \left(\sin \hat{\beta} \partial_\theta \left(f_4 \bar{\rho}\right) - \cos \hat{\beta} \partial_{\bar{z}} \left(f_{4\bar{\rho}}\right)\right) \\ - \Lambda \partial_\theta \left(f_5 \bar{\rho}\right) - \sigma \partial_{\bar{t}} \left(f_5 \bar{\rho}\right) = 0\end{gathered} \qquad 2.27$$

This expression contains only density and bulk modulus terms.

In order to solve the NGT equation, a perturbation method, introduced by Lund for gas bearings [12], is applied around a particular static eccentricity, resulting in the linearization of the equation to approximate its solution around its position. The method allows to compute the linear dynamic properties (stiffness and damping) of a gas bearing while keeping the numerical and computational cost low. The drawback is that the obtained solution are strictly valid only for infinitesimal amplitudes of motion around the static position. The center of the shaft, with constant eccentricity ratios $\epsilon_{0,x}$ and $\epsilon_{0,y}$ in the two directions perpendicular to the angular speed vector, is perturbed by an harmonic motion around the equilibrium position, of amplitude $\epsilon_{1,x}$ and $\epsilon_{1,y}$ and frequency ω_{ex} . The resulting clearance, illustrated in Figure 2.5, follows:

$$\bar{h} = \bar{h}_0 - \epsilon_{1x} \cos\theta e^{i\bar{t}} - \epsilon_{1y} \sin\theta e^{i\bar{t}} \tag{2.28}$$

$$= 1 - \epsilon_{0x} \cos\theta - \epsilon_{0y} \sin\theta - \epsilon_{1x} \cos\theta e^{i\bar{t}} - \epsilon_{1y} \sin\theta e^{i\bar{t}} \tag{2.29}$$

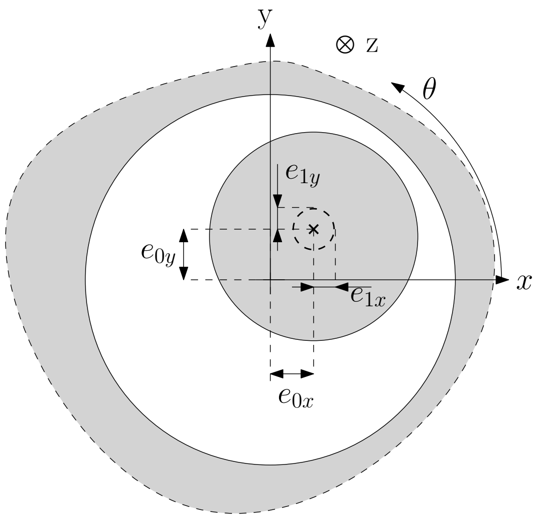

Figure 2.5 – Schematic representation of perturbed bearing

The density and bulk modulus follow the form of the perturbed clearance:

$$f_i = f_{0,j} + \epsilon_{1,x} f_{1x,j} e^{i\bar{t}} + \epsilon_{1,y} f_{1y,j} e^{i\bar{t}} \quad , j \in \{1, 2, 3, 4, 5\} \tag{2.30}$$

$$\bar{\rho} = \bar{\rho}_0 + \epsilon_{1x} \bar{\rho}_{1x} e^{i\bar{t}} + \epsilon_{1y} \bar{\rho}_{1y} e^{i\bar{t}} \tag{2.31}$$

$$\bar{\beta} = \bar{\beta}_0 + \epsilon_{1x} \left(\frac{\partial\bar{\beta}}{\partial\bar{\rho}}\right)_0 \bar{\rho}_{1x} e^{i\bar{t}} + \epsilon_{1y} \left(\frac{\partial\bar{\beta}}{\partial\bar{\rho}}\right)_0 \bar{\rho}_{1y} e^{i\bar{t}} \tag{2.32}$$

Eq. 2.30 to 2.32 are injected in Eq. 2.27. Zeroth and first order terms ($\mathcal{O}(\epsilon_{1,x})$ and $\mathcal{O}(\epsilon_{1,y})$) are grouped while neglecting higher order terms. It outputs three equation: a steady-state, non-linear partial differential equation at the equilibrium position (Eq. 2.33) and two linear Partial Differential Equations (PDEs), representing the pressure field when perturbed in two orthogonal directions, represented for one arbitrary direction in Eq. 2.34.

$$
\begin{array}{rcl}
\partial_{\theta\theta}\bar{\rho}_0 & \cdot & [\bar{\beta}_0 \cdot f_{1,0}] \\
+\partial_{\theta}\bar{\rho}_0 & \cdot & [\bar{\beta}_0 \cdot \partial_{\bar{z}} f_{2,0} - \Lambda \cdot f_{5,0} + f_{2,0} \cdot \partial_{\bar{z}}\bar{\beta}_0 + \bar{\beta}_0 \cdot \partial_{\theta} f_{1,0} \\
 & & f_{1,0} \cdot \partial_{\theta}\bar{\beta}_0 + c_s \cdot \sin\hat{\beta} \cdot f_{4,0}] \\
+\partial_{\bar{z}\bar{z}}\bar{\rho}_0 & \cdot & [\bar{\beta}_0 \cdot f_{3,0}] \\
+\partial_{\bar{z}}\bar{\rho}_0 & \cdot & [\bar{\beta}_0 \cdot \partial_{\theta} f_{2,0} + f_{2,0} \cdot \partial_{\theta}\bar{\beta}_0 + \bar{\beta}_0 \cdot \partial_{\bar{z}} f_{3,0} \\
 & & +f_{3,0} \cdot \partial_{\bar{z}}\bar{\beta}_0 - c_s \cdot \cos\hat{\beta} \cdot f_{4,0}] \\
+\partial_{\theta\bar{z}}\bar{\rho}_0 & \cdot & [2 \cdot \bar{\beta}_0 \cdot f_{2,0}] \\
+\bar{\rho}_0 & \cdot & [-\Lambda \cdot \partial_{\theta} f_{5,0} - c_s \cdot (\cos\hat{\beta} \cdot \partial_{\bar{z}} f_{4,0} - \sin\hat{\beta} \cdot \partial_{\theta} f_{4,0})] \\
 & = & 0
\end{array}
\tag*{2.33}
$$

$$
\begin{array}{rcl}
\partial_{\theta\theta}\bar{\rho}_1 & \cdot & [\bar{\beta}_0 \cdot f_{1,0}] \\
+\partial_{\theta}\bar{\rho}_1 & \cdot & [\bar{\beta}_0 \cdot \partial_{\bar{z}} f_{2,0} - \Lambda \cdot f_{5,0} + f_{2,0} \cdot \partial_{\bar{z}}\bar{\beta}_0 + \bar{\beta}_0 \cdot \partial_{\theta} f_{1,0} + f_{1,0} \cdot \partial_{\theta}\bar{\beta}_0 \\
 & & +\partial_{\bar{\rho}}\bar{\beta}_0 \cdot (f_{2,0} \cdot \partial_{\bar{z}}\bar{\rho}_0 + f_{1,0} \cdot \partial_{\theta}\bar{\rho}_0) + c_s \cdot \sin\hat{\beta} \cdot f_{4,0}] \\
+\partial_{\bar{z}\bar{z}}\bar{\rho}_1 & \cdot & [\bar{\beta}_0 \cdot f_{3,0}] \\
+\partial_{\bar{z}}\bar{\rho}_1 & \cdot & [\bar{\beta}_0 \cdot \partial_{\theta} f_{2,0} + f_{2,0} \cdot \partial_{\theta}\bar{\beta}_0 + \bar{\beta}_0 \cdot \partial_{\bar{z}} f_{3,0} + f_{3,0} \cdot \partial_{\bar{z}}\bar{\beta}_0 \\
 & & +\partial_{\bar{\rho}}\bar{\beta}_0 \cdot (f_{2,0} \cdot \partial_{\theta}\bar{\rho}_0 + f_{3,0} \cdot \partial_{\bar{z}}\bar{\rho}_0) - c_s \cdot \cos\hat{\beta} \cdot f_{4,0}] \\
+\partial_{\theta\bar{z}}\bar{\rho}_1 & \cdot & [2 \cdot \bar{\beta}_0 \cdot f_{2,0}] \\
+\bar{\rho}_1 & \cdot & [\partial_{\theta}(\partial_{\bar{\rho}}\bar{\beta}_0) \cdot (f_{2,0} \cdot \partial_{\bar{z}}\bar{\rho}_0 + f_{1,0} \cdot \partial_{\theta}\bar{\rho}_0) - c_s \cdot (\cos\hat{\beta} \cdot \partial_{\bar{z}} f_{4,0} - \\
 & & \sin\hat{\beta} \cdot \partial_{\theta} f_{4,0}) - \Lambda \cdot \partial_{\theta} f_{5,0} + \partial_{\bar{z}}(\partial_{\bar{\rho}}\bar{\beta}_0 \cdot (f_{2,0} \cdot \partial_{\theta}\bar{\rho}_0 + f_{3,0} \cdot \partial_{\bar{z}}\bar{\rho}_0) \\
 & & +\partial_{\bar{\rho}}\bar{\beta}_0 \cdot (2 \cdot f_{2,0} \cdot \partial_{\theta\bar{z}}\bar{\rho}_0 + f_{1,0} \cdot \partial_{\theta\theta}\bar{\rho}_0 + \partial_{\theta} f_{2,0} \cdot \partial_{\bar{z}}\bar{\rho}_0 + \partial_{\theta} f_{1,0} \cdot \partial_{\theta}\bar{\rho}_0 \\
 & & +f_{3,0} \cdot \partial_{\bar{z}\bar{z}}\bar{\rho}_0 + \partial_{\bar{z}} f_{2,0} \cdot \partial_{\theta}\bar{\rho}_0 + \partial_{\bar{z}} f_{3,0} \cdot \partial_{\bar{z}}\bar{\rho}_0) - i\sigma f_{5,0}] \\
+ & & \partial_{\theta}\bar{\beta}_0 \cdot (f_{2,1} \cdot \partial_{\bar{z}}\bar{\rho}_0 + f_{1,1} \cdot \partial_{\theta}\bar{\rho}_0) - c_s \cdot (\cos\hat{\beta} \cdot (f_{4,1} \cdot \partial_{\bar{z}}\bar{\rho}_0 + \bar{\rho}_0 \cdot \partial_{\bar{z}} f_{4,1}) \\
 & & -\sin\hat{\beta} \cdot (f_{4,1} \cdot \partial_{\theta}\bar{\rho}_0 + \bar{\rho}_0 \cdot \partial_{\theta} f_{4,1})) - \Lambda \cdot (f_{5,1} \cdot \partial_{\theta}\bar{\rho}_0 + \bar{\rho}_0 \cdot \partial_{\theta} f_{5,1}) \\
 & & +\partial_{\bar{z}}\bar{\beta}_0 \cdot (f_{2,1} \cdot \partial_{\theta}\bar{\rho}_0 + f_{3,1} \cdot \partial_{\bar{z}}\bar{\rho}_0) \\
 & & +\bar{\beta}_0 \cdot (2 \cdot f_{2,1} \cdot \partial_{\theta\bar{z}}\bar{\rho}_0 + f_{1,1} \cdot \partial_{\theta\theta}\bar{\rho}_0 + \partial_{\theta} f_{2,1} \cdot \partial_{\bar{z}}\bar{\rho}_0 + \partial_{\theta} f_{1,1} \cdot \partial_{\theta}\bar{\rho}_0 \\
 & & +f_{3,1} \cdot \partial_{\bar{z}\bar{z}}\bar{\rho}_0 + \partial_{\bar{z}} f_{2,1} \cdot \partial_{\theta}\bar{\rho}_0 + \partial_{\bar{z}} f_{3,1} \cdot \partial_{\bar{z}}\bar{\rho}_0) - \sigma\bar{\rho}_0\partial_{\bar{t}} f_{5,1}] \\
 & = & 0
\end{array}
\tag*{2.34}
$$

The boundary conditions usually applied are as follows for full journal bearings:

- Ambient pressure is imposed on the axial ends of the bearing

$$\bar{P}(\theta, \pm L_z/D) = 1 \qquad 2.35$$

- The pressure field is periodic in the circumferential direction

$$\bar{P}(\theta, \bar{z}) = \bar{P}(\theta + 2\pi, \bar{z}) \qquad 2.36$$

Plus, an axial mass flow continuity is imposed at the boundary between dissimilar grooved zones, typically between the grooved and land region at $\bar{z} = \pm L_{\text{land}}/D$:

$$\dot{m}_{z,\ominus} = \dot{m}_{z,\oplus} \qquad 2.37$$

There $\ominus$ and $\oplus$ denotes the limit before and after the boundary, respectively. For the case there a grooved zone ends to begin a smooth zone (land), the equation translates into the following equality:

$$\left[c_s f_4 \bar{\rho} \cos\hat{\beta} - f_2 \bar{\beta} \partial_\theta \bar{\rho} - f_3 \bar{\beta} \partial_z \bar{\rho}\right]_{\text{groove}} = \left[-\bar{h}^3 \bar{\beta} \partial_z \bar{\rho}\right]_{\text{land}} \qquad 2.38$$

Similarly, the continuity of axial mass flow is imposed at $\bar{z} = 0$. Imposing a axial mass flow of zero at this position would correspond to a bearing operating in symmetric conditions in terms of bearing geometry, displacement (purely radial) ambient conditions. The gain would be to decrease the simulation domain to a half of bearing, reducing the computation cost. However, preferring a mass flow continuity allows a broader field of applications, at the cost of a larger computational effort. The perturbation of the continuity equations leads to the following zeroth equation:

$$[c_s \cdot \cos\hat{\beta} \cdot f_{4,0} \cdot \bar{\rho}_0 - \bar{\beta}_0 \cdot f_{3,0} \cdot \partial_{\bar{z}} \bar{\rho}_0 - \bar{\beta}_0 \cdot f_{2,0} \cdot \partial_\theta \bar{\rho}_0]_{\text{groove}} = [\bar{h}_0^3 \cdot \bar{\beta} \cdot \partial_{\bar{z}} \bar{\rho}_0]_{\text{land}} \qquad 2.39$$

And the first order equation:

$$\begin{gathered}
[c_s \cdot \cos\hat{\beta} \cdot f_{4,0} \cdot \bar{\rho}_1 - \bar{\beta}_0 \cdot f_{2,1} \cdot \partial_\theta \bar{\rho}_0 - \bar{\beta}_0 \cdot f_{3,0} \cdot \partial_{\bar{z}} \bar{\rho}_1 - \bar{\beta}_0 \cdot f_{3,1} \cdot \partial_{\bar{z}} \bar{\rho}_0 \\
-\partial_{\bar{\rho}} \bar{\beta}_0 \cdot f_{2,0} \cdot \bar{\rho}_1 \cdot \partial_\theta \bar{\rho}_0 - \partial_{\bar{\rho}} \bar{\beta}_0 \cdot f_{3,0} \cdot \bar{\rho}_1 \cdot \partial_{\bar{z}} \bar{\rho}_0 \\
-\bar{\beta}_0 \cdot f_{2,0} \cdot \partial_\theta \bar{\rho}_1 + c_s \cdot \cos\hat{\beta} \cdot f_{4,1} \cdot \bar{\rho}_0]_{\text{groove}} \qquad 2.40 \\
= \\
\left[3\bar{h}_0^2 \cdot \bar{h}_1 \cdot \bar{\beta}_0 \cdot \partial_{\bar{z}} \bar{\rho}_0 + \bar{h}_0^3 \cdot \partial_{\bar{\rho}} \bar{\beta}_0 \cdot \bar{\rho}_1 \cdot \partial_{\bar{z}} \bar{\rho}_0 + \bar{h}_0^3 \cdot \bar{\beta}_0 \cdot \partial_{\bar{z}} \bar{\rho}_1\right]_{\text{land}}
\end{gathered}$$

The continuity of the pressure across the boundary between the dissimilar groove zones is also imposed. The system of equations is solved with a finite-difference method, as it will be developed later. The obtained static and perturbed densities are converted back to pressure using the compressibility factor Z ($P = Z\rho r T$), computed with an equation of state relevant to fluid:

$$\begin{array}{rl} \text{General} & \text{Ideal gas} \\ \bar{P}_0 = \frac{Z(\rho_0,T)}{Z(\rho_a,T)}\bar{\rho}_0 & \bar{P}_0 = \bar{\rho}_0 \\ \bar{P}_1 = \left(\frac{\partial \bar{P}}{\partial \bar{\rho}}\right)_{T,0}\bar{\rho}_1 & \bar{P}_1 = \bar{\rho}_1 \end{array} \tag{2.41}$$

Parameters Z and $\left(\frac{\partial \bar{P}}{\partial \bar{\rho}}\right)_T$ as well as viscosity are obtained using a fluid database [13]. The integration of the zeroth order pressure field results in the static load capacity of the bearing:

$$W_x = -R^2 P_a \int_{-L_z/D}^{L_2/D} \int_0^{2\pi} \bar{P}_0 \cos\theta \mathrm{d}\theta \mathrm{d}\bar{z} \tag{2.42}$$

$$W_y = -R^2 P_a \int_{-L_z/D}^{L_2/D} \int_0^{2\pi} \bar{P}_0 \sin\theta \mathrm{d}\theta \mathrm{d}\bar{z} \tag{2.43}$$

$$W = \sqrt{W_x^2 + W_y^2} \tag{2.44}$$

The load capacity is typically non-dimensionalized as follows:

$$\overline{W} = \frac{W}{\epsilon P_a L D} \tag{2.45}$$

The two perturbed pressure field corresponding to an excitation frequency ω_{ex} are integrated as follows to obtain the force coefficients corresponding to this particular frequency, in terms of impedances:

$$\begin{bmatrix} Z_{xx} & Z_{xy} \\ Z_{yx} & Z_{yy} \end{bmatrix} = \begin{bmatrix} K_{xx} & K_{xy} \\ K_{yx} & K_{yy} \end{bmatrix} + i\omega_{ex} \begin{bmatrix} C_{xx} & C_{xy} \\ C_{yx} & C_{yy} \end{bmatrix} \tag{2.46}$$

$$= -\frac{R^2 P_a}{h_0} \int_{-L_z/D}^{L_z/D} \int_0^{2\pi} \begin{bmatrix} \bar{P}_{1x}\cos\theta & \bar{P}_{1x}\sin\theta \\ \bar{P}_{1y}\cos\theta & \bar{P}_{1y}\sin\theta \end{bmatrix} \mathrm{d}\theta \mathrm{d}\bar{z} \tag{2.47}$$

The concept of critical mass describes the threshold rotor mass above which the bearing exhibits a self-excited instability in the form of a whirl of growing orbit. The method to compute this threshold is based on the frequency-dependent impedances of the gas bearing. An equivalent impedance Z is first defined as follows [12]:

$$Z_{eq} = \frac{1}{2}\left(Z_{xx} + Z_{yy}\right) \pm \sqrt{\frac{1}{4}\left(Z_{xx} - Z_{yy}\right)^2 + Z_{xy}Z_{yx}} \tag{2.48}$$

The critical frequency ω_c is the frequency of the whirl motion becoming unstable. It is found by finding the excitation frequency canceling the imaginary part of the equivalent impedance :

$$\text{Im}(Z_{eq}(\omega_c)) = 0 \tag{2.49}$$

For the equivalent spring mass system constituted of the equivalent impedance and a mass m, the critical mass m_c is the value of m corresponding to an eigenfrequency equal to ω_c, as illustrated in Figure 2.6:

$$m_c\omega_c^2 = Z_{eq}(\omega_c) \tag{2.50}$$

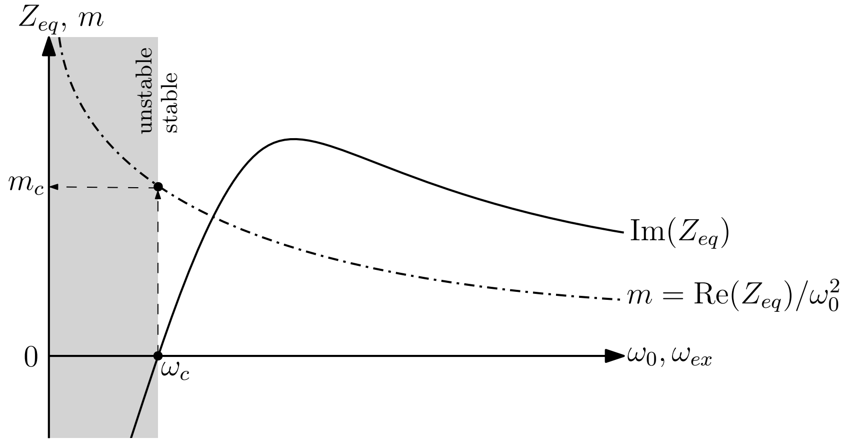

Figure 2.6 – Illustration of the evolution of the imaginary part of the equivalent impedance and the equivalent mass as a function the excitation frequency ω_{ex} and the eigenfrequency ω_0 respectively

Furthermore, the critical mass is usually used in non-dimensional form as follows:

$$M_c = m_c \frac{P_a}{2\mu^2 L}\left(\frac{h_0}{R}\right)^5 \tag{2.51}$$

2.3 Numerical implementation

2.3.1 Discretization and resolution scheme

In order to numerically solve Eq. 2.33 and 2.34, a finite difference scheme is applied. Terms in Eq. 2.33 and 2.34 are approximated following a central difference scheme:

$$\left(\frac{\partial\Psi}{\partial\theta}\right)_{i,j} = \frac{\Psi_{i+1,j} - \Psi_{i-1,j}}{2\Delta\theta} + \mathcal{O}(\Delta\theta^2) \qquad 2.52$$

$$\left(\frac{\partial^2\Psi}{\partial\theta^2}\right)_{i,j} = \frac{\Psi_{i+1,j} - 2\Psi_{i,j} + \Psi_{i-1,j}}{\Delta\theta^2} + \mathcal{O}(\Delta\theta^2) \qquad 2.53$$

$$\left(\frac{\partial\Psi}{\partial\bar{z}}\right)_{i,j} = \frac{\Psi_{i+1,j} - \Psi_{i-1,j}}{2\Delta\bar{z}} + \mathcal{O}(\Delta\bar{z}^2) \qquad 2.54$$

$$\left(\frac{\partial^2\Psi}{\partial\bar{z}^2}\right)_{i,j} = \frac{\Psi_{i+1,j} - 2\Psi_{i,j} + \Psi_{i-1,j}}{\Delta\bar{z}^2} + \mathcal{O}(\Delta\bar{z}^2) \qquad 2.55$$

$$\left(\frac{\partial^2\Psi}{\partial\theta\partial\bar{z}}\right)_{i,j} = \frac{\Psi_{i+1,j+1} - \Psi_{i-1,j} - \Psi_{i,j-1} + \Psi_{i-1,j-1}}{4\Delta\theta\Delta\bar{z}} + \mathcal{O}(\Delta\bar{z}\Delta\theta) \qquad 2.56$$

Where Ψ denotes equally $\bar{\rho}$, $\bar{\beta}$, $f_j (j \in \{1, 2, 3, 4, 5\})$, either in static of perturbed form. The considered grid is homogeneous, with constant values for $\Delta\theta$ and $\Delta\bar{z}$. The grid has N_θ and $N_{\bar{z}}$ points in the θ and $\bar{z}$ directions respectively (Figure 2.7).

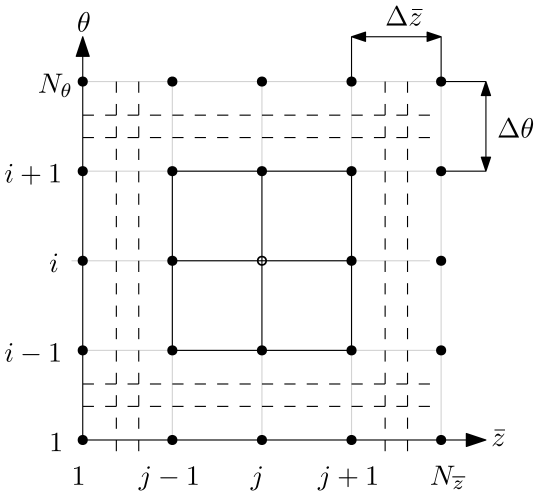

Figure 2.7 – Schematic representation of the discretization grid

Equations 2.39 and 2.40, which equalize the axial mass flows on the two sides of a boundary, need a forward and backward difference scheme in the $\bar{z}$ direction, depending on the considered side of the boundary:

$$\left(\frac{\partial\Psi}{\partial\bar{z}}\right)_{i,j,\ominus} = \frac{-\Psi_{i,j-2} + 4\Psi_{i,j-1} - 3\Psi_{i,j}}{2\Delta\bar{z}} + \mathcal{O}(\Delta\bar{z}^2) \quad 2.57$$

$$\left(\frac{\partial\Psi}{\partial\bar{z}}\right)_{i,j,\oplus} = \frac{\Psi_{i,j} - 4\Psi_{i,j+1} + \Psi_{i,j+2}}{2\Delta\bar{z}} + \mathcal{O}(\Delta\bar{z}^2) \quad 2.58$$

The discretized equations are written in the following matrix form, where bold characters are vectors:

$$\mathbf{A}_0(\boldsymbol{\rho}_0) \cdot \boldsymbol{\rho}_0 = \mathbf{b}_0 \quad 2.59$$

$$\mathbf{A}_{1x} \cdot \boldsymbol{\rho}_{1x} = \mathbf{b}_{1x} \quad 2.60$$

$$\mathbf{A}_{1y} \cdot \boldsymbol{\rho}_{1y} = \mathbf{b}_{1y} \quad 2.61$$

Figure 2.9 shows the general aspect of the matrices A in the case of a 5 × 5 grid (Figure 2.8) corresponding to a HGJB with no land region ($\gamma = 1$). In the case of the discretized zeroth order equation, the system is non-linear and the solution must be approached iteratively. The matrix $\mathbf{A}_0$ contains terms which rely implicitly on the density the bulk modulus β. Following [14], a guess density field is used to initialize the following process:

$$\boldsymbol{\rho}_0^{(n+1)} = (1-\kappa)\boldsymbol{\rho}_0^{(n)} + \kappa \cdot (\mathbf{A}_0^{-1}(\boldsymbol{\rho}_0^{(n)}) \cdot \mathbf{b}_0) \quad 2.62$$

where $\kappa \in [0, 1]$. At each iteration, the density-dependent terms are updated with the previously computed density vector and the system and the new density vector is computed. Convergence is considered when the following criterion ϵ, typically set at 10^{-4}, is met:

$$\left|\frac{\overline{\rho}_k^{(n)} - \overline{\rho}_k^{(n-1)}}{\overline{\rho}_k^{(n-1)}}\right| < \epsilon \quad \forall k \in \{1 \dots N_\theta \cdot N_{\bar{z}}\} \quad 2.63$$

Once the density vector converged, it is converted back to pressure as follows:

$$P = Z\rho rT \quad 2.64$$

where Z denotes here the compressibility factor evaluated at ρ and T from a fluid database. The global process is summarized in Figure 2.10.

2.3.2 Output and comparison

A test geometry, whose parameters referring to Figure 2.11 are listed in Table 2.1, is simulated with the implemented model. Examples of computed pressure fields are presented in Figure 2.12 for a symmetric bearing running at $\Lambda = 40$ and two different

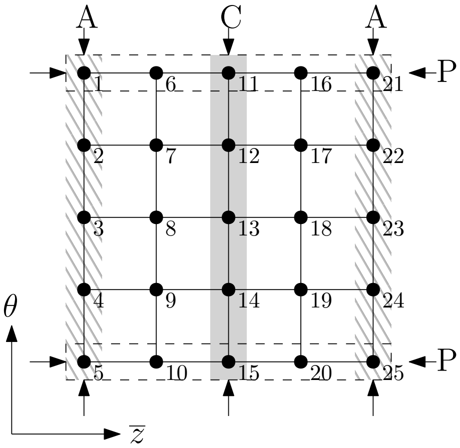

Figure 2.8 – 5 × 5 grid of a bearing domain. P: Periodicity boundary condition, A: ambient boundary condition, C: mass continuity condition

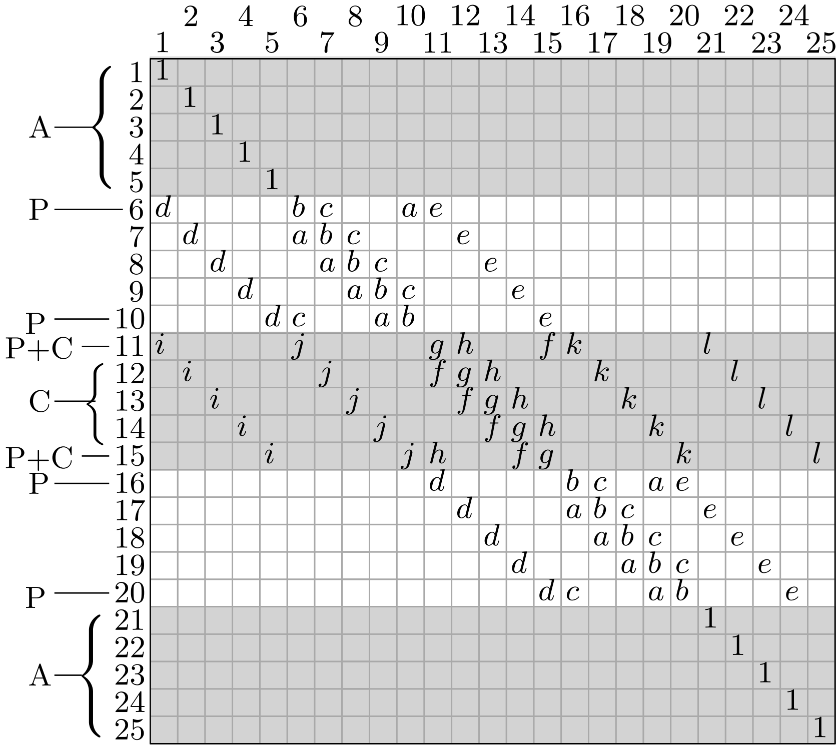

		1	2	3	4	5	6	7	8	9	10	11	12	13	14	15	16	17	18	19	20	21	22	23	24	25
A	1	1																								
	2		1																							
	3			1																						
	4				1																					
	5					1																				
P	6	d					b	c			a	e														
	7		d				a	b	c				e													
	8			d				a	b	c				e												
	9				d				a	b	c				e											
P	10					d	c			a	b					e										
P+C	11	i					j					g	h			f	k					l				
C	12		i					j				f	g	h				k					l			
	13			i					j				f	g	h				k					l		
	14				i					j				f	g	h				k					l	
P+C	15					i					j	h			f	g					k					l
P	16											d					b	c		a	e					
	17												d				a	b	c			e				
	18													d				a	b	c			e			
	19														d				a	b	c			e		
P	20															d	c			a	b				e	
A	21																					1				
	22																						1			
	23																							1		
	24																								1	
	25																									1

Figure 2.9 – Disposition of the terms in the matrices A for a 5 × 5 grid, in case of a HGJB with $\gamma = 1$. P: Periodicity boundary condition, A: ambient boundary condition, C: mass continuity condition

relative eccentricities. The sensitivity of the static pressure field against grid size is investigated for $\Lambda = 40$ and $\epsilon_x = 0.8$, with the total load capacity as a performance metric. The results are shown in Figure 2.13. The presented values are the relative error between each load capacity and the reference value evaluated at $(N_\theta = N_{\bar{z}} = 150)$. The

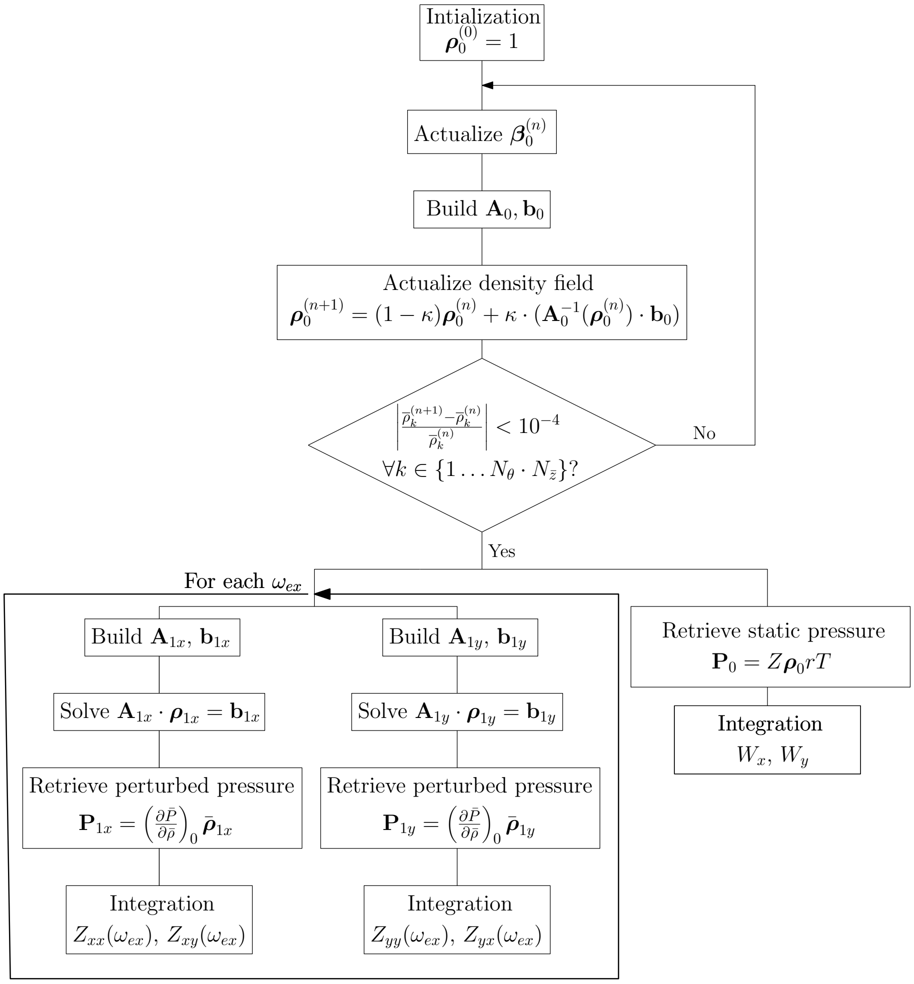
Intialization
$\boldsymbol{\rho}_0^{(0)} = 1$
Actualize $\boldsymbol{\beta}_0^{(n)}$
Build $\mathbf{A}_0, \mathbf{b}_0$
Actualize density field
$\boldsymbol{\rho}_0^{(n+1)} = (1-\kappa)\boldsymbol{\rho}_0^{(n)} + \kappa \cdot (\mathbf{A}_0^{-1}(\boldsymbol{\rho}_0^{(n)}) \cdot \mathbf{b}_0)$
$\left|\frac{\bar{\rho}_k^{(n+1)} - \bar{\rho}_k^{(n)}}{\bar{\rho}_k^{(n)}}\right| < 10^{-4}$
$\forall k \in \{1 \ldots N_\theta \cdot N_{\bar{z}}\}$?
No
Yes
For each ω_{ex}
Build $\mathbf{A}_{1x}$, $\mathbf{b}_{1x}$
Build $\mathbf{A}_{1y}$, $\mathbf{b}_{1y}$
Solve $\mathbf{A}_{1x} \cdot \boldsymbol{\rho}_{1x} = \mathbf{b}_{1x}$
Solve $\mathbf{A}_{1y} \cdot \boldsymbol{\rho}_{1y} = \mathbf{b}_{1y}$
Retrieve perturbed pressure
$\mathbf{P}_{1x} = \left(\frac{\partial \bar{P}}{\partial \bar{\rho}}\right)_0 \bar{\boldsymbol{\rho}}_{1x}$
Retrieve perturbed pressure
$\mathbf{P}_{1y} = \left(\frac{\partial \bar{P}}{\partial \bar{\rho}}\right)_0 \bar{\boldsymbol{\rho}}_{1y}$
Integration
$Z_{xx}(\omega_{ex})$, $Z_{xy}(\omega_{ex})$
Integration
$Z_{yy}(\omega_{ex})$, $Z_{yx}(\omega_{ex})$
Retrieve static pressure
$\mathbf{P}_0 = Z\boldsymbol{\rho}_0 rT$
Integration
W_x, W_y

Figure 2.10 – Process of iteratively solving the static pressure field to then compute the perturbed pressure field for each considered excitation frequency ω_{ex}

results show to be less sensitive on the size along θ than $\bar{z}$, while a good grid convergence is reached with $N_\theta = 100$ and $N_{\bar{z}} = 80$, which is applied for the rest of the investigation.

Table 2.1 – HGJB parameters employed for the examples of pressure fields

Parameter	Value
α	0.5
$\hat{\beta}$	155°
γ	1
$\bar{h}_g$	2
L/D	1
Λ	40

The static performance in eccentric position is compared to the simulation results of

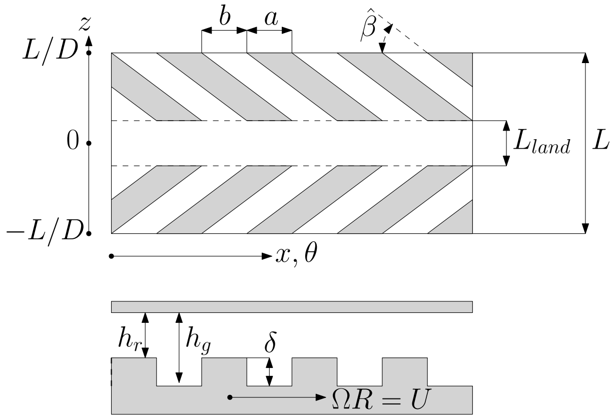

Figure 2.11 – Nomenclature of a HGJB

Bonneau and Absi [3], who implemented an Upwind Finite-Element scheme to resolve the ridge-groove pattern without the assumptions of the NGT. Their objective was to assess the validity domain of the NGT. The geometry of their investigated bearing is implemented in the present model and the normalized reaction force parallel to the displacement is computed for different relative eccentricites ϵ_x and compressibility numbers Λ. The results are shown in Figure 2.14. The two predictions are in good agreement for every considered relative eccentricity. The slight discrepancy visible between the two models can be explained, at least partially, by the fact that the reference uses only 12 ridge-groove pairs in its model, which is considered as low. At $\Lambda = 40$, the relative deviation at $\epsilon = 0.0001$, 0.6 and 0.8 is 9.0%, 8.4% and 4.6%, respectively. It has to be noted that in their article, the authors compare the eccentric FEM model with the concentric NGT and claim that the NGT is therefore unsuited to eccentric operation. The present implementation and results contradict this claim, suggesting that the NGT is as valid at large eccentricities as it is in concentric position.

The prediction of frequency-dependent force coefficients is indirectly compared with numerical results published in the literature. The reference data consist of the evaluation of minimal critical mass of HGJBs performed by Fleming and Hamrock [15]. They implemented Vohr and Chow's 1D version of the NGT with perturbation around the concentric position to optimize the geometry of HGJB, maximizing the minimum critical mass at different compressibility numbers Λ. This performance metric is defined as follows:

$$M_{c,min}(\Lambda) = \min_{\Lambda^\star \in [0,\Lambda]} M_c(\Lambda^\star) \tag{2.65}$$

$M_{c,min}$ is of practical interest since an accelerating rotor must remain stable at all compressibility numbers between 0 and the target value Λ. 6 HGJB geometries, corresponding to the optimum maximizing $M_{c,min}$ 6 different values of Λ, are listed in Table 2.2. The present implementation of the NGT with the perturbation method is employed

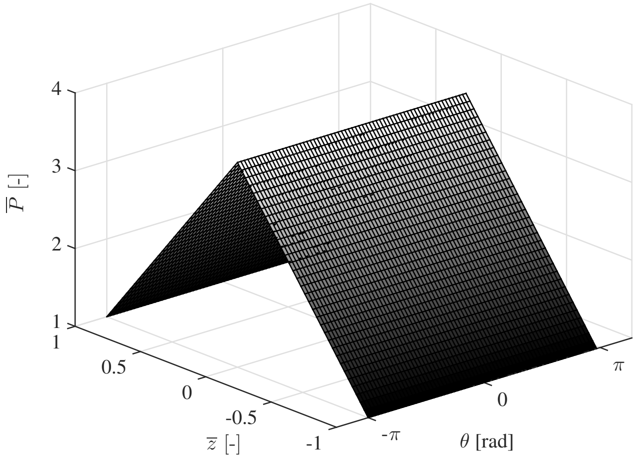

(a) $\epsilon = 0$

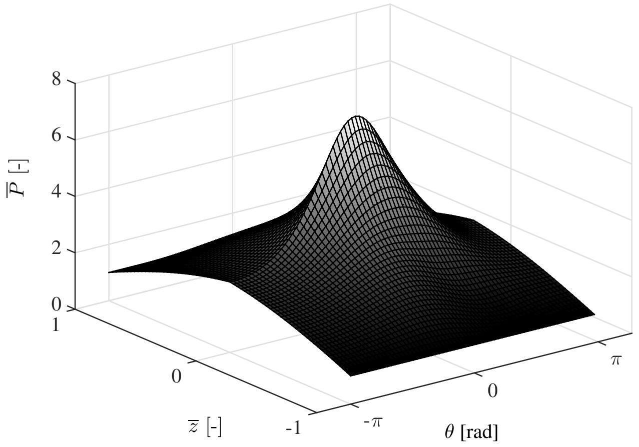

(b) $\epsilon = 0.5$

Figure 2.12 – Computed pressure fields for the test bearing at two different relative eccentricities

to simulates these geometries and retrieve their minimum critical mass, by scanning the range $[0, \Lambda]$ in 10 steps. The simulation assumes the lubricant to be an isothermal ideal gas. The results, displayed in Figure 2.15, are in very good agreement with the reference, within 2% relative error at $\Lambda = 40$.

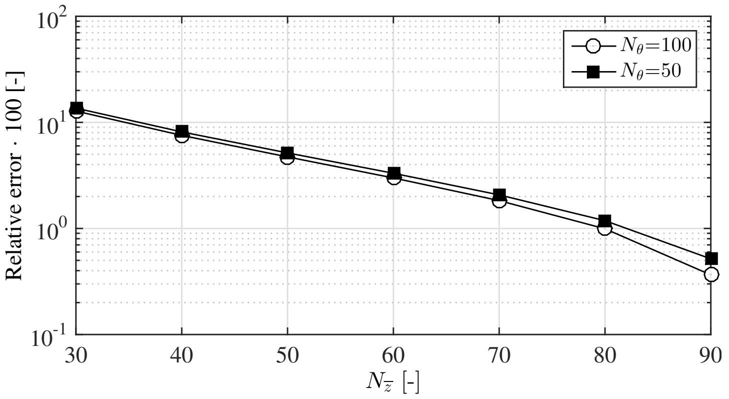

Figure 2.13 – Relative error made on the total load capacity at different grid sizes. The error is computed with the value evaluated at ($N_\theta = N_{\bar{z}} = 150$) as reference

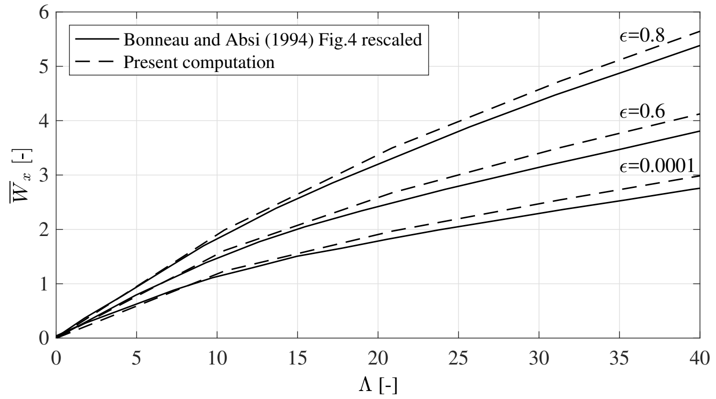

Figure 2.14 – Comparison of the computed reaction force in the radial direction with the output of the FEM model of Bonneau and Absi with 12 grooves. The original figure, assumed to have its vertical coordinate reported wrong, was rescaled using Fig. 3 of the reference, which corresponds well to Vohr and Chow [2]

Table 2.2 – HGJB geometries corresponding to the maximization of $M_{c,min}$ according to [15], for rotating grooves and $L_z/D = 1$

Λ	1	2	5	10	20	40
α	0.6	0.6	0.6	0.6	0.6	0.6
$\hat{\beta}$	143.8°	144.4°	145.9°	145.9°	158°	158.2°
γ	1	1	1	1	1	1
$\bar{\delta}$	1.25	1.37	1.54	1.54	2.10	2.06

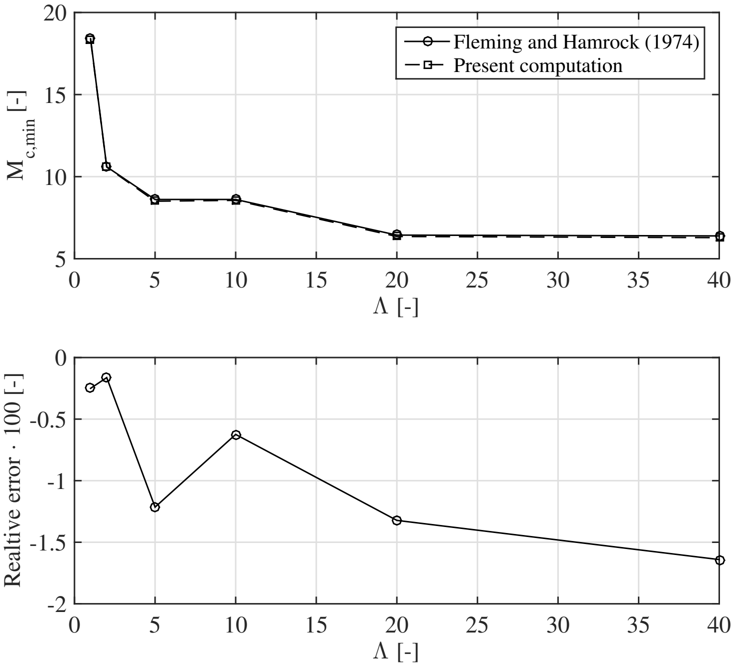

Figure 2.15 – Comparison of the computed minimum critical mass with the results from Fleming and Hamrock [15]

2.4 Experimental validation

Parts of the material presented in this section has been published in the following journal article:

Guenat, E., Schiffmann, J., 2020. Dynamic force coefficients identification of air-lubricated Herringbone Grooved Journal Bearing. Mechanical Systems and Signal Processing 136, 106498. doi:10.1016/j.ymssp.2019.106498

While the development of foil gas bearings was accompanied by a significant amount of experimental campaigns to validate the numerical models and get a deeper insight into the physics governing the bearings, the literature on experimental investigation of herringbone-grooved bearings is meager. Malanoski [16] studied the viability of the critical mass criteria for the prediction of stability on a 38.1 mm journal supported on partially-grooved HGJB. In accordance with the predicted critical mass, the shaft achieved stable operation at nominal speed (60 krpm). The bearing static stiffness was also measured at low eccentricity and was in good agreement with the theoretical prediction from the NGT, as most points fell within ±10% of the predicted value. Cunningham et al. [17] studied the stability of a similar layout, with 38.1 mm diameter shafts supported on two HGJBs by achieving a stable operation up to 60 krpm. Both fully and partially grooved bearings were investigated. The experimental campaign found a reasonable agreement between the stability predicted following the NGT and the critical mass criteria and the observed onset speeds of instability (Figure 2.16), with critical masses over-predicted by a factor 1.5 to 3 compared to experimental data. Later the same authors studied the static stiffness and load-carrying capacity of these rotors up to 50 krpm and eccentricity ratios of 0.8 [18]. They concluded that the load capacity was well predicted by the linearized NGT at low eccentricity, but followed a non-linear trend at high eccentricity ratios. Tananaka and Muraki [19] investigated the performance of an asymmetric HGJB supporting a 16 mm diameter rotor up to 40 krpm, where grooving is much longer on one of the two sides of the bearing in order to induce an axial flow alongside the rotor and generate axial thrust. 100 rotors were tested up to 20.000 start-up cycles each, without noticeable loss of performance. Yoshimoto and Takahashi [20] successfully investigated the ability of a 14 mm diameter asymmetric HGJB to act as viscous vacuum pump to lower the windage losses of the supported rotor. Fleming employed the NGT to study and design externally-pressurized partially grooved HGJBs, later implemented by Stanev et al. [21] in the form of 25.4 mm bearing, tested up to 120 krpm in non-loaded conditions and 40 krpm with an external load. No sign of instability was observed, in accordance with the stability analysis based on the NGT. Yoshimoto et al. [22] tested a 6 mm diameter rotor driven by an impulse turbine up to 600 krpm with the bushings mounted on bump foils in order to add damping to the system, thus increasing the onset speed of instability. Schiffmann [23] designed a high-speed refrigerant turbocompressor supported on NGT-designed 10 mm

HGJBs up to 210 krpm, with no sign of instability with both air and pressurized R134a as lubricants. For applications in precision machine tools, Ognjanovic [24] operated a 60 mm HGJB supported on rolling elements bearings with a floating bushing on which a radial load is applied. He concluded that the NGT tends to overestimate the load capacity of HGJB. Demierre et al. [25] used the NGT to design and operate a turbocompressor with refrigerant-lubricated 10 mm HGJBs for heat pumping and organic Rankine cycles with rotor speeds up to 200 krpm, with no sign of instability. Wagner [26] successfully used the NGT to design overheated steam-lubricated 8 mm HGJB supporting a fuel cell gas recirculator up to 180 krpm, which successfully achieved stable operation.

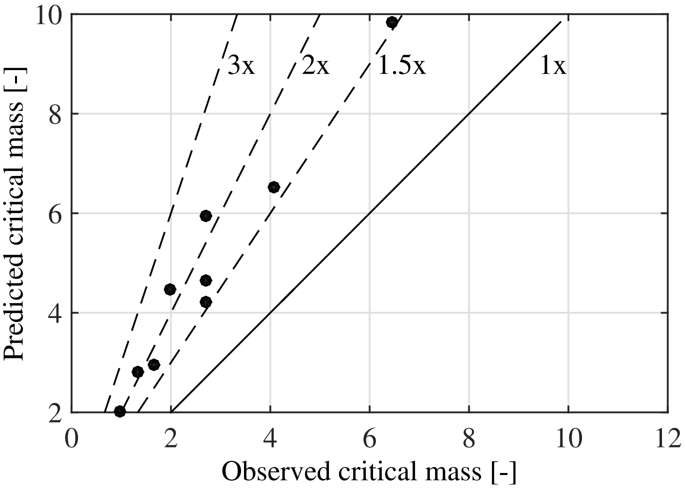

Figure 2.16 – Predicted critical mass against non-dimensional mass or rotors at their onset on instability, with the data of Cunningham [17]

Literature contains experimental data of load capacity and stability in terms of critical mass for HGJBs, scattered over several decades, as summarized in Table 2.3. However, the measurement of dynamic coefficients (frequency-dependent stiffness and damping) is missing from the HGJB literature. Their measurement is of high value since the synchronous performance (i.e. imbalance response) of a rotor as well as the stability analysis rely on them. It would serve to further assess the predictive performance of the NGT and, if it proves to be necessary, orient the research effort toward a more reliable design tool for spiral grooved bearings.

Different methods have been employed over the last decades to indirectly measure the force coefficients of gas lubricated bearings, mostly of foil and aerostatic bearings. They usually involve a rigidly supported rotating shaft equipped with a floating bearing on which a known dynamic force, typically generated by a impact hammer or a electromagnetic shaker and measured through a force gauge, is applied (Figure 2.17). The response of the bearing is recorded with an accelerometer or a displacement probe. This layout allows a convenient flexibility regarding the test bearing to be tested, since it does not play a significant role in the support of the rotating shaft. Disadvantages of such systems include

Table 2.3 – List of published experimental investigations of HGJB

	Bearing type											Test type	
	Fully grooved	Partially grooved	Hybrid	Asymmetric	Rotating grooves	Static grooves	Floating bearing	Max Ω [krpm]	Diameter [mm]	Radial clearance [µm]	Lubricant	Static Load	Free response
Hirs (1965)	●				●		●	30	40	14.5-33.0	Air	●	
Malanoski (1967)		●			●			60	38.1	12.6	Air		●
Cunningham et al. (1967)	●	●			●			60.83	38.1	8.9-18.0	Air		●
Cunningham et al. (1971)	●	●			●			60.83	38.1	8.9-18.0	Air	●	
Tanaki and Muraki (1991)				●	●			40	38.1	14 ; 16	Air		●
Yoshimoto and Takahashi (1999)				●	●			30	14	2.25	Air		●
Stanev et al. (2004)		●	●		●			120	25.4	10	Air		●
Yoshimoto et al. (2007)		●			●			600	6	4	Air		●
Schiffmann (2008)	●				●			250	10	3.5	R134a		●
Ognjanovic (2011)	●				●		●	60	60	14.5	Air	●	
Demierre (2013)	●				●			200	10	3.5	R134a		●
Miyanaga and Tomioka (2015)	●					●		460	6	4	Air		●
Wagner and Schiffmann (2019)	●				●			180	10	8	Steam		●

a large size and an increased complexity, as the shaft bearings must be significantly stiffer than the floating test bearing in order to minimize the parasitic motion of the rotating shaft, which usually implies the management of a secondary lubricant for these bearings (water, oil, grease). Moreover, the excitation of the floating bushing by a known force requires an accurate knowledge of the inertia set in motion in order to deduce the test bearing reaction force, which can be difficult depending on the way the floating bearing is attached to the shakers and the frame. An alternative layout involves a rotor entirely supported on two test bearings, with an excitation applied either on the bearing bushings of the shaft itself (unbalance, impact hammer). Measuring the force applied on the bushings as well as the response of the shaft allows to deduce the force coefficients of the two bearings. Figure 2.18 provides an schematic example of this configuration.

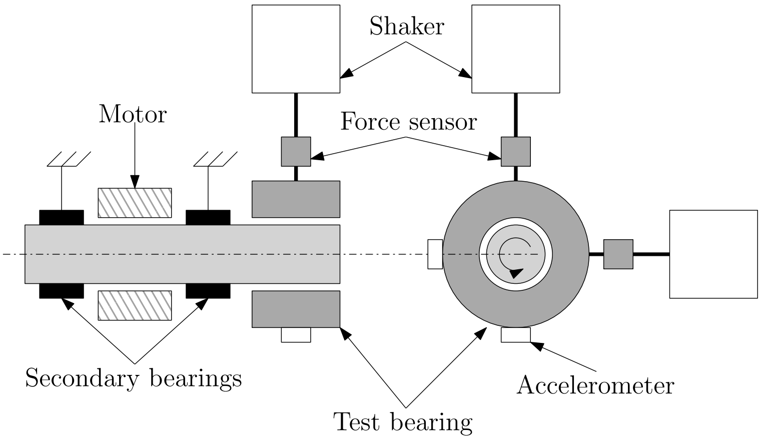

Figure 2.17 – Schematic of typical test rig for force coefficients identification, with the test bearing floating on a rigidly-mounted shaft, with shaker-induced excitations on the bushing, similarly to the rig of San Andres and Chirathadam [27]

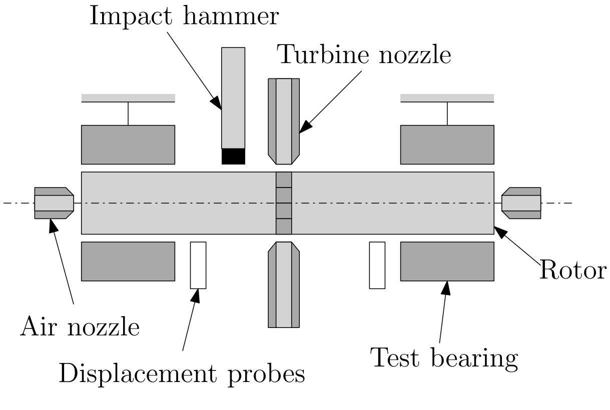

Figure 2.18 – Schematic of typical test rig for force coefficients identification, with the test bearing fixed, supporting a floating rotor, with an impact hammer exciting the journal, as investigated by Le Rouzic and Arghir [28]

The experimental identification of gas journal bearing force coefficients was pioneered by Fleming et al. [29] who built a test rig consisting of a floating rotor supported by two hybrid bearings and driven by an impulse turbine. A known unbalance was applied on the rotor and the 4 degrees of freedom of the shaft were recorded with capacitive sensors to recover the synchronous damping and stiffness of the bearings using the equations of motion of the system. Heshmat and Ku [30] investigated the force coefficients of a floating non-rotating bump foil bearing using electromagnetic shakers in orthogonal directions imposing a sine wave of constant frequency. Similar methods were applied by several research groups (Colon [31; 32], Etras [33], Matta [34], Rudolf [35; 36], San Andres and Chirathadam [27; 37; 38]) on hybrid, bump foil and metal-mesh foil bearings in rotation, applying either successive, sweeping or superposed sine waves on the shakers. A setup similar to Heshmat's was investigated by Howard and Dellacorte [39], this time with a rotating shaft and using an impact hammer to excite the bearing bushing on a board frequency spectrum, also applied later by San Andres and Chirathadam [37], Wang and Kim [40], and Rudolf et al. [35]. Magnetic bearings were employed by Bellabarba et al. [41] to support and excite a journal with a multiple-frequency signal on which a test hybrid bearing was mounted, allowing to determine the force coefficients at different excitation frequencies. Moore et al. [42] used an asynchronous rotor rotating inside the air-born test rotor to impose an excitation of controlled frequency. Larsen et al. [43] imposed an excitation in a non-rotating inner part of their floating test rotor, connected with ball bearings, to retrieve the force coefficients of bump foil bearings. Le Rouzic and Arghir [28] used an impact hammer to excite a rotor on aerostatic bearings and driven by an impulse turbine. The list of published experimental force coefficients identification of gas journal bearing is summarized in Table 2.4.

2.4.1 Test rig selection

Considering the scope of this thesis, which considers air as well as other fluids as lubricant, the design of the test rig to measure the dynamic coefficients of HGJBs is constrained by the following general specifications:

1. Cleanliness : No lubricant contamination with other substances such as grease, oil, or polluting fluid to ensure compatibility with other lubricant than air in confined environment
2. Complexity: Minimum reliance on auxiliaries to ease the design and maximize the compatibility with a confined configuration.
3. Compactness : Minimum bounding box volume and characteristic length, in order to keep a future pressure chamber as small as possible
4. Losses: Minimum power losses at high speed to relieve the heat management of the system in close-loop confined configuration
5. Versatility: Possibility to test different bearing geometries

Table 2.4 – List of published experimental investigations of HGJB

	Bearing type				Rig Type		Source of excitation					Excitation type				
	Bump Foil	Metal Mesh Foil	Cantilever Beam Foil	Hybrid / Aerostatic	Floating bearing	Floating rotor	Shaker	Unbalance	Magnetic bearing	Co-rotating shaft	Impact hammer	Unbalance	Sine	Multi-freq Sine	Impulse	Pseudo-random
Fleming et al. (1977)				●		●		●				●				
Heshmat and Ku (1994)	●				●		●						●			
Howard and Dellacorte (2001)	●				●						●				●	
Bellabarba et al. (2005)				●		●			●					●		
Colon et al. (2009)	●				●		●									
Etras et al. (2009)				●	●		●						●			●
Matta et al. (2010)				●	●		●						●		●	
Colon et al. (2010)	●				●		●							●		
Rudolf et al. (2010)	●				●		●						●			
San Andres and Chirathadam (2011)		●			●		●						●			
Moore et al. (2011)			●			●				●			●			
San Andres and Chirathadam (2011)		●			●						●				●	
Rudolf et al. (2012)				●		●		●			●	●			●	
San Andres and Chirathadam (2012)	●	●			●						●				●	
Wang and Kim (2013)	●			●	●						●				●	
Delgado (2015)				●	●		●						●			
Larsen et al. (2015)	●					●	●						●			
Le Rouzic and Arghir (2018)				●		●					●				●	
Etras and Delgado (2019)				●	●		●						●			

As a floating rotor configuration requires no other bearing than the test aerodynamic bearings, no secondary lubricant is needed for the secondary bearings (water, oil), which ensures i) a high lifetime at high speed, ii) moderate losses at high speed and iii) compactness, as only two bearings are necessary instead of three (one test bearing, two secondary bearings). The floating bearing configuration generally offers an increased versatility, as the test bearing can be easily changed with little influence on the system rotordynamic stability and reduced dependency on a fine balancing. However, if the grooves have to be manufactured on the rotor, a new rotor has to be manufactured for each testes geometry. Table 2.5 summarizes the comparison between the two test rig layouts. Since the floating bearing configuration requires secondary bearings that are stiffer than the test bearing, respecting specification 1 would require either oil-free rolling element bearings or aerostatic bearings, which respectively have poor high-speed capabilities and require auxiliaries. The floating rotor layout is therefore selected.

Table 2.5 – Qualitative comparison between the floating rotor and floating bearing configurations for the test rig

●:Advantageous, ◓:Average, ○: Disadvantageous

	Floating rotor	Floating bearing
Cleanliness	●	○
Complexity	◓	○
Compactness	●	◓
Losses	●	○
Versatility	○	◓

A comparison of means of excitation existing in the literature is presented in Table 2.6. Unbalance excitation is by far the most straightforward implementation, however it does not allow to recover much information from the bearings, as only synchronous properties can be identified. Impact hammer offers only one type of excitation and is complex to implement on a rotating shaft with limited access. Asynchronous co-rotating rotors and magnetic bearings suffer from a high complexity. The latter however offers a very large panel of excitation types. Shakers are preferred to other excitation sources because they allow a a broad excitation type, an accurate control of the input energy, as well as the possibility to apply a periodic excitation. Since the shaker cannot act on the rotor directly, they have to be mounted on the bearing bushings, which will then act on the rotor *via* the bearing to be characterized. Four floating piezo-electric shakers are used, two per bushing, with a relative angle of 90° in order to be able to excite in both directions to obtain linearly independent excitation sets (developed in detail in next subsection). To bypass the necessity to know the flexibly supported bushings inertias, displacement measurements are preferred over force measurements for the bushings. The measurement of all 8 degrees of freedom (2 positions of each bushing, 4 positions of the rotor) is accomplished via proximity probes (Figure 2.24). This reduces the necessary knowledge of inertias to the mass, and moments of inertias of the rotor.

Table 2.6 – Qualitative comparison between the excitation methods

●:Advantageous, ◓:Average, ○: Disadvantageous

	Magnetic bearing	Impact hammer	Shaker	Asynchronous rotor	Unbalance
Excitation versatility	●	◓	●	◓	○
Complexity	○	◓	●	○	●

2.4.2 Theoretical force coefficients identification

The present subsection introduces the theoretical aspect of the impedance identification of the rigid shaft supported on two HGJBs. The nomenclature and coordinates of a rigid shaft running on two flexibly supported bearings are presented in Figure 2.19. The following hypothesis are made to develop the equations of motion:

- The shaft is considered rigid and can therefore be defined in space with 4 degrees of freedom

- The tilting reaction forces of the HGJBs have a negligible effect on the system dynamics compared to the influence of radial reaction forces

- The system can be described as linear around its equilibrium position

The second hypothesis is justified when a relatively long distance separates the two journal bearings, as it will be discussed later.

The 4 equations of motions of the shaft can be written as follows:

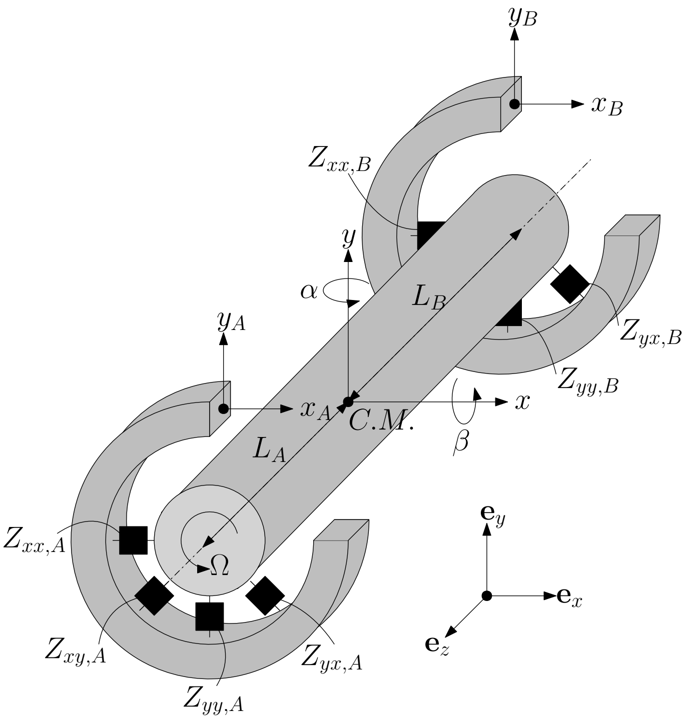

Figure 2.19 – Nomenclature and coordinates of the rotating shaft supported on two gas bearings

$$
\left\{
\begin{array}{ll}
m_R\ddot{x}+ & K_{xx,A}\left(x+L_A\alpha-x_A\right)+K_{xx,B}\left(x-L_B\alpha-x_B\right)+K_{xy,A}\left(y-L_A\beta-y_A\right)+\\
 & K_{xy,B}\left(x+L_B\beta-y_B\right)+C_{xx,A}\left(\dot{x}+L_A\dot{\alpha}-\dot{x}_A\right)+C_{xx,B}\left(\dot{x}-L_B\dot{\alpha}-\dot{x}_B\right)+\\
 & C_{xy,A}\left(\dot{y}-L_A\dot{\beta}-\dot{y}_A\right)+C_{xy,B}\left(\dot{x}+L_B\dot{\beta}-\dot{y}_B\right)=0\\
 & \\
m_R\ddot{y}+ & K_{yy,A}\left(y-L_A\beta-y_A\right)+K_{yy,B}\left(y+L_B\beta-y_B\right)+K_{yx_A}\left(x+L_A\alpha-x_A\right)+\\
 & K_{yx_B}\left(x-L_B\alpha-x_B\right)+C_{yy,A}\left(\dot{y}-L_A\dot{\beta}-\dot{y}_A\right)+C_{yy,B}\left(\dot{y}+L_B\dot{\beta}-\dot{y}_B\right)+\\
 & C_{yx_A}\left(\dot{x}+L_A\dot{\alpha}-x_A\right)+C_{yx_B}\left(\dot{x}-L_B\dot{\alpha}-\dot{x}_B\right)=0\\
 & \\
I_T\ddot{\alpha}- & I_P\dot{\beta}\Omega+K_{xx,A}L_A\left(x+L_A\alpha-x_A\right)-K_{xx,B}L_B\left(x-L_B\alpha-x_B\right)+\\
 & K_{xy,A}L_A\left(y-L_A\beta-y_A\right)-K_{xy,B}L_B\left(y+L_B\beta-y_B\right)+\\
 & C_{xx,A}L_A\left(\dot{x}+L_A\dot{\alpha}-\dot{x}_A\right)-C_{xx,B}L_B\left(\dot{x}-L_B\dot{\alpha}-\dot{x}_B\right)+\\
 & C_{xy,A}L_A\left(\dot{y}-L_A\dot{\beta}-\dot{y}_A\right)-C_{xy,B}L_B\left(\dot{y}+L_B\dot{\beta}-\dot{y}_B\right)=0\\
 & \\
I_T\ddot{\beta}+ & I_p\dot{\alpha}\Omega-K_{yy,A}L_A\left(y-L_A\beta-y_A\right)+K_{yy,B}L_B\left(y+L_B\beta-y_B\right)-\\
 & K_{yx,A}L_A\left(x+L_A\alpha-x_A\right)+K_{yx,B}L_B\left(x-L_B\alpha-x_B\right)-\\
 & C_{yy,A}L_A\left(\dot{y}-L_A\dot{\beta}-\dot{y}_A\right)+C_{yy,B}L_B\left(\dot{y}+L_B\dot{\beta}-\dot{y}_B\right)-\\
 & C_{yx,A}L_A\left(\dot{x}+L_A\dot{\alpha}-\dot{x}_A\right)+C_{yx,B}L_B\left(\dot{x}-L_B\dot{\alpha}-\dot{x}_B\right)=0
\end{array}
\right.
$$

A harmonic nature of the motion is assumed for a particular excitation frequency ω, allowing to express the displacements, velocities and accelerations as follows:

$$
\begin{aligned}
a &= \hat{a}e^{i\omega t} \\
\dot{a} &= i\omega\hat{a}e^{i\omega t} \\
\ddot{a} &= -\omega^2\hat{a}e^{i\omega t}
\end{aligned}
$$

where a designates alternatively one of the 8 coordinates of Figure 2.19. $\hat{a}$ is a complex number containing information on both amplitude and phase shift. Stiffness and damping coefficients are grouped in complex impedances Z :

$$Z = K + i\omega C \tag{2.66}$$

The 4 equations of motion reduce to the following expressions:

$$
\begin{cases}
-m_R\omega^2\hat{x} & +Z_{xx,A}\left(\hat{x} + L_A\hat{\alpha} - \hat{x}_A\right) + Z_{xx,B}\left(\hat{x} - L_B\hat{\alpha} - \hat{x}_B\right) + Z_{xy,A}\left(\hat{y} - L_A\hat{\beta} - \hat{y}_A\right) + \\
 & Z_{xy,B}\left(\hat{x} + L_B\hat{\beta} - \hat{y}_B\right) = 0 \\
 & \\
-m_R\omega^2\hat{y} & +Z_{yy,A}\left(\hat{y} - L_A\hat{\beta} - \hat{y}_A\right) + Z_{yy,B}\left(\hat{y} + L_B\hat{\beta} - \hat{y}_B\right) + Z_{yx_A}\left(\hat{x} + L_A\hat{\alpha} - \hat{x}_A\right) + \\
 & Z_{yx_B}\left(\hat{x} - L_B\hat{\alpha} - \hat{x}_B\right) = 0 \\
 & \\
-I_T\omega^2\hat{\alpha} & -I_P i\omega\hat{\beta}\Omega + Z_{xx,A}L_A\left(\hat{x} + L_A\hat{\alpha} - \hat{x}_A\right) - Z_{xx,B}L_B\left(\hat{x} - L_B\hat{\alpha} - \hat{x}_B\right) + \\
 & Z_{xy,A}L_A\left(\hat{y} - L_A\hat{\beta} - \hat{y}_A\right) - Z_{xy,B}L_B\left(\hat{y} + L_B\hat{\beta} - \hat{y}_B\right) = 0 \\
 & \\
-I_T\omega^2\hat{\beta} & +I_p i\omega\hat{\alpha}\Omega - Z_{yy,A}L_A\left(\hat{y} - L_A\hat{\beta} - \hat{y}_A\right) + Z_{yy,B}L_B\left(\hat{y} + L_B\hat{\beta} - \hat{y}_B\right) - \\
 & Z_{yx,A}L_A\left(\hat{x} + L_A\hat{\alpha} - \hat{x}_A\right) + Z_{yx,B}L_B\left(\hat{x} - L_B\hat{\alpha} - \hat{x}_B\right) = 0
\end{cases}
$$

The system of equations can be rewritten while grouping the impedance terms together in the following form:

$$\mathbf{Az} = \mathbf{b} \tag{2.67}$$

With

$$\mathbf{A} = \begin{bmatrix} a_1 & a_2 & 0 & 0 & a_3 & a_4 & 0 & 0 \\ 0 & 0 & a_5 & a_6 & 0 & 0 & a_7 & a_8 \\ a_9 & a_{10} & 0 & 0 & a_{11} & a_{12} & 0 & 0 \\ 0 & 0 & a_{13} & a_{14} & 0 & 0 & a_{15} & a_{16} \end{bmatrix} \tag{2.68}$$

$$\mathbf{z} = \begin{bmatrix} Z_{xx,A} & Z_{xy,A} & Z_{yy,A} & Z_{yx,A} & Z_{xx,B} & Z_{xy,B} & Z_{yy,B} & Z_{yx,B} \end{bmatrix}^T \tag{2.69}$$

$$\mathbf{b} = \begin{bmatrix} \omega^2 m_R \hat{x} & \omega^2 m_R \hat{y} & \omega^2 I_T \hat{\alpha} + I_P i\omega\hat{\beta}\Omega & \omega^2 I_T \hat{\beta} - I_p i\omega\hat{\alpha}\Omega \end{bmatrix}^T \tag{2.70}$$

The terms a_i composing $\mathbf{A}$ are developed in the Appendix B.

The system is not square, since only 4 equations are provided for 8 unknown variables. A additional set of equations, linearly independent from the first one, is necessary to obtain a unique solution for $\mathbf{z}$. Therefore, 4 more equations, obtained from a excitation performed in the orthogonal direction, are added to the system:

$$\begin{bmatrix} \mathbf{A}_1 \\ \mathbf{A}_2 \end{bmatrix} \mathbf{z} = \begin{bmatrix} \mathbf{b}_1 \\ \mathbf{b}_2 \end{bmatrix} \tag{2.71}$$

where indices 1 and 2 denote the components from the first and second test run respectively, which have to be linearly independent to ensure that the matrix $[\mathbf{A}_1, \mathbf{A}_2]^T$ is invertible. This is ensured by the orthogonality of the excitation directions.

In practice, the system is excited with an isolated sine on two parallel shakers simultaneously for a couple of seconds. Compared to impact and pseudo-random excitation, a sinusoidal excitation holds the following advantages:

- Accurate control of the excitation spectrum
- Limitation of non-linear effects by limiting the total displacement of the rotor
- Accurate control of the excitation amplitude at each frequency

The 8 displacements channels are filtered with a band-pass filter and a sine is fitted on each signal in time-domain with a a minimization of the quadratic error, obtaining the frequency, phase shift and amplitude of each displacement. Considering the harmonic behavior of the system, velocities and acceleration are retrieved from the displacement and used as input for the solution of 2.71.

2.4.3 Test rig description

To suit the scale of the current research interest in HGJB for small-scale turbomachinery, a rotor diameter of 16 mm is selected. The rotor is 176 mm in length and the space between the center of the two journal bearings is 72 mm (Figure 2.20). In order to investigate DN numbers above $1.5 \cdot 10^6$, a nominal rotational speed of 100 krpm is desired. To drive the rotor in ambient air, an impulse turbine located at the axial mid-span of the shaft is chosen for tests in atmospheric conditions. These turbines have been widely used in previous test rigs investigating HGJBs [17; 18; 22; 44] and other gas bearings [28; 31; 37]. They are straightforward to manufacture, implement and control if no excessive resisting torque is applied on the rotating shaft. They require compressed air to operate, which is not a problem as long as air is considered as lubricant. Stainless steel 1.4112 (X90CrMoV18) with a Diamond-Like Coating (DLC) are selected for the journal materials. Figure 2.21 shows the manufactured rotor with the two HGJBs and the impulse turbine. Using a 1D finite element code previously developed by the author using Timoshenko beam elements, the first bending mode of the free rotor at rest is evaluated (Figure 2.22). This estimation is confirmed experimentally by suspending the rotor on two soft strings with an accelerometer on one the extremities of the body. The rotor is hit with a soft hammer and the spectrum of the free response is computed. Results are visible in Figure 2.23 and show a first resonance frequency at 2280 Hz, within 2% relative discrepancy with the predicted value.

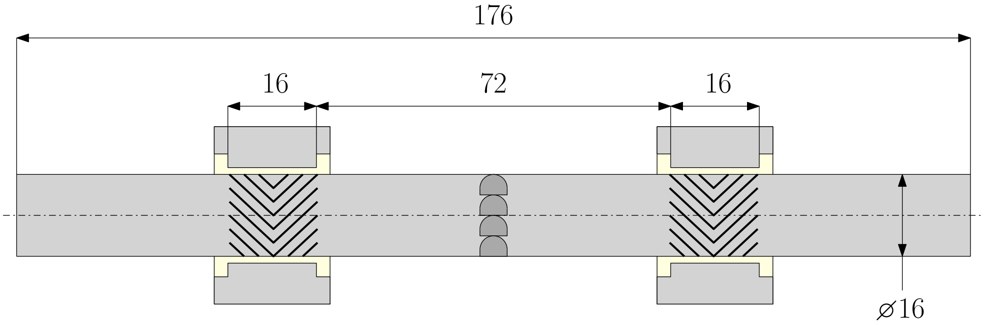

Figure 2.20 – Principal lengths of the considered test rotor

The HGJBs were designed applying a multi-objective optimization of the bearing-rotor system to simultaneously maximize stability and nominal clearance. The design variables are the nominal clearance h_0, the groove depth δ, the groove angle β, the groove length γ, the bearing aspect ratio L/D and the relative groove width α. The resulting Pareto front, showing the optimal design points, is shown in Figure 2.25. The point with the maximum logarithmic decrement is chosen as a basis to further explore the design space by freezing the parameters listed in Table 2.7.

A sensitivity analysis is performed to assess the robustness of the selected solution. Parameters h_0 and δ are varied in the vicinity of the nominal values (h_0 =7.6 µm and δ =18.1 µm) to explore the stable domain of the bearing and to deduce manufacturing

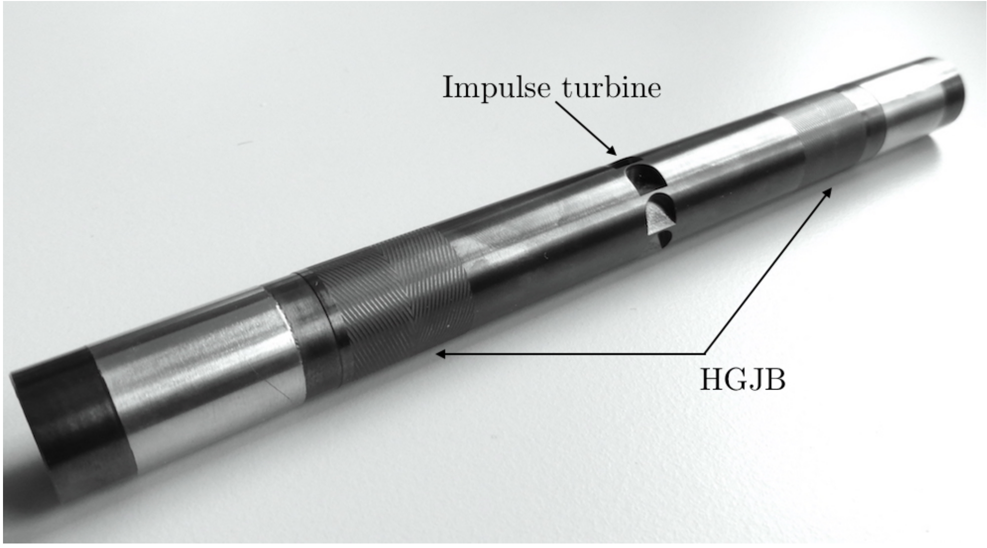
Impulse turbine
HGJB

Figure 2.21 – Picture of the investigated rotor, with the two HGJBs and the impulse turbine visible

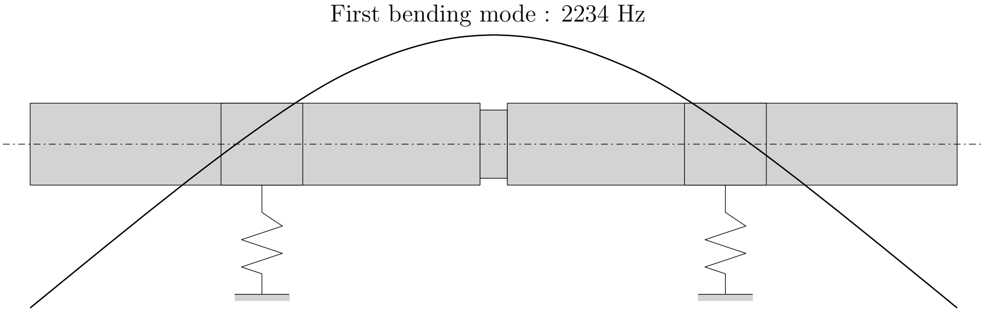
First bending mode : 2234 Hz

Figure 2.22 – Evaluation of the first bending mode at rest and without journal bearings

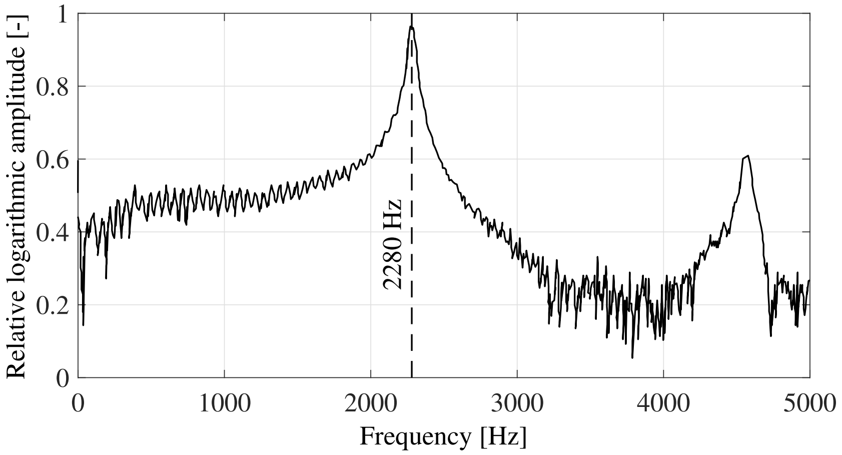

Figure 2.23 – Spectrum of the rotor free response (acceleration) after impulse from a soft hammer

Table 2.7 – HGJB geometrical parameters

α	$\hat{\beta}$	γ	L/D
0.65	160°	1	1

tolerances. Once the stable domain is identified, a maximum window is drawn in it representing the acceptable manufacturing tolerances in both h_0 and δ. Results are shown in Figure 2.26. The resulting values for the nominal clearance and the groove depth are:

$$h_0 = 7^{+1}_{-2}\mu\text{m} \tag{2.72}$$

$$\delta = 17^{+3}_{-5}\mu\text{m} \tag{2.73}$$

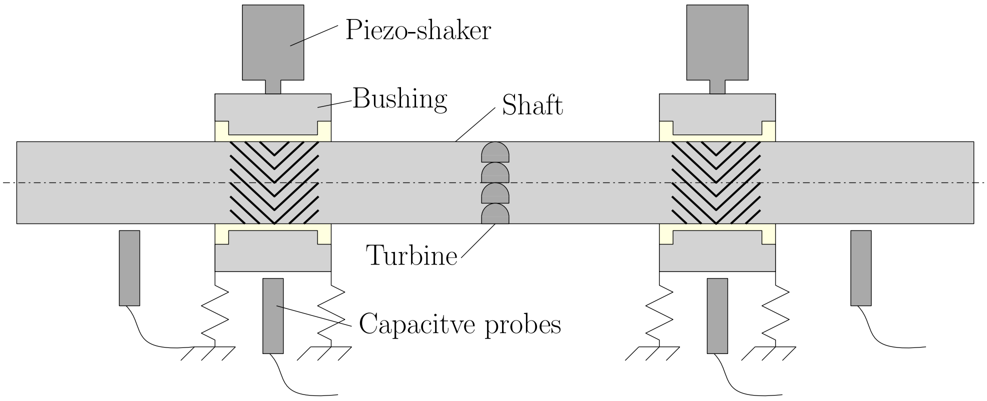

Figure 2.24 – Representation of the excitation-measurement setup in one plane. The same setup is repeated in the orthogonal plane.

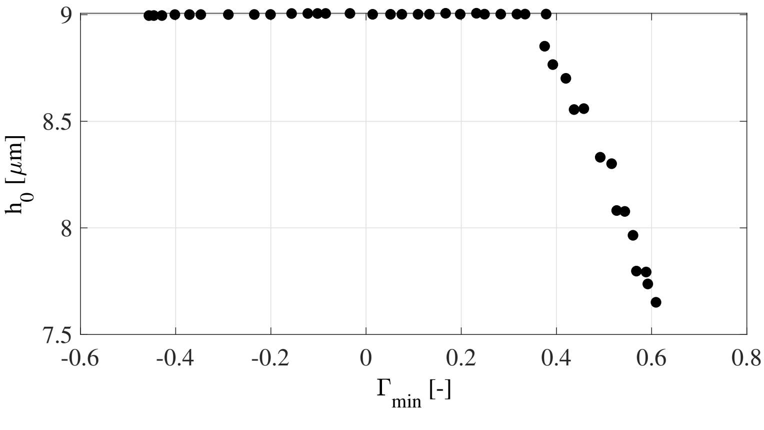

Figure 2.25 – Pareto front resulting from the two-objective optimization, showing the nominal clearance against the minimum logarithmic decrement Γ.

This design procedure was performed while neglecting the damping coefficient of the flexible supports. Therefore, the resulting manufacturing tolerances are conservative, since added damping coming brings a stabilizing effect on the system [45].

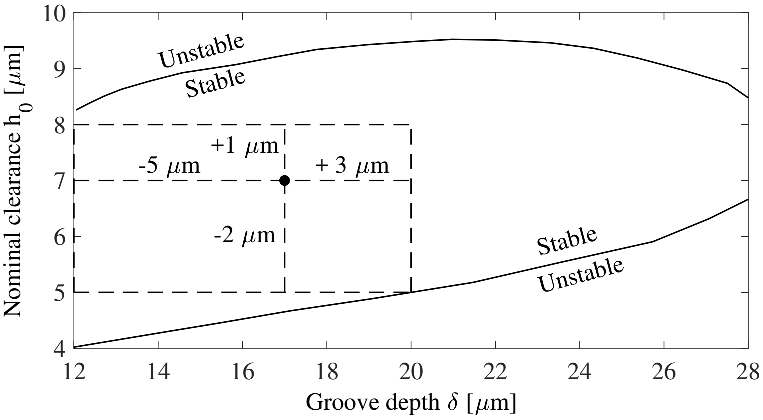

Figure 2.26 – Stable domain of the bearing and chosen manufacturing tolerances around a nominal point

As made necessary by the second theoretical hypothesis presented in 2.4.2, the geometry of the rotor enables the negligence of tilting stiffness in the system rotordynamics. Considering a simplified rotor model tilted by an angle θ around its geometrical center, supported on two bearings with translational stiffness K_y and tilting stiffness K_θ (Figure 2.27), the restoring torques T_y and T_θ are, respectively:

$$T_y = \frac{\theta L^2 K_y}{2} \tag{2.74}$$

$$T_\theta = 2\theta K_\theta \tag{2.75}$$

with the ratio:

$$T_r = \frac{T_\theta}{T_y} = \frac{4}{L^2}\frac{K_\theta}{K_y} \tag{2.76}$$

The designed HGJB are expected to provide a direct translational and tilting stiffness in the order of $2\,\mathrm{MN\,m^{-1}}$ and $400\,\mathrm{N\,m\,rad^{-1}}$ respectively. Applying these numbers in Equation 2.76 in the range of bearing center distance considered for the rotor yields the results shown in Figure 2.28. The actual bearing center distance is 88 mm, resulting in $T_r = 0.051$, which is considered sufficiently small to discard the influence of tilting stiffness in the rotordynamics.

As the NGT assumes an infinite number of groove-ridge pairs, a high number of grooves ensures a minimum discrepancy between the theory and the actual performance. A trade-off exists between the number of grooves and their minimum width limited by manufacturing, thus determining the maximal feasible number of grooves. The groove circumferential width was selected to be 1 mm in order to have 30 groove-ridge pairs on each bearing (Figure 2.29). The bushings consist of a tungsten carbide ring press-fitted onto the compliant supports to allow for a radial displacement. The supports

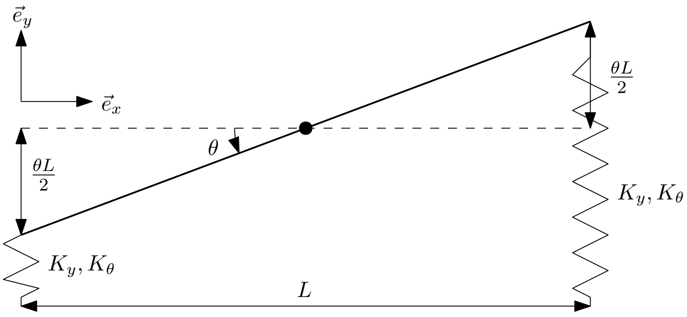

Figure 2.27 – Simplified rotor model assessing the relative influence of tilting stiffness on restoring torque

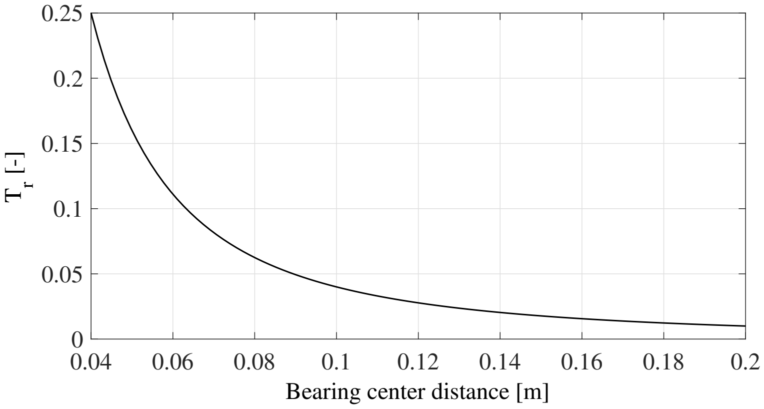

Figure 2.28 – Ratio of tilting stiffness over translational stiffness in the shaft restoring torque

are monolithic stainless steel bodies (Figures 2.30 and 2.31) with four flexible blades of 0.5 mm thickness with an axial span of 30 mm. The outer surface of the parts is conical for positioning purpose. The flexible blades were designed to provide a radial stiffness of approximately $2\,\mathrm{MN\,m^{-1}}$, in the same order of magnitude as the expected total radial stiffness of the investigated HGJBs. Figure 2.33 presents the assembly of the rotor mounted in the flexible supports equipped with piezo-shakers and the 8 capacitive sensors, model CSH05-CAm1,4 of *MicroEspilon* and their nomenclature. The floating shakers, model HP1-1000-20-VS of *Piezosystem Jena*, are mounted directly on the moving part of the flexible supports, which also include a PT100 temperature probe (*Kritex* model W05-2, class B) in their bulk, as represented in Figure 2.32. This assembly fits into a solid steel frame accommodating the different parts and measurement probes, shown is Figure 2.35. On top of the mentioned PT100 and capacitive sensors, two infra-red thermometer (*MircroEpsilon* CT-SF02-C3) recording the journal temperature and an optical trigger (contrast sensor of Keyence, not presented in Fig. 2.35) equip the test rig. A cut view of the assembly, including the turbine stator, is shown in Figure 2.34. The turbine air distributor is presented in an orthogonal cut-view in Figure 2.36. Compressed air enters an annular volume two inlets and expanded through 9 circumferential nozzles onto the 8 rotating pockets.

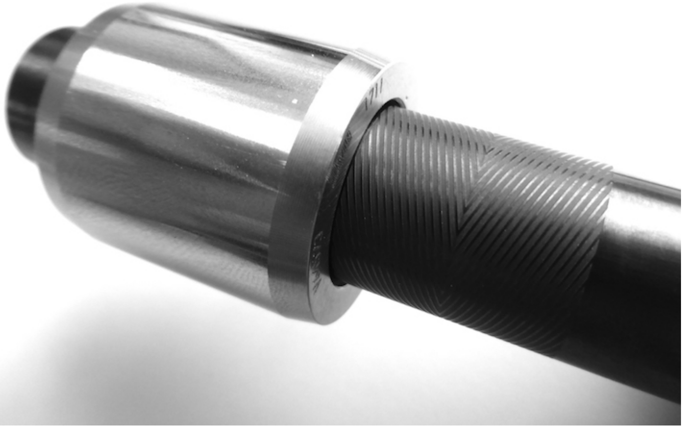

Figure 2.29 – View of one of HGJB and its bushing

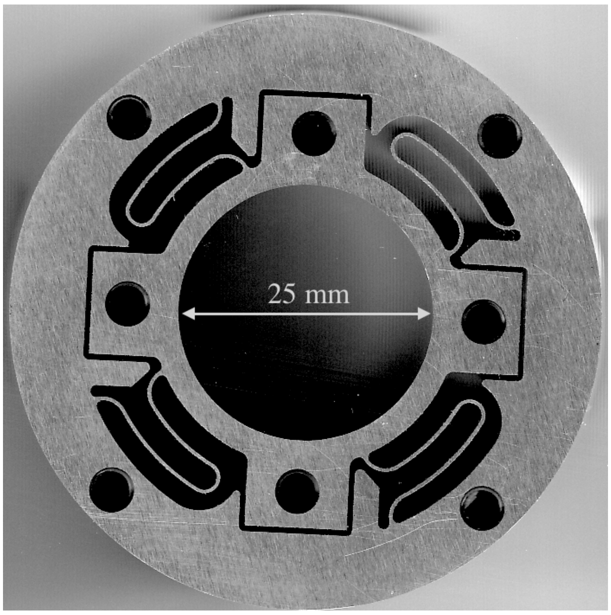

Figure 2.30 – Front view of a monolithic flexible bushing support

After manufacturing, the actual bearing clearances are determined by a specialized workshop by measuring the journal and bushing diameter at three angular positions and 5 different axial positions at a stabilized temperature of 21 °C. The results are presented in Figure 2.37 and summarized in Table 2.8. The measurements suggest that the clearance is not constant in axial and circumferential direction, as each plane suffers from a significant circularity error. In Table 2.8, the mean maximum and minimum represent respectively the average value of each of the maximum and minimum clearance measured at each plane of the bearing. Bearing B has a slightly smaller mean clearance than bearing A.

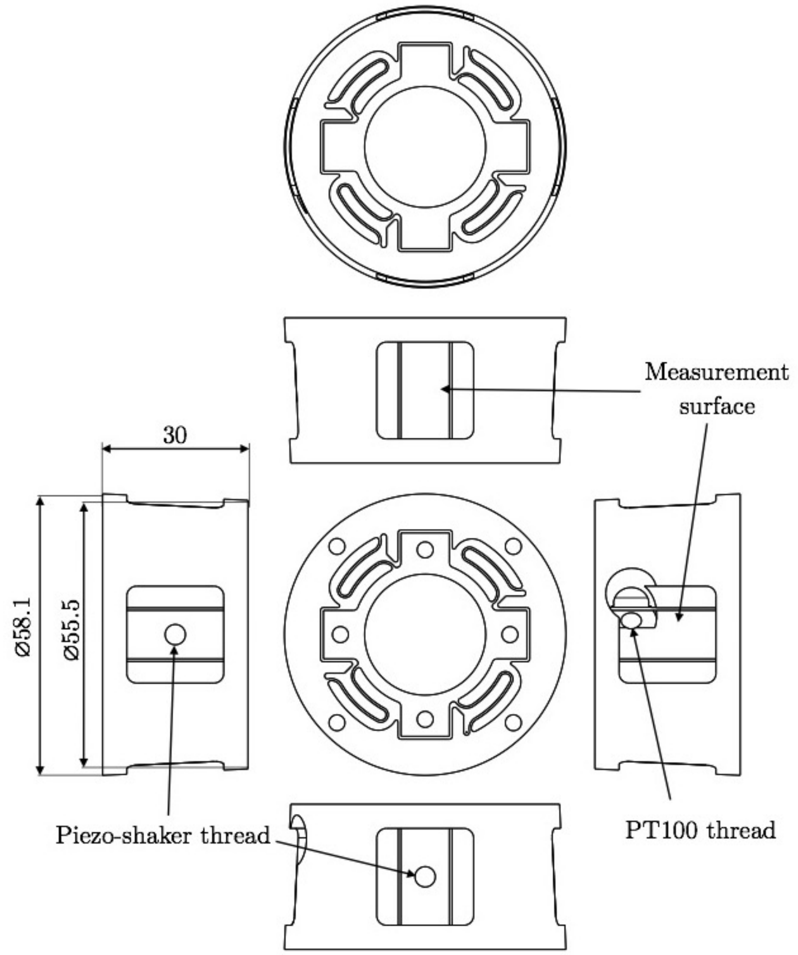
Measurement surface
30
Ø58.1
Ø55.5
Piezo-shaker thread
PT100 thread

Figure 2.31 – Projected views of the flexible bearing support

The groove depth was measured in several location using a rugosimeter as described in Appendix C. The depth was measured between 15 and 17 µm, as illustrated in Figure 2.38.

Table 2.8 – Summary of the average, mean minimum, mean maximum and extreme values of measured clearances

	Bearing A	Bearing B
Mean clearance	8.3 µm	7.8 µm
Mean minimum	7.3 µm	7.4 µm
Mean maximum	9.2 µm	8.3 µm
Absolute minimum	6.8 µm	6.7 µm
Absolute maximum	9.9 µm	9.0 µm

The centrifugal growth of the rotor is computed with the following equation:

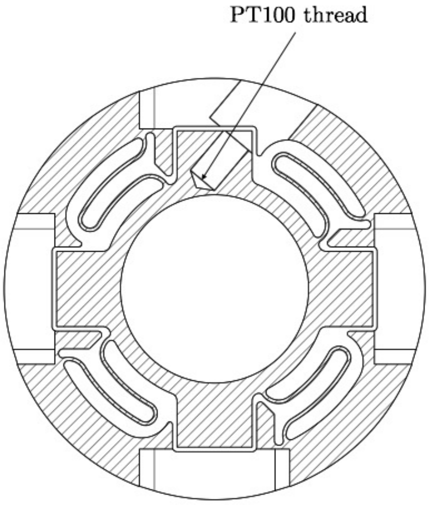
PT100 thread

Figure 2.32 – Cut view of the flexible bearing support showing the location of the PT100 probe

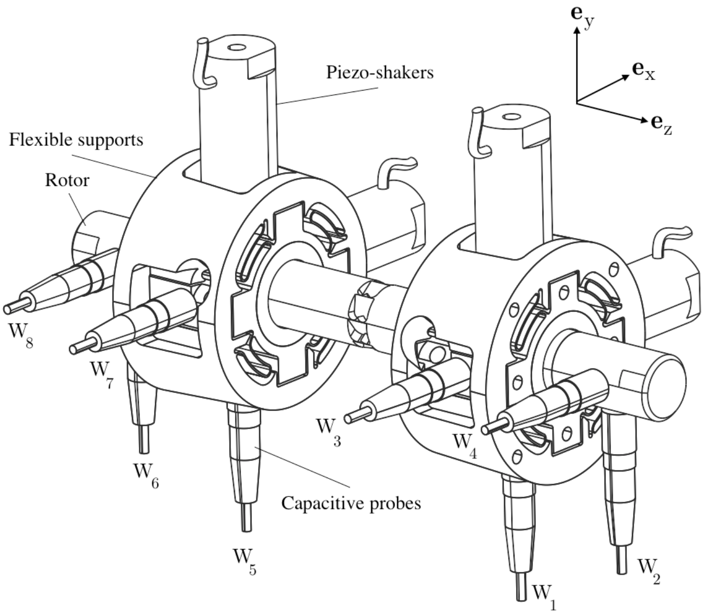
$\mathbf{e}_y$
$\mathbf{e}_x$
$\mathbf{e}_z$
Piezo-shakers
Flexible supports
Rotor
W8
W7
W6
W5
W3
W4
W1
W2
Capacitive probes

Figure 2.33 – Partial assembly showing the rotor mounted in the flexible supports equipped with piezo-shakers and the 8 capacitive sensors, denoted W_1 to W_8

$$\Delta h = \frac{\rho R^3(1-\nu)}{4E}\Omega^2 \tag{2.77}$$

The computed growth for the actual rotor (E=200 GPa, ρ=7700 kg m^{-3}, ν=0.2) is pre-

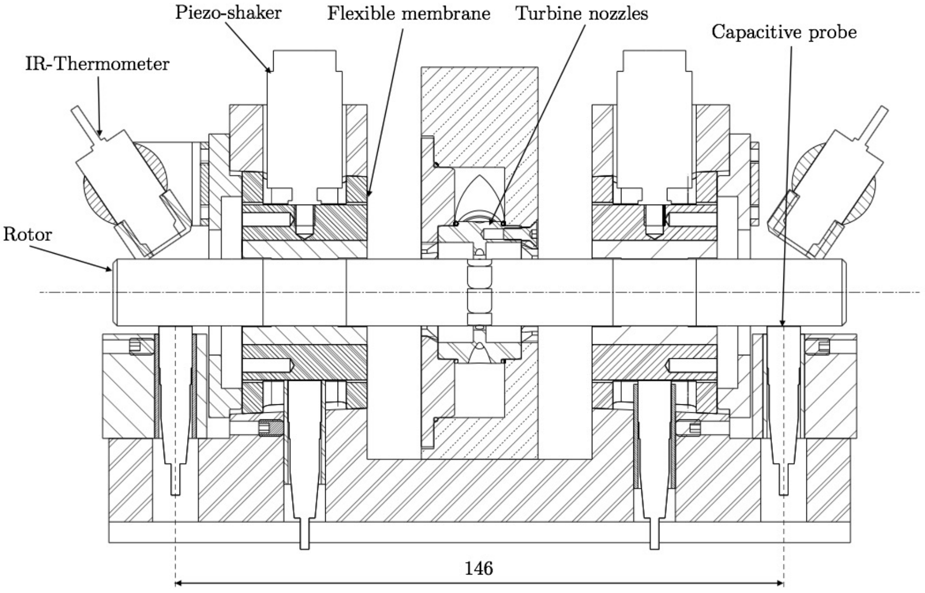
Piezo-shaker
Flexible membrane
Turbine nozzles
Capacitive probe
IR-Thermometer
Rotor
146

Figure 2.34 – Cut-view of the experimental apparatus showing the main components : capacitive sensors, piezo-shakers, rotor, turbine. The axial bearings are not represented on this view

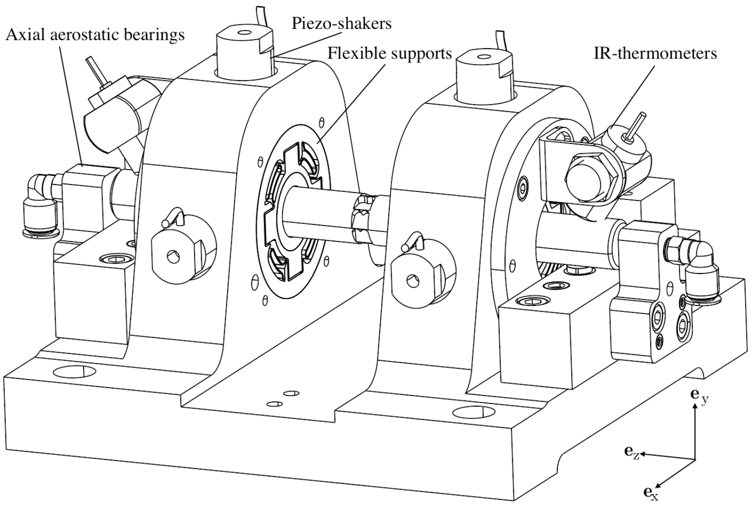
Axial aerostatic bearings
Piezo-shakers
Flexible supports
IR-thermometers
$\mathbf{e}_y$
$\mathbf{e}_z$
$\mathbf{e}_x$

Figure 2.35 – Near-complete assembly, with the steel frame accommodating the different organs. The turbine distributor around the impulse turbine is missing for presentation purpose

sented in Figure 2.39. The radial growth at maximum speed reaches 0.7 µm.

The apparatus is first positioned vertically in order to relief the journal bearing from any static radial load, where the weight is entirely supported on one of the axial aerostatic

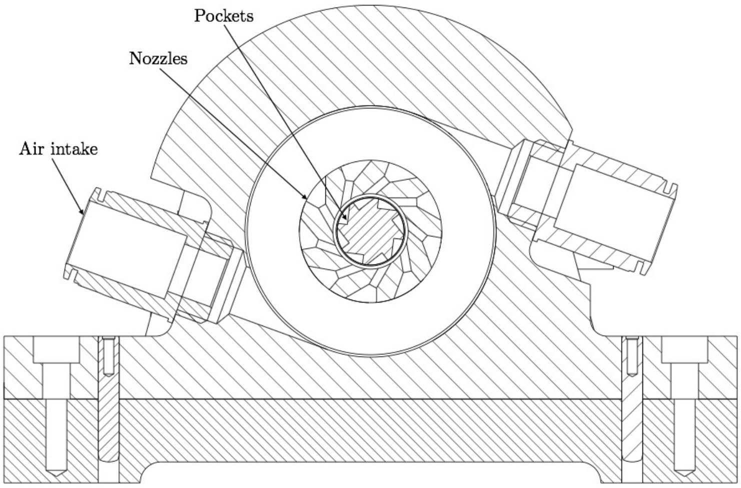
Pockets
Nozzles
Air intake

Figure 2.36 – Cut-view of the turbine distributor. Compressed air enters via two inlets, is equalized in an annular volume and expanded in 9 circumferential nozzles

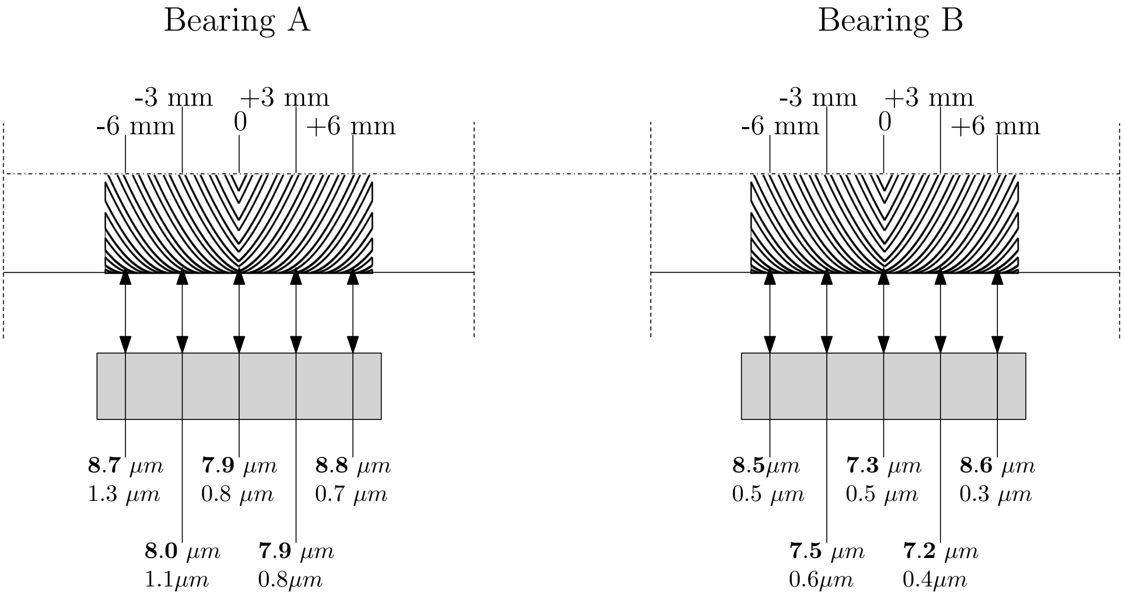
Bearing A
-3 mm
+3 mm
-6 mm
0
+6 mm
8.7 μm
1.3 μm
7.9 μm
0.8 μm
8.8 μm
0.7 μm
8.0 μm
1.1μm
7.9 μm
0.8μm
Bearing B
-3 mm
+3 mm
-6 mm
0
+6 mm
8.5μm
0.5 μm
7.3 μm
0.5 μm
8.6 μm
0.3 μm
7.5 μm
0.6μm
7.2 μm
0.4μm

Figure 2.37 – Clearances of the two HGJBs measured on three angular location at each of 6 axial locations. Upper and lower values indicate the maximum and minimum values measures. The bold value indicate the mean of the three measures

bearings with a absolute supply pressure of 240 kPa. The axial bearing consist of a 16 mm-diameter tube with a 5 mm restrictor covered by an O-ring glued on its surface, as represented in Figure 2.40 . The O-ring provides a compliant surface to accommodate misalignment between the bearing and the shaft lateral surface, allowing for a lubricating film to effectively form between the O-ring and the shaft. Plus, it provides substantial axial damping in case of unexpected pneumatic hammer, as well as a soft sacrificial

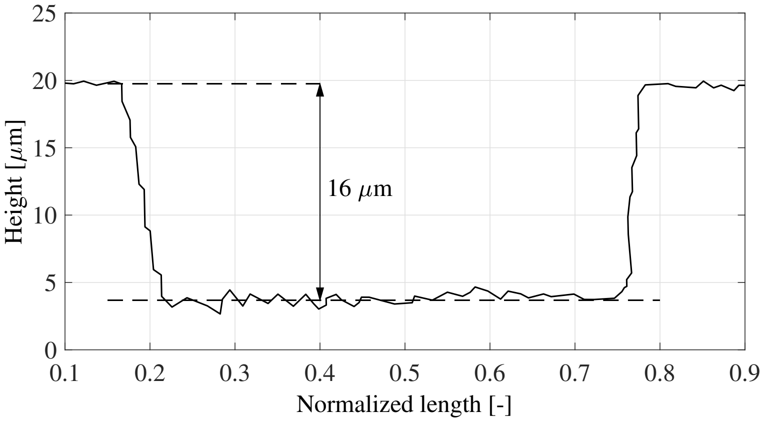

Figure 2.38 – Example of groove-ridge profile used to determine the groove depth

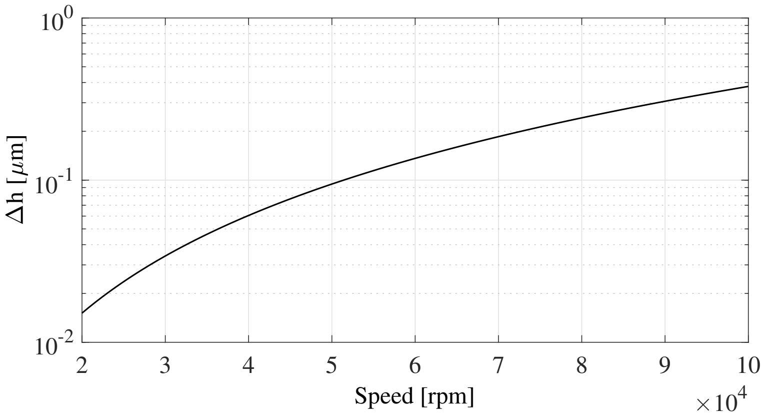

Figure 2.39 – Radial centrifugal growth against rotor speed

surface in case of direct contact with the rotating shaft. Figure 2.41 shows a picture of the experimental setup ready for start-up.

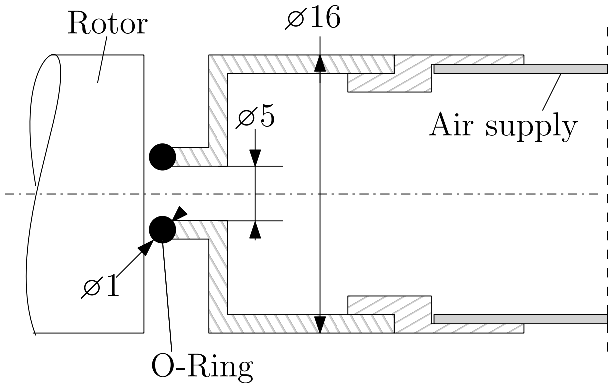

Figure 2.40 – Schematic cut-view representation of the aerostatic axial bearing

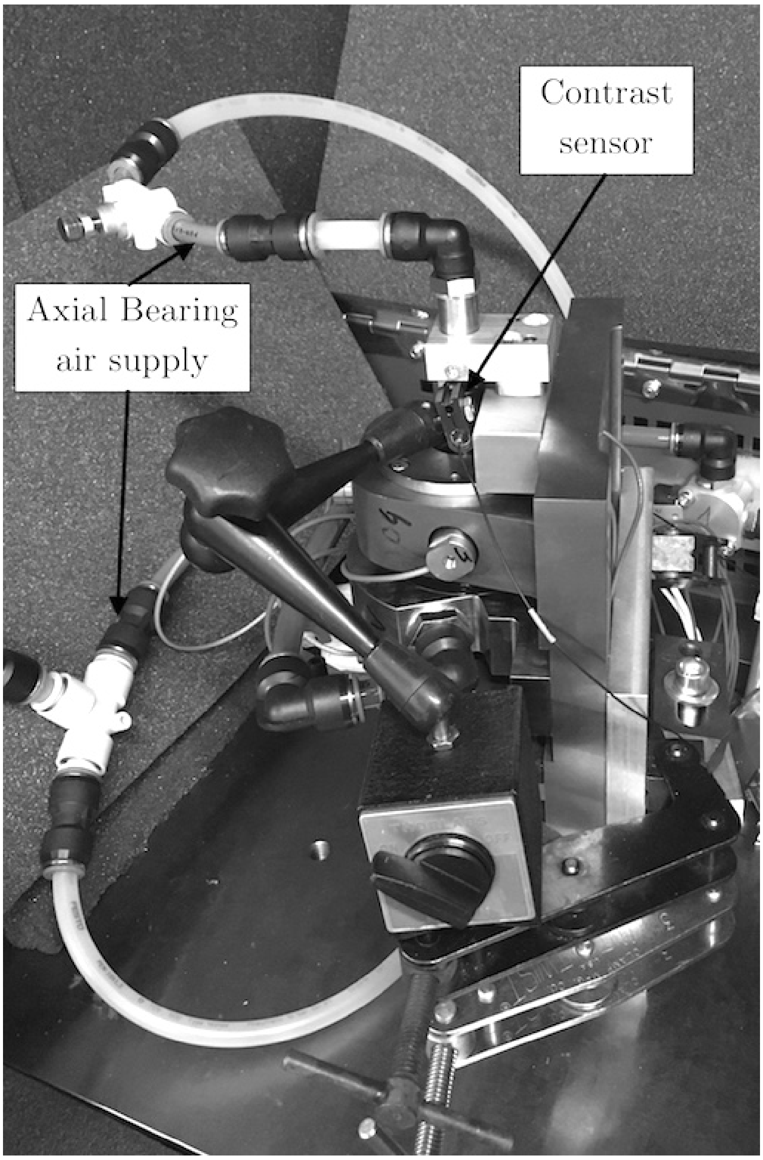
Contrast sensor
Axial Bearing air supply

Figure 2.41 – Experimental apparatus in vertical position

Uncertainties

The sources of uncertainty regarding the measurements have several sources :

- Uncertainty of the measurement chain (linearity, target roundness, resolution, random error)
- Filtering and fitting errors
- Errors on rotor parameters (rotor mass, bearing distance, position of center of mass)

The first and second group of uncertainties affect the 8 displacement channels both in phase and amplitude. However, the first group of uncertainties is not significant compared to the second group, the filtering and fitting errors, when the sine wave of each channel corresponding to the excitation frequency is isolated from the raw time-domain signal. They affect both amplitude and phase of the identified sine waves and are treated in the Appendix D.5.4. The third group affect all non-displacement parameters involved in the equations of motion 2.66. They are estimated in Appendix D.1-D.4, with the output shown in Table 2.9.

Table 2.9 – Fixed and variable rotordynamic model parameters nominal value and associated uncertainties as estimated in Appendix D

Symbol	Name	Value	Uncertainty
m_R	Rotor mass	$0.267\,176\,\mathrm{kg}$	$3\,\mathrm{mg}$
I_P	Axial inertia	$8.83 \cdot 10^{-6}\,\mathrm{kg\,m^2}$	$2.50 \cdot 10^{-7}\,\mathrm{kg\,m^2}$
I_T	Transverse inertia	$7.01 \cdot 10^{-4}\,\mathrm{kg\,m^2}$	$1.12 \cdot 10^{-5}\,\mathrm{kg\,m^2}$
L_W	($\mathrm{W}_{2,4,6,8}$) - C.M distance	$73\,\mathrm{mm}$	$0.25\,\mathrm{mm}$
$L_{A,B}$	Bearing - C.M distance	$44\,\mathrm{mm}$	$0.25\,\mathrm{mm}$

Symbol	Name	Relative uncertainty
Ω	Rotational speed	1%
ω	Excitation frequency	0.1%

These sources of error affect the uncertainty σ_i of each i^{th} variable involved in the computation of the impedance terms. Once these uncertainties are identified and quantified, their propagation on the output is computed as follows:

$$\sigma_j = \sqrt{\sum_{i=1}^{N} \left(\frac{\partial Z_j}{\partial x_i} \sigma_i \right)^2} \qquad 2.78$$

where Z_j designates any component of the impedance vector $\mathbf{z}$ of Equation 2.69 and x_i any of the system parameters (such as listed in Table 2.9) or of the measured variables (displacement, rotational speed, etc). Equation 2.78 is solved numerically by applying a central finite difference scheme to evaluate the partial derivatives of Z:

$$\frac{\partial Z_j}{\partial x_i} \approx \frac{Z_j(x_i + \Delta x_i) - Z_j(x_i - \Delta x_i)}{2\Delta x_i} \qquad 2.79$$

2.4.4 Results

For each rotational speed, the following procedure is applied:

1. PID-controlled acceleration up to nominal speed, within 100 rpm of the nominal speed
2. Excitation of shakers in one plane for 4 seconds at a particular frequency f_1
3. Non-excited operation of the rotor for 30 seconds
4. Excitation of shakers in the orthogonal plane for 4 seconds at a particular frequency f_1
5. Non-excited operation of the rotor for 30 seconds
6. Repetition of points 2 to 5 with the next excitation frequency f_2, until the last frequency f_n is excited
7. Interruption of the turbine air supply and coast down

The evolution of the rotational speed in time is shown in Figure 2.42 for a measurement campaign at 100 krpm. The 3 phases of a test, namely the acceleration, the steady state and the coast down are visible. The evolution of the bushing and rotor temperatures are shown in Figure 2.43. Both bearings experience a rise in temperature after the acceleration phase up to 26 °C and 28 °C for bearings A and B respectively, reaching a maximum at approximately t= 200 s and slowly decreasing afterwards. At the moment the turbine is cut to initiate the coast down, the bushings experience a short rise in temperature, highlighting the cooling effect of the air turbine on the system. The waterfall plot presenting the spectrum of the channel W_3, measuring the position of the bushing A in the direction $\vec{e}_x$, is shown in Figure 2.44. The synchronous vibration of the shaft running at 100 krpm is visible as well as the pairs of excitation peaks. The excitation frequencies range from 400 Hz to 1700 Hz, with a step of 100 Hz. On top of these expected signatures, a sub-synchronous frequency content is visible at $f \approx 250$ Hz, generated by the turbine. As soon as the turbine is cut to initialize the coast down, these vibrations vanish. After each signal of the two excitation sets has been band-filtered and fitted with a sine to identify its amplitude and phase, these informations are injected in Equation 2.67 to obtain the force coefficients. Figure 2.45 shows the amplitude of each signal at each excitation frequency for the considered run. The maximum amplitude recorded for this run is 1.3 µm, while the total amplitude of the orbit without the influence of the shakers, shown in Figure 2.46, is in the order 1 µm in radius at nominal speed.

The identified force coefficient of the bearings A and B at 100 krpm are presented in Figures 2.51 and 2.52, respectively. The results are presented against the excitation frequency normalized by the rotational frequency. On top of the experimental results, the predictions from the NGT with perturbation around a concentric position, based on the measured clearance and groove depth measurements, are displayed. The nominal case corresponds to the mean measured clearance of the bearing and the nominal groove depth (16 µm). The dotted lines correspond to the absolute upper and lower bounds of the predictions

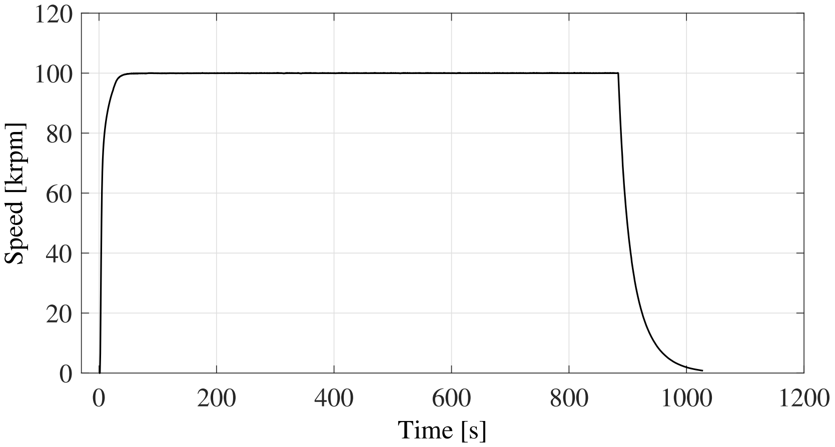

Figure 2.42 – Speed over time for a test run at 100 krpm

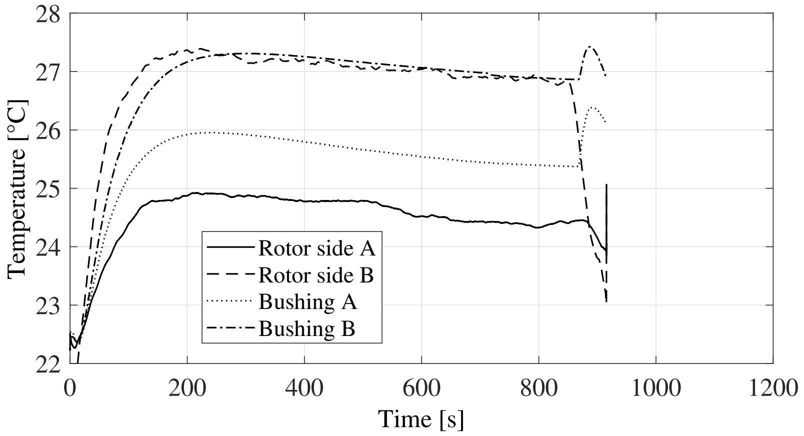

Figure 2.43 – Bushings and rotor temperature during the run at 100 krpm

based on the measured maximum clearance, minimum clearance, and uncertainty on the groove depth. Dashed lines show the predictions based on the mean minimum and maximum clearance, with the nominal groove depth. The effect of differential thermal growth, due to the difference in thermal expansion coefficients as well as in temperature between rotor and bushing, are shown in Figures 2.47 and 2.48 and are taken into account for the prediction of impedances with the NGT-based model. In general, the prediction are in good qualitative agreement with the data, but quantitatively overestimates the force coefficients. The rising trend of direct stiffness toward higher excitation frequencies is captured, as well as the non-monotonic behavior of the cross-coupled stiffness. The trend of the direct damping is qualitatively captured, with a near stagnation followed by a slow decrease. In general, both bearing show an very isotropic behavior for all force coefficients. Measurement uncertainties tend to increase with the excitation frequency, mostly because the rotor motion under excitation decreases with frequency, as is can be expected from a dynamic system supercritical regime. Therefore, the signal-to-noise

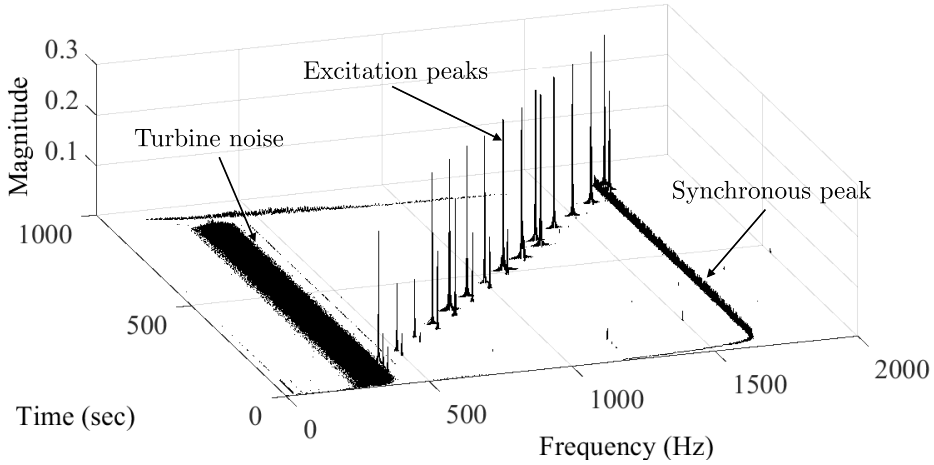

Figure 2.44 – Waterfall plot of the test run spectrum, with excitation signatures, synchronous vibration and turbine sub-synchronous noise visible

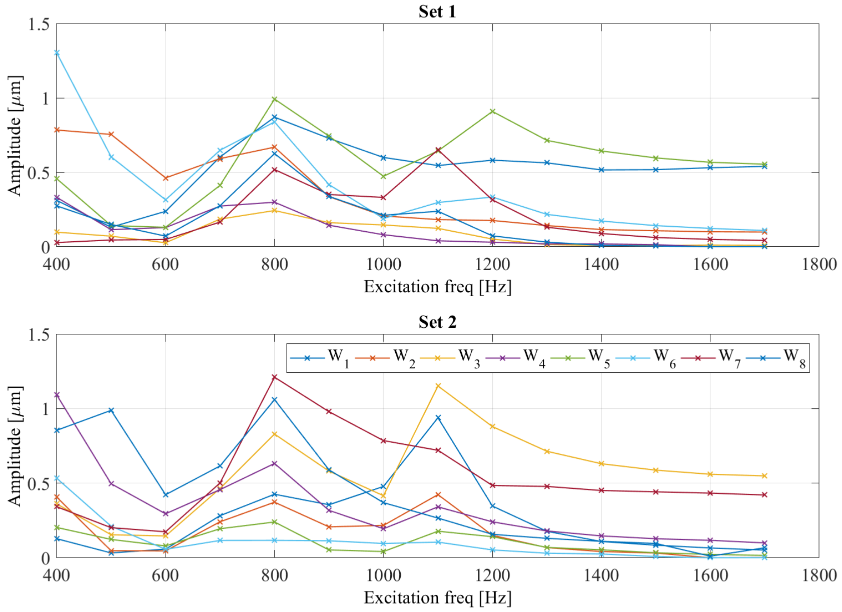

Figure 2.45 – Amplitude of identified signals on the 8 proximity probes at different excitation frequencies, for the two orthogonal excitation runs

ratio becomes less favorable and leads to relatively larger uncertainties. The influence of each model parameter uncertainty is displayed in Figures 2.49 and 2.50 for stiffness and damping coefficients respectively, evaluated at 700 Hz. The asymmetric sensitivity of the two bearings on the common system parameters (Ω, ω, m_R, I_P, I_T, $L_{A/B}$, L_W) is explained by the dependency of the sensitivity on the phase and amplitude of W_i, $i = 1..8$, which is different between the two bearings.

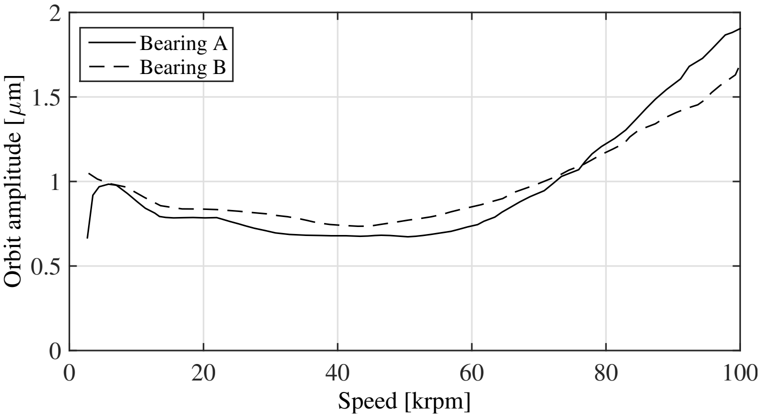

Figure 2.46 – Peak-to-peak amplitude (diameter of the orbits of the bearings as different rotational speeds

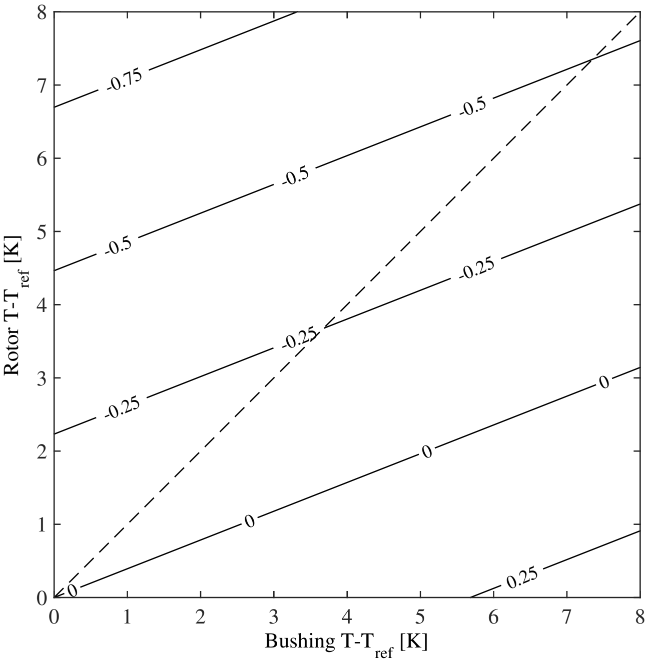

Figure 2.47 – Isovalue lines for the change in radial clearance (in µm) due to the change of temperature of the rotor and bushing from the reference temperature T_{ref} =21 °C

The results for the rotational speeds 50, 60, 70, 80 and 90 krpm are presented in the Appendix E. The model predictions are generally in good accordance with experimental data, although the case corresponding to the largest clearance provides the closest predictions to the data. Interestingly, the prediction seems to be quantitatively better for bearing A and high excitation frequencies, where it first follows the trend of the low clearance predictions at lower frequencies and slightly diverge toward the nominal case

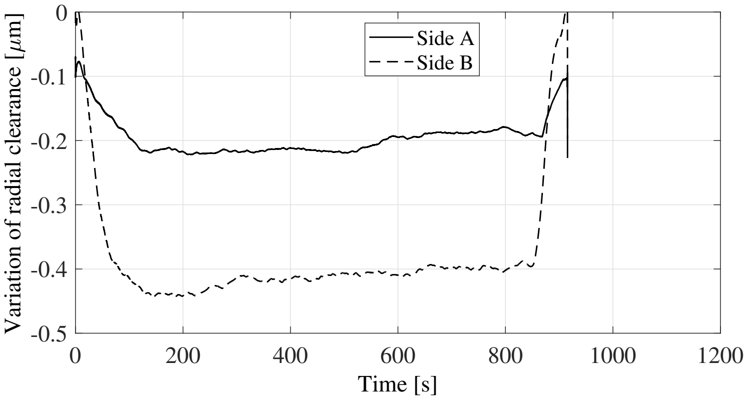

Figure 2.48 – Change of radial clearance due to thermal expansion as a function of time for the test run at 100krpm, computed from Fig.2.47 the temperature profile of Fig.2.43

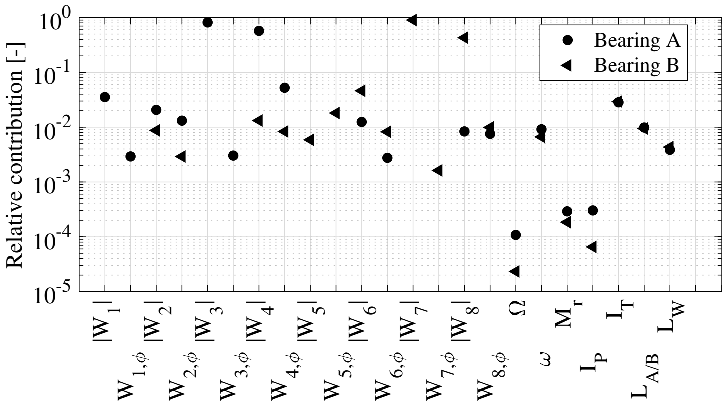

(a) Direct stiffness

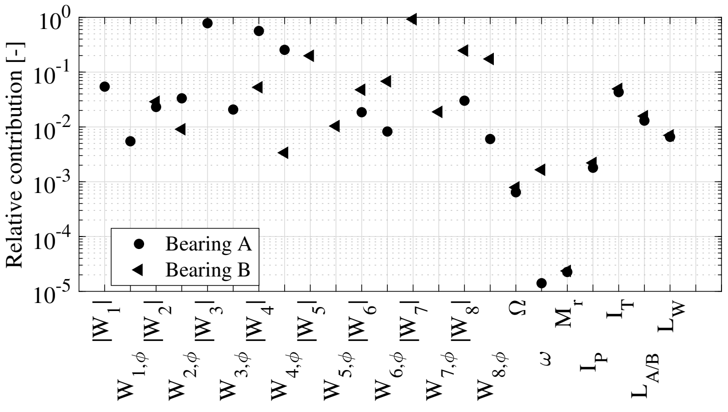

(b) Cross-coupled stiffness

Figure 2.49 – Parametric contribution of uncertainties on K_{xx} and K_{xy} for 100 krpm at an excitation frequency of 700 Hz

predictions as the frequency increases. Overall, the Narrow-Groove Theory coupled with the perturbation method provides good predictions of the bearing force coefficients.

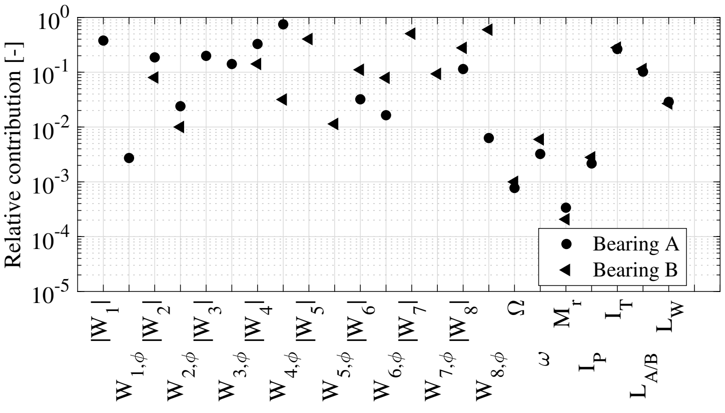

(a) Direct damping

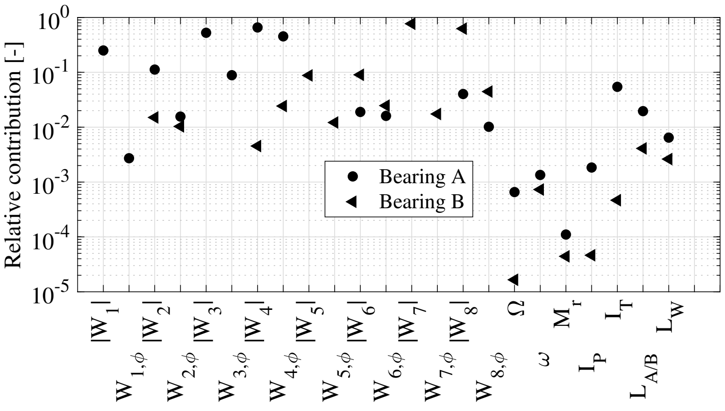

(b) Cross-coupled damping

Figure 2.50 – Parametric contribution of uncertainties on C_{xx} and C_{xy} for 100 krpm at an excitation frequency of 700 Hz

2.4.4.1 Effect of excitation amplitude

As the predictive tool employs the perturbation method, only the linear force coefficients can be predicted. However, any non-infinitesimal excitation might also trigger a non-linear response from the system, not accounted for in the rotordynamic model, but which would affect the value of the estimated linear coefficients. To address this point, a test run at constant rotational speed and excitation speed is performed at 70 krpm and two excitation frequencies ($f_{ex}/f_{rot} = 0.60$ and 0.77), respectively, otherwise following the same procedure as presented before, with the difference that the voltage amplitude imposed on the shakers is progressively increased. The results are presented in Figure 2.53 for K_{xx}, K_{xy}, C_{xx} and C_{xy} for bearing A. Increasing the voltage applied on the shakers tends to increase the excitation amplitude and decrease the uncertainty on the estimated linear parameters, thanks to a improved signal-to-noise ratio. Among the coefficients shown here, only C_{xx} exhibits a significant evolution with the excitation amplitude, probably explained by the increasing influence of non-linear damping in the motion of the rotor-bushings system. The positive trend observed at higher perturbations indicate positive higher-order damping coefficients. To a lesser extend, the non-linearity is also observed in K_{xy}, whose decrease indicate negative higher-order behavior. The frequency-dependent results of Figures 2.51 and 2.52 for 100 krpm, as well as in the Appendix E, are excited with an relative amplitude of the rotor in the bushings of the order of 1 µm, which is a good trade-off between uncertainty of the prediction and influence of the non-linear terms.

2.4.4.2 Effect of gravity

In an attempt to highlight the effect of static eccentricity on the identified force parameters, the orientation of the test rig is changed and the test repeated. The test rig is placed horizontally, such that the $\mathbf{e_y}$ vector is now co-linear with the gravity vector. The tests are repeated at 50 krpm. The static load per bearing is 1.3 N. The center of the rotor shifted by 1.5 µm compared to the vertical unloaded position, which, assuming the vertical position as the center of the bearing, corresponds to an eccentricity ratio between 15.1 and 22.0 % (with the clearance reported in Fig.2.37). Results for 50 krpm are shown in Figure 2.55. There is no significant effect of gravity on the investigated force coefficients that can be resolved within the uncertainty of the measures. A shift toward higher values is visible for the coefficient K_{yy}, however in modest proportions.

2.5 Chapter conclusion

The perturbed NGT was implemented using a 2-D FDM scheme in order to compute the load capacity and the dynamic impedance of HGJBs at different static eccentricities. The numerical outputs were compared to published numerical results, either obtained by the NGT of by solving the Reynolds equation over the grooved bearings. A very good agreement between the implementation the references was found, including the predictions at high at high eccentricity ratios, against the widespread belief that the NGT is limited to the concentric position. In order to validate the NGT and the perturbation method in their ability to predict the linear force coefficient of Herringbone-Groove Journal Bearings, a test rig was designed and built to measure the frequency-dependent force coefficients of HGJBs for the first time in the published literature. The rig consists of an air-driven rotor supported on two HGJBs, whose bushings are flexibly supported and actively excited radially in both directions by piezoelectric shakers. Solid body motions of shaft and bushings are recorded to deduce the bearing impedances without the need of force measurements, which is commonly used in the literature. Measurements where performed at speeds between 50 and 100 krpm and excitation frequencies between 400 Hz and 1700 Hz. Predicted direct and cross-coupled stiffness and damping coefficients were found to be in good qualitative agreement with the experimental data. However, the predictions tend to quantitatively overestimate the measured stiffness and damping coefficients. The circularity error in the manufacturing of the journal bearings, both on rotor and stator side, render the accurate assessment of the data-model deviation difficult to resolve. The present section yields the following concluding remarks :

- A force coefficient estimation without force measurements, relying only on displacement measurements, is feasible and demonstrated
- The prediction of force coefficients based on the perturbed NGT is in good qualitative agreement with the experimental data
- The perturbed NGT tends to overestimate quantitatively the force coefficients
- The largest measured clearance seems to be the relevant metric in the performance prediction of a particular bearing
- The linearity of force coefficient is observed up to large dynamic eccentricity ratio ($\approx 30\%$). Only the direct damping and the cross-coupled stiffness exhibit a non-linearity within the investigated perturbations

The reliability of the bearing modeling strategy suggest that the implemented tools can be expanded further to include advanced gas lubrication such as real-gas lubrication, humid air condensation and be applied to advanced grooved bearing designs.

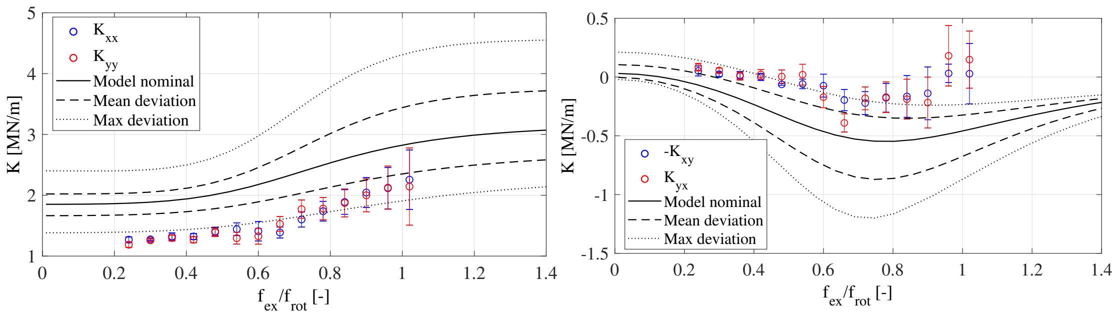

Direct stiffness

Cross-coupled stiffness

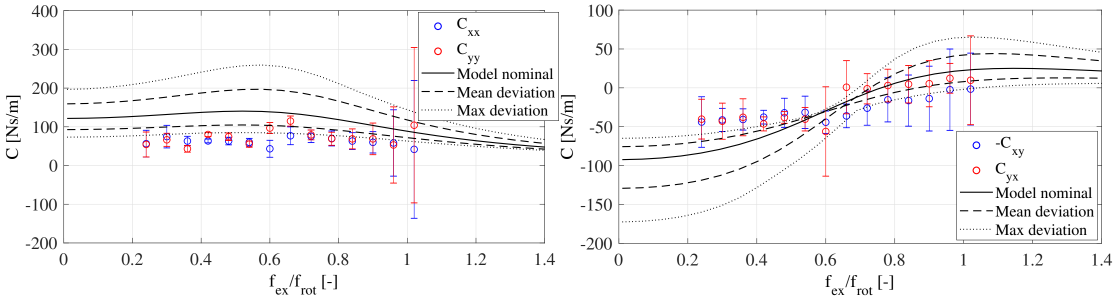

Direct damping

Cross-coupled damping

Figure 2.51 – Results of identified force coefficient of bearing A for 100krpm in ambient air

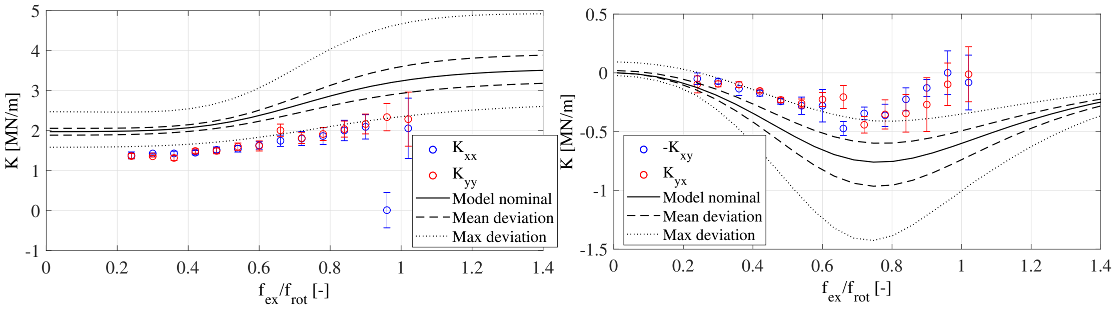

Direct stiffness

Cross-coupled stiffness

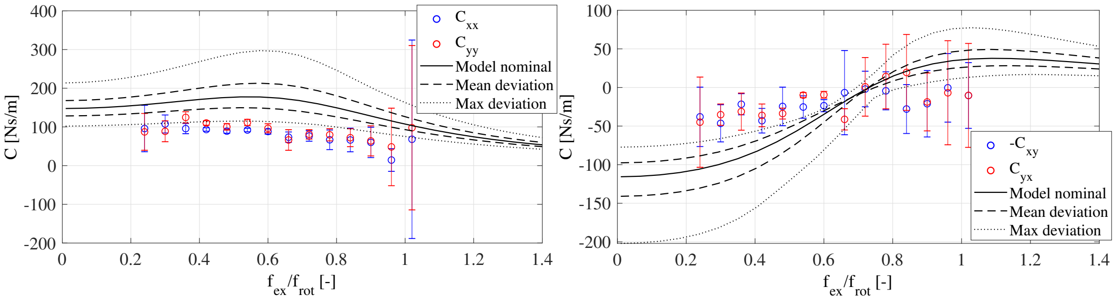

Direct damping

Cross-coupled damping

Figure 2.52 – Results of identified force coefficient of bearing B for 100krpm in ambient air

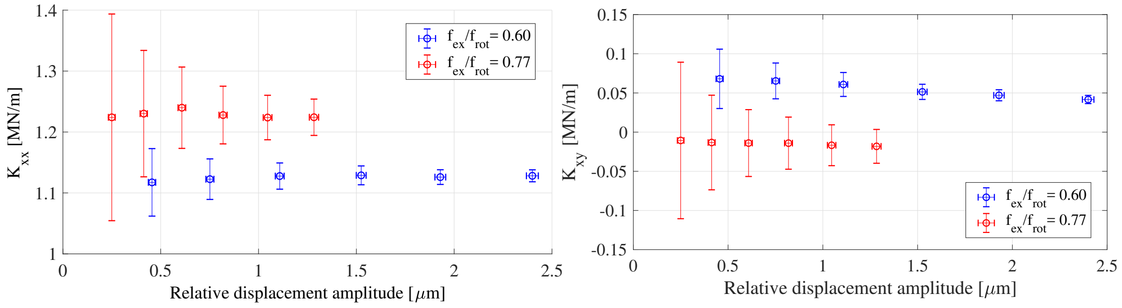

Direct stiffness

Cross-coupled stiffness

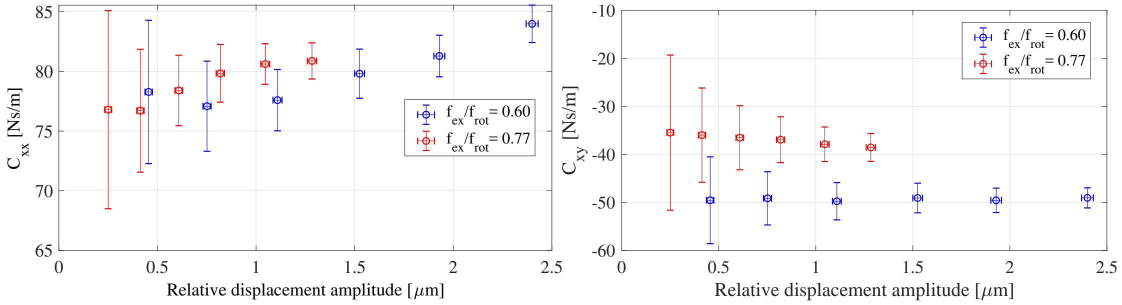

Direct damping

Cross-coupled damping

Figure 2.53 – Results of identified force coefficient of bearing A for 70 krpm in ambient air at two relative excitation frequencies and different excitation amplitude

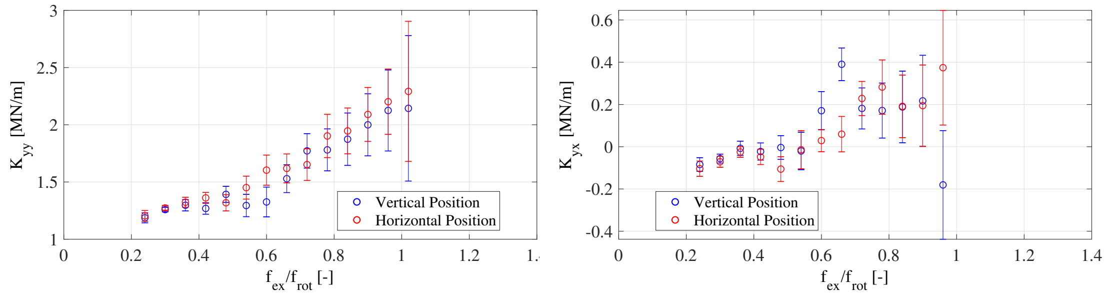

Direct stiffness

Cross-coupled stiffness

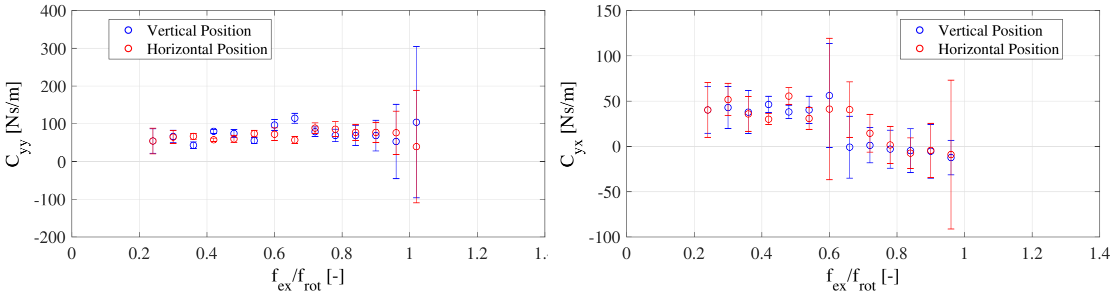

Direct damping

Cross-coupled damping

Figure 2.54 – Effect of orientation on the measured performance at 100 krpm

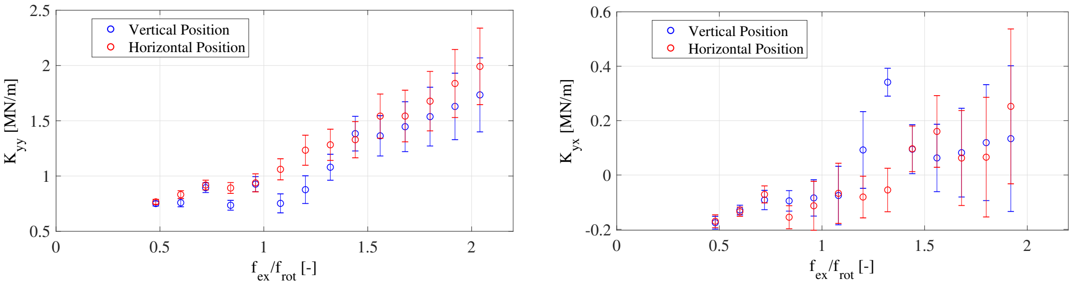

Direct stiffness

Cross-coupled stiffness

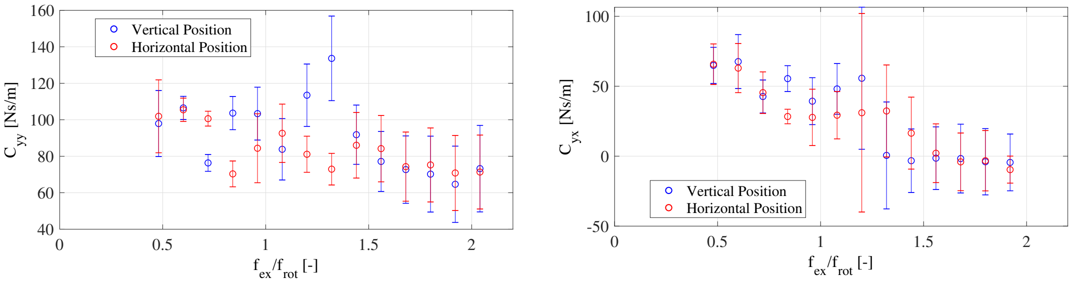

Direct damping

Cross-coupled damping

Figure 2.55 – Effect of orientation on the measured performance at 50 krpm

Bibliography

[1] R. Whipple, The Inclined Groove Bearing, Tech. rep., United Kingdom Atomic Energy Authority. Research Group. Atomic Energy Research Establishment, Harwell, Berks, England (1958).

[2] J. H. Vohr, C. Y. Chow, Characteristics of herringbone-grooved, gas-lubricated journal bearings, Journal of Basic Engineering 87 (3) (1965) 568–576. `doi:10.1115/1.3650607`.

[3] D. Bonneau, J. Absi, Analysis of aerodynamic journal bearings with small number of herringbone grooves by finite element method, Journal of Tribology 116 (4) (1994) 698–704. `doi:10.1115/1.2927320`.

[4] N. Zirkelback, L. San Andrés, Finite element analysis of herringbone groove journal bearings: A parametric study, Journal of Tribology 120 (2) (1998) 234–240. `doi:10.1115/1.2834415`.

[5] V. Castelli, J. H. Vohr, Performance characteristics of herringbone- grooved journal bearings operating at high eccentricity ratios and with misalignment, Gas Bearing Symposium (14) (1967) 1–17.

[6] N. Miyanaga, J. Tomioka, Stability analysis of herringbone-grooved aerodynamic journal bearings for ultra high-speed rotations, International Journal of Materials, Mechanics and Manufacturing 4 (3) (2015) 156–161. `doi:10.7763/IJMMM.2016.V4.246`.

[7] M. T. C. Faria, Some performance characteristics of high speed gas lubricated herringbone groove journal bearings, JSME International Journal Series C Mechanical Systems, Machine Elements and Manufacturing 44 (3) (2001) 775–781. `doi:10.1299/jsmec.44.775`.

[8] V. N. Constantinescu, V. Castelli, On the local compressibility effect in spiral-groove bearings, Journal of Lubrication Technology 91 (1) (1969) 79–86. `doi:10.1115/1.3554902`.

[9] Y. Yu, G. Pu, K. Jiang, Modeling and analysis of the static characteristics and dynamic responses of herringbone-grooved thrust bearings, IOP Conference Series: Materials Science and Engineering 280 (1) (2017) 012006. `doi:10.1088/1757-899X/280/1/012006`.

[10] F. C. Hsing, Formulation of a generalized narrow groove theory for spiral grooved viscous pumps, Journal of Lubrication Technology 94 (1) (1972) 81–85. `doi:10.1115/1.3451640`.

[11] S. Y. Chien, M. S. Cramer, A. Untaroiu, Compressible Reynolds equation for high-pressure gases, Physics of Fluids 29 (11) (2017) 116101. `doi:10.1063/1.5000827`.

[12] J. W. Lund, Calculation of stiffness and damping properties of gas bearings, Journal of Lubrication Technology 90 (4) (1968) 793–803. `doi:10.1115/1.3601723`.

[13] I. H. Bell, J. Wronski, S. Quoilin, V. Lemort, Pure and Pseudo-pure Fluid Thermophysical Property Evaluation and the Open-Source Thermophysical Property Library CoolProp, Industrial & Engineering Chemistry Research 53 (6) (2014) 2498–2508. `doi:10.1021/ie4033999`.

[14] A. Looser, Gas bearing with active magnetic damping for ultra-high-speed electrical drive systems., Ph.D. thesis, ETH ZURICH, Zurich (2013). `doi:10.3929/ethz-a-010174834`.

[15] D. P. Fleming, B. J. Hamrock, Optimization of self-acting herringbone journal bearing for maximum stability, in: Proceedings of the fifth international gas bearing symposium, 1974.

[16] S. B. Malanoski, C. H. T. Pan, The static and dynamic characteristics of the spiral-grooved thrust bearing, Journal of Basic Engineering 87 (3) (1965) 547–555. `doi:10.1115/1.3650603`.

[17] R. E. Cunningham, D. P. Fleming, W. J. Anderson, Experimental stability studies of the herringbone-grooved gas-lubricated journal bearing, Journal of Lubrication Technology 91 (1) (1969) 52–57. `doi:10.1115/1.3554896`.

[18] R. E. Cunningham, D. P. Fleming, W. J. Anderson, Experimental load capacity and power loss of herringbone grooved gas lubricated journal bearings, Journal of Lubrication Technology 93 (3) (1971) 415–422. `doi:10.1115/1.3451610`.

[19] K. Tanaka, H. Muraki, Performance of air-lubricated hydrodynamic bearing spindles for laser scanners, Journal of Tribology 113 (3) (1991) 609–614. `doi:10.1115/1.2920667`.

[20] S. Yoshimoto, A. Takahashi, A method of reducing windage power loss in a laser scanner mirror by using the pumping effect of herringbone-grooved gas journal bearings, Journal of Tribology 121 (3) (1999) 506–509. `doi:10.1115/1.2834096`.

[21] P. T. Stanev, F. Wardle, J. Corbett, Investigation of grooved hybrid air bearing performance, Proceedings of the Institution of Mechanical Engineers, Part K: Journal of Multi-body Dynamics 218 (2) (2004) 95–106. `doi:10.1243/146441904323074558`.

[22] S. Yoshimoto, M. Miyatake, K. Nagata, Instability of herringbone grooved aerodynamic floating bush bearings flexibly supported by foils with hemispherical bumps, in: ASME/STLE 2007 International Joint Tribology Conference, Parts A and B, ASME, 2007, pp. 261–263. `doi:10.1115/IJTC2007-44234`.

[23] J. Schiffmann, D. Favrat, Experimental investigation of a direct driven radial compressor for domestic heat pumps, International Journal of Refrigeration 32 (8) (2009) 1918–1928. `doi:10.1016/j.ijrefrig.2009.07.006`.

[24] I. Ognjanovic, Experimental contribution to the mechanics of herringbone grooved journal air bearings, Ph.D. thesis, École Polytechnique Fédérale de Lausanne, Lausanne (2011). `doi:10.5075/epfl-thesis-4879`.

[25] J. Demierre, A. Rubino, J. Schiffmann, Modeling and experimental investigation of an oil-free microcompressor-turbine unit for an organic rankine cycle driven heat pump, Journal of Engineering for Gas Turbines and Power 137 (3) (2014) 032602–032602–10. `doi:10.1115/1.4028391`.

[26] P. H. Wagner, Integrated design, optimization, and experimental realization of a steam-driven micro recirculation fan for solid oxide fuel cell systems, Ph.D. thesis, École Polytechnique Fédérale de Lausanne, Lausanne (2019). `doi:10.5075/epfl-thesis-9337`.

[27] L. San Andrés, T. A. Chirathadam, Metal mesh foil bearing: Effect of motion amplitude, rotor speed, static load, and excitation frequency on force coefficients, Journal of Engineering for Gas Turbines and Power 133 (12) (2011) 122503. `doi:10.1115/1.4004112`.

[28] J. Le Rouzic, M. Arghir, Experimental analysis of angled injection aerostatic hybrid bearings, Journal of Engineering for Gas Turbines and Power 140 (2) (2017) 022504. `doi:10.1115/1.4037873`.

[29] D. P. Fleming, W. J. Thayer, R. E. Cunningham, Experimental dynamic stiffness and damping of externally pressurized gas-lubricated journal bearings, Tech. rep., NASA TN D-8270 (1976).

[30] H. Heshmat, C.-P. R. Ku, Structural damping of self-acting compliant foil journal bearings, Journal of Tribology 116 (1) (1994) 76. `doi:10.1115/1.2927050`.

[31] M. J. Conlon, A. Dadouche, W. M. Dmochowski, R. Payette, J.-P. Bédard, B. Liko, Experimental evaluation of foil bearing performance: Steady-state and dynamic results, in: Volume 6: Structures and Dynamics, Parts A and B, ASME, 2009, pp. 981–992. `doi:10.1115/GT2009-60186`.

[32] M. J. Conlon, A. Dadouche, W. M. Dmochowski, R. Payette, J.-P. Bédard, A comparison of the steady-state and dynamic performance of first- and second-generation foil bearings, in: Volume 6: Structures and Dynamics, Parts A and B, ASME, 2010, pp. 453–462. `doi:10.1115/GT2010-23683`.

[33] B. Ertas, M. Drexel, J. Van Dam, D. Hallman, A general purpose test facility for evaluating gas lubricated journal bearings, Journal of Engineering for Gas Turbines and Power 131 (2) (2008) 022502–022502–8. `doi:10.1115/1.2979004`.

[34] P. Matta, M. Arghir, O. Bonneau, Experimental analysis of cylindrical air-bearing dynamic coefficients, Tribology Transactions 53 (3) (2010) 329–339. `doi:10.1080/10402000903283318`.

[35] L. Rudloff, M. Arghir, O. Bonneau, P. Matta, Experimental analyses of a first generation foil bearing: Start-up torque and dynamic coefficients, in: Proceedings of ASME Turbo Expo 2010: Power for Land, Sea and Air, 2010, pp. 241–251. `doi:10.1115/GT2010-22966`.

[36] L. Rudloff, M. Arghir, O. Bonneau, S. Guingo, G. Chemla, E. Renard, Experimental analysis of the dynamic characteristics of a hybrid aerostatic bearing, Journal of Engineering for Gas Turbines and Power 134 (8) (2012) 082503. `doi:10.1115/1.4006060`.

[37] L. San Andrés, T. A. Chirathadam, Identification of rotordynamic force coefficients of a metal mesh foil bearing using impact load excitations, Journal of Engineering for Gas Turbines and Power 133 (11) (2011) 112501. `doi:10.1115/1.4002658`.

[38] L. San Andrés, T. Abraham Chirathadam, A metal mesh foil bearing and a bump-type foil bearing: Comparison of performance for two similar size gas bearings, Journal of Engineering for Gas Turbines and Power 134 (10) (2012) 102501. `doi:10.1115/1.4007061`.

[39] S. Howard, C. Dellacorte, M. J. Valco, J. M. Prahl, H. Heshmat, Dynamic stiffness and damping characteristics of a high-temperature air foil journal bearing, Tribology Transactions 44 (4) (2001) 657–663. `doi:10.1080/10402000108982507`.

[40] Y. P. Wang, D. Kim, Experimental identification of force coefficients of large hybrid air foil bearings, in: Volume 7B: Structures and Dynamics, ASME, 2013, p. 10. `doi:10.1115/GT2013-95765`.

[41] E. Bellabarba, R. Ruiz, S. Díaz, V. Rastelli, A test rig for air bearings dynamic characterization, in: World Tribology Congress III, American Society of Mechanical Engineers, 2005, pp. 7–8. `doi:doi.org/10.1115/WTC2005-63036`.

[42] J. J. Moore, A. Lerche, T. Allison, D. L. Ransom, D. Lubell, Development of a high speed gas bearing test rig to measure rotordynamic force coefficients, Journal of Engineering for Gas Turbines and Power 133 (10) (2011) 102504. `doi:10.1115/1.4002865`.

[43] J. S. Larsen, A. J. T. Hansen, I. F. Santos, Experimental and theoretical analysis of a rigid rotor supported by air foil bearings, Mechanics & Industry 16 (1) (2015) 106. `doi:10.1051/meca/2014066`.

[44] N. Miyanaga, J. Tomioka, Development of herringbon-grooved aerodynamic journal bearing systems for ultra-high-speed rotations, Key Engineering Materials 656-657 (2015) 652–657. `doi:10.4028/www.scientific.net/KEM.656-657.652`.

[45] T. Waumans, J. Peirs, F. Al-Bender, D. Reynaerts, Aerodynamic journal bearing with a flexible, damped support operating at 7.2 million DN, Journal of Microme-

chanics and Microengineering 21 (10) (2011) 104014. `doi:10.1088/0960-1317/21/10/104014`.

3 Non-ideal gas lubrication

Historically, the modelling of aerodynamic bearings has relied extensively on the ideal gas assumption, which simplifies considerably the solution to the non-linear differential equation. As rigid aerodynamic bearings have been often applied to atmospheric air or noble gases for applications in gyroscopes and turbomachinery, the modelling of more complex gas behavior was not crucial for reliable operation of airborne machines. However, with the recent development of process-gas lubricated machines, for example with CO_2 and synthetic refrigerants for energy applications, as well as of blowers and compressors for fuel cells in the automotive industry, subject to numerous cold starts in a wide range of ambient conditions, the validity of the ideal gas assumption can be questioned. In particular, new applications might face the following issues:

- Refrigerant-lubricated turbomachinery:
  - Real-gas effects leading to an increased compressibility of the fluid as the molecules in gas phase start to interact, as illustrated in Figure 3.1a . This effect is triggered by the proximity of the critical point in high-pressure conditions.
  - Gas condensation due to near-isothermal compression. Since the compression in a gas bearing happens nearly isothermally, the saturation point (dew point) can be reached if the system operates in near-saturated conditions. It can lead to a partial or total condensation of the lubricant, as represented in Figure 3.1c.
- Automotive fuel cell blower/compressor:
  - Humid air effects, where the dew point of the gas mixture (N_2-O_2-H_2O) is reached within the aerodynamic bearing because of the near-isothermal compression. The water vapor contained in the mixture reached the saturation partial pressure and starts to condensate (Figure 3.1b, leading an increase of overall gas compressibility.

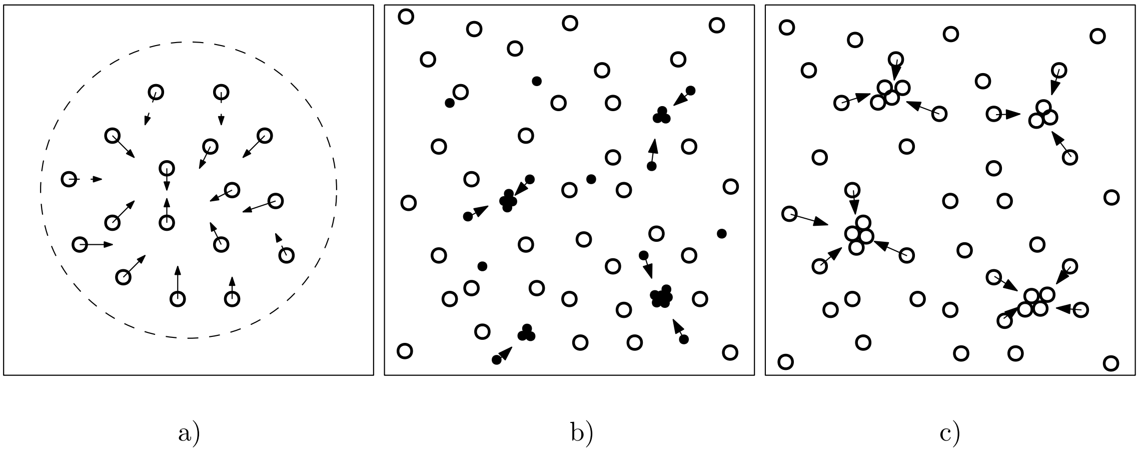

Figure 3.1 – Illustration of the three situations studied in this Chapter: the real-gas effects leading to an increases gas compressibility (a), the humid air effect resulting from the partial condensation of water contained in air (b) and the partial condensation of a pure fluid (c)

The goal of this chapter is to investigate qualitatively and quantitatively such effects resulting from non-ideal gas lubrication on the static and dynamic performance of rigid aerodynamic bearings. The chapter, composed of three sections, explores these effects on Plain Journal Bearings (PJBs) and Herringbone Groove Journal Bearing (HGJBs) using the Reynolds equation and the Narrow Groove Theory (NGT) in a design-oriented approach. First, the real-gas effects on the performance of slider and journal bearings are assessed. The load capacity as well as the stability of the bearings are investigated in non-dimensional numbers. A model accounting for the partial condensation of water contained in humid air is presented and studied on journal bearings. Finally, a Reynolds equation suitable for condensing pure fluid is presented, numerically implemented and experimentally validated using an original test rig. Each section led to a publication in a peer-reviewed journal stated at the beginning of each section.

3.1 Real gas effects

Parts of the material presented in this section has been published in the following journal article:

Guenat, E., Schiffmann, J., 2018. Real-gas effects on aerodynamic bearings. Tribology International 120, 358–368. DOI:10.1016/j.triboint.2018.01.008

3.1.1 Introduction

Gas bearing equipping closed-loop turbomachinery for heat pump or ORC cycles are typically lubricated with synthetic working fluids having a relatively low critical point, with the high-pressure side of the loop being at a significant fraction of the critical point. Because the compression occurring in the thin gas film of a bearing is usually assumed isothermal, the pressure in the fluid film can get, in some situation, very close to the critical point (Figure 3.2), triggering real-gas effects acting on the behavior of the lubricant film.

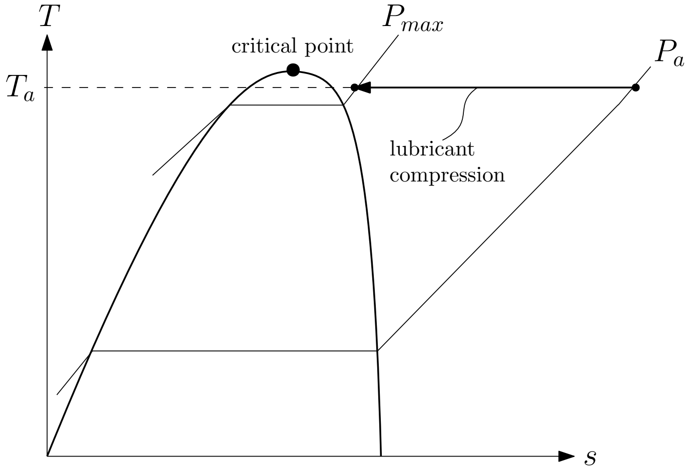

Figure 3.2 – Schematic representation in a temperature-entropy diagram of an isothermal compression starting from ambient pressure P_a to the saturation pressure P_{max}, close to the critical point

Historically, aerodynamic bearings were designed by solving the Reynolds equation under the assumption of an ideal gas lubricant [1]. Recent works have implemented real-gas effects in the Reynolds equation in order to complete their bearing models, however, with a limited investigation of the qualitative or quantitative differences between the ideal- and real-gas lubrication. Schiffmann and Favrat[2] investigated the real-gas effects on the properties of HGJBs using the NGT and addressed the consequences on the optimal design of such bearings. They observed that the real-gas effects can have a negative influence on the stability and change the optimal geometry. Conboy [3] simulated a foil thrust gas bearing lubricated with CO_2 with the Reynolds equation including real-gas effects, however without investigating the effects of this consideration on the performance of the final design. Xu and Kim [4] developed a thermo-elastic model applied on a foil thrust bearing lubricated with CO_2 and R245fa, including real-gas effects. They showed that the real-gas consideration reduces the peak-pressure in the fluid film, however in moderated proportions due to the high temperature of the fluid film in the investigated cases. Fairuz and Jahn [5] investigated the real-gas effects on dry seals using a bulk-flow model and found that the real-gas effects were beneficial for the sealing properties thanks to the increased density. In general, prior work lacks of generalization regarding the role of both the lubricant and the operating conditions. In addition, an in-depth description of the effects of real gas on the bearing performance, and their consequences on bearing design are missing.

This present section aims to (1) address the real-gas effects on different aerodynamic bearing geometries both for static and dynamic performance on a wide range of operating conditions, (2) investigate these effects with multiple working fluids in a large domain of reduced temperature and pressure and (3) express the results in terms of non-dimensional numbers in order to ensure a high level of generality.

The Reynolds equation is adapted to express the density field in aerodynamic bearings, with the bulk modulus as a parameter accounting for the real-gas effect. The perturbation method is applied to obtain the dynamic properties of the fluid film. The ratios of critical mass and load capacity with regards to the ideal-gas lubrication serves as metrics for the characterization of the real-gas effects on a Rayleigh step slider bearing, a PJB and a HGJB. 10 fluids of different chemical nature (HCFC, HFC, HC and natural working fluids) are investigated on a wide range of operating conditions with the use of reduced temperature and pressure, compressibility number and ambient Reynolds number as non-dimensional parameters.

3.1.2 Theory

The pressure distribution in an aerodynamic bearing is modeled by using the Reynolds equation under the assumption of a thin fluid film (properties are lumped across the film thickness), isoviscosity, negligible inertia effects and Newtonian fluids. Since real-gas effects are associated with high-density fluids, the Reynolds number in the bearing can reach a level where turbulence has to be included in the constitutive lubrication equation. In order to account for the laminar-turbulent transition, correction terms are added to the Reynolds equation according to prior work suggesting expressions for these terms

[6–8]. The Reynolds equation with the turbulence correction terms is given as follows:

$$\partial_X\left(\frac{\rho G_x h^3}{12\mu}\partial_X P\right)+\partial_z\left(\frac{\rho G_z h^3}{12\mu}\partial_z P\right)=\frac{U}{2}\partial_X(\rho h)+\partial_t(\rho h) \qquad 3.1$$

G_z and G_x are the turbulence correction terms perpendicular and parallel to the direction of motion, respectively. Correlations suggested by Constantinescu [6] are used in this work since they are valid for both smooth and discontinuous surfaces:

$$G_x=(1+0.001133Re^{0.9})^{-1} \qquad 3.2$$

$$G_z=(1+0.000358Re^{0.96})^{-1} \qquad 3.3$$

where $Re = U\rho h/\mu$. This correlation is valid for $10^3 < Re < 3\cdot 10^4$. For laminar flows, $G_{\|} = G_{\perp} = 1$. The ambient Reynolds number is introduced in order to compare different bearings operating in similar conditions:

$$Re_a=\frac{U\rho_a h_0}{\mu} \qquad 3.4$$

where ρ_a corresponds to the density at ambient conditions, U the surface velocity and h_0 the nominal clearance.

Due to the presence of turbulence correction factors, the harmonic clearance perturbation applied on the non-dimensional Reynolds equation in polar coordinates (Eq. 2.27) in order to recover static and linearized dynamic performance of the bearing results in a perturbation different from the one derived in the previous chapter:

$$\begin{aligned}
\bar\rho &= \bar\rho_0+\epsilon_{1x}\bar\rho_{1x}e^{i\bar t}+\epsilon_{1y}\bar\rho_{1y}e^{i\bar t} && 3.5\\
\bar\beta &= \bar\beta_0+\epsilon_{1x}\left(\frac{\partial\bar\beta}{\partial\bar\rho}\right)_0\bar\rho_{1x}e^{i\bar t}+\epsilon_{1y}\left(\frac{\partial\bar\beta}{\partial\bar\rho}\right)_0\bar\rho_{1y}e^{i\bar t} && 3.6\\
G &= G_0+\epsilon_{1x}\left(\left(\frac{\partial G}{\partial\bar\rho}\right)_0\bar\rho_{1x}e^{i\bar t}+\left(\frac{\partial G}{\partial\bar h}\right)_0\cos\theta e^{i\bar t}\right) && 3.7\\
&\quad+\epsilon_{1y}\left(\left(\frac{\partial G}{\partial\bar\rho}\right)_0\bar\rho_{1y}e^{i\bar t}+\left(\frac{\partial G}{\partial\bar h}\right)_0\sin\theta e^{i\bar t}\right)
\end{aligned}$$

The correction factors G depend on both the density and the clearance, which leads to two dynamic terms when perturbed. However, it does not affect the numerical method followed to retrieve both static performance and dynamic force coefficients described previously.

Similarly, the NGT can be adapted to adopt turbulence correction factors. Hsing [9] derived the NGT applied to HGJB including correction terms in order to account for the turbulence in the lubrication film. The equations are equivalent to the laminar form of the theory when G terms accounting for turbulence are set to 1 [10]. The resulting differential equation is recalled here:

$$\begin{aligned}\partial_\theta\left[\bar{\beta}\left(f_1\partial_\theta\bar{\rho}+f_2\partial_{\bar{z}}\bar{\rho}\right)\right]+\partial_{\bar{z}}\left[\bar{\beta}\left(f_2\partial_\theta\bar{P}+f_3\partial_{\bar{z}}\bar{P}\right)\right]&\\+c_s\left(\sin\hat{\beta}\partial_\theta(f_4\bar{\rho})-\cos\hat{\beta}\partial_{\bar{z}}(f_6\bar{\rho})\right)&\\-\Lambda\partial_\theta(f_5\bar{\rho})-\sigma\partial_{\bar{t}}(f_5\bar{\rho})=0&\end{aligned}\tag{3.8}$$

The present parameters f_i are defined differently from the laminar case developed in Chapter 2:

$$f_1=\frac{g_{1\theta}+g_2\sin^2\hat{\beta}}{g_3}\tag{3.9}$$

$$f_2=\frac{g_2\sin\hat{\beta}\cos\hat{\beta}}{g_3}\tag{3.10}$$

$$f_3=\frac{g_{1z}+g_2\cos^2\hat{\beta}}{g_3}\tag{3.11}$$

$$f_4=\frac{\bar{h}_g^3G_{\theta g}-\bar{h}_r^3G_{\theta r}}{g_3}\tag{3.12}$$

$$f_5=\alpha\bar{h}_g+(1-\alpha)\bar{h}_r\tag{3.13}$$

$$f_6=\frac{\bar{h}_g^3G_{zg}-\bar{h}_r^3G_{zr}}{g_3}\tag{3.14}$$

With

$$\begin{aligned}g_{1\theta}=&\bar{h}_g^3\bar{h}_r^3[(1-\alpha)(\cos^2\hat{\beta}G_{zg}+\sin^2\hat{\beta}G_{\theta g})G_{\theta r}+\\&\alpha(\cos^2\hat{\beta}G_{zr}+\sin^2\hat{\beta}G_{\theta r})G_{\theta g}]\end{aligned}\tag{3.15}$$

$$g_2=(\bar{h}_g^3G_{zg}-\bar{h}_r^3G_{zr})(\bar{h}_g^3G_{\theta g}-\bar{h}_r^3G_{\theta r})\alpha(1-\alpha)\tag{3.16}$$

$$\begin{aligned}g_3=&(1-\alpha)\bar{h}_g^3(\cos^2\hat{\beta}G_{zg}+\sin^2\hat{\beta}G_{\theta g})+\\&\alpha\bar{h}_r^3(\cos^2\hat{\beta}G_{zr}+\sin^2\hat{\beta}G_{\theta r})\end{aligned}\tag{3.17}$$

Correction factors G_{ir} and G_{ig}, $i=\theta,z$, are evaluated at the Reynolds number corresponding to $h=h_r$ and $h=h_g$, respectively. Note that $\hat{\beta}$ denotes the groove angle while β and $\bar{\beta}$ denote the dimensional and non-dimensional bulk modulus, respectively.

3.1.3 Results and discussion

The model developed above is applied for different geometries of aerodynamic bearings in order highlight the real-gas effects on the lubrication performance in terms of load capacity and stability.

3.1.3.1 Infinitely wide step slider bearing

The steady-state form of Equation 3.8 is solved for an infinitely wide step slider bearing (neglecting the variation of pressure in the z direction) operating at $\Lambda = 3$ and 10, assuming a laminar regime in the thin film. In the case of slider bearings (Figure 3.3), Λ is defined as follows:

$$\Lambda = \frac{6\mu U L_x}{P_a h_0^2} \qquad 3.18$$

The boundary conditions are $\bar{p} = 1$ at $\bar{x} = 0$ and $\bar{x} = 1$, where $\bar{x} = X/L_x$. The lubricant is R134a (a typical heat pump working fluid) at reduced ambient conditions corresponding to $T_r = T_a/T_c = 1$ and $P_r = P_a/P_c = 0.5$. The pressure distributions for ideal gas and real gas are compared in Figure 3.4. The real gas consideration leads to a redistribution of the pressure, with a lowered peak pressure compared to the pressure when the ideal-gas law is assumed. For $\Lambda = 3$, the pressure of the real gas reaches a slightly higher value than the ideal one for $\bar{x} \in [0.5, 1]$, leading to an overall load capacity increased by 1%. The load capacity in its non-dimensional form is defined by Equation 3.19.

$$\overline{W} = \int_0^1 (\bar{P} - 1)\mathrm{d}\bar{x} \qquad 3.19$$

At $\Lambda = 10$, this increased pressure zone (as a result of real-gas effects) is confined to $\bar{x} \in [0.8, 1]$ and is negatively compensated by a lowered pressure in the remaining domain, resulting in a load capacity 8.5% lower than the ideal gas case.

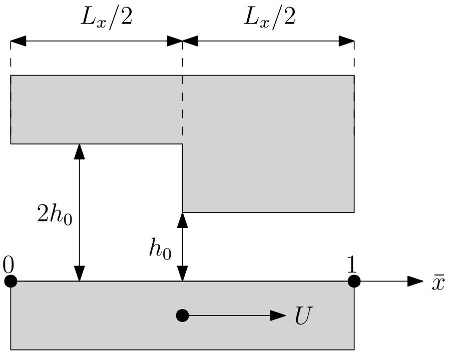

Figure 3.3 – Geometry of the studied step bearing

Figure 3.5 shows the evolution of the non-dimensional load capacity with the compressibility number for the considered slider bearing lubricated with R134a and highlights the compressibility effects associated with real gas consideration. The temperature is fixed to the critical value while the relative pressure is varied. The ideal-gas case shows that the load capacity evolves linearly for small compressibility numbers before deviating to reach a limit value corresponding to the solution for $\Lambda \to \infty$. The linear domain is due to the quasi-incompressiblity of the lubricant at low speed. This linear range is affected by the real gas effects. The points A, B and C in Figure 3.5 indicate the location

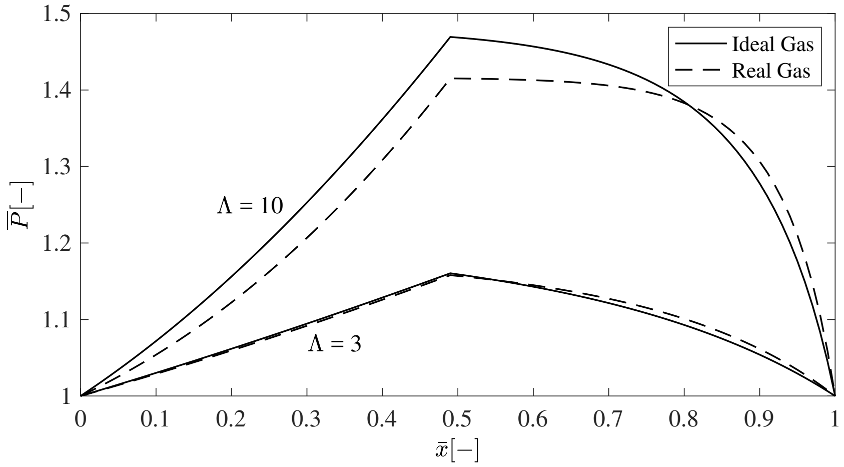

Figure 3.4 – Comparison of pressure distribution in a step slider bearing for two compressibility numbers, with R134a at $T_r = 1$, $P_r = 0.5$

where a 10%-difference between the actual load capacity and the one predicted by the incompressible solution occurs. As the pressure is increased toward the critical value, the real-gas effects get amplified and the 10%-difference location is shifted toward smaller compressibility numbers. The real-gas effects in the sub-critical domain increase the compressibility of the fluid, since the parameter $(\partial_\rho P)_T$ decreases as the critical point is approached. This has the effect to shift the appearance of compressibility effects to lower compressibility numbers compared to the ideal-gas behavior, thus narrowing the validity of the quasi-incompressible behavior. The value of $\Lambda^{(10\%)}$ corresponding to the 10%-deviation point can be estimated within a 2%-error interval using Equation 3.20.

$$\Lambda_{rg}^{(10\%)} = \Lambda_{ig}^{(10\%)} \cdot (\partial_{\bar{\rho}} \bar{P})_{T,a} \tag{3.20}$$

Thus, this equation can help to estimate the validity domain of the incompressible solution in real-gas lubrication based on the ideal-gas case.

This bearing configuration is simulated for a wide range of ambient conditions with the following parameter serving as a metric to compare the real- and ideal-gas load capacity:

$$W_r = \frac{W_{rg}}{W_{ig}} \tag{3.21}$$

Figures 3.6 and 3.7 represent the iso-W_r lines for R134a at $\Lambda = 1$ and $\Lambda = 10$ respectively. The cases close to the saturation line achieving saturation conditions inside the gas film are discarded, thus leaving an empty space between the saturation line and the isolines. At constant pressure, a reduction of the temperature increases the influence of the real gas consideration, so does an increase in pressure at constant temperature. The deviation from the ideal-gas lubrication increases with the compressibility number, which has the

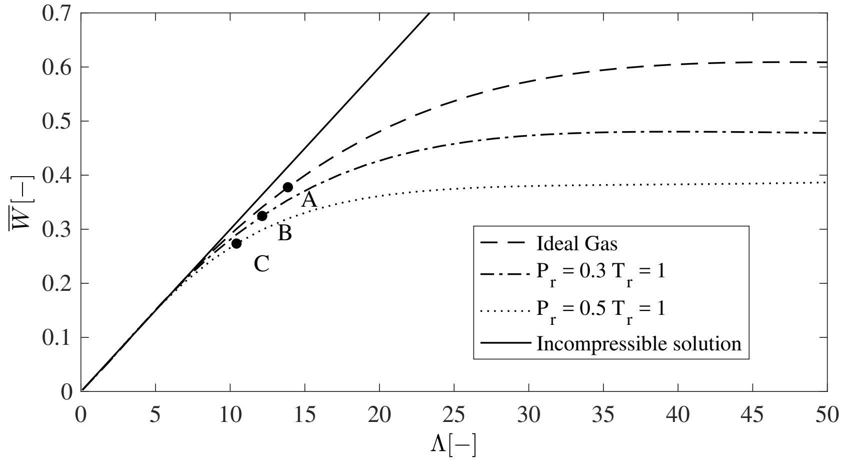

Figure 3.5 – Evolution of the non-dimensional load capacity of an infinitely wide Rayleigh step bearing as a function of Λ for R134a. The dots indicate the points of a 10%-deviation from the incompressible solution

effect of shifting the isolines to lower pressure levels. Note that at $\Lambda = 1$ real-gas effects tend to increase the load capacity, whereas at $\Lambda = 10$ it is decreases significantly.

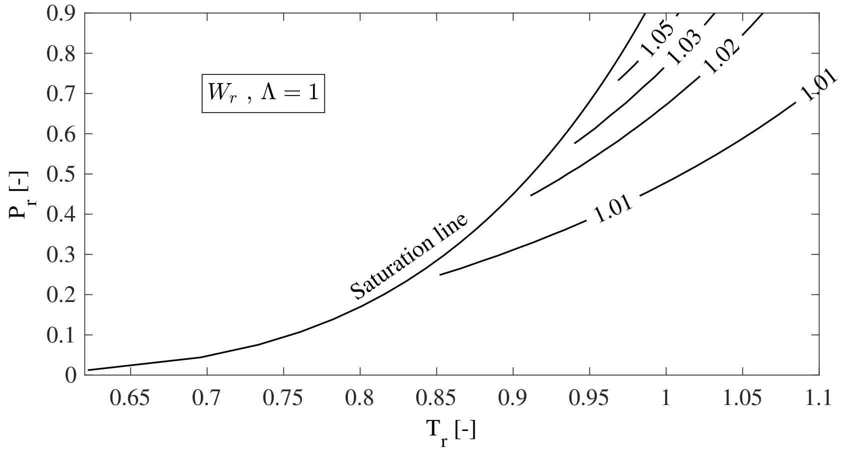

Figure 3.6 – Isolines of W_r for a step slider bearing at $\Lambda = 1$ with R134a

Figure 3.8 shows the difference between the maximum and the minimum value of W_r for a given ambient condition among 10 working fluids of different chemical nature, including both synthetic and natural fluids (R123, R134a, R170, R22, R245fa, R290, R600a, R717, R718, R744) at $\Lambda = 10$. The term *composite saturation curve* indicates the saturation curve bounding the phase change of the 10 considered working fluids. The maximum deviation in load capacity within the considered domain is below 4% in this case and below 1% for $\Lambda = 1$, which allows to conclude that the load capacity of a step slider bearing is nearly independent of the nature of the fluid if the reduced ambient conditions are known. Further, a representation in the reduced pressure and reduced temperature domain is

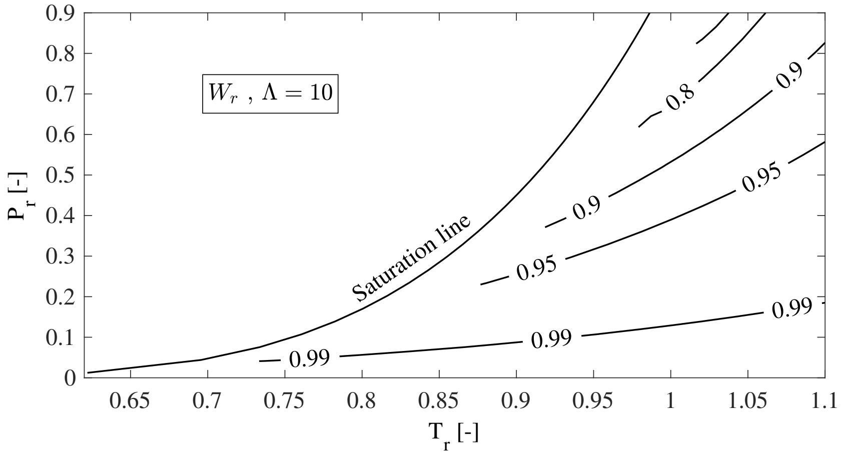

Figure 3.7 – Isolines of W_r for a step slider bearing at $\Lambda = 10$ with R134a

suggested to be sufficient to adequately map the real-gas effects in a gas-lubricated slider bearings.

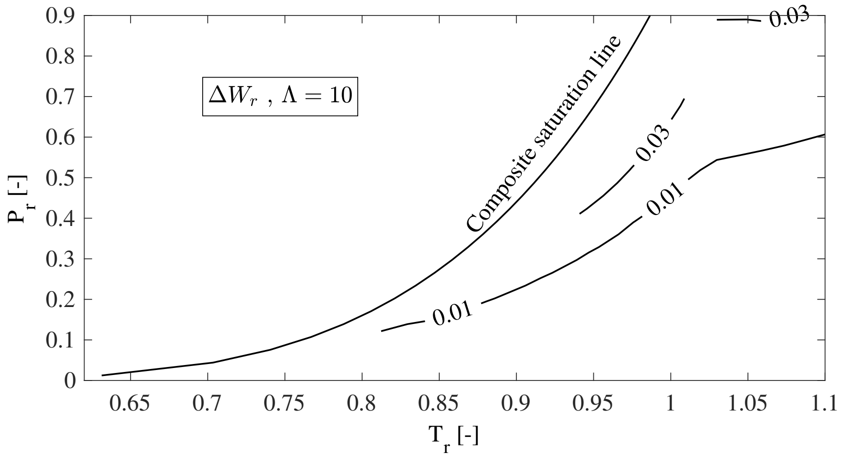

Figure 3.8 – Isolines of maximum deviation of W_r between 10 different fluids for a step slider bearing at $\Lambda = 10$ as a function of reduced pressure and temperature

The dependency of the results on the reduced pressure and temperature alone can be mostly explained by the compressibility factor Z ($Z = \frac{P}{\rho r T}$) and the parameter $(\partial_{\overline{\rho}}\overline{P})_T$. Figures 3.9 and 3.10 respectively show the isolines of Z and $(\partial_{\overline{\rho}}\overline{P})_T$ in the $T_r - P_r$ space. The trend appears to be very similar to the isolines of load capacity ratio shown in Figures 3.6 and 3.7.

When following isolines of Z in the single-phase gas domain and computing the load capacity ratio, the obtained values fall in a very narrow range, as represented in Figure 3.11 for $\Lambda = 10$. For values of Z close to 1 (i.e. following the ideal gas law), the maximum deviation of W_r in the investigated domain is very small. In general, getting closer to the saturation point while keeping a constant ambient compressibility factor tend to increase

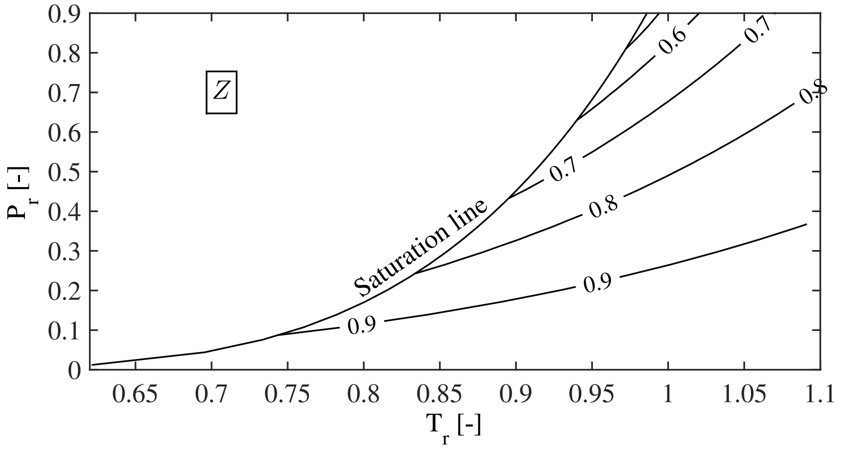

Figure 3.9 – Isolines of compressibility factor Z (R134a) in the $T_r - P_r$ space

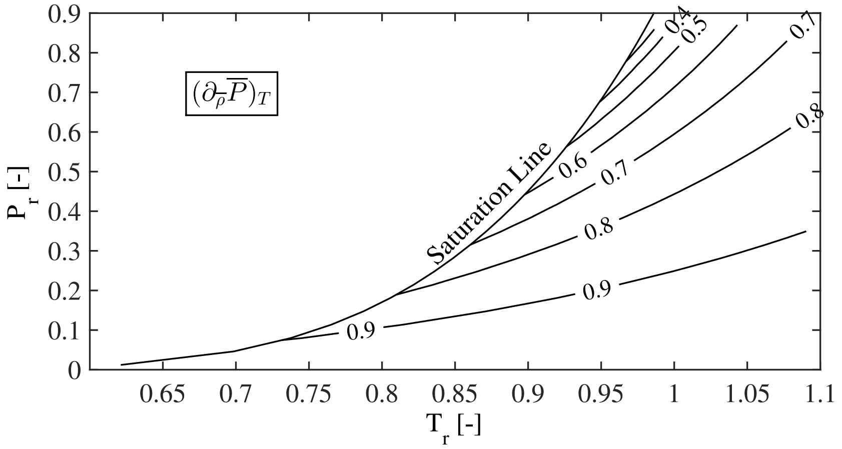

Figure 3.10 – Isolines of parameter $(\partial_{\overline{\rho}}\overline{P})_T$ (R134a) in the $T_r - P_r$ space

the real-gas effects, translated here in a decrease of load capacity. This deviation grows as the ambient compressibility factor decreases, indicating that this metric alone becomes less effective as a mean to describe the real-gas effects occurring in the gas film.

The compressibility number, having an influence of the maximum pressure reached in the gas film, also plays a role in this relationship. Figure 3.12 presents the load capacity ratio W_r along a isolines of compressibility factor Z for different compressibility numbers Λ. Increasing Λ leads to higher deviations of W_r along the isoline.

Figure 3.13 shows the maximum deviation over the 10 different working fluids over different isolines of Z. In general, a higher reduced temperature tends to decrease the discrepancy among the fluids and this reduction is stronger for lower compressibility factors. The small reported discrepancies indicate that the ambient compressibility factor is an effective metric to quantify the real-gas effects occurring for a given geometry and a given compressibility number, independently of the fluid. However, using the

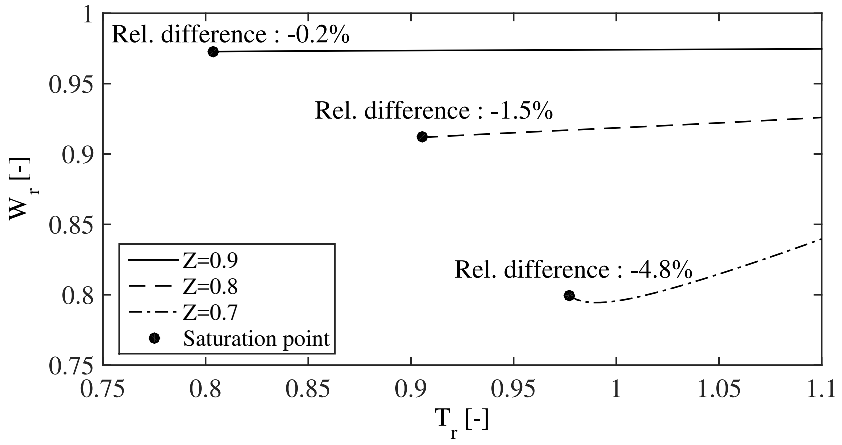

Figure 3.11 – Value of W_r along three different isolines of Z in the $T_r - P_r$ domain, for a step slider bearing ($\Lambda = 10$, R134a). The relative difference is indicated for each value of Z between the saturation point and $T_r = 1.1$

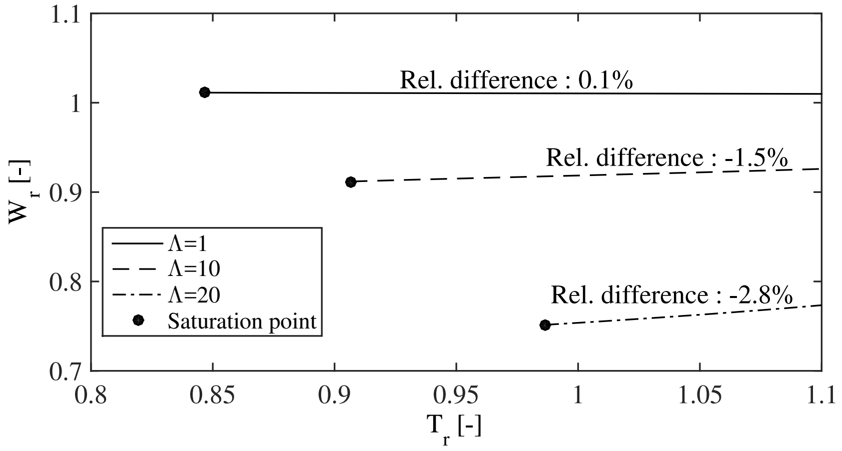

Figure 3.12 – Value of W_r along the isoline of $Z = 0.8$ in the $T_r - P_r$ domain, for a step slider bearing at three different values of Λ (R134a)

compressibility factor is not practical, as is a non-trivial parameter which cannot be measured directly, while temperature and pressure are, usually, readily available together with their respective critical values, thus justifying the use of the ambient reduced temperature and pressure.

3.1.3.2 Plain Journal Bearing

The same approach in the $P_r - T_r$ domain is applied to a PJB operating at an eccentric position with a length over diameter ratio L_z/D of 1. Simulations considering real- and ideal-gas lubrication in laminar regime are compared using the ratio of load capacity W_r (Equation 3.19) and the ratio of critical mass M_r as performance metrics, where M_r is

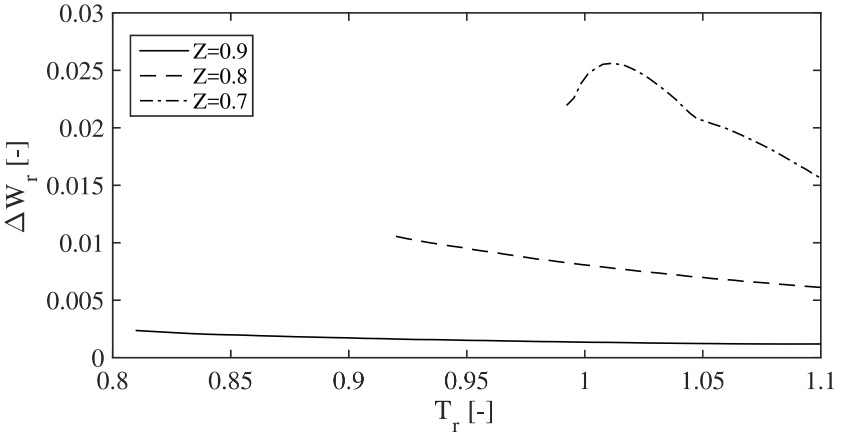

Figure 3.13 – Maximum deviation on W_r over 10 different fluids along the isoline of $Z = 0.8$ in the $T_r - P_r$ domain, for a step slider bearing at $\Lambda = 10$. The relative difference is indicated for each value of Z between the saturation point and $T_r = 1.1$

defined such as:

$$M_r = \frac{M_{c,rg}}{M_{c,ig}} \tag{3.22}$$

Results for the load capacity ratio are presented in Figures 3.14 and 3.15 for compressibility number 1 and 10 respectively, simulating a bearing at an eccentricity ratio $\epsilon = e/h_0$ of 20% and lubricated with R134a. As observed with the slider bearing at high compressibility number, real-gas effects negatively affect the load capacity and become more significant as the compressibility number Λ increases. The evolution of W_r with the compressibility number for three different ambient conditions is shown in Figure 3.16, which emphasizes this observation. The load capacity ratio diverges quickly from unity before reaching a limit value for high Λ, corresponding to the limit solution for $\Lambda \to \infty$. The limit value depends on the distance of the ambient conditions from the critical point, the point of highest P_r being the most affected by the real-gas effects. Figure 3.17 presents the pressure profile at the mid-span of the PJB at an eccentricity ratio of 0.6 along the x-axis, lubricated with R134a at $P_r = 0.75$, $T_r = 1$ and $\Lambda = 1$. The unperturbed pressure distribution is affected both in amplitude and distribution, leading to load components unequally affected by the real-gas consideration: the radial component drops by 8.5% and the tangential one by 45 %, resulting in a reduction of total load capacity of 28 % compared to the ideal-gas case. As a consequence of this unequal change in load distribution, the attitude angle is affected and brought to lower absolute values, as shown in Figure 3.18. The reduction of the attitude angle is an indication of an increased stability as a result of the real-gas effects.

Figures 3.19 and 3.20 depict the evolution of the critical mass ratio M_r for $\Lambda = 1$ and 10 respectively. Interestingly, real-gas effects appear to have a positive influence at low compressibility numbers that vanishes, however, at high compressibility numbers. The evolution of the critical mass ratio for three ambient conditions against the compressibility

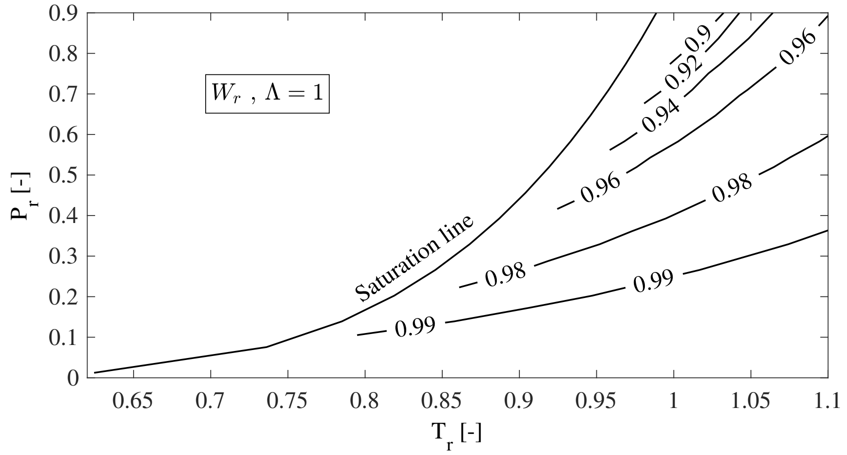

Figure 3.14 – Isolines of W_r for a PJB (ϵ_x=0.2, $\epsilon_y = 0$, R134a) at $\Lambda = 1$

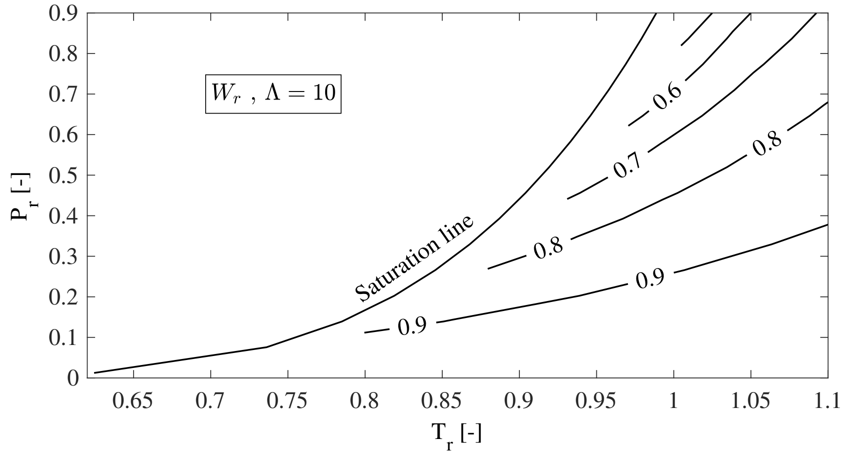

Figure 3.15 – Isolines of W_r for a PJB (ϵ_x=0.2, ϵ_y=0, R134a) at $\Lambda = 10$

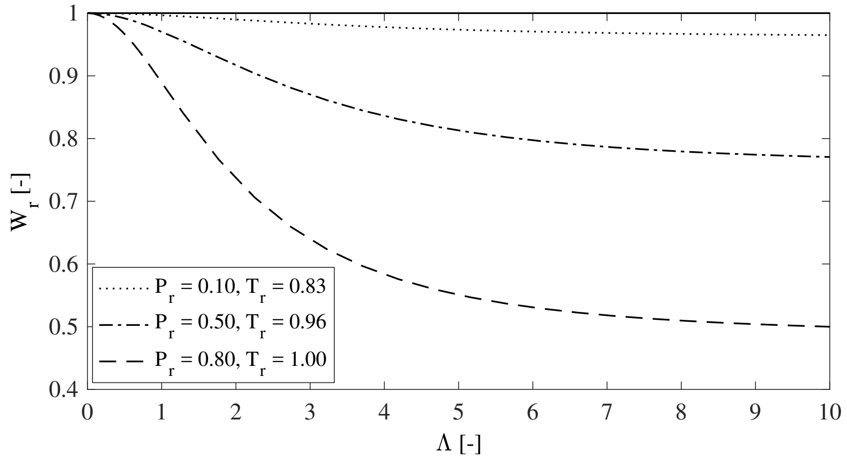

Figure 3.16 – Evolution of W_r with Λ for a PJB (ϵ_x=0.2, ϵ_y=0, R134a)

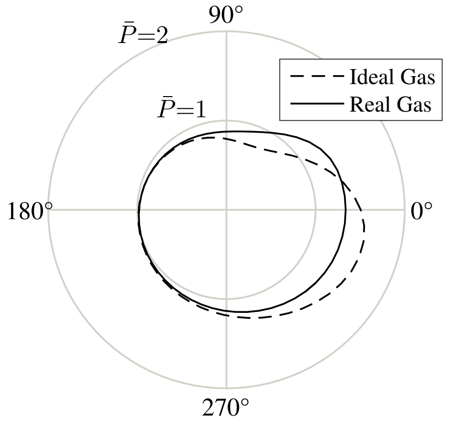

Figure 3.17 – Mid-span pressure profiles of a PJB (ϵ_x=0.6, ϵ_y=0) at $\Lambda = 1$ with R134a at $P_r = 0.75$ and $T_r = 1$

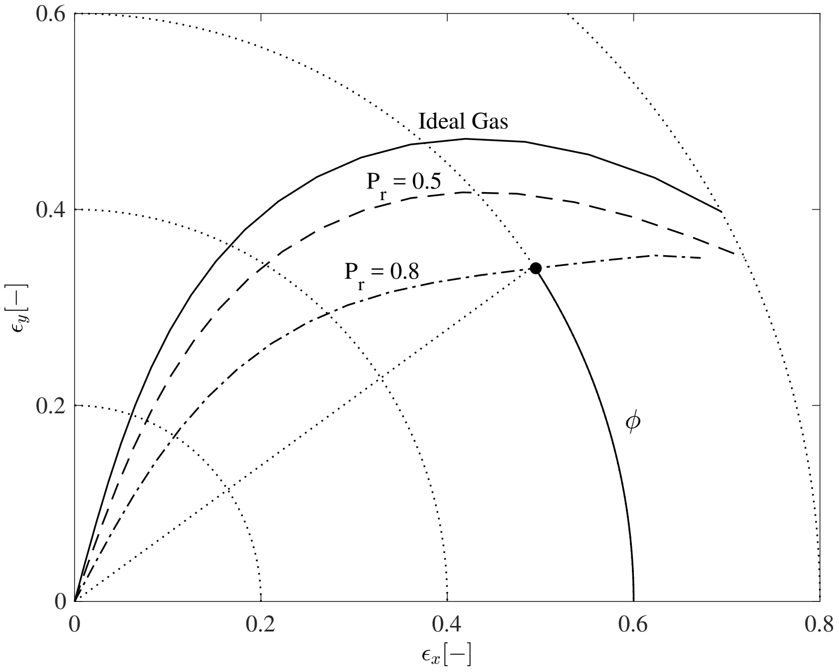

Figure 3.18 – Static locus of a PJB lubricated with R134a at $\Lambda = 1$ and $T_r = 1$ with a force acting along the x-axis. The angle ϕ designates the tilt angle of an arbitrary point

number Λ is presented in Figure 3.21 and shows a monotonically decreasing trend starting from values well above unity. At $\Lambda \approx 2$ the critical mass ratio reaches approximately 1 for the three operating conditions, the unity threshold being postponed to slightly higher compressibility numbers as the distance from critical point increases.

The similarity between working fluids in the $P_r - T_r$ domain remains verified with PJBs, for both considerations of stability and load capacity, as presented in Figures 3.22 and 3.23, where the maximum deviation between fluids is reported for each ambient condition

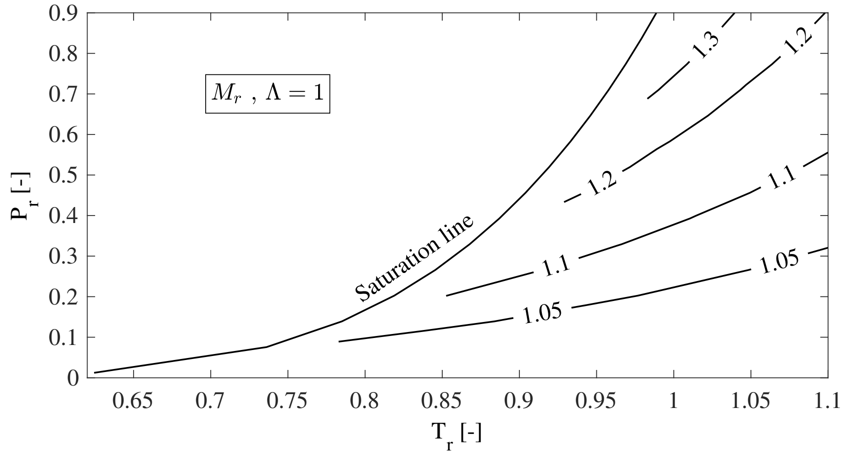

Figure 3.19 – Isolines of M_r for a PJB (ϵ_x=0.2, $\epsilon_y = 0$, R134a) at $\Lambda = 1$

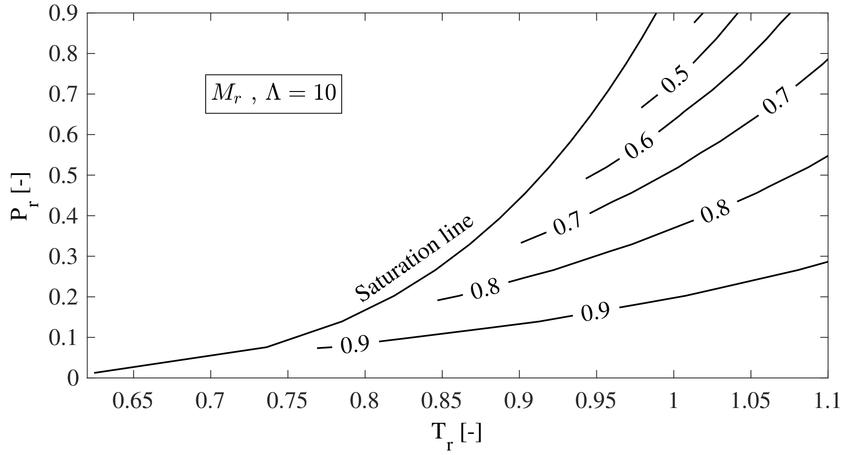

Figure 3.20 – Isolines of M_r for a PJB (ϵ_x=0.2, $\epsilon_y = 0$, R134a) at $\Lambda = 10$

at $\Lambda = 10$ and $\epsilon_x = 0.2$. The maximum deviation observed between the same 10 fluids as previously cited remains below 4% for both metrics. Increasing the eccentricity ratio to 0.5 does not change the value of the maximum observed deviation.

As for the slider bearing, characterizing the real-gas effects on the bearing performance using the ambient compressibility factor Z is valid here for both W_r and M_r. Figure 3.24 shows the value of W_r for a PJB along different isolines of Z in the $T_r - P_r$ space. The deviation of the value over the considered domain is small. At constant compressibility factor, the proximity of the saturation enhances further the real gas effects, since W_r presents the largest deviation from unity. At low ambient compressibility factor, the knowledge of this variable alone is not sufficient to satisfactorily characterize the real-gas effects on the load capacity, as a variation of nearly 19% is observed from the saturation point up to $T_r = 1.1$, which ranges in reduced pressure from $P_r = 0.45$ to $P_r = 1.1$. Although it does not reach the same quality level as for the prediction of W_r, the

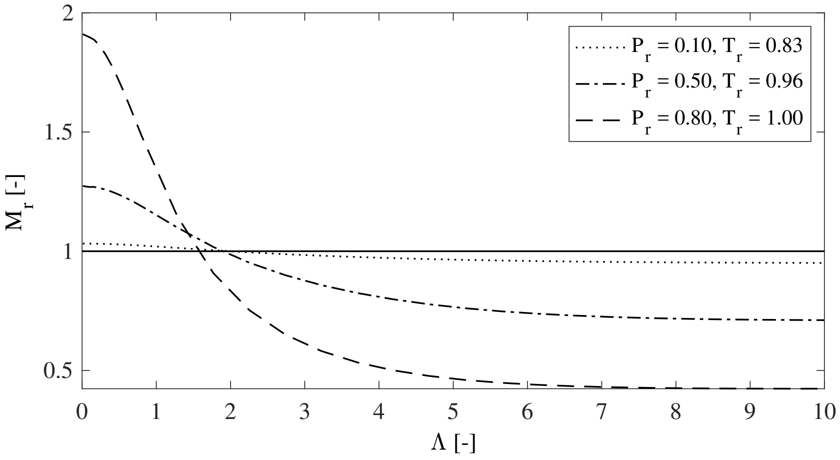

Figure 3.21 – Evolution of the critical mass ratio with the compressibility number for a PJB (R134a, ϵ_x=0.2, $\epsilon_y = 0$)

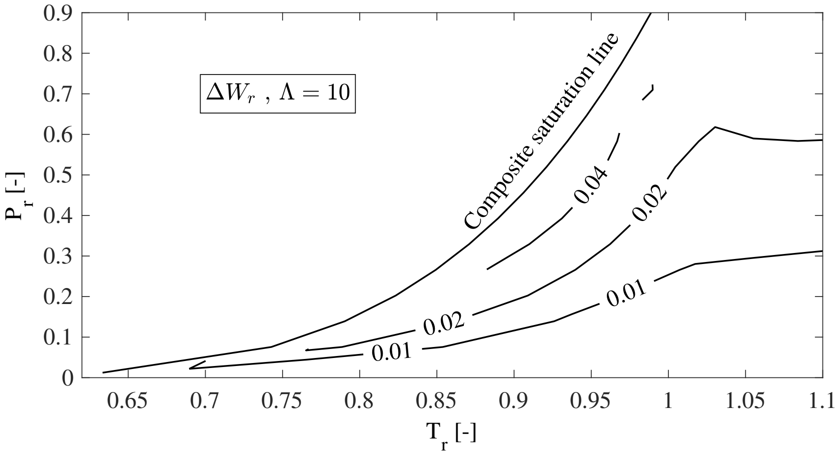

Figure 3.22 – Isolines of maximum deviation of W_r between 10 fluids for a PJB (ϵ_x=0.2, ϵ_y=0) at $\Lambda = 10$

consistency of the prediction of M_r along an isoline of z is good at high values of Z but fails as the ambient compressibility factor decreases, as shown in Figure 3.25. In this Figure, showing results for $\Lambda = 10$, the variation of M_r along the lines $Z = 0.8$ $Z = 0.7$ (which corresponds to a minimum reduced pressure of $P_r = 0.25$) reaches 12 and 38% respectively. Reducing the compressibility number Λ from 10 to 1 reduces the variation of M_r considerably, while doubling to $\Lambda = 20$, not represented here, has a very small influence on the predicted values because of the limit solution for $\Lambda \to \infty$.

3.1.3.3 Herringbone-Grooved Journal Bearings

A fully grooved HGJB ($\gamma = 1$) with the grooved member rotating is analyzed following the same strategy as for the PJB. The geometry is inspired from the optimal design computed

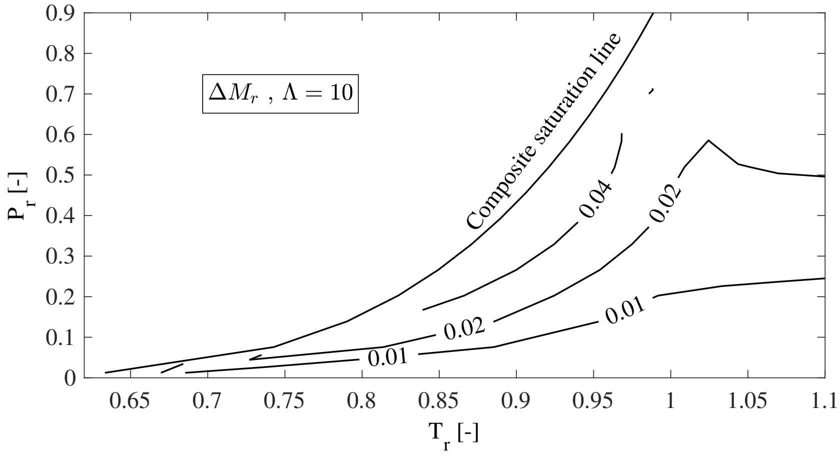

Figure 3.23 – Isolines of maximum deviation of M_r between 10 fluids for a PJB (ϵ_x=0.2, ϵ_y=0) at $\Lambda = 10$

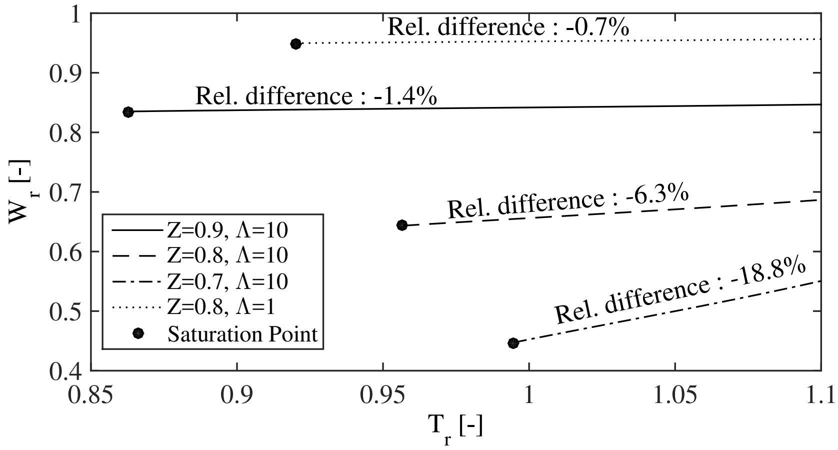

Figure 3.24 – Value of W_r along three different isolines of Z in the $T_r - P_r$ domain, for a PJB operated at $\epsilon_x = 0.5$ in R134a

by Flemming and Hamrock [11] for $\Lambda = 1$. The groove depth over clearance ratio h_g/h_r at a concentric position is 2, the groove angle $\hat{\beta}$ is 150°, the groove aspect ratio α is 0.5 and the length over diameter ratio L_z/D is 1. The flow regime is laminar. Figure 3.26 shows the ratio of critical mass for the considered bearing at concentric position and $\Lambda = 1$, using R134a. Qualitatively, the trend is comparable to the PJB. However, the trend changes radically as Λ increases, as presented in 3.27 for $P_r = 0.5$ and R134a. At constant pressure and increasing temperature, M_r is first below unity, then reaches the point of maximum stability and finally decays asymptotically to unity at very high temperatures. This behavior is visible in Figure 3.28 for different ambient conditions at fixed Λ. Note the relatively large range of ambient conditions where real-gas effects yield to an increased stability compared to the ideal-gas lubrication case. A line of very high stability is suggested to appear above a certain value of compressibility number, where

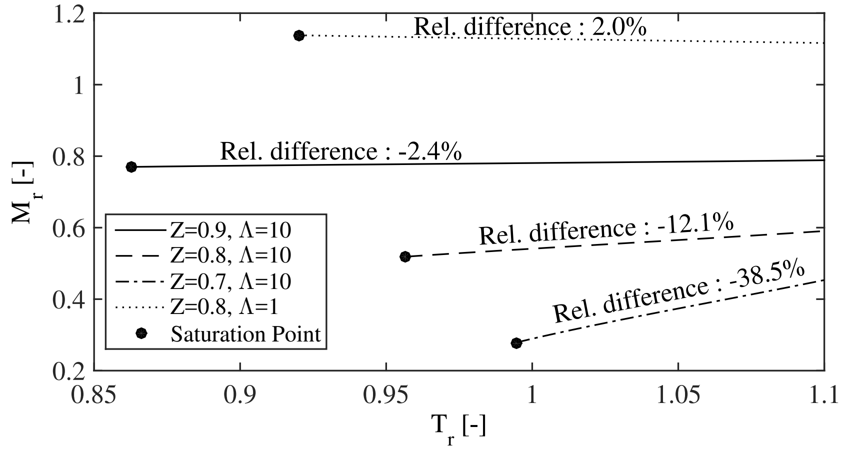

Figure 3.25 – Value of M_r along three different isolines of Z in the $T_r - P_r$ domain, for a PJB operated at $\epsilon_x = 0.5$ in R134a

the critical mass computed under the real-gas consideration tends to infinity. In such cases, the condition of Equation 2.49 is satisfied for a whirl frequency ω of very small values, while the amplitude of the equivalent impedance is not significantly affected. As a result, a very high critical mass is obtained (Equation 2.50). The position of these lines is presented in Figure 3.29. The lines are shifted toward higher T_r and lower P_r as the compressibility number increases. For low values of Λ, the line interferes with the saturation line and is no longer observable.

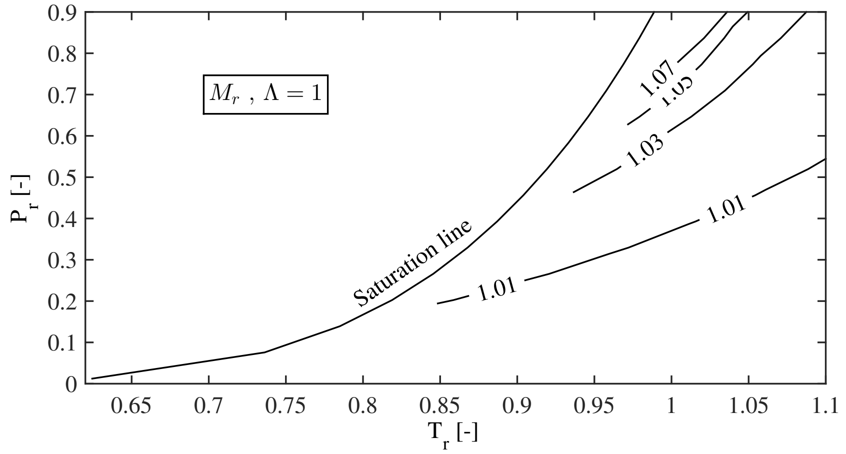

Figure 3.26 – Isolines of M_r for a HGJB (ϵ=0, R134a) at $\Lambda = 1$

The same behavior is observed for the 10 working fluids mentioned previously. Figure 3.30 represents the positions of the maximum stability for each fluid at $\Lambda = 10$, with R170 and R245fa which bound the other fluids. All the lines are confined in a domain whose width grows with reduced pressure, which suggests that the similarity between fluids loses its validity when the HGJB operating conditions approach the critical pressure. In this zone, the quantitatively small deviation between fluids observed previously is not verified

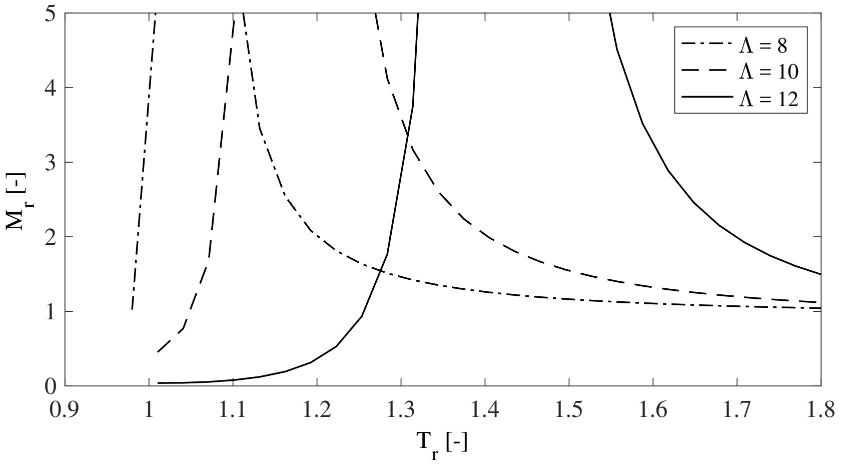

Figure 3.27 – Evolution of M_r with T_r at $P_r = 0.5$ (R134a, $\epsilon = 0$)

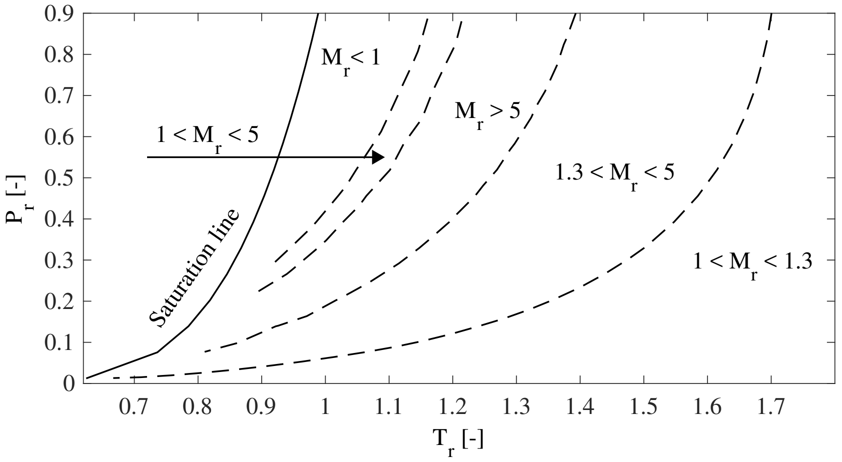

Figure 3.28 – Different domains of value of M_r for a HGJB (ϵ=0, R134a) at $\Lambda = 10$

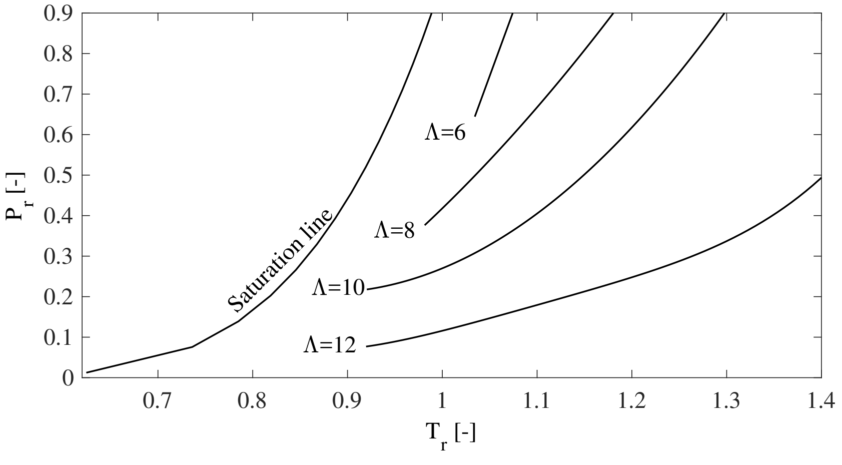

Figure 3.29 – Position of the lines of maximum stability for a HGJB (ϵ=0, R134a)

for HGJB because of the strong slopes observed in Figure 3.27, where a small deviation in the position along T_r results in a very significant deviation in M_r.

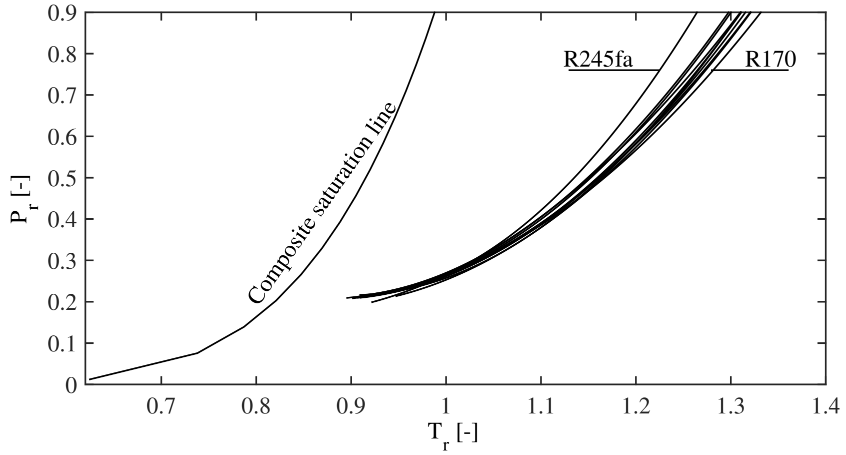

Figure 3.30 – Position of the lines of maximum M_r for HGJB lubricated with 10 different fluids at $\Lambda = 10$

As for the slider bearing and the PJB, the compressibility factor Z evaluated at ambient conditions appears to be a relevant variable when characterizing the real-gas effects on the load capacity ratio W_r. Figure 3.31 shows the evolution of this metric along three isolines of Z when varying the reduced temperature. The relative deviation along the considered domain is slightly larger than for the PJB at similar compressibility factors, explained at least partially by the larger maximum pressure reached in this case ($\overline{P} = 2.0$ against $\overline{P} = 1.3$, both at $\Lambda = 10$). For the stability, however, the singularity observed in the evolution of the ratio of critical speed M_r causes this variable to vary considerably along isolines of Z, as shown in Figure 3.32. For $Z = 0.9$, the singular point of infinite stability is reached, which yield to enormous relative variation in the vicinity of this point. Although the singularity is not reached on the two other isolines considered, the relative variation on M_r is large. As visible in Figure 3.33, the line $Z = 0.9$ is in the vicinity of the line of maximum stability for the studied case ($\epsilon = 0$, $\Lambda = 10$). The two lines are very close one from another and eventually cross, which cause the particularly strong variation of M_r in this region. Therefore, the ambient compressibility factor alone is not sufficient to reliably characterize the real-gas effects on the stability of a HGJB.

From a design perspective, the minimum value of the critical mass between the targeted value of compressibility number Λ and 0 bears a particular importance, since it indicates the stability threshold of a bearing accelerating from rest to nominal speed.

Figure 3.34 shows the evolution of this metric for three real gas cases and the ideal gas reference. The two plateaus, experienced by the ideal gas case between $\Lambda = 5$ and 17 and at $\Lambda > 30$, are shifted toward higher values of minimum critical mass as the reduced pressure increases. The first plateau is shortened by its end as the real gas effects are

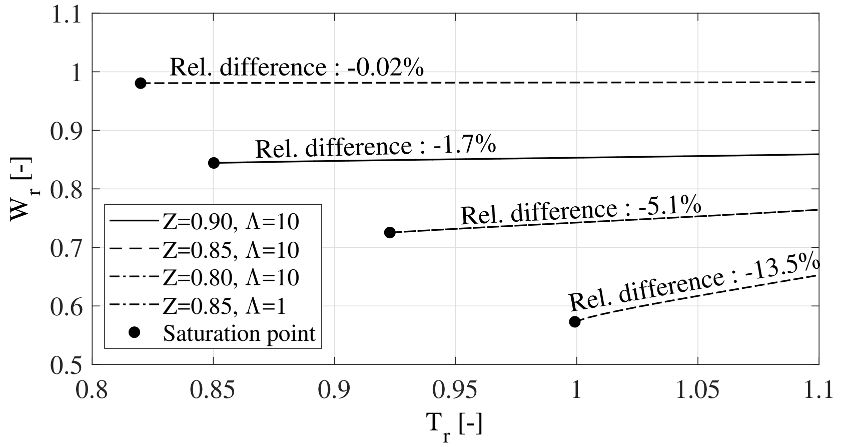

Figure 3.31 – Variation of W_r for a HGJB along three different isolines of Z in the $T_r - P_r$ domain (R134a, $\epsilon = 0.2$)

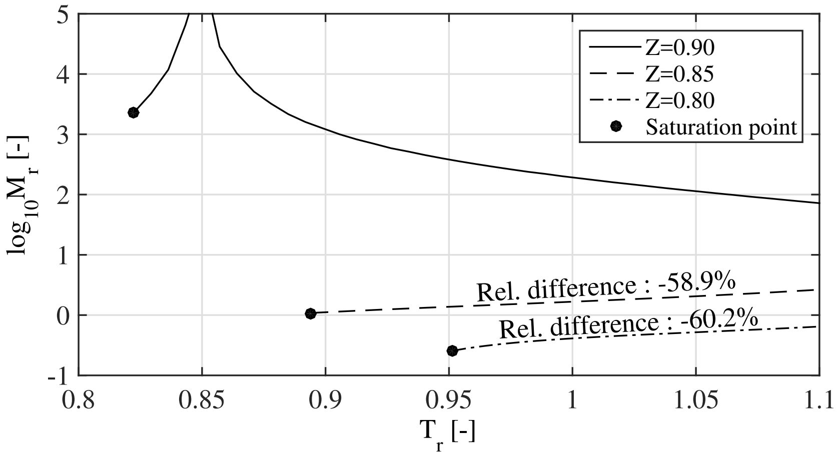

Figure 3.32 – Variation of M_r for a HGJB along three different isolines of Z in the $T_r - P_r$ domain (R134a, $\epsilon = 0$, $\Lambda = 10$)

enhanced.

The ratio of minimum critical mass is defined to compare the minimum value of the critical mass in this range:

$$M_{r,min} = \frac{\min\limits_{\Lambda^* \in [0,\Lambda]} M_{c,rg}}{\min\limits_{\Lambda^* \in [0,\Lambda]} M_{c,ig}} \qquad 3.23$$

Figure 3.35 shows the ratio of minimum critical mass with the ideal gas case as reference. Four zones can be distinguished along the $\Lambda = 0$:

- First zone: Negligible influence of real gas effect on the minimum critical mass, up to $\Lambda \approx 3 - 5$

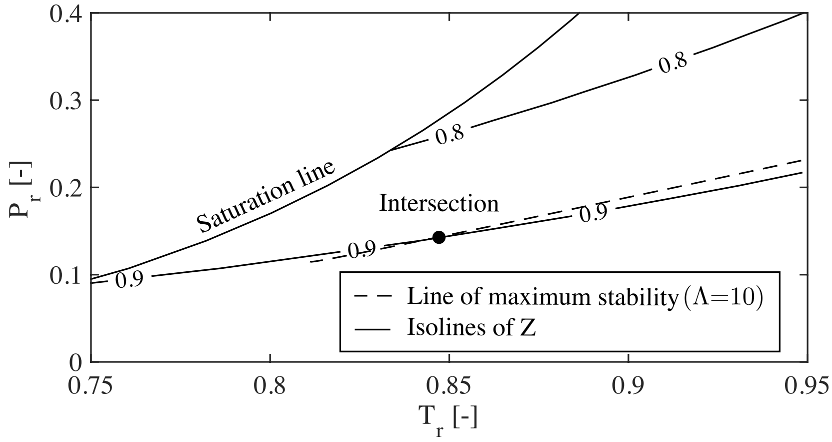

Figure 3.33 – Isolines of Z in the $T_r - P_r$ domain together with the line of maximum stability of a HGJB operating in R134a at $\epsilon = 0$ and $\Lambda = 10$

- Second zone: Constant moderated positive influence, up to $\Lambda = 13 - 17$
- Third zone: localized negative influence with a significant drop in minimum critical mass, up to $\Lambda \approx 21 - 25$
- fourth zone: increasingly positive influence on the minimum critical mass as Λ increases

The real-gas effects have a net negative influence on the critical mass only if the nominal compressibility number is lower than a threshold of $\Lambda \approx 20$, where a particular attention should be paid to ensure the stability of bearing design under the ideal-gas assumption operating in a real-gas environment.

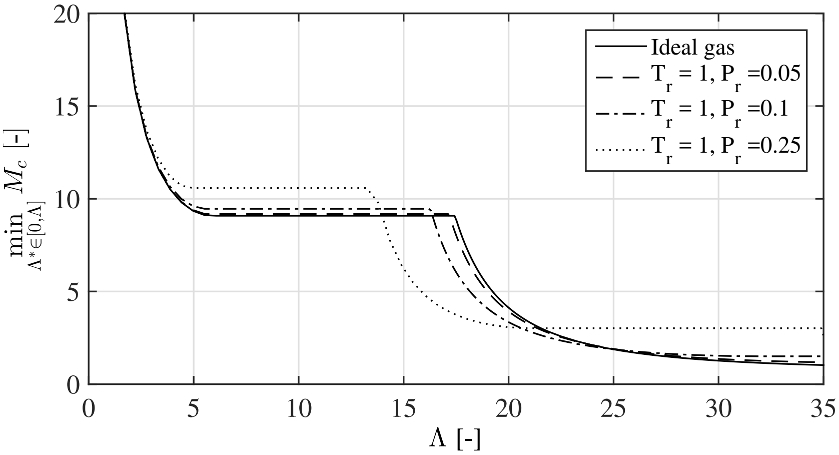

Figure 3.34 – Evolution of the minimum critical mass with the compressibility number for different ambient reduced pressures (R134a)

Regarding the real-gas effects on the load capacity of HGJB, the trend is linear against Λ

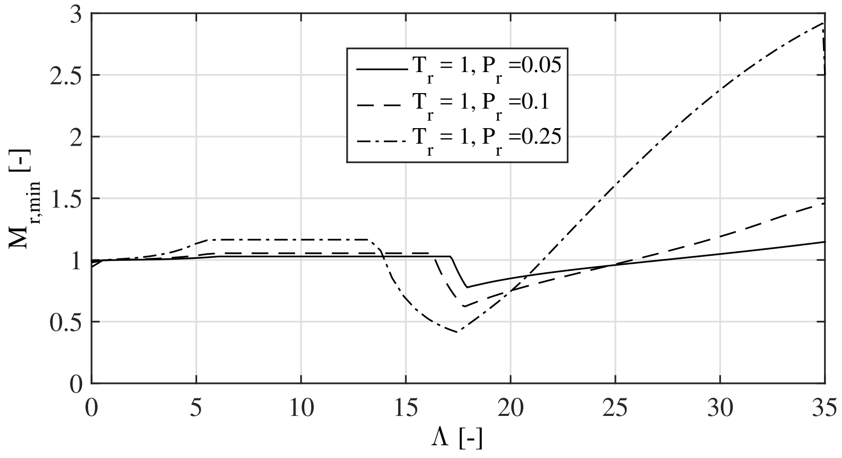

Figure 3.35 – Evolution of the ratio of minimum critical mass with the compressibility number for different ambient reduced pressures (R134a)

beyond a certain value, as shown in Figure 3.36. The convergence toward a limiting solution as seen with the PJB in Figure 3.16 is not present here, because of the hypothesis behind the NGT. The NGT relies on the assumption of a constant pressure gradient between each groove-ridge pair, strictly valid for an incompressible lubricant only. Constantinescu showed that this assumption is valid even at relatively large values of Λ in the case of HGJB. However, due to the enhanced compressibility induced by the real-gas effects, the validity domain of the NGT is narrowed, which is supported by Figure 3.5 for a step bearing. Therefore, results from the NGT around the critical point should be treated with caution, even at moderated values of Λ. Constantinescu introduced the local compressibility number Λ_l, defined as follows:

$$\Lambda_l = \bar{h}_g^{-2} \alpha \frac{a+b}{L} \Lambda \sin^2 \hat{\beta} \tag{3.24}$$

He suggested $\Lambda_l = 0.1 - 0.15$ as threshold values of compressibility effects. Employing the observation made for the slider bearing in Equation 3.20, the threshold can be adapted for real-gas lubrication with the use of Equation 3.20:

$$\Lambda_{l,rg} = \bar{h}_g^{-2} \alpha \frac{a+b}{L} \frac{\Lambda}{(\partial_{\bar{\rho}} \bar{P})_{T,a}} \sin^2 \hat{\beta} < 0.1 - 0.15 \tag{3.25}$$

The threshold of $\Lambda_{l,rg} = 0.1 - 0.15$ can be assumed to estimate the limit of validity of quasi-incompressible NGT in real-gas lubrication.

3.1.3.4 Real-gas effects with turbulence

Effects of turbulence are implemented by using Constantinescu's correction terms. Figure 3.37 presents the evolution of W_r for an eccentric PJB as a function of Λ for three different values of ambient Reynolds numbers Re_a. The drop in load capacity ratio due to the

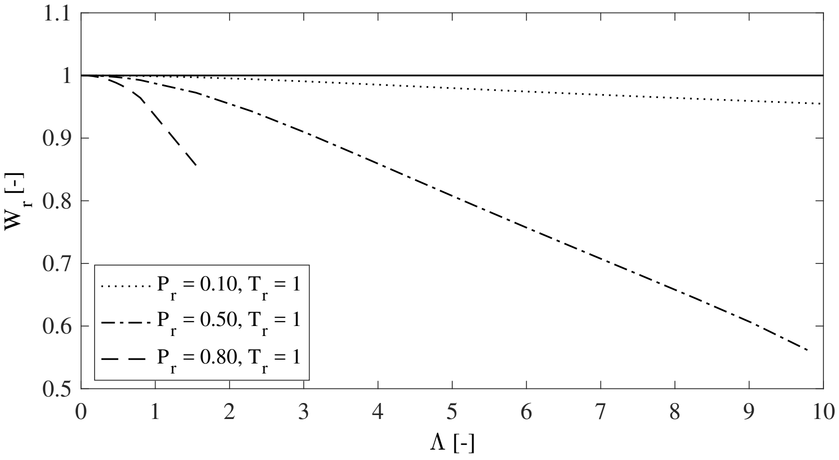

Figure 3.36 – Evolution of W_r with Λ for HGJB at $\epsilon_x = 0.2$, $\epsilon_y = 0$ (R134a)

real-gas effects observed in laminar regime (Figure 3.16) occurs more sharply and at lower compressibility numbers with increasing ambient Reynolds numbers. Qualitatively, the real-gas effects are not significantly affected compared to the laminar lubrication. In substance, turbulence tends to enhance the real-gas effects. A similar observation is valid for the critical mass ratio shown in Figure 3.38, although the trend in turbulent regime differs after the initial drop since M_r recovers linearly after the extremum, thus achieving improved values of M_r past a particular value of Λ. It has to be noted that the critical mass and load capacity ratios are defined for equal ambient Reynolds numbers.

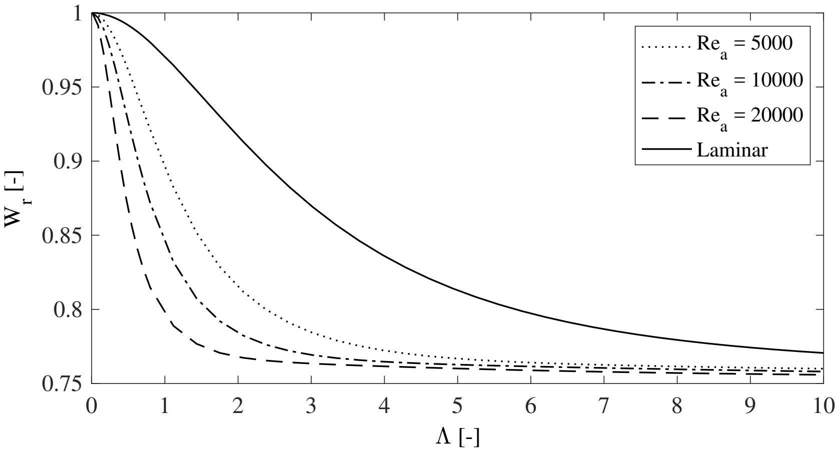

Figure 3.37 – Evolution of W_r for PJB at $\epsilon_x = 0.2$ with turbulent flow ($P_r = 0.5$, $T_r = 1$, R134a)

The region of very high critical mass ratio observed for HGJB still exists in the turbulent regime. The behavior of M_r on both sides of this region is not qualitatively affected, however the position of the line in the $P_r - T_r$ domain depends on the ambient Reynolds number. Figure 3.39 shows the evolution of M_r with the reduced temperature at constant reduced pressure and compressibility number. For the particular operating condition

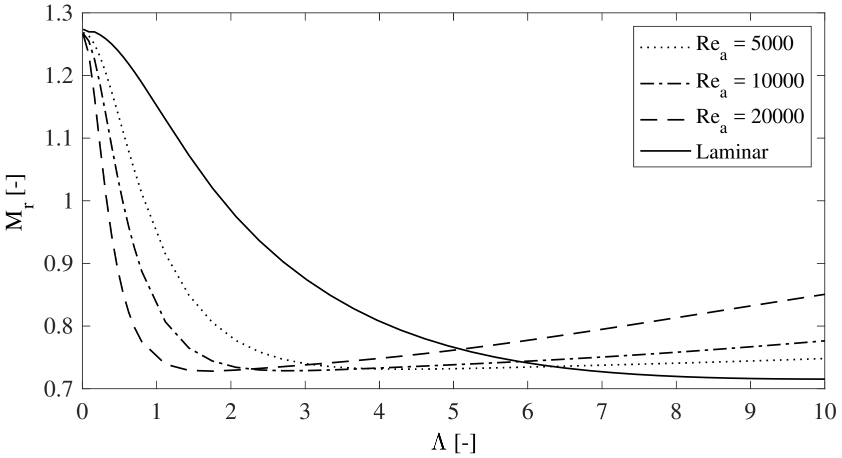

Figure 3.38 – Evolution of M_r for PJB at $\epsilon_x = 0.2$ with turbulent flow ($P_r = 0.5$, $T_r = 1$, R134a)

(Λ, P_r), the point of local peak stability is not visible in the laminar regime but appears as the ambient Reynolds numbers increases, thus shifting the position of the extremum toward higher reduced temperature, such as symbolically illustrated in Figure 3.40. Thus, compared to the laminar flow regime, the domain where $M_r < 1$ is expanded. As a result of turbulence, a safe bearing design is more difficult to achieve.

The use of another correlation for the turbulence correction terms is not expected to influence the results significantly, since they systematically lead to a reduced Poiseuille flow and, as a results, an increased overall density in the fluid film domain which amplifies the real-gas effects.

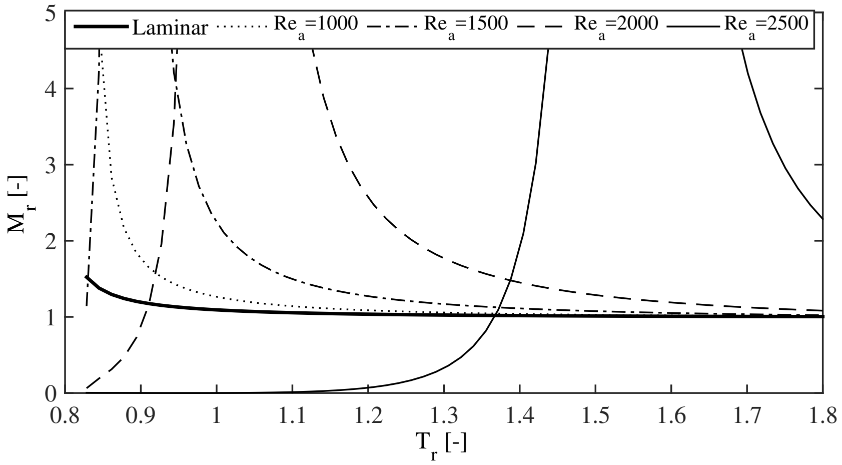

Figure 3.39 – Evolution of M_r for HGJB at $\epsilon = 0$ with different values of Re_a ($P_r = 0.2$, $\Lambda = 5$, R134a)

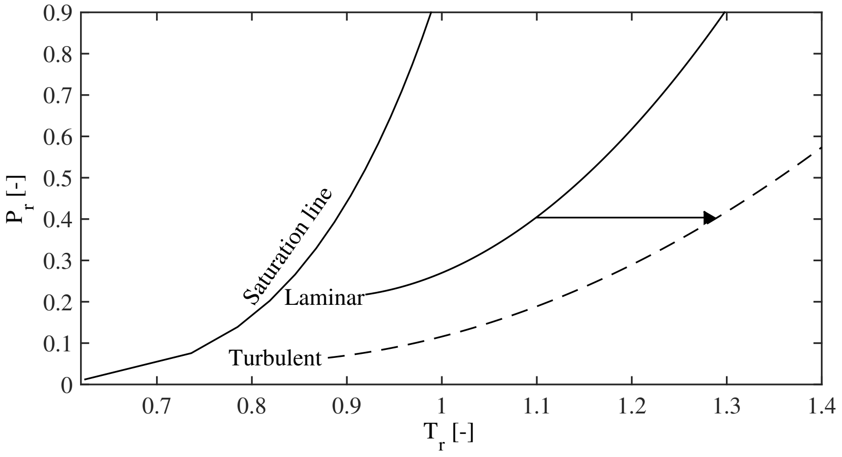

Figure 3.40 – Qualitative illustration of the evolution of the maximum stability line as the ambient Reynolds number increases for a given Λ

3.1.4 Conclusion

The Reynolds equation was expressed in terms of density instead of pressure, with the appearance a thermodynamic parameter addressing real-gas effects, the bulk modulus. Static and dynamic resolutions of this equation were performed on different bearing geometries and led to the following observations:

1. Real-gas effects strongly depend on the value of the reduced pressure P_r and temperature T_r, showing that the proximity of the critical point amplifies real-gas effects in bearings. The ambient compressibility factor Z is an effective variable to characterize the real-gas effects on the load-carrying capacity of aerodynamic bearings. However, it is not sufficient to assess the stability of a grooved bearing, which displays a considerable variation for the same ambient value of Z

2. In general, real-gas effects negatively affect the load capacity of journal bearings (PJB and HGJB), although a 6%-increase was computed for a step slider bearing at a low value of Λ

3. Depending on the operating and ambient conditions, the critical bearing mass is either positively or negatively affected by the real-gas effects. At moderated values of Λ, the effect is positive on PJB, but becomes negative beyond a threshold value of $\Lambda \approx 2$. For HGJB, the critical mass ratio can reach very high values along a line in the $P_r - T_r$ domain. Its position depends on the value of Λ.

4. Deviation from the ideal-gas behavior evaluated for a particular fluid is valid for other fluids of diverse chemical nature with a moderated error for PJB and step slider bearing. This is observed as long as the similitude of geometry, compressibility number and reduced temperature and pressure is verified. This agreement between

different fluids is also observed for HGJB, where lines of high stability appear in the same region of the $P_r - T_r$ domain, although the absolute value of the deviation is large near these high-stability regions.

5. The validity of the incompressible solution to the Reynolds equation is limited to lower values of Λ due to the rising effect of real gas. The threshold of validity can be estimated from the ambient value of the parameter accounting for real-gas effects and the ideal-gas threshold. By extension, a modified threshold of validity for the quasi-incompressible NGT based on [12] is suggested for real-gas lubrication of HGJB.
6. The presence of turbulence enhances the real-gas effects on both the load capacity and the stability. The drop in load capacity ratio is more pronounced at low compressibility numbers and the regions of high stability observed for HGJB are shifted to higher reduced temperature and lower reduced pressure.

Considering these observations, the position of the operation point in the $P_r - T_r$ domain is suggested to be the most relevant design variable when designing a gas bearing-rotor system. Because of the high pressure build-up in HGJB, particular care should be taken in the design of such bearings in order to take advantage of the real-gas effects and avoid their possible negative influence. The real-gas effects tend to phase out at high reduced temperature and low reduced pressure.

Bibliography

[1] D. D. Fuller, A Review of the State-of-the-Art for the Design of Self-Acting Gas-Lubricated Bearings, Journal of Lubrication Technology 91 (1) (1969) 1–16. `doi:10.1115/1.3554857`.

[2] J. Schiffmann, D. Favrat, The effect of real gas on the properties of Herringbone Grooved Journal Bearings, Tribology International 43 (9) (2010) 1602–1614. `doi:10.1016/j.triboint.2010.03.006`.

[3] T. M. Conboy, Real-Gas Effects in Foil Thrust Bearings Operating in the Turbulent Regime, Journal of Tribology 135 (3) (2013) 031703–031703–12. `doi:10.1115/1.4024048`.

[4] F. Xu, D. Kim, Three-Dimensional Turbulent Thermo-Elastohydrodynamic Analyses of Hybrid Thrust Foil Bearings Using Real Gas Model (2016) V07BT31A030`doi:10.1115/GT2016-57766`.

[5] Z. Fairuz, I. Jahn, The influence of real gas effects on the performance of supercritical CO 2 dry gas seals, Tribology International 102 (2016) 333–347. `doi:10.1016/j.triboint.2016.05.038`.

[6] V. N. Constantinescu, Basic Relationships in Turbulent Lubrication and Their Extension to Include Thermal Effects, Journal of Lubrication Technology 95 (2) (1973) 147–154. `doi:10.1115/1.3451755`.

[7] G. G. Hirs, A Bulk-Flow Theory for Turbulence in Lubricant Films, Journal of Lubrication Technology 95 (2) (1973) 137–145. `doi:10.1115/1.3451752`.

[8] C.-W. Ng, C. H. T. Pan, A Linearized Turbulent Lubrication Theory, Journal of Basic Engineering 87 (3) (1965) 675–682. `doi:10.1115/1.3650640`.

[9] F. C. Hsing, Formulation of a Generalized Narrow Groove Theory for Spiral Grooved Viscous Pumps, Journal of Lubrication Technology 94 (1) (1972) 81–85. `doi:10.1115/1.3451640`.

[10] J. H. Vohr, C. Y. Chow, Characteristics of Herringbone-Grooved, Gas-Lubricated Journal Bearings, Journal of Basic Engineering 87 (3) (1965) 568–576. `doi:10.1115/1.3650607`.

[11] D. P. Fleming, B. J. Hamrock, Optimization of self-acting herringbone journal bearing for maximum stability, in: Proceedings of the fifth international gas bearing symposium, 1974.

[12] V. N. Constantinescu, V. Castelli, On the Local Compressibility Effect in Spiral-Groove Bearings, Journal of Lubrication Technology 91 (1) (1969) 79–86. `doi:10.1115/1.3554902`.

3.2 Humid air effects

Parts of the material presented in this section has been published in the following journal article:

Guenat, E., Schiffmann, J., 2018. Effects of humid air on aerodynamic journal bearings. Tribology International 127, 333–340. DOI:10.1016/j.triboint.2018.06.002

3.2.1 Introduction

The use of aerodynamic bearings expands progressively to domains where the ambient conditions cannot be satisfactorily conditioned, either due to economical or to technical reasons. In particular, gas bearing-supported pressurizers of Proton-Exchange Membrane (PEM) fuel cells [1–3] for automotive applications are subject to a large range of ambient temperatures and relative humidities. Thus, the knowledge of the effect of ambient humidity on the performance of an aerodynamic bearing is necessary to ensure the viability of a given design.

Water vapor contained in humid air (HA) is subject to condensation if the saturation pressure is reached within the fluid film of gas-lubricated bearings, especially because the gas compression in the lubricant film is usually considered isothermal (Figure 3.41). The resulting effects might influence the bearing behavior. Several works [4; 5] theoretically and experimentally investigated the influence of HA on the static pressure field of hard disk drive heads, showing that vapor condensation can occur, which reduces the pressure in the bearing, leading to a reduction of the head's flying height. For the same application, Hua et al. [6] performed transient simulations investigating the settling time of the flying head and showed that HA effects affect the final state of the bearing. In the previously mentioned works, the simulation method to model HA effects consists in applying a correction on the pressure field obtained from the ideal-gas form of the Reynolds equation. Kirpekar et al. [7] introduced a modification of the Reynolds equation to obtain a more rigorous approach. Ma et Liu [8; 9] investigated the dynamic phase equilibrium in the mixture to conclude to the quasi-immediacy of the thermodynamic equilibrium in the gas film. Aoki et al. [10] experimentally highlighted the influence of the water film thickness on the behavior of the bearing in ultra-thin film lubrication. More recently, the same phenomenon was further studied by Choi et al. [11]. Tani et al.[12] measured the clearance loss in a slider bearing lubricated with with water-nitrogen and ethanol-nitrogen mixtures and further confirmed the clearance reduction in humid conditions. Ma et al. [13] theoretically studied the influence of the adsorbed water film on the heat transfer in a slider bearing, highlighting an increase of the heat transfer coefficient. Matthes et al. [14; 15] experimentally investigated the influence of relative humidity on the touch-down power (energy dissipated during a contact between mobile and static parts) of an aerodynamic slider bearing. They reported a reduction of touch-down energy loss with increasing humidity ratios. The literature on the HA-lubricated bearings is still limited to slider geometries with ultra-thin film lubrication applied to data storage, with no application to journal bearings, despite the growing interest for aerodynamic bearings employed in humid environments.

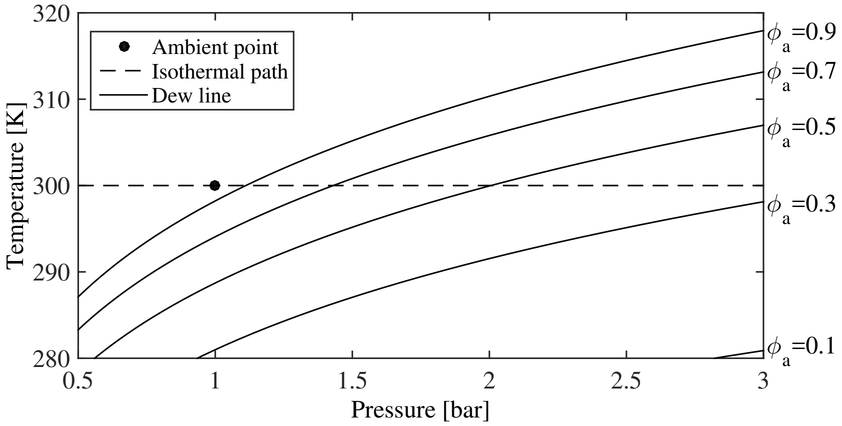

Figure 3.41 – Dew lines in a Pressure-Temperature diagram, with the black dot as reference point. Starting from the point and following the dashed isothermal line, condensation can be reached at higher pressure depending on the ambient relative humidity (ϕ_a), when the corresponding dew line is crossed

The present work investigates the HA effects on the performance of PJBs and of HGJBs. The objectives are to: (1) develop an expression of the Reynolds equation for HA-lubricated journal bearings, (2) evaluate the deviation of HA-lubricated journal bearing from ideal-gas lubrication in terms of load capacity and whirl stability in a large range of ambient temperatures, relative humidities and operating conditions and (3) devise design guidelines for robust design considering HA effects.

The Reynolds equation for compressible fluids is adapted to express the local density, exhibiting the bulk modulus whose expression depends on whether the saturation conditions are locally met or not. The expression of the bulk modulus is derived from the classical humid air theory and accounts for the drying effect of condensing vapor. The perturbation method is applied on the Reynolds equation and a finite difference scheme is used to solve the equations. Static and dynamic bearing properties are obtained by integration of the pressure fields. The concept of critical mass is used as a stability metric regarding the whirl instability. The deviation of HA lubrication from the ideal-gas case is investigated for both PJB and HGJB in terms of load capacity and critical mass. The selected HGJB geometry maximizes the stability at moderated compressibility number ($\Lambda = 1$). The considered operating conditions vary in temperature from 275 to 370 K, in relative humidity from 0 to 1 with different eccentricity ratios and compressibility numbers up to 30. Based on the generated results, a set of design guidelines is suggested for the design of HA-lubricated journal bearings based on the ideal-gas Reynolds equation.

3.2.2 Theory

HA lubrication implies a condensable gas mixture of water (condensable) and air, considered as non-condensable. The main working hypotheses in the following development are as follows: (1) the gas film is isothermal, (2) the thermodynamic equilibrium is instantaneous as suggested by Ma et Liu [8], (3) only the gas phase is considered. The hypothesis (1) is justified by the large contact area of the gas film with the rotor and bushings. These areas are heterogeneous nucleation sites justifying (2) and the very small volume of condensed water regarding the gas phase justifies (3).

Since the practical problem targeted in the present work involves an atmospheric pressure, both gases (air and water vapor) are considered as ideal. However, for an isothermal gas, the saturation partial pressure of water can be reached within the fluid film as a mixture pressure increases. At this point (dew point), water vapor starts condensing and limits its contribution to the mixture pressure build-up on which the bearing relies to serve its purpose. At this point, the behavior of the mixture deviates from an ideal gas, namely:

$$P = \rho r_a T \tag{3.26}$$

where r_a is the specific gas constant of the ambient HA. In order to account for the condensation effects, Equation 3.26 is not used to substitute the density with the pressure in Reynolds equation. Instead, the changes of variable of equation 2.24 to 2.25 are applied:

$$\frac{\partial P}{\partial X} = \left(\frac{\partial P}{\partial \rho}\right)_T \cdot \frac{\partial \rho}{\partial X}, \qquad \frac{\partial P}{\partial z} = \left(\frac{\partial P}{\partial \rho}\right)_T \cdot \frac{\partial \rho}{\partial z} \tag{3.27}$$

Where $(\partial_\rho P)_T$ is associated to the bulk modulus β of the lubricant gas:

$$\rho \left(\frac{\partial P}{\partial \rho}\right)_T = \beta \tag{3.28}$$

Further, the Reynolds equation changes from what has been developed previously in this work by the presence of a non-constant viscosity, subject to changes because of HA effects:

$$\partial_\theta \left(\frac{\bar{\beta}\bar{h}^3}{\bar{\mu}} \partial_\theta \bar{\rho}\right) + \partial_{\bar{z}} \left(\frac{\bar{\beta}\bar{h}^3}{\bar{\mu}} \partial_{\bar{z}} \bar{\rho}\right) = \Lambda \partial_\theta \left(\bar{\rho}\bar{h}\right) + \sigma \partial_{\bar{t}} \left(\bar{\rho}\bar{h}\right) \tag{3.29}$$

With $\bar{\mu} = \mu/\mu_a$.

The perturbation method, developed in chapter 2.2, is applied to retrieve static and dynamic performance of the bearing. The presence of the normalized viscosity in the Reynolds equation is novel to the HA analysis, since it now considered as a function of the density and is also affected by the perturbation:

$$\frac{1}{\bar{\mu}} = \frac{1}{\bar{\mu}_0} + \epsilon_{1x}\left(\frac{-1}{\bar{\mu}^2}\frac{\partial\bar{\mu}}{\partial\bar{\rho}}\right)_0 \bar{\rho}_{1x}e^{i\bar{t}} + \epsilon_{1y}\left(\frac{-1}{\bar{\mu}^2}\frac{\partial\bar{\mu}}{\partial\bar{\rho}}\right)_0 \bar{\rho}_{1y}e^{i\bar{t}} \tag{3.30}$$

The method developed in chapter 2.2 is applied to segregate static and dynamic terms, to solve the differential equations and to compute the performance of the bearing. Similarly, the NGT is adapted to accommodate to non-constant viscosity:

$$\begin{aligned}\partial_\theta\left[\frac{\bar{\beta}}{\bar{\mu}}\left(f_1\partial_\theta\bar{\rho} + f_2\partial_{\bar{z}}\bar{\rho}\right)\right] + \partial_{\bar{z}}\left[\frac{\bar{\beta}}{\bar{\mu}}\left(f_2\partial_\theta\bar{\rho} + f_3\partial_{\bar{z}}\bar{\rho}\right)\right]& \\ +c_s\left(\sin\hat{\beta}\partial_\theta(f_4\bar{\rho}) - \cos\hat{\beta}\partial_{\bar{z}}(f_4\bar{\rho})\right)& \\ -\Lambda\partial_\theta(f_5\bar{\rho}) - \sigma\partial_{\bar{t}}(f_5\bar{\rho}) = 0&\end{aligned} \tag{3.31}$$

where parameters f_i are identical to those presented in chapter 2.1.

The problem of HA lubrication consists in the expression of $(\partial_{\bar{\rho}}\bar{P})_T$. As long as the saturation partial pressure of water vapor is not locally reached, the mixture is assumed to be an ideal gas. Thus, the term $(\partial_{\bar{\rho}}\bar{P})_T$, encapsulated in the bulk modulus, is equal to unity:

$$(\partial_{\bar{\rho}}\bar{P})_T = \frac{\rho_a}{P_a}(\partial_\rho P)_T = \frac{\rho_a r_a T}{P_a} = 1 \tag{3.32}$$

Only when the saturation pressure is met, condensing water will stop building up pressure, leading to $(\partial_{\bar{\rho}}\bar{P})_T < 1$, thus, departing from the ideal-gas behavior.

The ideal-gas equation for the gas mixture is:

$$P = \rho r T \tag{3.33}$$

The value of $(\partial_\rho P)_T$ is simply:

$$(\partial_\rho P)_T = rT + \rho T\partial_\rho r \tag{3.34}$$

where r is the mixture specific gas constant

$$r = \frac{r_{air} + w r_{vap}}{1 + w} \tag{3.35}$$

and w is the humidity ratio defined as the ratio of mass water vapor per unit mass of dry air:

$$w = \frac{M_{vap}}{M_{air}} \tag{3.36}$$

The value of w of the gas phase is defined locally depending on whether the saturation conditions are met or not:

$$w = \min(w_a, w^*(T_a, P)) \tag{3.37}$$

w^* is the saturation humidity ratio, which is a function of the ambient temperature and local pressure as follows:

$$w^* = \frac{\tilde{m}_{vap}}{\tilde{m}_{air}} \frac{P^*_{vap}(T_a)}{P - P^*_{vap}(T_a)} \tag{3.38}$$

where P^*_{vap} is the saturation pressure of water that depends on the temperature only, computed using a fluid database [16]. Since Equation 3.29 deals with density rather than pressure, it is convenient to have an expression of w^* as a function of density. For that purpose Equation 3.33 is inserted in Equation 3.38 and w^* is isolated:

$$w^* = \frac{-c_2 + \sqrt{c_2^2 - 4c_1c_3}}{2c_1} \tag{3.39}$$

with

$$c_1 = (\rho r_{vap} T - P^*_{vap}) \tag{3.40}$$

$$c_2 = r_{air}\rho T - P^*_{vap}(1 + \tilde{m}_{vap}/\tilde{m}_{air}) \tag{3.41}$$

$$c_3 = P^*_{vap}\tilde{m}_{vap}/\tilde{m}_{air} \tag{3.42}$$

If saturation is reached and the water content in the gas phase decreases, the mixture viscosity evolves accordingly. It is expressed from [17] as follows:

$$\mu = \frac{(1 - \tilde{c}_{vap}) - \mu_{air}}{1 - \tilde{c}_{vap} + \tilde{c}_{vap}\Phi_{av}} + \frac{\tilde{c}_{vap}\mu_{vap}}{\tilde{c}_{vap} + (1 - \tilde{c}_{vap})\Phi_{va}} \tag{3.43}$$

where

$$\Phi_{av} = \frac{\sqrt{2}}{4}\left(1 + \frac{\tilde{m}_{air}}{\tilde{m}_{vap}}\right)^{-0.5}\left(1 + \left(\frac{\mu_{air}}{\mu_{vap}}\right)^{0.5}\left(\frac{\tilde{m}_{vap}}{\tilde{m}_{air}}\right)^{0.25}\right)^2 \tag{3.44}$$

$$\Phi_{va} = \frac{\sqrt{2}}{4}\left(1 + \frac{\tilde{m}_{vap}}{\tilde{m}_{air}}\right)^{-0.5}\left(1 + \left(\frac{\mu_{vap}}{\mu_{air}}\right)^{0.5}\left(\frac{\tilde{m}_{air}}{\tilde{m}_{vap}}\right)^{0.25}\right)^2 \tag{3.45}$$

$\tilde{c}_{vap}$ is the molar concentration of water vapor in the gas phase, related to the humidity ratio as follows:

$$\tilde{c}_{vap} = \frac{1}{1 + \frac{\tilde{m}_{vap}}{w\tilde{m}_{air}}} \tag{3.46}$$

The deviation from the ideal-gas law and the change of viscosity provide the necessary tools for the modeling of HA-lubricated journal bearings.

3.2.3 Numerical computations and results

Journal bearings lubricated with condensable humid air are compared to equivalent non-condensable (ideal gas) cases using two performance metrics, namely the load capacity ratio W_r and the critical mass ratio M_r, defined as follows:

$$W_r = \frac{W_{cond}}{W_{non-cond}} \tag{3.47}$$

$$M_r = \frac{M_{c,cond}}{M_{c,non-cond}} \tag{3.48}$$

$$\tag{3.49}$$

Both the investigated geometries have a L/D ratio of 1. Moreover, the HGJB geometry is based on the design obtained in [18] maximizing the minimum critical mass for the range $\Lambda \in [0, 5]$ (Equation 2.65) when the grooved member rotates:

$$\alpha = 0.6 \tag{3.50}$$

$$\hat{\beta} = 145.8^\circ \tag{3.51}$$

$$\bar{\delta} = 1.25 \tag{3.52}$$

Unless specified differently, the presented simulations are performed at an ambient temperature of 308 K, which is assumed to represent a pessimistic temperature for humid environments. A first simulation of the PJB running at $\Lambda = 30$, and $\epsilon_x = 0.5$ allows to understand the consequences of humid air lubrication. Figure 3.42 presents the pressure relative to the ambient at the mid-span of the considered bearing and the relative deviation of the pressure compared to the non-condensable case with an ambient relative humidity of 0.8. The relative humidity ϕ is defined as follows:

$$\phi = \frac{P_{vap}}{P^*_{vap}} \tag{3.53}$$

The pressure is not only affected in the zone where it exceeds the dew point, exhibiting a reduction larger than 0.8% , but also outside this zone, although the deviation is even more modest. The pressure field is globally affected because of the elliptical characteristic of the Reynolds equation. The pressure value at one particular point affects the entire fluid film domain. This kind of observation is impossible with HA effects considered *a posteriori*, on top of the pressure field computed with non-condensable gas lubrication, as usually seen in the literature [4–6].

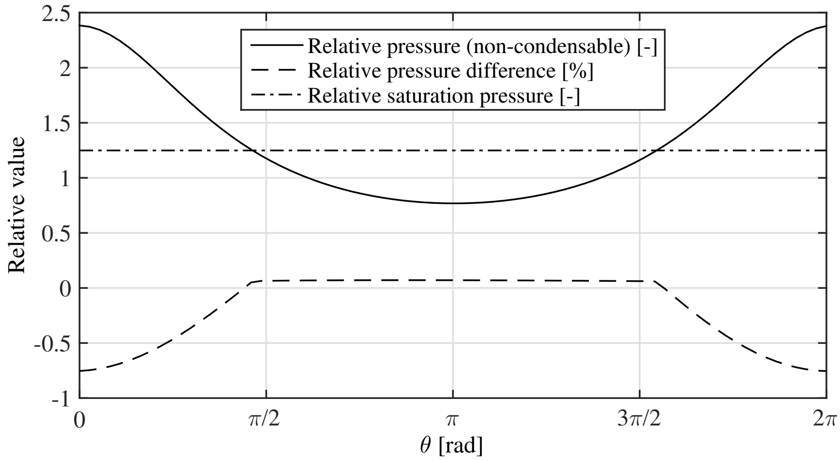

Figure 3.42 – Relative pressure and deviation along the circumference of a PJB at $\bar{z} = 0$, $\epsilon_x = 0.5$, $\phi_a = 0.8$ and $\Lambda = 30$. The pressure profile under condensable conditions is not represented, as it is indistinguishable from the non-condensable case

Figure 3.43 presents the isolines of the load capacity ratio W_r for the PJB at $\epsilon_x = 0.5$ as a function of the ambient relative humidity ϕ_a and the compressibility number Λ. Load capacity drops when the saturation pressure is reached inside the bearing and the condensation onset is reached at lower values of ϕ_a as Λ increases, until it converges toward a limit value. This is due to the well-known limiting solution for PJB with $\Lambda \to \infty$, at which a limit pressure field is reached. With a maximum relative deviation of approximately 1.5% at this ambient temperature, the loss of load capacity remains low at all values of compressibility number, even at high ambient relative humidity. Deviation of this order of magnitude can be considered as negligible from a practical point of view.

Figure 3.44 depicts the evolution of M_r with ϕ_a and Λ. Once the saturation pressure is reached within the gas film, the condensation effects have a small yet negative influence on M_r. Such a modest evolution of the critical mass remains without consequences on the practical design and performance of a PJB.

Figures 3.45 and 3.46 present the same approach with the HGJB for W_r and M_r respectively, at $\epsilon_x = 0.05$. The load capacity is negatively affected by the condensation, with a maximum deviation of less than 1%. Regarding the stability in the saturated domain, M_r is above unity on the left side of the line $\Lambda \approx 9$ and below unity on its right

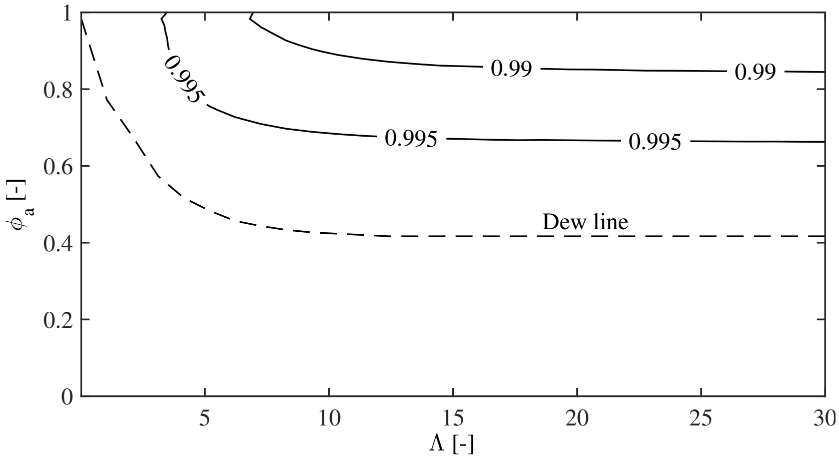

Figure 3.43 – Isolines of W_r for PJB at $\epsilon_x = 0.5$ ($T_a = 308$ K)

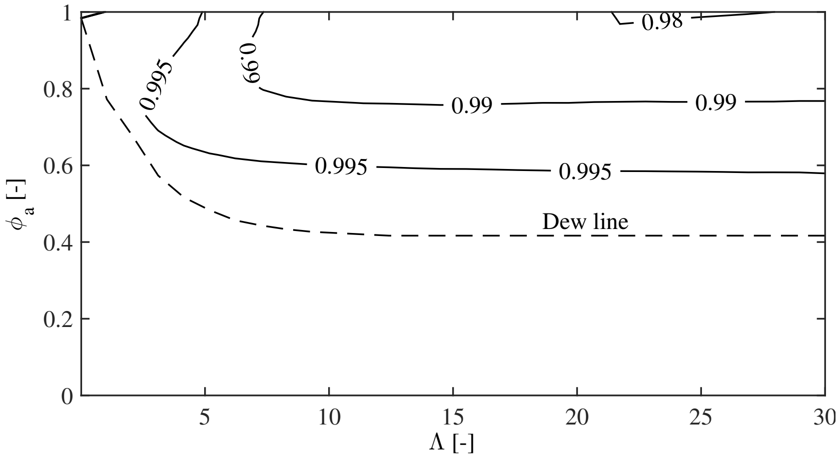

Figure 3.44 – Isolines of M_r for PJB at $\epsilon_x = 0.5$ ($T_a = 308$ K)

side. The largest low- and high-deviation values are reached at the line itself, with a very abrupt change of trend. The underlying phenomenon is the point of very high stability observed for HGJB for particular values of Λ. Under the condition of saturated humid air lubrication, the position of this stability peak is shifted to slightly lower values of Λ (Figure 3.47), explaining the abrupt variation of M_r in this zone. The divergence of the 25%-deviation lines along the ϕ_a axis translates a rise in the amplitude of this variation with the ambient humidity ratio. However, M_r gets close to 1 as soon as the operating conditions deviate from this particular zone.

Following the definition of Eq. 3.23 adapted to a comparison between condensable and non-condensable lubrication, Figure 3.48 depicts the evolution of M_r and $M_{r,min}$ with Λ^* for the saturated ambient condition ($\phi_a = 1$). The improvement of critical mass observed for the condensable lubrication on the left-hand side of the turn-over point at $\Lambda^* \approx 9$ is translated into a moderately improved value of the minimum critical mass ($\approx 3\%$).

Past this point, $M_{r,min}$ coincides with the line of M_r, resulting in a depreciation of the minimum critical mass reaching 25%, which is not negligible from a design perspective.

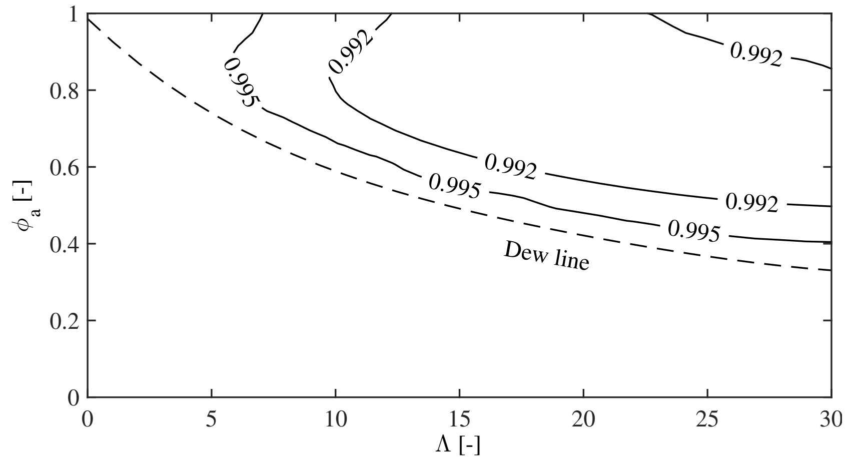

Figure 3.45 – Isolines of W_r for HGJB at $\epsilon_x = 0.05$ ($T_a = 308$ K)

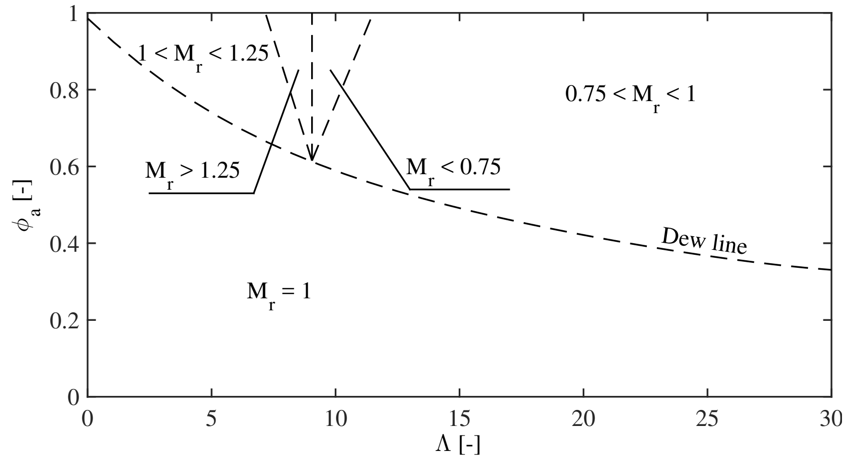

Figure 3.46 – Isolines of M_r for HGJB at $\epsilon_x = 0.05$ ($T_a = 308$ K)

The knowledge of the HA-effects on the synchronous stiffness and damping presents a practical interest to predict the imbalance response of a rotor. The total stiffness and damping ratio in the x direction are defined as follows:

$$K_{x,r} = \frac{\left(\sqrt{K_{xx}^2 + K_{yx}^2}\right)_{cond}}{\left(\sqrt{K_{xx}^2 + K_{yx}^2}\right)_{non-cond}} \tag{3.54}$$

$$C_{x,r} = \frac{\left(\sqrt{C_{xx}^2 + C_{yx}^2}\right)_{cond}}{\left(\sqrt{C_{xx}^2 + C_{yx}^2}\right)_{non-cond}} \tag{3.55}$$

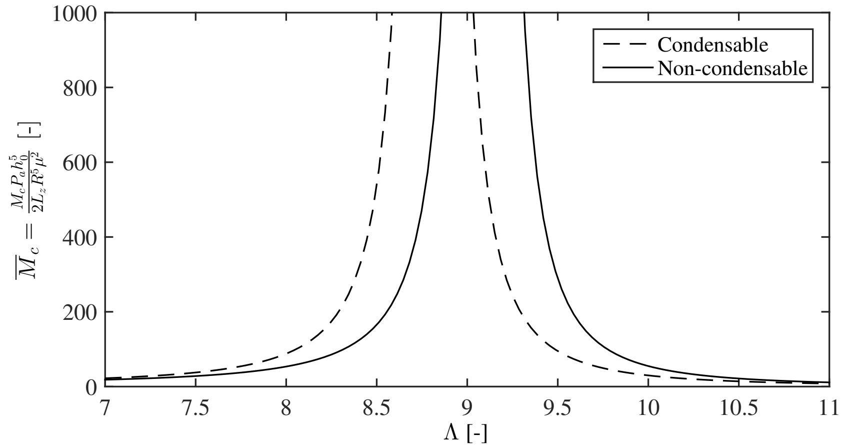

Figure 3.47 – Critical mass for HGJB at $\epsilon_x = 0.05$ ($T_a = 308$ K, $\phi_a = 1$) as a function of Λ with and without vapor condensation

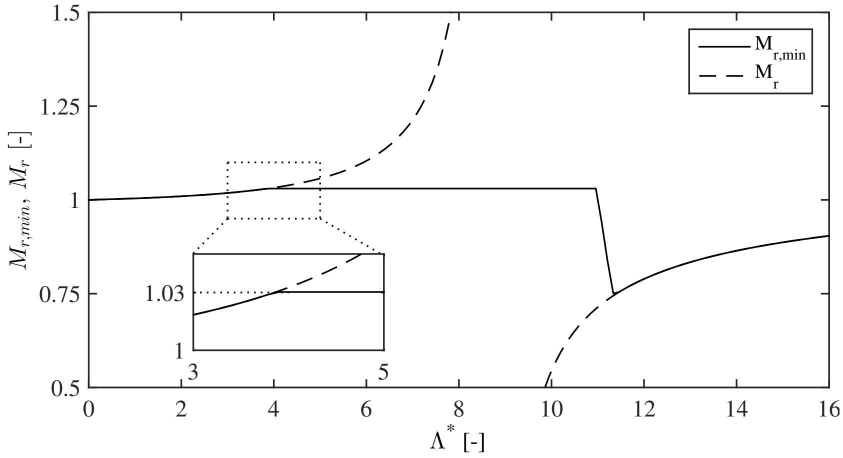

Figure 3.48 – M_r and $M_{r,min}$ for HGJB at $\epsilon_x = 0.05$ ($T_a = 308$ K, $\phi_a = 1$) as a function of Λ

Figure 3.49 presents the synchronous value of these two parameters for the PJB and HGJB as a function of Λ. The stiffness ratio is slightly above 1 for small values of Λ, however without practical significance. The PJB case exhibits a constantly decreasing trend at higher compressibility numbers, converging around a loss lower than 1.5%. The HGJB shows a modest loss of stiffness at intermediate values of Λ and an equally modest gain at low and high values of Λ. However, the deviation remains lower than ±0.5% in all investigated cases, which can be regarded as negligible. Qualitatively, the damping ratio behaves similarly to the stiffness ratio for the PJB, with a rapid decrease and a nearly constant plateau at approximately -2.5% for high values of Λ. The damping ratio of the HGJB exhibits a different trend, as a local minimum at $\Lambda \approx 6$ is visible with a reduction of nearly 3%. At higher compressibility numbers, this parameter increases and exceeds unity with a gain lower than 0.5%. In a practical perspective, the synchronous dynamic coefficients of both bearings can be considered as independent of HA effects.

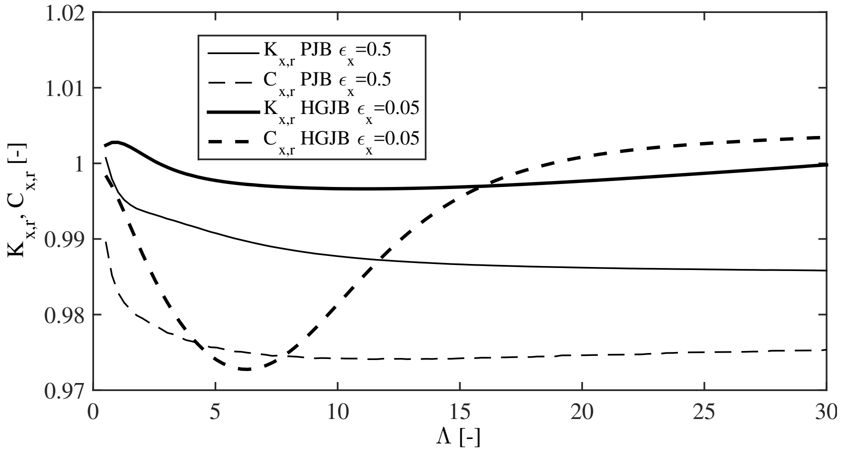

Figure 3.49 – Evolution of total stiffness and damping ratio for PJB and HGJB (T_a = 308 K, $\phi_a = 1$) as a function of Λ

The effects of the eccentricity ratio on the considered bearings are presented in Figure 3.50, at $\Lambda = 10$ and $\phi_a = 0.9$. The evolution of W_r shows no clear trend for the HGJB and diminishes for the PJB as soon as the saturation point is reached, yet in an insignificant order of magnitude. The value of M_r for the HGJB increases slightly because of the further shift in the critical mass curve. The M_r of the PJB shows a local minimum at $\epsilon_x \approx 0.17$, however at levels without practical implications. Both metrics for HGJB are affected by humid-air effects already at a concentric position because of the inherent pressure build-up due to the grooved pattern, while saturation is reached only above $\epsilon_x \approx 0.1$ for the PJB.

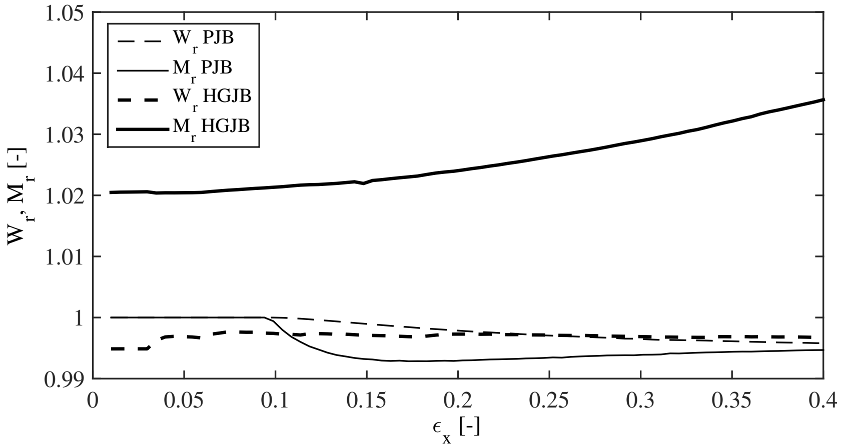

Figure 3.50 – Evolution of W_r and M_r for HGJB and PJB with the eccentricity ratio (T_a= 308 K. Λ=5, ϕ_a=0.9)

Figure 3.51 presents the evolution of the minimum value of $M_{r,min}$ for $\Lambda^* = 50$ with the eccentricity ratio, in saturated ambient conditions. This metric shows a minimum at concentric position and relaxes as the eccentricity ratio increases.

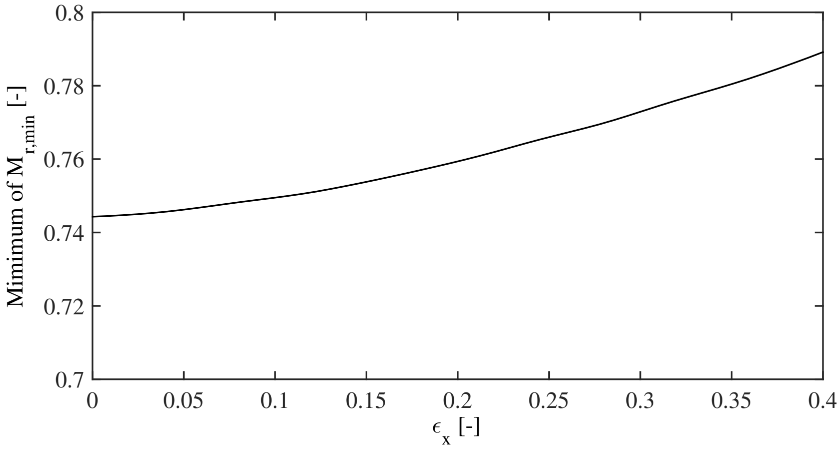

Figure 3.51 – Evolution of the minimum value of $M_{r,min}$ for $\Lambda^* = 50$ with the eccentricity ratio for HGJB (T_a= 308 K, ϕ_a=1)

The effects of the ambient temperature are presented in Figure 3.52 for both PJB and HGJB at $\phi_a = 0.9$. The concentration of water in the gas mixture increases with temperature at equal value of relative humidity, thus enhancing the effects of humid-air lubrication at high ambient temperature. All metrics are affected in significant proportions at temperatures approaching 100 $°C$. The strong enhancement of M_r for the HGJB is due to the fact that the stability peak is shifted to lower values of Λ as the temperature increases with constant ϕ_a. For both bearings, the load capacity is reduced by 2% at a temperature of 330 K. In the same Figure, the minimum value of $M_{r,min}$ of a HJGB for $\Lambda^* = 50$ in saturated ambient conditions is shown in order to represent the worst case scenario. The temperature has a significant influence, since this indicator approaches 0 near 100 $°C$. The humid air effects are still significant on this indicator at lower temperatures, since the 10%-reduction threshold is located at 290 K.

The influence of liquid water droplets formed in the bearing clearance due to condensation can be questioned, since the formation of a liquid phase in the lubrication film can threaten the viability of the bearing. However, because of its significant difference of density at near-normal conditions (three orders of magnitude), the liquid phase, which was neglected in the previous computations, might occupy an insignificant volume in the mixture. In order to analyze this, the void fraction, defined as the volume of gas phase over the total two-phase volume, is used:

$$\delta = \frac{v_{gas}}{v_{liquid} + v_{gas}} \qquad 3.56$$

Figure 3.53 shows the "1-void fraction" of the mixture for different ambient temperature and $\phi_a = 1$ in the situation where all the water from the saturated solution condenses, which is an overestimation of reality. Under this assumption, the void fraction gets the

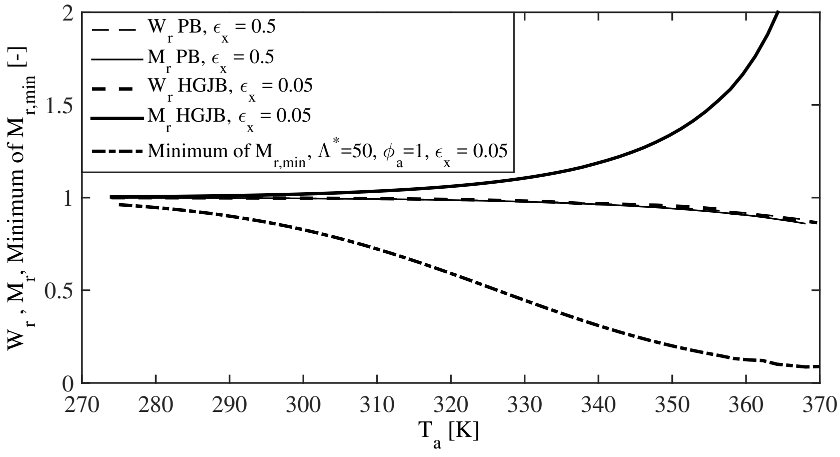

Figure 3.52 – Evolution of W_r and M_r for HGJB and PJB with the ambient temperature ($\Lambda = 5$, ϕ_a=0.9), together with the evolution of the minimum value of $M_{r,min}$ for ϕ_a=1

following expression:

$$\delta = \frac{1}{1 + w_a \rho_{air}/\rho_w} \tag{3.57}$$

The minimum value barely reaches 99% for T just below 100 $°C$, which is suggested to be sufficiently large to discard any risk linked to the formation of a local liquid film in the bearing clearance.

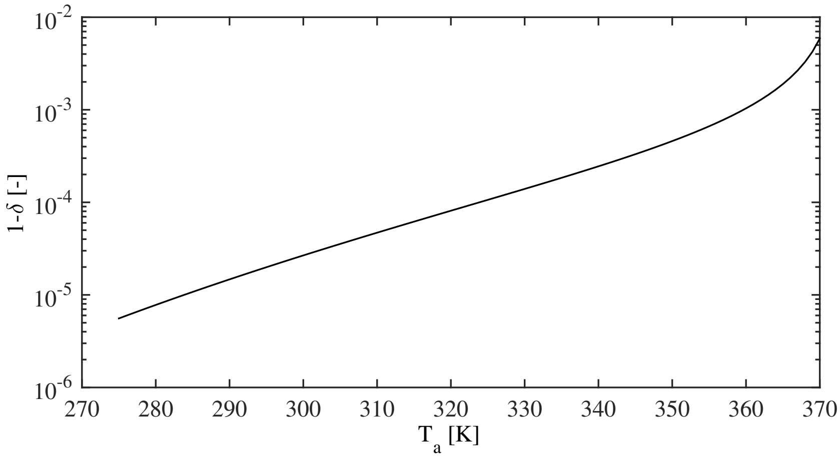

Figure 3.53 – Void fraction as a function of temperature in the limit case where all the water content condenses (ϕ_a=1)

3.2.4 Conclusions

A modified form of the Reynolds equation suited for humid-air lubrication was developed and applied to grooved and plain journal bearings on a wide range of operating conditions (compressibility number, eccentricity ratio, ambient temperature and relative humidity). Cases accounting for vapor condensation in the lubrication film were compared to non-condensable cases (ideal gas) in terms of load capacity and stability (critical mass). The investigations lead to the following observations:

- Humid air (HA) lubrication affects the pressure distribution in a lubrication gas film even at locations where the pressure does not exceed the dew pressure
- Consequences of HA lubrication are in general more significant at high compressibility numbers Λ, ambient humidity ratios and eccentricity ratios. High levels of ambient temperature increase the sensitivity of load capacity and stability to humid-air effects, as the mass concentration of water in air increases
- Herringbone-grooved journal bearings (HGJB) are more sensitive to HA effects than plain journal bearings (PJB), notably because of their inherent pressure build-up even at concentric position, whereas PJBs require a higher eccentricity to develop HA effects.
- Vapor condensation negatively affects the load capacity of journal bearings, however without practical significance at temperature levels met in atmospheric conditions ($T_a < 310$ K). The critical mass of PJBs is affected in negligible proportions, while HGJBs can experience a significantly reduced critical mass at particular compressibility numbers, with a reported reduction up to 25% in realistic atmospheric temperatures. In consequence, an equivalent margin is suggested on the critical mass to ensure a safe operation of HGJBs designed from the non-condensable Reynolds equation.
- In realistic situations, the presence of liquid droplets in the bearing clearance is unlikely to be a threat to the integrity of the system due to the very small void fraction calculated in worst-case scenarii.

Bibliography

[1] D. Zhao, B. Blunier, F. Gao, M. Dou, A. Miraoui, Control of an Ultrahigh-Speed Centrifugal Compressor for the Air Management of Fuel Cell Systems, IEEE Transactions on Industry Applications 50 (3) (2014) 2225–2234. `doi:10.1109/TIA.2013.2282838`.

[2] Y. Wan, J. Guan, S. Xu, Improved empirical parameters design method for centrifugal compressor in PEM fuel cell vehicle application, International Journal of Hydrogen Energy 42 (8) (2017) 5590–5605. `doi:10.1016/j.ijhydene.2016.08.162`.

[3] S. Burgmann, T. Fischer, M. Rudersdorf, A. Roos, A. Heinzel, J. Seume, Development of a centrifugal fan with increased part-load efficiency for fuel cell applications, Renewable Energy 116 (2018) 815–826. `doi:10.1016/j.renene.2017.09.075`.

[4] B. Strom, Shuyu Zhang, Sung Chang Lee, A. Khurshudov, G. Tyndall, Effects of Humid Air on Air-Bearing Flying Height, IEEE Transactions on Magnetics 43 (7) (2007) 3301–3304. `doi:10.1109/TMAG.2007.897085`.

[5] S. Zhang, B. Strom, S.-C. Lee, G. Tyndall, Simulating the Air Bearing Pressure and Flying Height in a Humid Environment, Journal of Tribology 130 (1) (2008) 011008. `doi:10.1115/1.2805424`.

[6] W. Hua, W. Zhou, B. Liu, S. Yu, C. H. Wong, Effect of environment humidity and temperature on stationary and transient flying responses of air bearing slider, Tribology International 42 (8) (2009) 1125–1131. `doi:10.1016/j.triboint.2008.09.010`.

[7] S. Kirpekar, O. Ruiz, Computing the performance of an air bearing in humid conditions, Applied Physics Letters 94 (23) (2009) 234103. `doi:10.1063/1.3139757`.

[8] Y. Ma, B. Liu, Contribution of water vapor to slider air-bearing pressure in hard disk drives, Applied Physics Letters 90 (22) (2007) 223502. `doi:10.1063/1.2743745`.

[9] Y. Ma, B. Liu, Further Study of the Effect of Water Vapor on Slider Air Bearing, IEEE Transactions on Magnetics 45 (11) (2009) 5006–5009. `doi:10.1109/TMAG.2009.2029421`.

[10] Y. Aoki, K. Takahashi, J. Li, J. Xu, Y. Ooeda, Humidity effect on head-disk clearance, Microsystem Technologies 17 (5-7) (2011) 1051–1056. `doi:10.1007/s00542-011-1291-1`.

[11] J. Choi, N.-C. Park, Y.-P. Park, K.-S. Park, E.-J. Hong, Y. Lee, C.-S. Kim, Analysis of Thermal Flying-Height Control System About Humid Air Condition in Hard Disk Drive, in: ASME 2014 Conference on Information Storage and Processing Systems, 2014, p. V001T01A015. `doi:10.1115/ISPS2014-6958`.

[12] H. Tani, J. Tomita, S. Koganezawa, N. Tagawa, Effect of Vapor Lubrication on Head–Disk Clearance and Slider Wear in Inert Gas Environments, in: ASME 2014 Conference on Information Storage and Processing Systems, 2014, p. V001T01A007. `doi:10.1115/ISPS2014-6931`.

[13] Y. S. Ma, W. D. Zhou, S. K. Yu, W. Hua, Adsorbed Water Film and Heat Conduction from Disk to Slider in Heat-Assisted Magnetic Recording, Tribology Letters 56 (1) (2014) 93–99. `doi:10.1007/s11249-014-0388-y`.

[14] L. M. Matthes, R. Brunner, B. Knigge, F. E. Talke, Head Wear of Thermal Flying Height Control Sliders as a Function of Bonded Lubricant Ratio, Temperature, and Relative Humidity, Tribology Letters 60 (3) (2015) 39. `doi:10.1007/s11249-015-0614-2`.

[15] L. M. Matthes, F. E. Spada, A. Ovcharenko, B. E. Knigge, F. E. Talke, Effect of Head–Disk Interface Biasing and Relative Humidity on Wear of Thermal Flying Height Control Sliders, Tribology Letters 65 (2) (2017) 44. `doi:10.1007/s11249-017-0828-6`.

[16] I. H. Bell, J. Wronski, S. Quoilin, V. Lemort, Pure and Pseudo-pure Fluid Thermophysical Property Evaluation and the Open-Source Thermophysical Property Library CoolProp, Industrial & Engineering Chemistry Research 53 (6) (2014) 2498–2508. `doi:10.1021/ie4033999`.

[17] P. Tsilingiris, Thermophysical and transport properties of humid air at temperature range between 0 and 100C, Energy Conversion and Management 49 (5) (2008) 1098–1110. `doi:10.1016/j.enconman.2007.09.015`.

[18] D. P. Fleming, B. J. Hamrock, Optimization of self-acting herringbone journal bearing for maximum stability, in: Proceedings of the fifth international gas bearing symposium, 1974.

3.3 Thin film gas condensation in gas bearings

Parts of the material presented in this section has been published in the following journal article:

Guenat, E., Schiffmann, J., 2019. Isothermal gas condensation in thin film lubrication, Journal of Tribology 141 (11), . DOI:10.1115/1.4044447

3.3.1 Introduction

Process gas-lubricated bearings for energy applications (mostly for heat pumping [1] and waste heat recovery application [2; 3]), typically involve high pressure lubricants. On top of the real-gas effects associated with high pressure (and therefore dense) gases, a phase change can theoretically occur inside a lubricating gas film, as the compression in a gas bearing happens nearly isothermally. If the ambient conditions around the bearing are already in the vicinity of the saturation curve, the gas film may locally reach the saturation conditions, as schematically represented in Figure 3.54. Schiffmann [4] operated a HGJB-supported turbocompressor in R134a at an ambient pressure of 550 kPa and 34 °C in vicinity of the bearings, resulting on a margin factor of only 1.56 on the pressure. Moreover, the efficiency of heat pumps is generally improved when the superheat at the compressor inlet is minimized, therefore advocating for gas bearings operating very close to the saturation curve already at ambient conditions.

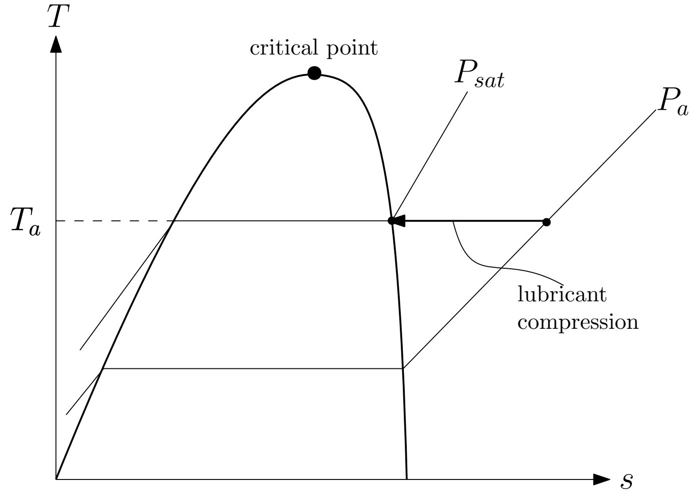

Figure 3.54 – Schematic representation in a temperature-entropy diagram of an isothermal compression starting from ambient pressure P_a to the saturation pressure P_{sat} corresponding to the ambient temperature T_a

Experimental hints of such condensation were reported at the dawn of the gas bearing "golden age" [5–7] in externally-pressurized steam bearings. Elwell [5] observed traces of liquid droplet in an aerodynamic journal bearing lubricated with humid air and suggested they are the result of moisture condensation due to the isothermal condensation in the gas film. Siegler and Zwick [8], in the context of metal vapor lubricated thrust bearings, discussed that the saturation pressure of lubricant might limit the maximum pressure in the gas film. Orcutt investigated the effect of pressure and temperature of aerostatic steam-lubricated thrust [6] and journal [7] bearings, concluding that feeding the bearing with saturated steam was affecting negatively both the static (load capacity) and dynamic (pneumatic hammer stability) of the bearings. Unterberg and Ausman [9] developed a model for saturated vapor lubrication based on the Reynolds equation with condensation. They realized that the Poiseuille flow term must vanish under the condition of isothermal compression when condensation occurs and solved the Reynolds equation for an infinitely long journal bearing. The introduced mathematical treatment of the Couette flow term alone in the saturated zone is, however, not physically justified, as the authors neglected the transition of the Reynolds equation from an elliptical to a hyperbolic form but assumed an elliptic nature of the equation. In the mean time, the similar problem in liquid-lubricated bearings, cavitation, benefited from an significant development handling effectively the transition between the single-phase (elliptical) and two-phase (hyperbolic) domain of a fluid film. The treatment of the boundary conditions between the two domain received a particular attention. The Jakobson-Floberg-Olsson (JFO) theory [10; 11] established a Reynolds-equation based model respecting the continuity across the boundaries of the two-phase domain. It is, however, not convenient to solve numerically, since the two zones are treated separately and the two-phase zone is *a priori* unknown. Elrod [12] developed an algorithm based on finite difference able to to treat as one equation both the single and two phase zones, predicting the onset and reformation of the cavitation zone successfully. Vijayaraghavan [13; 14] further improved the numerical treatment of Elrod's algorithm and studied the analogy of the two-phase isothermal Reynolds equation with non-viscous trans-sonic flows [15]. Despite the developments in cavitation modelling, this significant progress were not transposed to the issue of condensation in gas bearings. Zuber and Dougherty [16] proposed a form of Reynolds equation for non-equilibrium condensing vapors, with source and sink terms in the lubricant film to account for the difference of density between the two phases. The equation requires nucleation models for these non-equilibrium terms, which were not investigated by the authors. Recent works have investigated two-phase flows in seal [Arauz and San Andres], but the applications, involving strong axial flows in journal bearing, turbulence, liquid-dominated flows and very large clearances, depart form the cases of high-speed gas bearings, which usually deal with gas-dominated, laminar flows in fluid films a couple of micrometers thick, where no simple physical model is available in the literature.

The present section aims to 1) introduce an version of Elrod's algorithm with Vijayaraghavan's numerical treatment adapted to condensing gas bearings under isothermal conditions, 2) theoretically study the condensation effects on one-dimensional gas slider bearing layouts and 3) validate the model predictions with data from an original test apparatus.

Elrod's [12] and Vijayaraghavan's [13] work is adapted for thin gas film lubrication in saturation conditions in 1D. A finite difference method is employed to numerically solve the modified Reynolds equation for three 1D slider bearings layouts. Effects of condensation on the pressure and density fields of these gas bearings are studied in a large range of saturation density ratios and compressibility numbers. Investigation also covers the effects of condensation on the static performance of the gas bearing geometries in term of load capacity. A test apparatus is introduced for the measurement of the pressure in the lubricant film in a Rayleigh step journal bearing, lubricated with a synthetic working fluid: R245fa. The predictions of the gas condensation model are confronted to the in-situ pressure measurements.

3.3.2 Theory

The implementation of thin film gas condensation begins with the steady-state, non-dimensional form of the Reynolds equation in 1D, neglecting the Poiseuille term in the direction perpendicular to the bearing motion, under the isothermal assumption:

$$-\partial_{\bar{x}}\left(\bar{\beta}\bar{h}^3\partial_{\bar{x}}\bar{\rho}\right)+\Lambda\partial_{\bar{x}}\left(\bar{\rho}\bar{h}\right)=0 \qquad 3.58$$

with the non-dimensionalization as follows:

$$\bar{\rho}=\rho/\rho_a \quad \bar{\beta}=\beta/P_a=\rho\partial_\rho P/P_a \quad \bar{x}=x/L \quad \bar{h}=h/h_0 \quad \Lambda=\frac{6\mu UL}{P_a h_0^2} \qquad 3.59$$

where β relates to the bulk modulus defined as $\beta=\rho\partial_\rho P$. A switch function g, introduced by Elrod to ease numerical treatment [12], is used to express in the Poiseuille flow term such that:

$$g=\begin{cases}1, & \bar{\rho}<\bar{\rho}_{sat}\\ 0, & \bar{\rho}\geq\bar{\rho}_{sat}\end{cases} \qquad 3.60$$

$$-\partial_{\bar{x}}\left(g\bar{\beta}\bar{h}^3\partial_{\bar{x}}\bar{\rho}\right)+\Lambda\partial_{\bar{x}}\left(\bar{\rho}\bar{h}\right)=0 \qquad 3.61$$

Formally and under the isothermal assumption, β reduces to 0 under saturation conditions, since P is limited to its temperature related saturation value. The assumption of instantaneous thermodynamic equilibrium is supported a study of the nucleation rate presented in Appendix F. However, numerical convenience pushes to keep β non-zero holding the ideal gas assumption and to update the local value of g to zero. Under the ideal-gas assumption, $\bar{\beta}$ and $\overline{P}$ respectively become:

$$\bar{\beta} = \frac{\rho \partial_\rho P}{P_a} = \frac{\rho r T_a}{P_a} = \overline{P} \tag{3.62}$$

$$\overline{P} = \begin{cases} \bar{\rho}, & \bar{\rho} < \bar{\rho}_{sat} \\ \bar{\rho}_{sat}, & \bar{\rho} \geq \bar{\rho}_{sat} \end{cases} \tag{3.63}$$

In the two-phase domain, the Poiseuille flow terms vanish to leave only the Couette flow term of Eq. 3.58:

$$\partial_{\bar{x}}(\bar{\rho}\bar{h}) = 0 \quad \text{Therefore} \quad \bar{\rho}\bar{h} = cst \tag{3.64}$$

The effect of condensation on the Poiseuille term switches the form Reynolds equation from elliptic to hyperbolic [15]. In consequence, transmission of information in the two-phase film is strictly downstream, in analogy to trans-sonic flows, until the film exits the two-phase domain. This change of form is numerically represented in the Couette term using the switch function g. Following the method of Vijayaraghavan [13], the Couette term is discretized in such a way that it exhibits an upwind finite difference scheme in the two-phase domain and a central finite difference scheme in the single phase domain:

$$\partial_{\bar{x}}(\bar{\rho}\bar{h}) \approx \frac{a\bar{\rho}_{i+1}\bar{h}_{i+1} + b\bar{\rho}_i\bar{h}_i + c\bar{\rho}_{i-1}\bar{h}_{i-1}}{2\Delta\bar{x}} \tag{3.65}$$

With

$$a = \frac{g_{i+1} + g_i}{2} \quad b = 2 - \frac{g_{i+1} + 2g_i + g_{i-1}}{2} \quad c = -\left(2 - \frac{g_i - g_{i-1}}{2}\right) \tag{3.66}$$

In the case where a point and both its neighbours ($i-1$,i,$i+1$) are non-saturated, then $a = 1$, $b = 0$ and $c = -1$, leading to a central difference scheme. In the opposite case where the three points are in saturated conditions, then $a = 0$, $b = 2$ and $c = -2$, resulting to an upwind difference scheme for the Couette term.

Following Vijayaraghavan [13], the Poiseuille term can be rewritten as follows for numerical convenience:

$$g\frac{\partial \bar{\rho}}{\partial \bar{x}} = \frac{\partial[g(\bar{\rho} - \rho_{sat}/\rho_a)]}{\partial \bar{x}} - (\bar{\rho} - \rho_{sat}/\rho_a)\frac{\partial g}{\partial \bar{x}} = \frac{\partial[g(\bar{\rho} - \rho_{sat}/\rho_a)]}{\partial \bar{x}} \tag{3.67}$$

This treatment is possible because the spatial derivative of g is equal to zero everywhere, except on the boundary of the two-phase domain, where $\rho = \rho_{sat}$.

Therefore, the Poiseuille term can be numerically approximated as follows:

$$\begin{aligned}-\partial_{\bar{x}}\left(\bar{\beta}\bar{h}^3 g\partial_{\bar{x}}\bar{\rho}\right) =& -\partial_{\bar{x}}\left(\bar{\beta}\bar{h}^3\partial_{\bar{x}}\left(g(\bar{\rho}-\rho_{sat}/\rho_a)\right)\right)\\ =&\frac{-1}{\Delta\bar{x}}\Big(\bar{\beta}_{i+1/2}\bar{h}^3_{i+1/2}g_{i+1}(\bar{\rho}_{i+1}-\rho_{sat}/\rho_a)\\ &-(\bar{\beta}_{i+1/2}\bar{h}^3_{i+1/2}+\bar{\beta}_{i-1/2}\bar{h}^3_{i-1/2})g_i(\bar{\rho}_i-\rho_{sat}/\rho_a)\\ &+\bar{\beta}_{i-1/2}\bar{h}^3_{i-1/2}g_{i-1}(\bar{\rho}_{i-1}-\rho_{sat}/\rho_a)\Big)\end{aligned} \quad 3.68$$

The system of equation resulting from the discretization of Eq.3.61 is expressed in the matricial form and solved according to equations 2.59 to 2.63.

3.3.3 Numerical computations and results

The numerical model is employed to simulate different geometries of infinitely wide slider bearings as shown in Fig 3.55: A parabolic bearing (Case A), a Rayleigh-step bearing (Case B) and a wedge bearing (Case C). For all three configurations, the ratio of largest and smallest film height is 2. The boundary conditions of Eq. 3.61 are :

$$\bar{\rho} = 1 \text{ at } \bar{x} = 0 \text{ and } \bar{x} = 1 \quad 3.69$$

The film height for the three bearing configurations is expressed as follows:

$$\bar{h} = 4\bar{x}^2 - 4\bar{x} + 2 \qquad \text{Case A} \qquad 3.70$$

$$\bar{h} = \begin{cases} 2, & \bar{x} < 0.5 \\ 1, & \bar{x} \geq 0.5 \end{cases} \qquad \text{Case B} \qquad 3.71$$

$$\bar{h} = 2 - \bar{x} \qquad \text{Case C} \qquad 3.72$$

The lubrication model for a condensable lubricant is applied for a given saturation density $\bar{\rho}_{sat}$ and for different compressibility numbers Λ in order to investigate the effects of condensation on the density and pressure fields. First, the saturation density $\bar{\rho}_{sat}$ is varied while keeping a constant compressibility number $\Lambda = 20$ (Fig 3.56, 3.58 and 3.60). Λ is then varied at constant saturation density $\bar{\rho}_{sat}$ (Fig 3.57, 3.59 and 3.61). The bearing domain is discretized in 330 points, which achieves excellent grid convergence.

In all investigated cases, the density and pressure lines merge in the single phase domain because of the ideal gas assumption ($\overline{P} = \bar{\rho}$). However, they diverge in the two-phase domain, where the density is governed by the equation $\partial_{\bar{x}}(\bar{\rho}\bar{h}) = 0$ and the pressure is limited to the saturation pressure associated with the ambient temperature. The density increases by forming liquid in the fluid film, therefore lowering its vapor quality. A sharp density drop suddenly occurs in the second half bearing domain down to the saturation

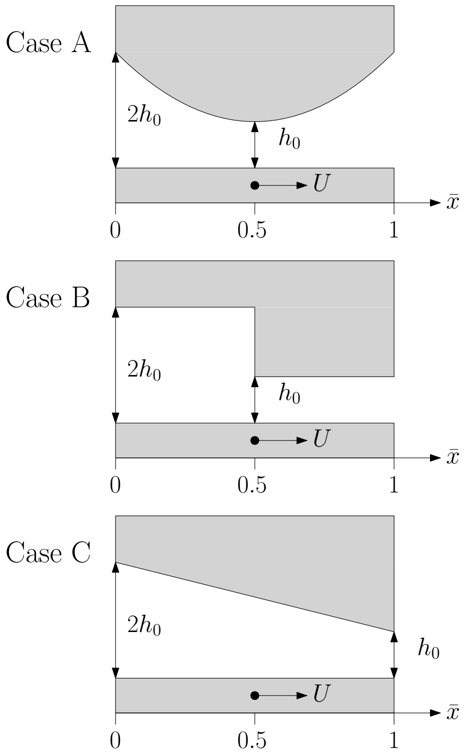
Case A
$2h_0$
h_0
U
$\bar{x}$
0
0.5
1
Case B
$2h_0$
h_0
U
$\bar{x}$
0
0.5
1
Case C
$2h_0$
h_0
U
$\bar{x}$
0
0.5
1

Figure 3.55 – Description of the three evaluated 1D bearing geometries: Parabolic, Rayleigh step and wedge

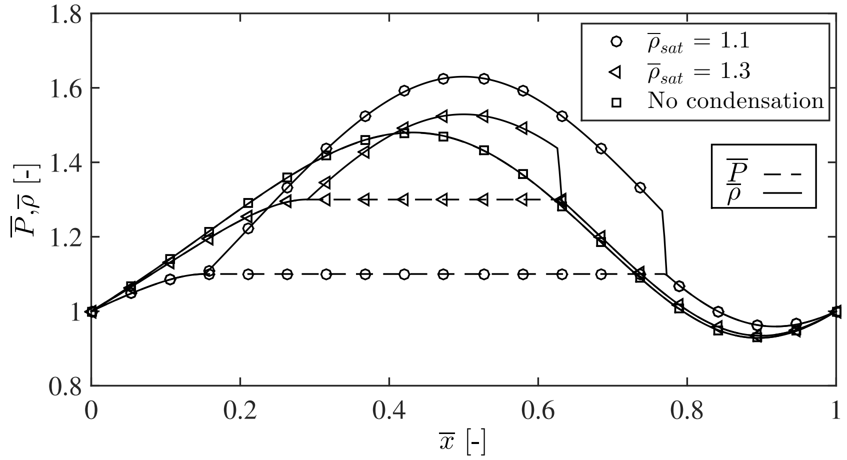

Figure 3.56 – Pressure and density profiles in Case A for different saturation densities at $\Lambda = 20$

level, ending the two-phase zone.

In cases A and C, the Poiseuille flow must vanish in the single phase zone just prior to reaching saturation in order to respect the mass continuity. As a result, the condition $\partial_{\bar{x}}\overline{\rho} = 0$ is met upstream of the condensing zone. Interestingly, the saturation conditions

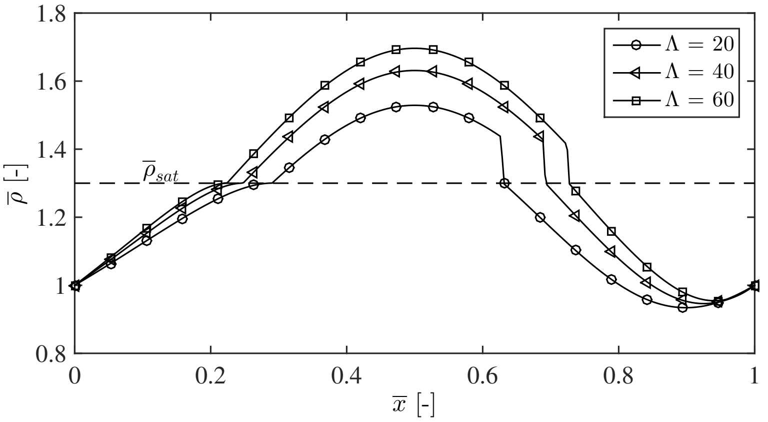

Figure 3.57 – Density profiles in Case A for different compressibility numbers and $\bar{\rho}_{sat} = 1.3$

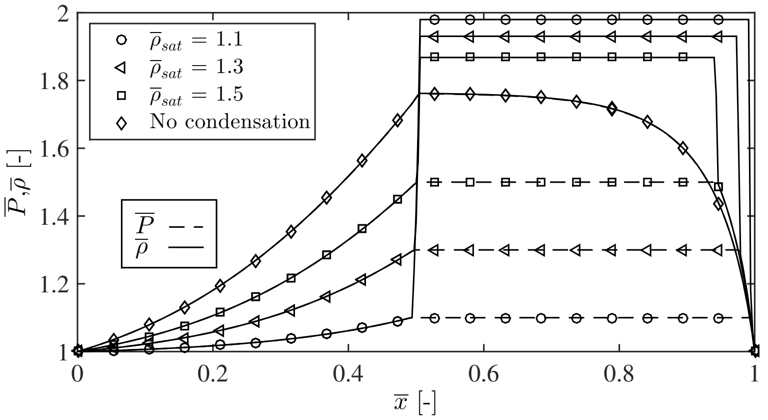

Figure 3.58 – Pressure and density profiles in Case B for different saturation densities and $\Lambda = 20$

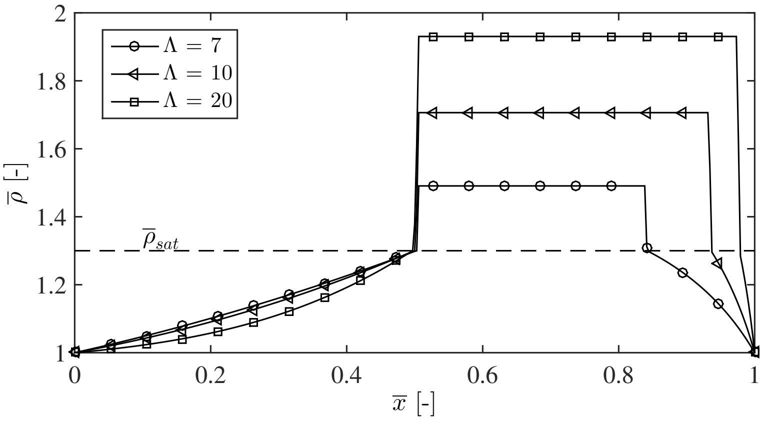

Figure 3.59 – Density profiles in Case B for different compressibility numbers and $\bar{\rho}_{sat} = 1.3$

are always met at the position of the step in case B, independently of the compressibility number Λ and the saturation density $\bar{\rho}_{sat}$, as long as it is met in the density field. The

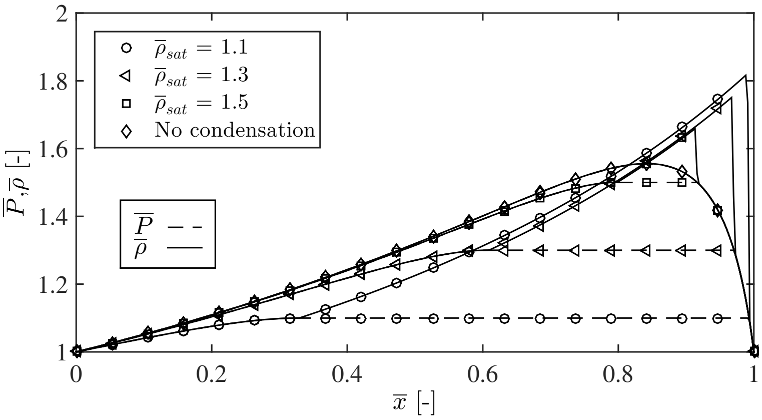

Figure 3.60 – Density profiles in Case C for different saturation densities and $\Lambda = 20$

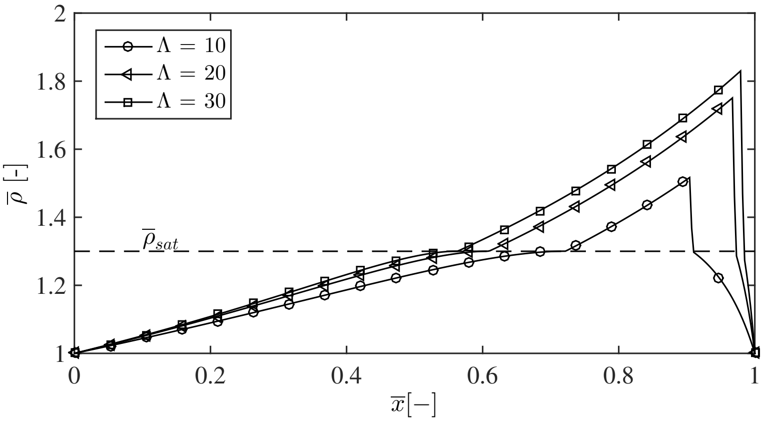

Figure 3.61 – Density profiles in Case C for different compressibility numbers and $\bar{\rho}_{sat} = 1.3$

pressure derivative is non-zero at the onset of two-phase flow because of the discontinuity in the clearance. However, compressibility number and saturation density influence the density in the two-phase zone and the point where the flow re-enters the single phase regime. A larger compressibility number as well as a smaller saturation density translate into a higher two-phase density and a postponed two-phase domain exit point.

The effect of decreasing $\overline{P}_{sat}$ on the pressure and density field of Case A is represented in Fig. 3.56. As the saturation pressure decreases, the effect of condensation of the upstream single-phase flow increases, locally reducing the slope in the profiles. The onset of condensation occurs closer to the leading edge, while the maximum density in the two-phase zone is larger when the saturation pressure is lower. The sharp decrease of density, happening in the second half of the bearing, is postponed toward the trailing edge as $\overline{\rho}_{sat}$ decreases. However, following Eq. 3.64, the location of the maximum density is independent of the saturation pressure and corresponds to the point of minimum clearance within the condensing zone. As far as Case A is concerned, an increase of compressibility number is qualitatively similar to a decrease of saturation pressure, as shown in Fig. 3.57.

Increasing Λ leads to a spatially extended two-phase domain as well as a higher maximum density at the point of smallest clearance. The amplitude of the density drop at the end of the two-phase domain is not significantly affected by the variation of compressibility number. Figure 3.58, representing the density and pressure fields of Case B for different saturation pressures, displays a different behavior. The saturation conditions are always met at the position of the step, independently of the saturation density $\overline{P}_{sat}$, as long as condensation is met in the density field. The discontinuity in the clearance allows the pressure derivative just upstream of the condensation onset to be non-zero, while respecting the mass flow conservation across the step. The density remains at a constant value in the two-phase domain, in accordance with Eq. 3.64. As the saturation pressure decreases, the density increases and the end of the saturated domain is shifted toward the trailing edge. The effect of compressibility number on the density field, shown in Fig. 3.59, are small upstream of the condensation onset, but significant downstream of it. Both the density plateau in saturation, the location of the density drop and the second single-phase domain depend significantly on the compressibility number. A higher value is associated with a larger density level in saturation and a postponed re-entry point in the single-phase regime, mechanically leading to a larger pressure between this point and the trailing edge of the bearing.

Since the maximum achievable pressure in the gas film is limited by the saturation pressure due to the local occurrence of condensation can affect significantly the load carrying capacity of the bearing can be affected significantly. It is calculated as follows:

$$\overline{W} = \int_0^1 \overline{P} - 1 \mathrm{d}\bar{x} \tag{3.73}$$

In order to quantitatively assess the condensation effect on the load capacity, the following metric is defined:

$$W_r = \frac{\overline{W}_{cond}}{\overline{W}_{non-cond}} \tag{3.74}$$

The load capacity ratio W_r is shown for different saturation densities against the compressibility number Λ in Figures 3.62 to 3.64 for cases A, B and C respectively. The load capacity can be reduced down to 10% of its single-phase value for the Rayleigh step bearing (case B) at a relative saturation density of 1.1 and $\Lambda > 40$. As the effects of condensation on load capacity are generally negative, the load capacity can be slightly increased at low relative saturation densities and low compressibility numbers and for cases A and B, with a maximum computed value 6% higher than the single phase performance. This is induced by a local increase in pressure downstream of the onset of condensation in the bearing, as represented in Figure 3.65 for case B at $\Lambda = 2$.

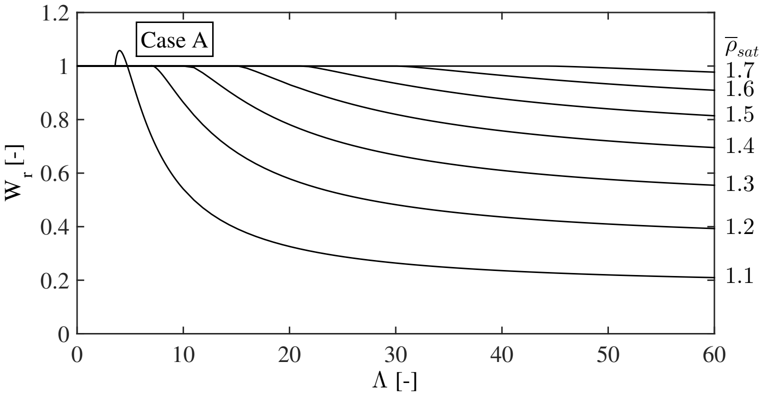

Figure 3.62 – Load capacity ratio in Case A for different saturation densities

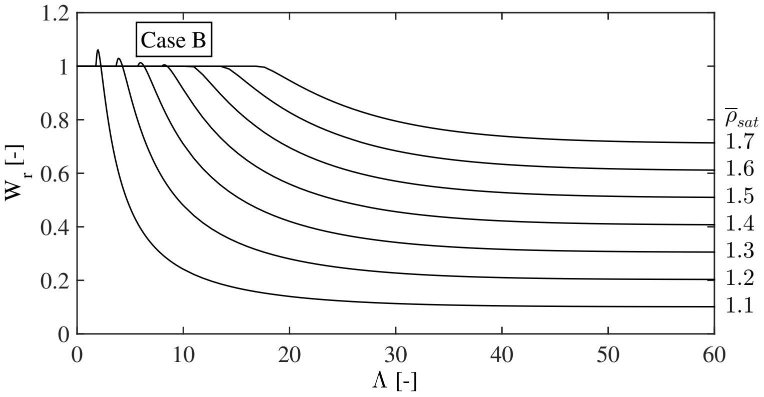

Figure 3.63 – Load capacity ratio in Case B for different saturation densities

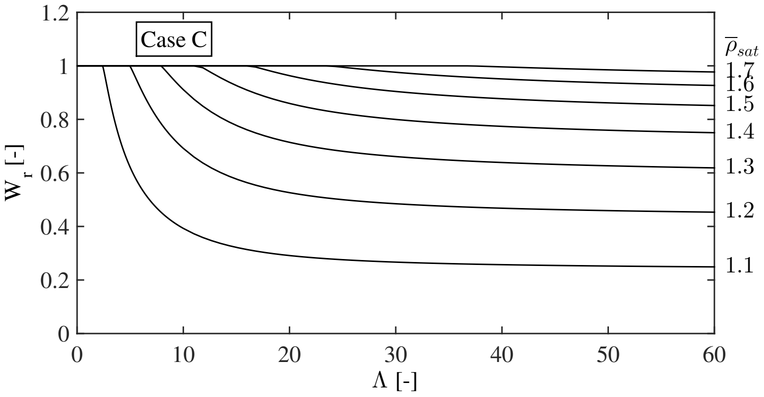

Figure 3.64 – Load capacity ratio in Case C for different saturation densities

3.3.4 Experimental validation

3.3.4.1 Experimental setup

A possibility to assess the theory developped above is to measure the pressure inside a gas bearing and highlight signatures of condensation in the measurements, such as the

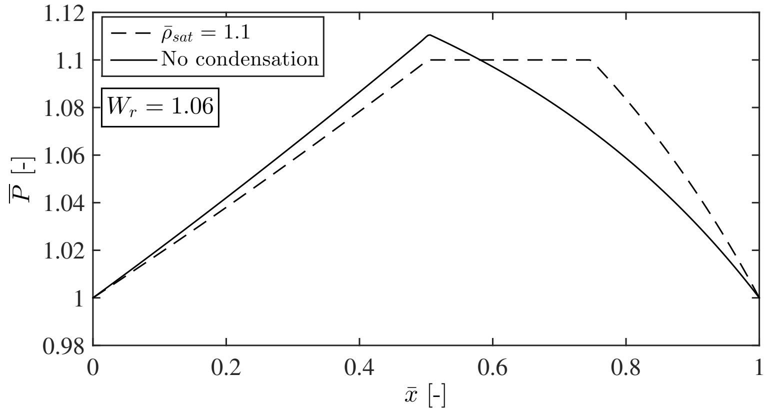

Figure 3.65 – Local increase in the pressure profile leading to a net gain in load capacity. Case B, $\Lambda = 2$

anomaly of pressure evolution when condensation occurs. A journal bearing with one or several axial grooves establishing ambient pressure is suitable to simulate the behavior of slider bearings since each segment of the bearing is independent of the others. Any of the three investigated geometries can be implemented in a journal bearing by repeating the slider bearing circumferentially.

A pressure chamber offering a volume of ID300x700 is used to contain the test bearing in a condensable atmosphere. Because of the uncertainty regarding the pressure capabilities of the chamber, a gas with an evaporation point close to 300 K is necessary, keeping the inner pressure close to 1 bar, yet with a positive pressure difference with the atmospheric conditions to prevent pollution of the chamber in case of leakage. The working fluid R245fa meets these requirements while being readily available on the market. At 300 K, its saturation pressure is 160 kPa, as shown in Figure 3.66.

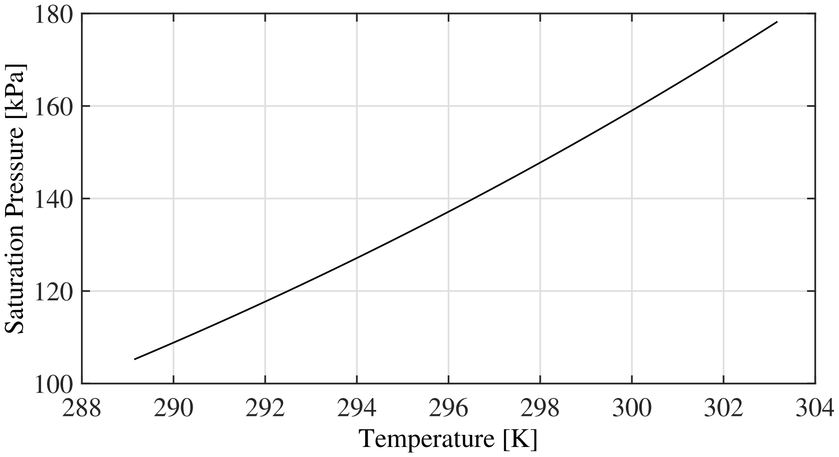

Figure 3.66 – Saturation pressure of R245fa

Because it can be manufactured easily and provides a large pressure build-up in the gas film, the Rayleigh step journal bearing is selected to equip the journal bearing. A number of three independent steps over the circumference is a good trade-off between stability and angular span of a pocket, which must allow a in-situ pressure measurement of several locations. In order to keep the manufacturing costs low, the rotor-bearing system must be kept as compact and simple as possible. The design converges therefore toward a very short steel rotor whose entire circumferential surface is gas lubricated, meaning that the gas bearing is of the same length as the rotor itself. This design is directly inspired from Kingbury's experiment [17], who first investigated a gas lubricated bearing in 1897 in the form of a ⌀152 mm 22.9 kg plain bearing driven by hand or by a hand drill (Figure 3.67). 5 pressure taps disposed axially allowed to measure the pressure inside the gas film. In the present experiment, a high speed DC motor drives the rotor via a coupling made of a flexible hose and a o-ring, inserted inside a bore in the rotor centre. A diameter of 20 mm is chosen, together with a length-diameter ratio of 1, in order to keep the losses low while ensuring a sufficient tilt stiffness to the bearing. The diameter allows to have 5 measurement taps distributed along one of the three steps in the circumferential direction.

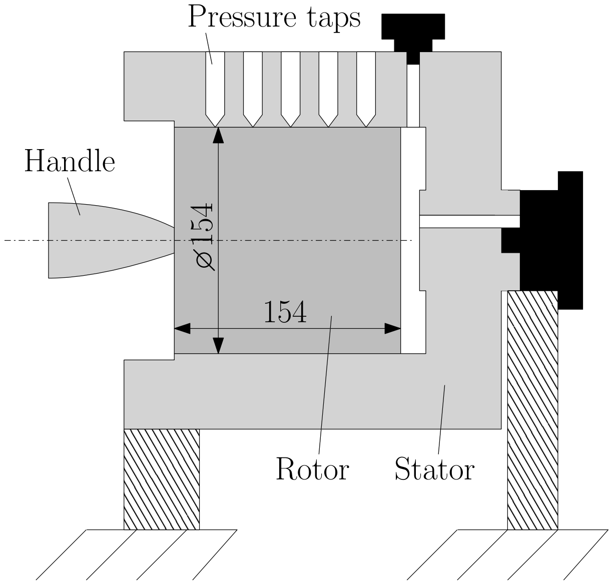

Figure 3.67 – Cut-view of Kingburry's gas bearing apparatus presented in 1897

Unlike the 1D bearing studied previously, the change in clearance is not placed at the mid-span of the pocket but at 26% of the active length in order to increase the pressure build-up in the gas film and allow to position multiple pressure taps in the region after the step, where the pressure anomalies are expected to occur. The electric motor is chosen to be robust against special atmosphere, to allow high speeds an to provide a sufficient torque. The Maxon Motors *EXC SPEED 13M*, rated at 74 krpm and suited for high-temperature steam sterilization, is chosen to drive the system. It provides a torque of 3.34 mNm at nominal speed. Nominal bearing clearance h_0 and step depth δ, defined on Figure 3.68 are determined studying simultaneously three metrics: 1) the maximum pressure, which has to be large in order to ease the apparition of saturation conditions, 2) the critical mass of the bearing, which has to be significantly above the mass of the rotor and 3) the viscous drag torque, which must lay below the capabilities of the drive. Using the same simulation procedure and perturbation method as described in Chapter 2, the static and dynamic performances of the Rayleigh step bearing are simulated. An example of computed static pressure field is presented in Figure 3.69, for 70 krpm, h_0 =6 µm and δ =10 µm. Figure 3.70 shows the maps of critical mass, maximum pressure ratio and drag torque for a speed of 70 krpm in R245fa. The mass of the rotor, made of steel, is estimated to be 0.050 kg. Because the rotor will be commissioned in atmospheric conditions, it has to run correctly in air as well, leading to the results in Figure 3.71. A clearance h_0 of 6 µm and a step depth δ of 10 µm allow a 10-fold margin on the critical mass and a large pressure ratio in refrigerant within the torque capabilities of the motor. However, because of the higher viscosity of air inducing a higher viscous torque, the maximum speed of the motor will not be reachable in atmospheric conditions.

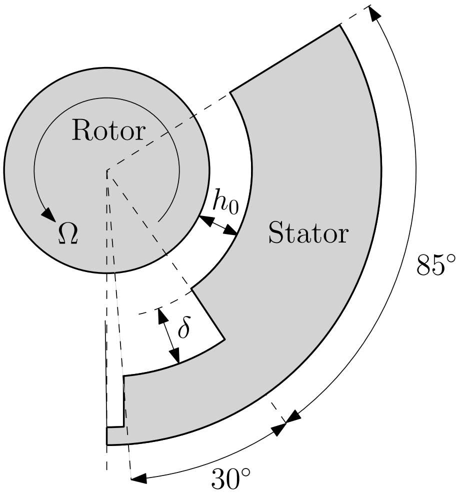

Figure 3.68 – Illustration of the geometry numerically simulated, with only one pocket represented

The bearing and the rotor are manufactured using lapping for the low-clearance zone and EDM-wiring for the steps. Nominal clearance and step depth are realized with an uncertainty of 0.3 µm and 1 µm respectively. A rough hole is first bored in the bearing center, together with the radial hole for the capillary tubes. Tungsten carbide capillaries are press-fitted before the inner diameter of the bearing is lapped to achieve the desired dimensions as well as a smooth interface between the capillaries and the bearing. A point of glue ensures the the air tightness of the assembly (Figure 3.72). Finally, the steps are manufactured on the inner surface with a 30 µm EDM-wiring process. Because the wire is significantly larger that the height of the desired step, the resulting shape is a truncated circle (Figure 3.73). However, this deviation should have little influence on the performance of the bearing, since the change of clearance occurs on a very short distance compared to the circumferential length of the pocket. The feed grooves, 1 mm deep and 5° wide, separate the pads by establishing $\overline{P} = 1$ between them. As displayed

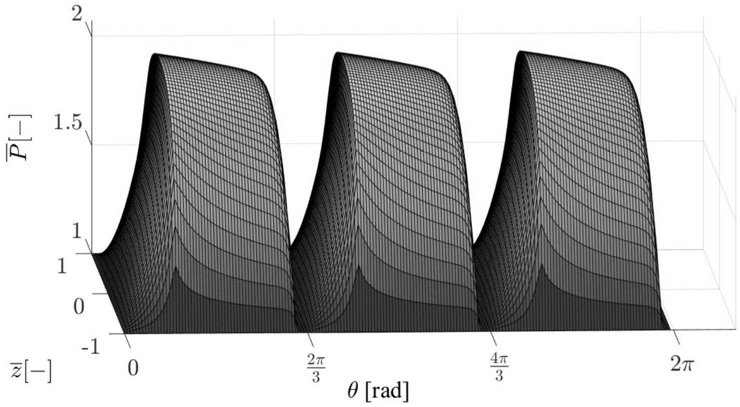

Figure 3.69 – Computed static pressure field of the Rayleigh step bearing for 70krpm, h_0 =6 µm and δ =10 µm, in air (1 bar, 305 K).

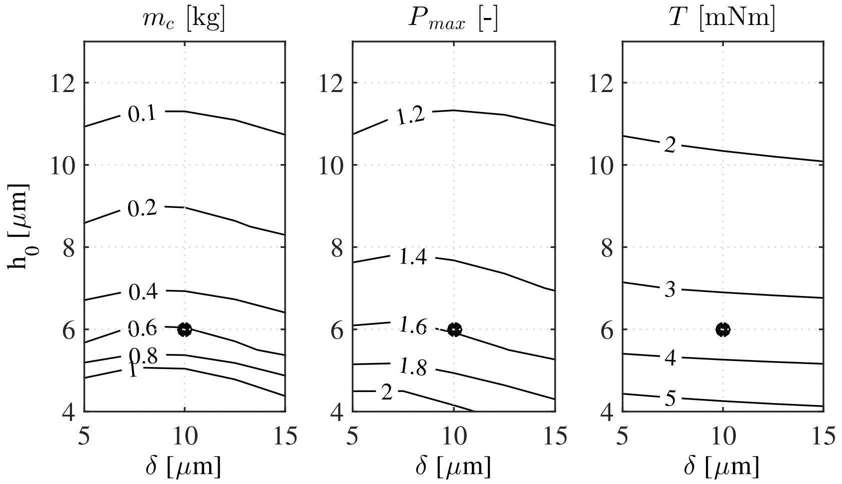

Figure 3.70 – Critical mass, maximum relative pressure and drag torque in R245fa (1.4 bar, 305 K) for different step depths and clearances. The dots indicate the selected nominal values of h_0 and δ

in Figure 3.75a, the taps are located at 17°, 37°, 57°, 77° and 97° following the same circumferential reference as Figure 3.75a. In order to capture the point of maximum pressure in the gas film, only 2° separate the location of the clearance restriction and the center of the second tap (Figure 3.74).

The inner diameter of the capillaries results from a trade-off between the diameter of the orifice and the settling time of the pressure in the volume between the capillary and the pressure transducer. To address this trade-off, the settling time is predicted using a simplified model of the situation. A dead cavity, of volume V and pressure P, is connected to the environment by a capillary of length L and diameter d (Figure 3.77). Following [18] and assuming that the pressure profile along the capillary is linear and that the conditions are isothermal, the differential equation establishing the pressure at

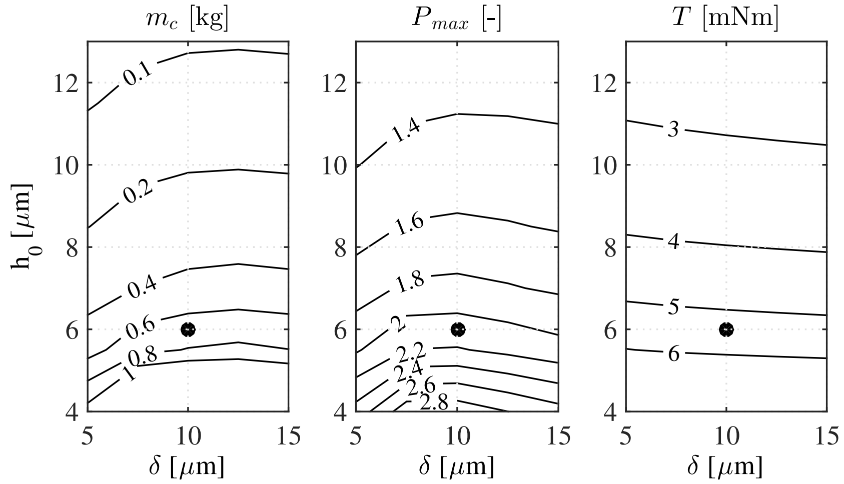

Figure 3.71 – Critical mass, maximum relative pressure and drag torque in air (1 bar, 305 K) for different step depths and clearances. The dots indicate the selected nominal values of h_0 and δ

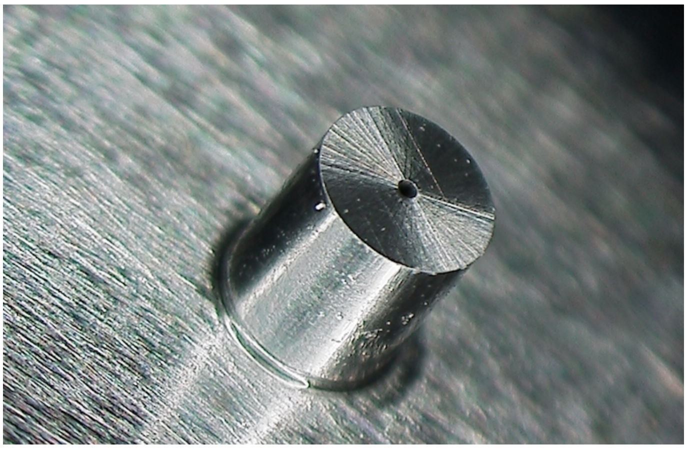

Figure 3.72 – Close-view on one of the pressure taps on the external surface of the bearing

the right end of the capillary is:

$$\left(\frac{\partial P}{\partial t}\right)_{z=1} = -\frac{\pi d^2 L}{8V}\left(\frac{\partial P^2}{\partial z}\right)_{z=1} \qquad 3.75$$

where d and L are the capillary diameter and length, respectively, and V is the cavity volume. Equation 3.75 is solved assuming 1 m of hose length, 2 mm inner diameter, with the following initial condition:

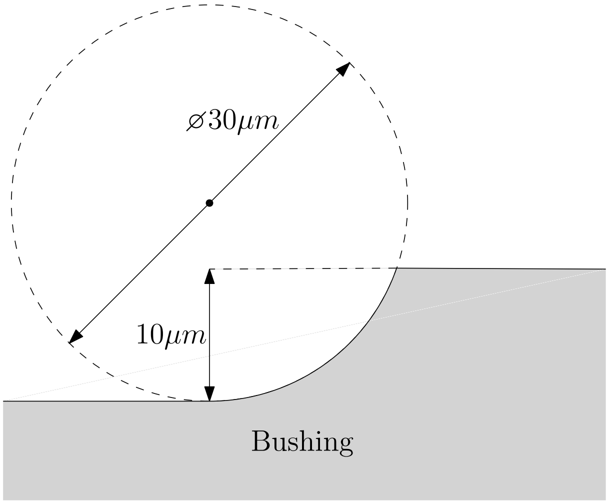

Figure 3.73 – Shape of the step resulting from the EDM process wire real-size wire diameter

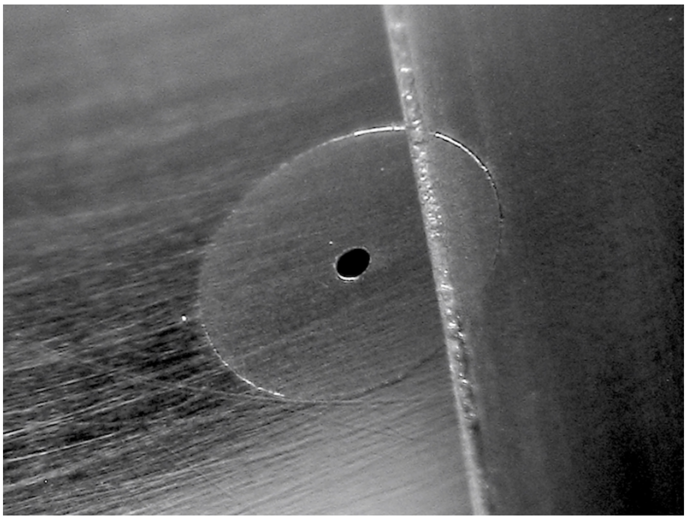

Figure 3.74 – Interface between the second pressure tap and the inner diameter of the bearing. The straight line is the delimitation of the step manufactured with EDM

$$P_0(t=0) = 2P_V(t=0) \tag{3.76}$$

Figure 3.78 shows the settling time ($P_V = 0.99 \cdot P_0$) of the cavity pressure against the capillary diameter. A hole diameter of 200 µm achieves a settling time of 0.23 s, equivalent to a cut-off frequency of approximately 5 Hz, which allows to have an effective low-pass filter while having a sufficient reactivity for practical uses. In reality, the environment is not an infinite reservoir of gas, but the gas thin film, which will itself provide a limitation

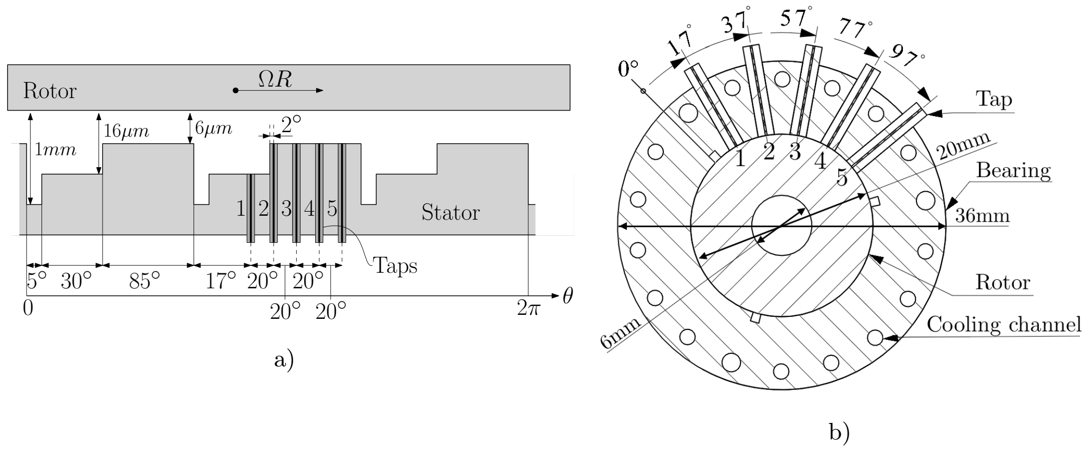
Rotor
ΩR
1mm
16μm
6μm
2°
1
2
3
4
5
Stator
Taps
5°
30°
85°
17°
20°
20°
0
20°
20°
2π
θ
a)
0°
17°
37°
57°
77°
97°
Tap
1
2
3
4
5
20mm
Bearing
36mm
Rotor
Cooling channel
6mm
b)

Figure 3.75 – Geometry of the Rayleigh step journal bearing in the circumferential direction (a) and Cut of the motor-rotor-bearing system perpendicular to the rotor axis (b)

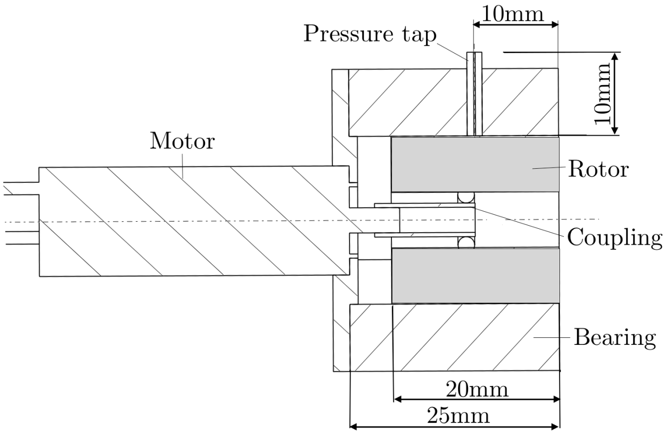
Pressure tap
10mm
10mm
Motor
Rotor
Coupling
Bearing
20mm
25mm

Figure 3.76 – Axial cut of the motor-rotor-bearing system: 1) Motor 2) Bearing 3) Rotor 4) Coupling 5) Pressure tap

on the supply in fluid to feed the capillary, resulting to a longer effective settling time than the one computed here.

The rotor is dynamically balanced on two planes with a residual imbalance less than 5 mg mm. The assembled rotor and bearing are shown in Figure 3.79. Drill marks resulting from the balancing process are visible on the axial surface of the rotor. The 5 pressure taps connected to the measurement tube are visible on the top of the bearing.

In order to suppress the effect of weight, a vertical position is chosen for the motor-rotor-bearing system (MRBS). A closed-loop cooling circuit circulates water in the bearing

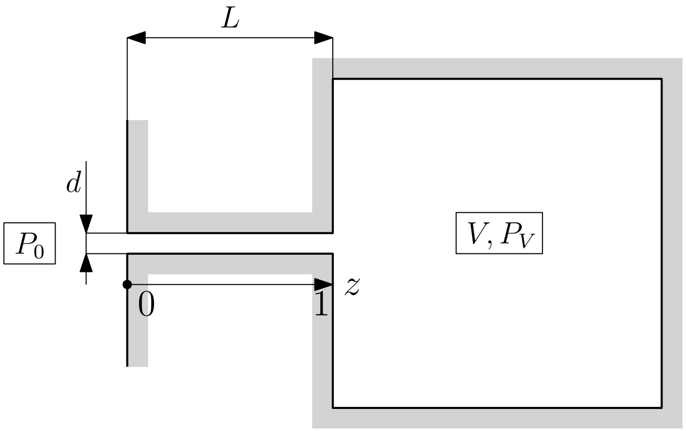

Figure 3.77 – Representation of the capillary system with gas reservoir

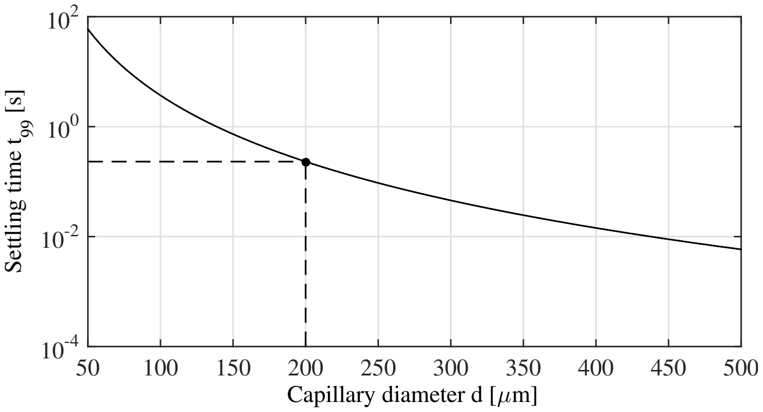

Figure 3.78 – Pressure settling time in the taps against capillary diameter. Dashed lines indicated the selected diameter and the corresponding settling time

axial cooling channels at a nearly constant mass flow rate. A 0.28 mm-diameter K-type thermocouple with a measurement uncertainty of ± 0.5 K is placed and glued in the feed groove before the instrumented pocket (Figure 3.82).

The temperature of the cooling reservoir is monitored using a high-precision reference PT100 thermometer with an uncertainty of ±0.01 K. The angular velocity is assessed using the back-electromotive force sensed by the motor controller. At the considered pressure levels, the pressure scanner has an uncertainty of ±0.002 bar on the 5 pressure taps and the pressure in the pressure chamber, measured via a sixth tube. Direct current fed coils heat the pressure measurement pipes in the chamber in order to prevent undesired condensation in the measurement pipes. A scheme and a picture of complete the test apparatus are shown in Figures 3.80 and 3.81 respectively.

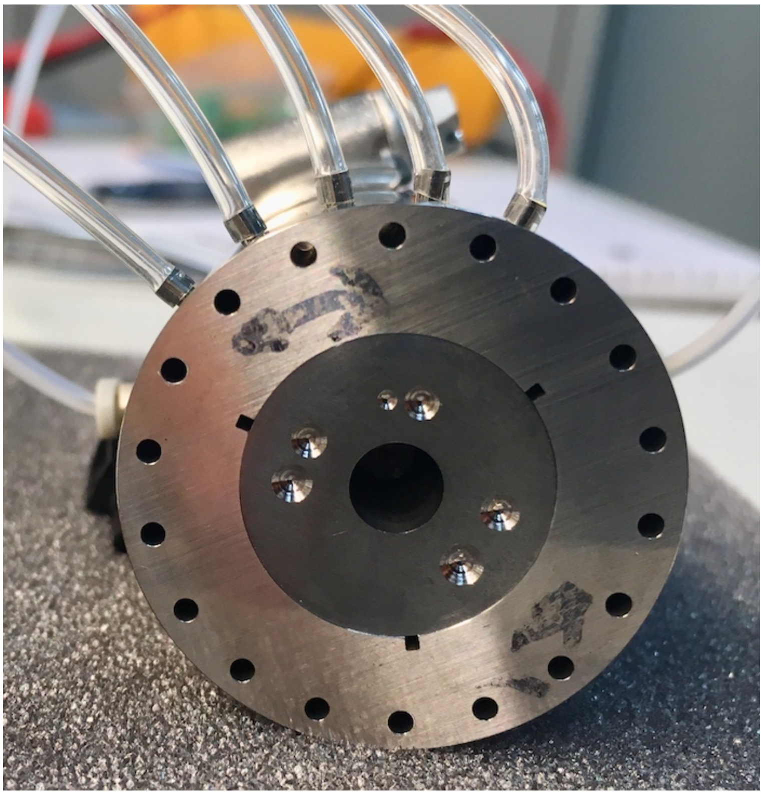

Figure 3.79 – Rotor-Bearing assembly, with marks of balancing visible

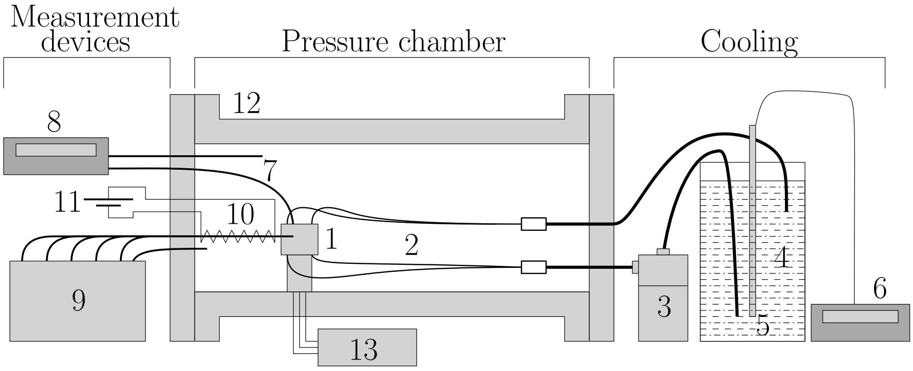

Figure 3.80 – Test apparatus: 1.MRBS 2.Cooling circuit 3.Circulation pump 4.Water reservoir 5.High-precision thermometer probe 6.Thermometer reader 7.Thermocouples 8.Thermocouple reader 9.Pressure scanner 10.Pressure pipe heater 11.DC source 12.Vessel 13.Motor drive

3.3.4.2 Test runs in air

The MRBS is assembled and tested in atmospheric conditions (air, $P_a = 0.965 \pm 0.01 bar$) up to 40 krpm in successive steps. Figure 3.83 presents the measurement of gauge pressure at the 5 pressure taps. Between the velocity steps, an acceleration of 2 krpm/s imposed

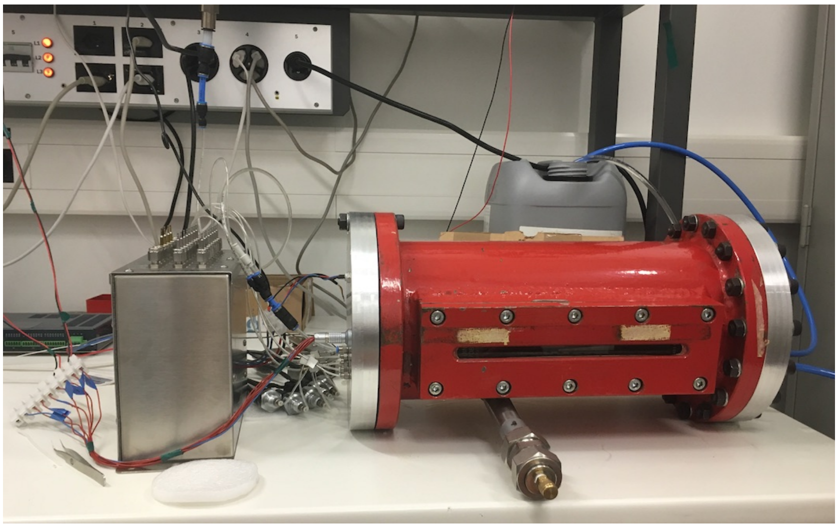

Figure 3.81 – The pressure chamber (red, right) and the pressure scanner (left) of the test apparatus. The cooling water reservoir is visible behind the tank

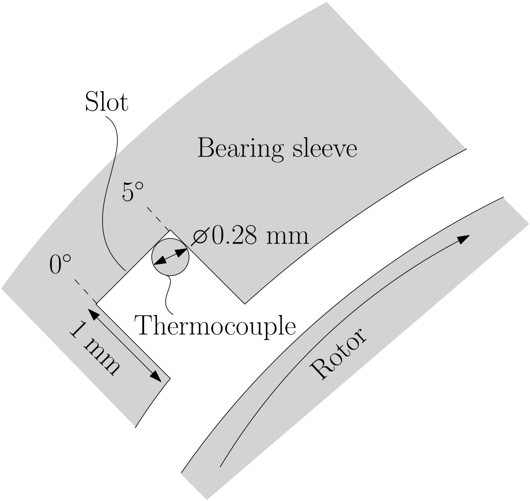

Figure 3.82 – Location of the bearing thermocouple

to the motor and a elapsed time of 100 s or more is waited for the pressure in the taps to reach their steady-state value before the next acceleration is started. The temperature in the bearing is recorded at the end of each step.

For validation purpose, the output of the simulation code used for the design of the MRBS is compared to the pressure measurements at different speeds (Figure 3.84). The predictions include the measurements uncertainty on the step depth and the nominal clearance of the bearing. The simulation code is in good agreement with the experimental data, as all measurement points fall in the predicted domain. As the speed increases, the contribution of the Couette term in the Reynolds equation becomes increasingly dominant over the Poiseuille terms. This allow the lubrication model with isothermal condensation, implemented in 1D (neglecting the Poiseuille term perpendicular to the velocity vector), to be used to predict effectively the pressure field, as visible in Figure 3.85. Although the trend in the predicted pressure field past the bearing step differs sensibly between the 1D and 2D models, all measurement points fall within the prediction of both tools. This can be considered as a validation of the code, as far as ideal non-condensable gas lubrication is concerned.

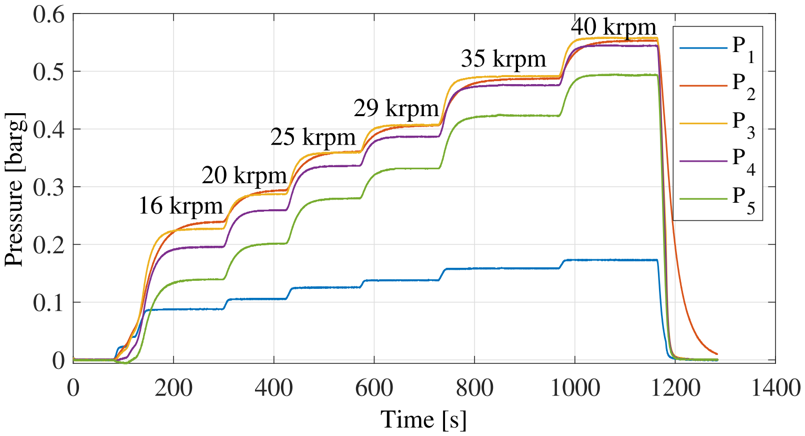

Figure 3.83 – Measured gauge pressure in time for different steps in speed toward 40 krpm

3.3.4.3 Test runs in R245fa

The next step consists in testing the MRBS in an atmosphere of R245fa far from the saturation conditions, such that the event of local condensation in the gas film can be neglected. The system is installed in the pressure chamber before sealing and vacuuming it down to a residual pressure of 80 Pa. Refrigerant is then released in the chamber up to a pressure of 96 kPa. The MRBS is accelerated up to 3.6 krpm and steadily kept at this speed for a few seconds before ramping up to 30 krpm, with an acceleration of 2 krpm/s. This regime is held a certain time before coasting down to rest. The active cooling of the bearing permits a low temperature increase over the run. The measured pressures at t=100 s are compared to the 1D model predictions in Figure 3.87, taking into account the uncertainty on the bearing clearance and step depth. The bearing temperature at this moment is 23.4 °C, which corresponds to a saturation pressure of 140 kPa, or a relative pressure of 1.46, which is here not reached in the gas film. As for air in nearly normal conditions, the predicted pressure values fall within the predicted domain.

In order to trigger condensation inside the bearing gas film, the following procedure is followed. The pressure of R245fa in the chamber is increased up to 118 kPa, which corresponds to a saturation temperature of 18.9 °C and the cooling circuit is started with an initial water tank temperature of 17 °C. The losses in the feed pump and natural

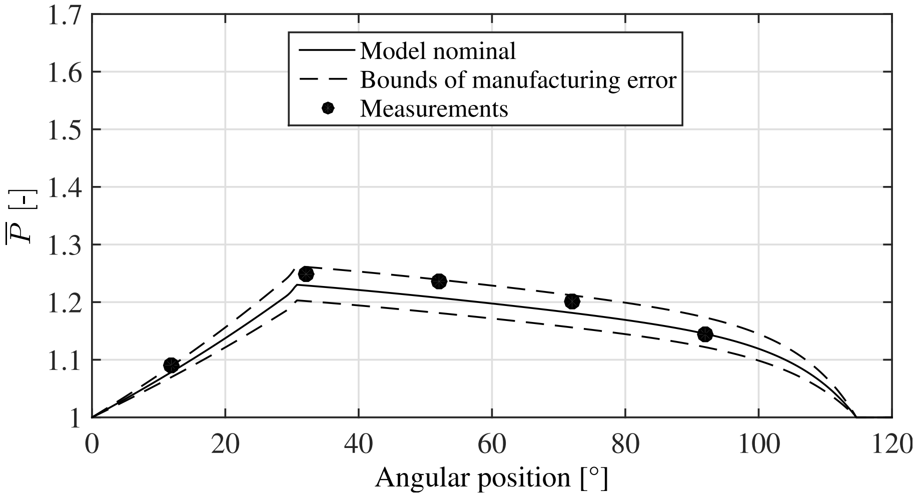

(a) 16 krpm

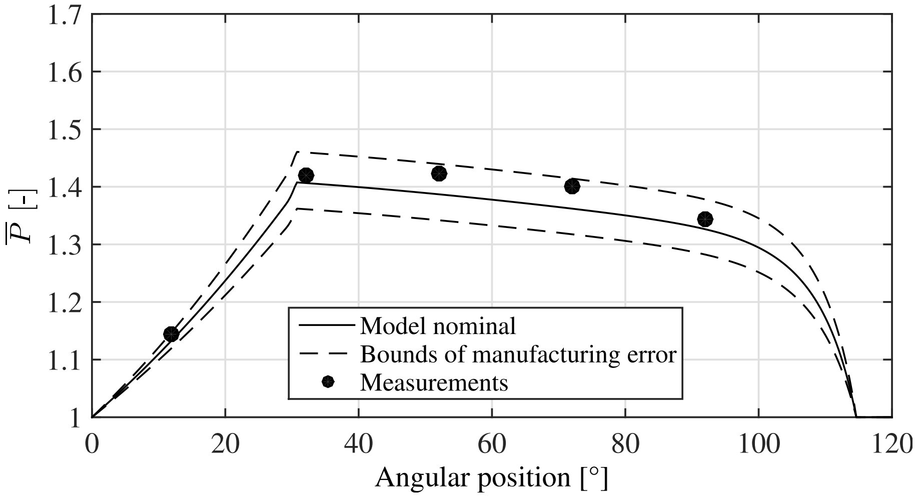

(b) 29 krpm

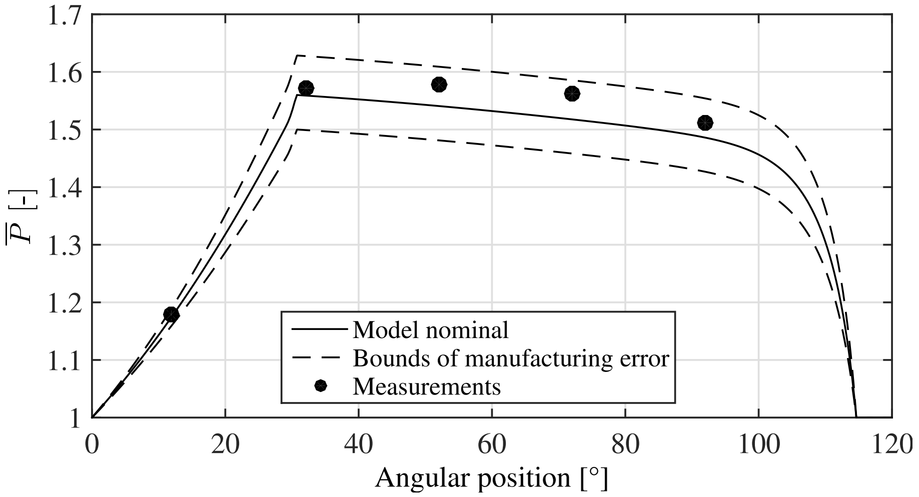

(c) 40 krpm

Figure 3.84 – Predicted and measured pressure fields in air at three different speeds. Bearing temperatures are 31.0, 34.2 and 42.1 °C respectively

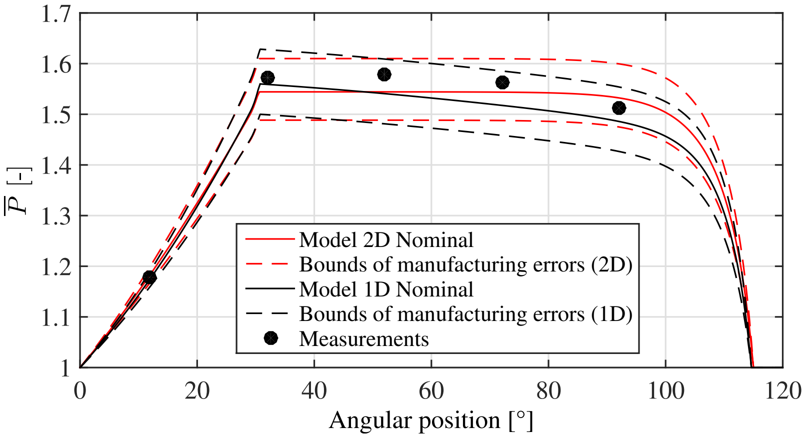

Figure 3.85 – Comparison 1D and 2D model-measurements in ambient air at 40 krpm. Measurements uncertainty bounds are smaller that the diameter of the dots

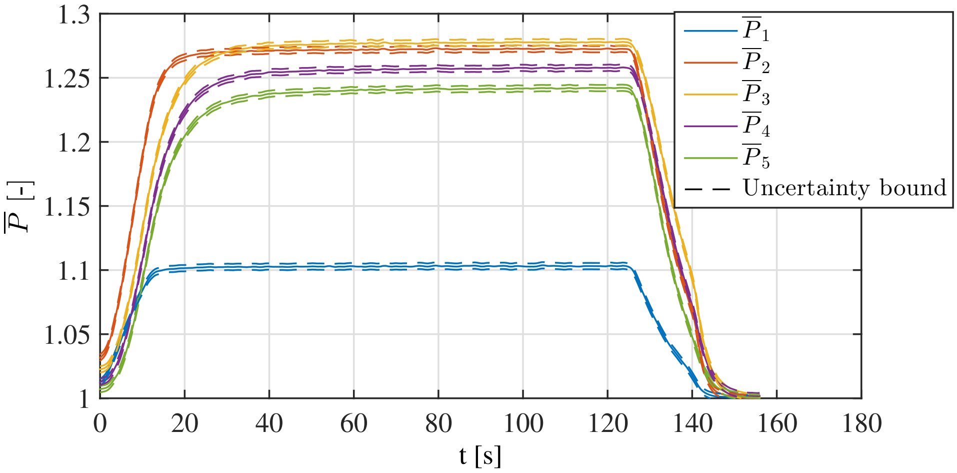

Figure 3.86 – Measured pressures against time in R245fa, $T_{bearing} = 23.4°\text{C}$ $P_a = 96.0$ kPa, accelerating from 3.6 to 30 krpm

convection between the pipes and the ambient air slowly increase the temperature of the cooling circuit over time. As the temperature at the pump intake reaches 21 °C, which allows a margin to condensation of 2.1 K, an acceleration scheme identical to the one previously applied is followed: acceleration to 3.6 krpm followed by a constant ramp up to 30 krpm. The cruise speed is held for several minutes while the temperature in the bearing and at the pump intake, as well as the pressures, are recorded. Figure 3.88 presents the measured relative pressure in the gas film, as well as the relative saturation pressure corresponding to the temperatures measured in the bearing and at the pump intake. An uncertainty of ±0.1 K, larger than the actual uncertainty, is applied on the cooling water temperature measurement in order to appreciate the effect of temperature on the saturation pressure.

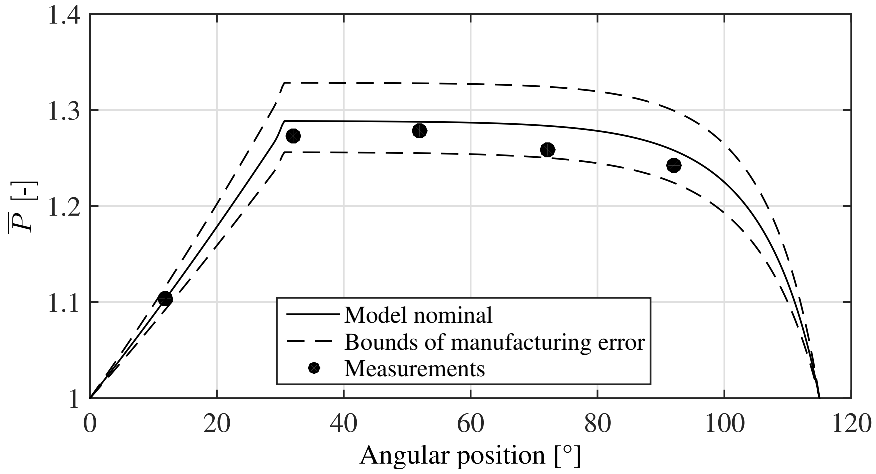

Figure 3.87 – Comparison model-measurements in ambient air in non-saturated R245fa at 30 krpm, corresponding to $t = 100s$ in Fig. 3.86. Measurements uncertainty bounds are smaller that the diameter of the dots

After the acceleration at 30 krpm, the pressures P_2 to P_5 behave nearly as one until t =300 s, with a trend very similar to the temperature of the bearing measured close to the measurement point P_1, in the feed groove. This limit pressure followed by P_2 to P_5 increases as the bearing temperature rises, with an equivalent saturation temperature equal to 0.5 K above the nominal value of the measured temperature, within the uncertainty. Qualitatively, this is very different from the data recorded away from the saturation point (Figure 3.86) and this can be seen as a first hint of the occurrence of isothermal condensation in the gas film.

However, having in mind the temperature level of the cooling water circuit, the temperature of the capillaries walls must lay between the warm bearing surface and the cold channels transporting the coolant in the bearing. As a consequence, pressure taps P_2 to P_5 might be in saturated conditions and one cannot exclude the occurrence of droplets formation in the measurement capillaries, which can have an influence on the pressure value measurement performed at the other end of the pipes.

The measurement of channel P_1 provides a more robust argument supporting the hypothesis of the condensing gas film. The pressure evolves with time beyond the settling time previously observed in non-saturated conditions (Figure 3.86, $t \approx 12$ s), although the pressure is low enough to discard the saturation everywhere in the measurement chain between the gas film and the pressure transducer. The change in pressure at this location indicates varying pressure elsewhere downstream in the gas film, in particular between 100 and 400 s. This allows to suppose that the pressure profile is influenced by both the temperature and the film pressure downstream of P_1, since the observed change of pressure is more significant than the increase of viscosity (which increases by 1.4% over between 0 and 1000 s due to the rise in temperature).

Because of the potential condensation happening at their other end, capillaries 2 to 4 might act as mass sinks and perturb the pressure in the gas film, thus perturbing the pressure measured in P_1. To assess this effect, a test run in similar conditions to the one shown in Figure 3.86 is performed. However, a manifold joining together the pressure taps 2 to 5 to the ambient pressure of the chamber is let open as the rotor is builds up speed from 3.6 to 30 krpm. The manifold is closed after a couple of seconds, isolating the pressure taps from the ambient. Taps 2 to 5 start to build-up pressure until equilibrium is reach with the gas film and the gas sinks end. Figure 3.89 shows the pressure measured at P_1, with the manifold closed at t=35 s. The pressure variation is $\overline{P} = 0.01$, which is significantly smaller than the pressure variation of P_1 in Figure 3.88 despite the fact that the manifold manipulation represent a pessimistic scenario due to the very large pressure difference it creates across the capillaries. It can therefore be concluded that the evolution of pressure of P_1 is due to a condensation pocket downstream of P_1.

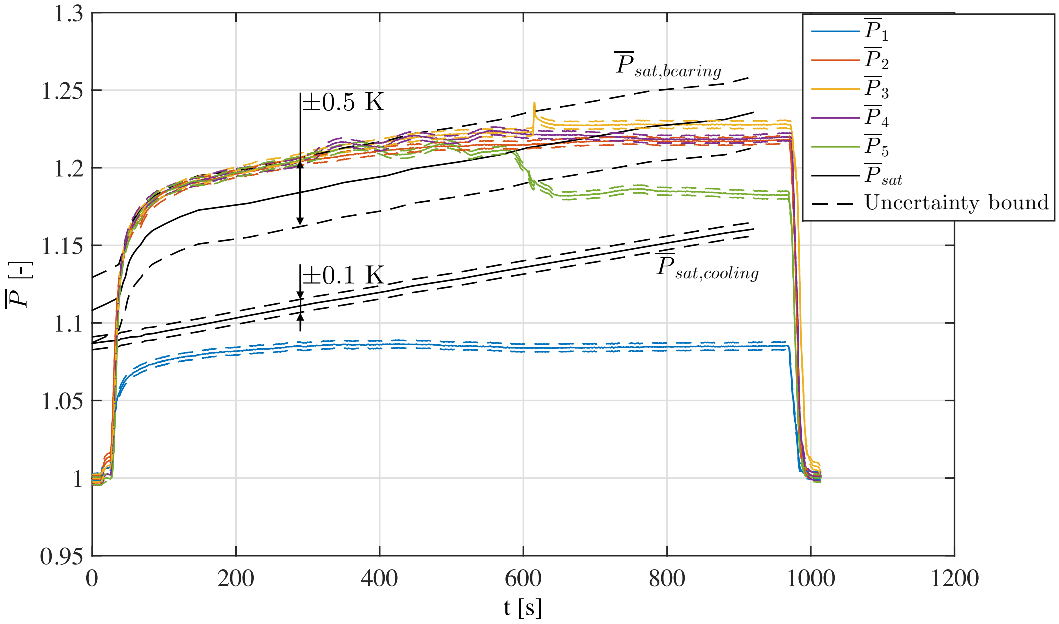

Figure 3.88 – Measured pressures and computed saturation pressures against time

The condensation model is used to predict the pressure at the location of the pressure taps for a varying value of $\bar{\rho}_{sat}$ and compared to the measurements based on the measured bearing temperature. Since the saturation pressure based on the upper error band of the measured bearing temperature captures well the recorded pressure increases after the start, this value is used to calculate $\bar{\rho}_{sat}$ in the model. Comparisons are shown in Figures 3.90 and 3.91. Two interesting aspects are highlighted: first, the rising trend in P_1 experimentally observed appears in the simulations, although the predicted values are lower than the measured ones. Second, the sudden decrease of P_5 occurring around

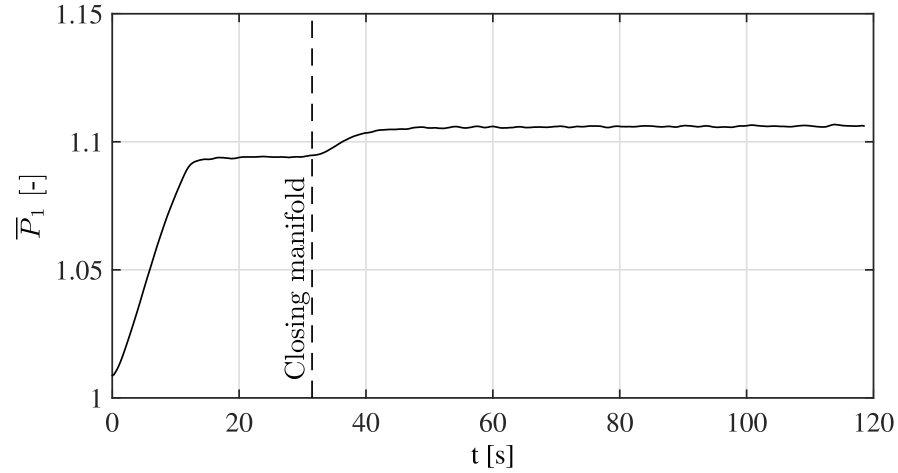

Figure 3.89 – Influence of the opening and closing of the taps 2 to 5 on the pressure $\overline{P}_1$

t =600 s is predicted by the model. The sudden drop in pressure corresponds to the switch from the two-phase hyperbolic form of the Reynolds equation to the single phase, elliptical form, which is a consequence of the slowly rising temperature. The model also predicts a similar yet much smaller transition in P_4, which is not experimentally observed. The oscillations in the measurements of $\overline{P}_4$ and $\overline{P}_5$ between t =300 s and t =600 s, are not captured by the model. They might be due successive condensation and evaporation of liquid droplets in the pressure taps. Similarly, the sudden peak after t =600 s in $\overline{P}_3$ is not captured by the model and can also be explained by the sudden evaporation of a metastable liquid droplet in the tap.

In a summary, the experimental campaign together with the the theoretical model clearly suggests the occurrence of condensation in a fluid film of a gas lubricated bearing operated close to the saturation line. The condensation is very sensitive to the local bearing temperature and the measurements seem to imply that condensing zones might appear and disappear, thus suggesting a dynamic behavior.

3.3.4.4 Vibrations analysis

The acceleration of the rotor very close to saturation conditions led to several touch-downs at moderated speeds between 20 and 40 krpm. An accelerometer was installed on the surface of the MRBS in order to capture radial vibrations and test at low temperature were conducted to find a possible spectral signature of the condensation. A typical waterfall plot is shown in Figure 3.92, for an ambient pressure of 116 kPa and an bearing temperature of 20.3 $°C$. The rotor is accelerated steadily until touch-down occurs at approximately 40 krpm. Although parasitic peaks are visible at 50 and 150 Hz, there is no sign of typical sub-synchronous whirl vibration before the crash at $t = 35s$. This result suggests that the touch-down was not induced by typical whirl instability. Possible

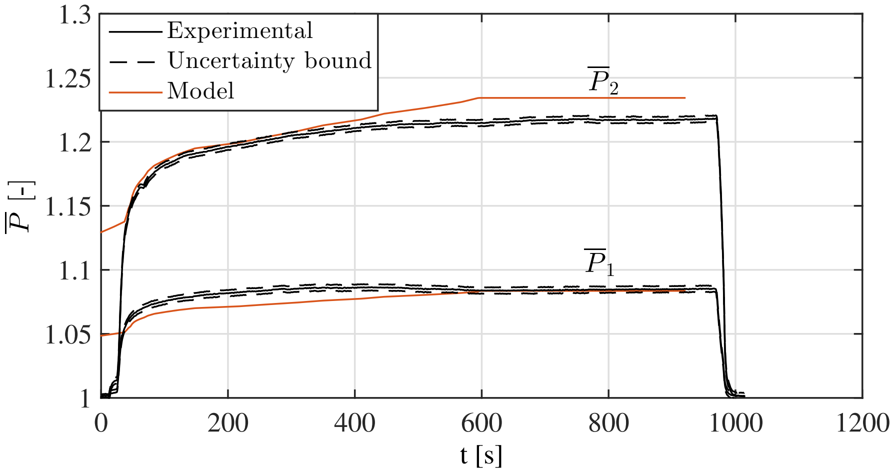

Figure 3.90 – Model-experimental comparison of $\overline{P}_1$ and $\overline{P}_2$ over time

explanations could be a reduction of the total synchronous stiffness of the bearing, leading to an excessive unbalance response form the rotor, or to a condensation pocket large enough to locally affect the load capacity, leading thus to an internal parasitic load.

3.3.5 Conclusions

Starting from the reference Jakobson-Floberg-Olsson theory and Elrod's algorithm for cavitation in liquid-lubricated bearings, a physically consistent method was proposed to model isothermal condensation in gas-lubricated bearings and applied on three 1D geometries in a wide range of compressibility numbers and relative saturation pressures. A test rig was developed to validate the model, consisting of a short rotor supported on one 3-pocket Rayleigh step bearing with one of the pocket instrumented with 5 pressure taps for in-situ pressure measurements of the gas film. The test apparatus was enclosed in a R245fa-pressurized chamber. Experimental and numerical results are in good aggrement. The concluding remarks are as follows:

- Isothermal condensation limits the achievable pressure level in the lubricating film to the saturation pressure associated to the bearing temperature
- The pressure in the two-phase domain can locally be higher than the level reached in similar yet non-saturated conditions
- Although the load capacity generally decreases in presence of condensation in the gas film, some conditions allow an improvement on the load capacity of 6% at low compressibility numbers because of the effect mentioned in the previous point
- The developed model and numerical solving scheme are in good qualitative and quantitative agreement with the collected experimental data

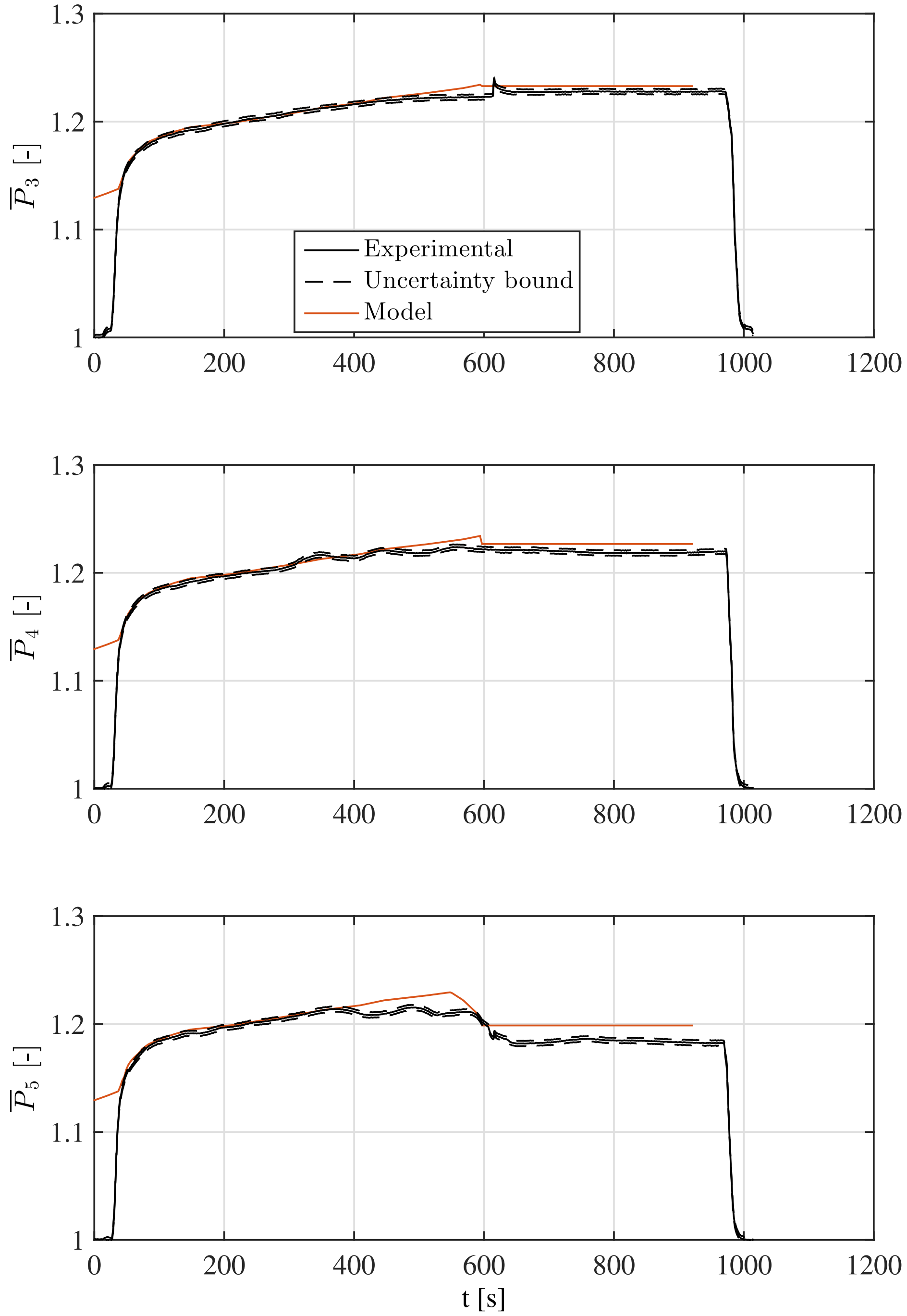

Figure 3.91 – Model-experimental comparison of $\overline{P}_3$, $\overline{P}_4$ and $\overline{P}_5$ over time

- Condensation-induced crashes were experienced, with no particular spectral signature in the subsynchronous or supersynchronous domain

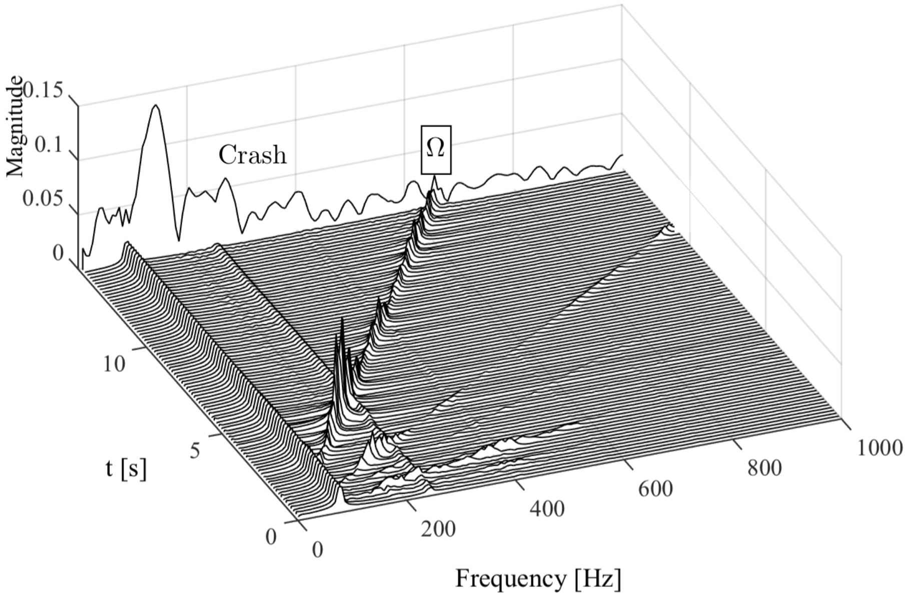

Figure 3.92 – Spectrum between start and touch-down of the rotor in R245fa, $P_a = 117\,\text{kPa}$

Additional developments are necessary to further assess the effects of condensation on the dynamic properties (stability, force coefficients) of bearings of finite length (2D). Furthermore, a considerable yet necessary work would involve modelling of condensation in HGJBs, with or without a modified NGT. Because of the local incompressibility assumption of the NGT, it fails to capture the isothermal condensation, since this state corresponds to a infinite compressibility of the fluid. Therefore, condensation in a grooved bearing can only be captured by a disrectization of the Reynolds equation resolving the individual grooves, which increases considerably the complexity the problem.

3.4 Chapter conclusion

This chapter aimed at investing the effects arising from non-ideal gas lubrication on the performance of aerodynamic bearings, either caused by an increased compressibility (single-phase real gas effects), by a partial condensation in a gas mixture (humid air effects) or by the condensation of a pure fluid as lubricant. The Reynolds equation was adapted to address each of the problem and numerically solved for different bearing geometries and operating conditions. Unlike the meager literature existing in these topics, the investigated cases were all described in non-dimensional numbers in order to keep a high level of generalization.

Although local exceptions exist, these effects tend to reduce the performance of aerodynamic bearings compared to the lubrication under the ideal gas assumption. Only the stability of a journal bearing experiencing real-gas effects, expressed as critical mass, showed a significant potential improvement. Single-phase real-gas effects and pure fluid condensation in general have a strong negative influence on the load capacity, while the partial condensation of water in humid air have can significantly reduce the stability of a HGJB without any significant effect on its load capacity.

The numerical implementation of the Reynolds equation adapted for pure fluid condensation was experimentally validated with a dedicated test rig operating in air and R245fa, providing for the first time *in situ* pressure measurements of a Rayleigh step journal bearing both in air and synthetic working fluid. It further supports the assumption of isothermal gas in aerodynamic bearings and sets a bridge between the cavitation occurring in liquid-lubricated bearings and condensation in aerodynamic bearings.

Future work should focus on a two-dimensional implementation of the Reynolds equation for condensable fluids able to assess of the stability of condensing aerodynamic bearings. Because of the highly non-linear behavior of a condensing thin gas film, the perturbation method might not be valid to extract the impedances and evaluate the stability of a journal bearing. Therefore, time-domain integration of the bearing's equations of motion should be investigated, which would require a significant research effort. Because the Narrow-Groove Theory used to described the pressure field on a grooved bearing in incompatible with the infinite compressibility of a condensing isothermal gas, the effect of condensation on Herringbone Grooved Journal Bearings should be investigated by numerically solving the Reynolds equation on a domain resolving each groove-ridge pair, which is a very challenging and demanding exercise.

Bibliography

[1] A. Javed, C. Arpagaus, S. Bertsch, J. Schiffmann, Small-scale turbocompressors for wide-range operation with large tip-clearances for a two-stage heat pump concept, International Journal of Refrigeration 69 (2016) 285–302. `doi:10.1016/j.ijrefrig.2016.06.015`.

[2] K. Rosset, V. Mounier, E. Guenat, J. Schiffmann, Multi-objective optimization of turbo-ORC systems for waste heat recovery on passenger car engines, Energy 159 (2018) 751–765. `doi:10.1016/j.energy.2018.06.193`.

[3] V. Mounier, L. C. Mendoza, J. Schiffmann, Thermo-economic optimization of an ORC driven heat pump based on small scale turbomachinery and comparison with absorption heat pumps, International Journal of Refrigeration 81 (2017) 96–110. `doi:10.1016/j.ijrefrig.2017.05.021`.

[4] J. Schiffmann, Integrated design, optimization and experimental investigation of a direct driven turbocompressor for domestic heat pumps, Ph.D. thesis, École Polytechnique Fédérale de Lausanne, Lausanne (2008). `doi:10.5075/epfl-thesis-4126`.

[5] R. Elwell, Observations on the performance of self- acting gas journal bearings. part II : Moisture condensation in self-acting gas bearings, Tech. rep., General Electric Laboratory, Contract Nonr-2844(00) (1961).

[6] F. K. Orcutt, Experimental investigation of two-phase flow in thrust bearings, Tech. rep., Mechanical Engineering Incorporated, MTI-62TR40 (1963).

[7] F. K. Orcutt, D. E. Dougherty, S. B. Malanoski, C. H. T. Pan, Investigation of externally pressurized steam-lubricated journal bearing, Journal of Lubrication Technology 90 (4) (1968) 723–730. `doi:10.1115/1.3601708`.

[8] R. S. Siegler, E. Zwick, Alkali Metal Vapor Lubricated Bearings on Space Vehicle Closed Cycle Power Conversion System, Tech. rep., SAE International, n.610064, Warrendale, PA (1961). `doi:10.4271/610064`.

[9] W. Unterberg, J. S. Ausman, Condensing vapor lubrication of self-acting long journal bearings, Journal of Basic Engineering 88 (1966) 236–245. `doi:10.1115/1.3645813`.

[10] B. Jakobsson, L. Floberg, The finite journal bearing considering vaporization, Journal of Wear 190 (1957) 1–116. `doi:10.1016/0043-1648(58)90453-8`.

[11] K. O. Olsson, Cavitation in dynamically loaded bearings, Tech. rep., Chalmers University of Technology (1965).

[12] H. G. Elrod, A cavitation algorithm, Journal of Lubrication Technology 103 (1974) 350—-354. `doi:10.1115/1.3251669`.

[13] D. Vijayaraghavan, T. G. Keith, Development and evaluation of a cavitation algorithm, Tribology Transactions 32 (2) (1989) 225–233. `doi:10.1080/10402008908981882`.

[14] D. Vijayaraghavan, T. G. Keith, Grid transformation and adaption techniques applied in the analysis of cavitated journal bearings, Journal of Tribology 112 (1) (1990) 52–59. `doi:10.1115/1.2920230`.

[15] D. Vijayaraghavan, T. G. Keith, D. E. Brewe, Extension of transonic flow computational concepts in the analysis of cavitated bearings, Journal of Tribology 113 (1991) 539. `doi:10.1115/1.2920657`.

[16] N. Zuber, D. E. Dougherty, The field equations for two-phase reynolds film flow with a change of phase, ASLE Transactions 25 (1982) 108–116. `doi:10.1080/05698198208983072`.

[17] A. Kingsbury, Experiments With An Air-Lubricated Journal, Journal of the American Society of Naval Engineers, inc 9 (2) (1897) 267–292. `doi:10.1111/j.1559-3584.1897.tb05692.x`.

[18] J. Sato, Settling Times of Pressure Measurements through Capillary Tubes, AIAA Journal 17 (10) (1979) 1061–1067. `doi:10.2514/3.61278`.

4 Advanced bearing design

Although the Narrow Groove Theory has been developed decades ago and represented a breakthrough in the development of stable aerodynamic bearings, the recent gain of interest of Herringbone Groove Journal Bearings (HGJBs) and Spiral Groove Thrust Bearings (SGTBs) for industrial applications are facing some limitations of the current technology. The first problem arises from manufacturing. The stability of a bearing-rotor system is very dependent on the bearing clearance and results in very tight manufacturing tolerances. The production is therefore costly as it demands a high accuracy to keep the reject rate at acceptable levels. This is a cost bottleneck for the mass industrialization of gas bearings. The current approach in integrated design of airborne machinery consist in maximizing the dynamic stability (expressed as a critical mass or a logarithmic decrement). However, maximizing the stability does not necessarily maximize the robustness of the solution against manufacturing deviations, which is actually the sought objective. An efficient and reliable optimization techniques suited for robust design is needed to improve the reliability and therefore the marketability of aerodynamic bearings.

The second aspect regards the development of oil-free turbomachinery applications, which impose a large axial load on the thrust bearing, in particular with single-wheel compressors where the net axial thrust force cannot be internally compensated among the wheels. In medium size oil-free turbomachinery, the axial load is typically supported on Gas Foil Thrust Bearings (GFTBs) because of their robustness against impurities, thermal deformations and large displacements. However, their limited load capacity compared to liquid-lubricated bearings is a bottleneck to the implementation of large machinery supported on aerodynamic bearings. A possible mean of improved performances is to improve the pressurization capabilities of the foil bearing by the addition of texturing similar to grooved bearings. While compliant foil bearings and grooved rigid bearings have coexisted for decades, there had been surprisingly almost no attempt to hybridize the two families in a search for better performances enabling the implementation of this technology on large turbomachinery. An exploration of this pathway is needed to assess the potential of such hybrid gas bearings.

This chapter intends to fill these two gaps by 1) proposing a design optimization strategy for aerodynamic bearings in order to maximize the robustness against manufacturing deviation and by 2) exploring the possibility to improve the compliant foil bearing design with the addition of spiral grooves. The chapter is composed of two sections, each covering one of the two presented issues. The first section proposes a new multi-objective optimization approach maximizing the robustness of HGJBs against manufacturing deviations on its critical design parameters. The second part investigates a novel thrust gas bearing design, consisting in a foil thrust bearing enhanced with spiral grooves, with the objective to improve its load carrying capacity and decreasing its drag torque. Each part was published in the form of a journal article cited in the beginning of each section.

4.1 Gas Foil Spiral Groove Thrust Bearing

Part of the material composing this section has been published in the journal article:

Guenat, E., Schiffmann, J., 2019. Performance potential of gas foil thrust bearings enhanced with spiral grooves. Tribology International 131, 438–445. DOI: 10.1016/j.triboint.2018.11.003

4.1.1 Introduction

GFTBs are widely used in oil-free airborne applications such as microturbomachinery. While the first applications of this technology were small-scale with modest loads, global research efforts are being made toward the application of the compliant gas bearing technology to upscaled systems, with larger loads, in order to broader the scope of application of GFTBs and oil-free bearings in general.

Heshmat [1] proposed a model of GFTB considering the compliant bump foil as a simple elastic foundation and performed a parametric study to identify the geometry maximizing the load capacity. A considerable effort was spent by the community on the refinement of this model, implementing more complex foundation models or refining the method for the computation of the compliance coefficient. The layout of GFTB studied by Heshmat is a widely used design in oil-free turbomachinery applications such as supercritical CO_2 compressors [2] or turbochargers [3]. Moreover, the model developed decades ago by Heshmat is still of use in the recent literature, showing a reasonable agreement with experimental data [2–4]. The upscaling trend in size of rotors supported on foil bearings is limited by their load capacity and drag losses, which may lead to a delicate thermal management [5]. Scaling laws do not play in favor of larger applications, as showed by Prasad [6] and Dellacorte [7]. To overcome this intrinsic limitation, researchers have investigated numerous possibilities to further increase the load capacity of GFTBs. The clearance distribution was optimized by Lehn [8] to maximize the load capacity using a gradient-based optimization. A hybrid foil thrust bearings was investigated by Lee et Kim [9], where compressed air is supplied to the bearing fluid film in order to sustain a thin lubricating gas film even at high load. Magnetic bearings can also be a solution to relieve the aerodynamic bearing, as suggested by Heshmat et al. [10]. Both alternatives imply the use of auxiliaries, which is costly in terms of space, investment and power and reduces the reliability.

In the meantime, the development of rigid SGTBs followed a parallel path, starting with Malanoski and Pan [11] who applied the Narrow Groove Theory (NGT) to model grooved thrust bearings. However, this technology is limited to very small-scale machines because of the tight manufacturing tolerances required. The recent literature brought a promising improvement potential in terms of static stiffness and dynamic stability for grooved bearings with non-constant groove parameters, with the work of Hashimoto et al. [12] and Schiffmann [13].

Despite the progress accomplished, the two technologies remain isolated one from another. An early attempt to combine the SGTB with a compliant structure was realized by Licht in 1981 [14] with a full bearing based on Malanoski's rigid design. The compliant structure was designed such that the top foil remains parallel to the runner under load in order to preserve the validity of Malanoski's performance predictions. Unfortunately, no model was proposed and the improvement potential was not assessed. Based on this work it is hypothesized that the addition of spiral grooves on a GFTB's top foil can be of practical interest in the quest of enhanced load capacities and eased thermal management. Moreover, the manufacturing of grooves is inexpensive and could even be retrofitted on existing GFTBs.

The present work investigates the use of spiral grooves manufactured on the GFTB's top foil to improve the load capacity and/or to reduce the drag losses. The objective are to: (1) develop a model for Gas Foil Spiral Groove Thrust Bearings (GFSGTB), (2) investigate the static performance of such bearings in comparison to their ungrooved equivalent in terms of load capacity and losses and (3) devise design guidelines.

The GFTB model of Heshmat, including a simple foundation model for the compliant structure, is combined with the modified Reynolds equation of the NGT to model the pumping action of logarithmic grooves manufactured on the top foil of the bearing. Multi-objective optimizations are performed for various geometries (ramp depth) and operating conditions in order to identify trade-offs in terms of load capacity and losses. Compressibility numbers up to 1000 are evaluated. The potential of the new bearing geometry is highlighted, as well as its limitations. Based on these results, a set of design guidelines is suggested to take advantage of the new layout.

4.1.2 Theory

The layout under investigation consists in an inward-pumping spiral groove thrust bearing, where grooves are located on the outer diameter (Fig.4.2). Initially, the subsection covering the angle θ_R, referred as *ramp*, is converging (Fig. 4.1) with a depth h_R and a nominal clearance h_0. The Narrow Groove Theory is employed to predict the overall pressure in the grooved region of the bearing, assuming a infinite number of groove-ridge pairs, hence the pressure variation over a groove-ridge pair vanishes globally, while varying linearly between a groove and the following ridge locally. This hypothesis is equivalent to a local incompressibility of the lubricant. It allows an efficient and effective modelling of groove patterns without the need of fine grid size to capture the grooves individually. The first use of this theory to analyze a SGTB was done by Malanoski and Pan [11]. The analysis was later supported by Zirkelback and San Andres [15] with the finite element method. Only the resulting differential equation, as developed in [16] for an isothermal and isoviscous ideal gas is displayed here in the steady state form:

$$\begin{aligned}\partial_\theta\left[\bar{P}\left(\frac{1}{\bar{r}}f_1\partial_\theta\bar{P}+f_2\partial_{\bar{z}}\bar{P}\right)\right]+\partial_{\bar{r}}\left[\bar{P}\left(f_2\partial_\theta\bar{P}+f_3\bar{r}\partial_{\bar{r}}\bar{P}\right)\right]\\+c_s\left(\bar{r}\sin\beta\partial_\theta(f_4\bar{P})-\cos\beta\partial_{\bar{r}}(\bar{r}^2f_4\bar{P})\right)=\Lambda\bar{r}\partial_\theta(f_5\bar{P})\end{aligned}\qquad 4.1$$

where the geometry is presented in Figures 4.1 and 4.2 and functions f_i are developed in Eq. 2.19. This equations applies to the entire bearing domain, reducing to the normal Reynolds equation in the land region, where $\bar{h}_g=\bar{h}_r=\bar{h}$.

The modeling of the soft support is based on the work by Heshmat [1] using a simple foundation model for the compliant structure. The non-dimensionalization of the governing equation is performed as follows:

$$\bar{P}=P/P_a\quad\bar{r}=r/R_o\quad\bar{h}_{r/g}=h_{r/g}/h_0\quad\Lambda=\frac{6\mu\Omega R_o^2}{P_ah_0^2}\qquad 4.2$$

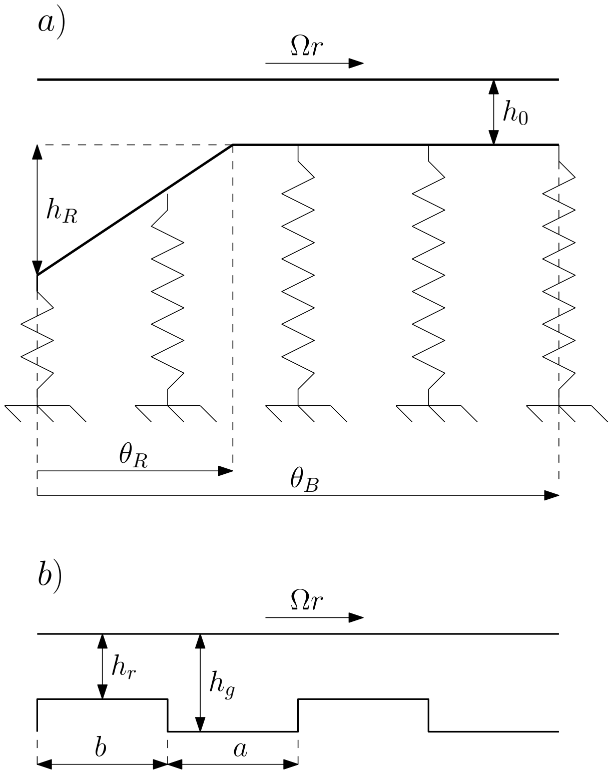

Figure 4.1 – Geometry and nomenclature of GFSGTB

The non-dimensional ridge and groove clearances are expressed as a function of the

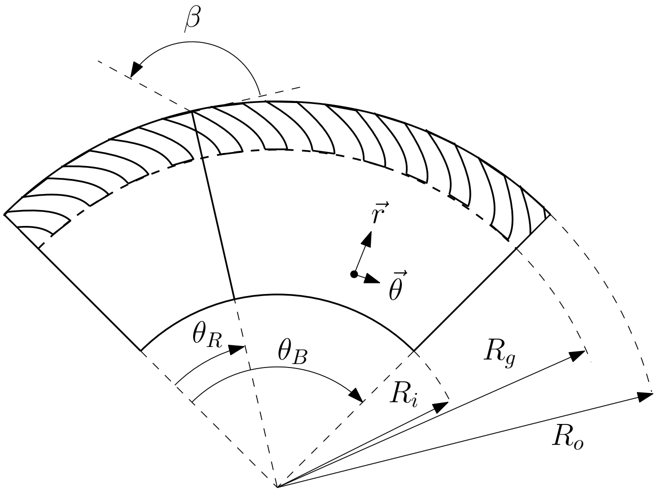

Figure 4.2 – Geometry and nomenclature of inward-pumping GFSGTB

position and local pressure :

$$\begin{aligned}\bar{h}_r &= 1 - \epsilon + g(\theta) + \alpha_F(\bar{P} - 1)\\ \bar{h}_g &= \bar{h}_r + \bar{\delta}\end{aligned} \tag{4.3}$$

where the compliance α_F is expressed as follows:

$$\alpha_F = \frac{P_a s}{K_f h_0} \tag{4.4}$$

$g(\theta)$ expresses the change in clearance in the converging sector of the fluid film domain:

$$g(\theta) = \max\left[\bar{h}_R\left(1 - \theta/\theta_R\right), 0\right] \tag{4.5}$$

The term ϵ is the eccentricity ratio, defined as $\epsilon = e/h_0$, with e being the axial displacement of the rotating smooth disk from its nominal position. The boundary conditions of Eq. 4.1 are ambient pressure at $\bar{r} = R_i/R_o$, $\bar{r} = 1$, $\theta = 0$, $\theta = \theta_B$. On the line $\bar{r} = R_g/R_o$, the continuity of the pressure is imposed, as well as the continuity of the radial mass flow rate across the land and grooved region:

$$\dot{m}_{r,groove} = \dot{m}_{r,land} \quad (\bar{r} = R_g/R_o) \tag{4.6}$$

which leads to the following expression:

$$(c_s f_4 \bar{r}\cos\beta - f_2\frac{1}{\bar{r}}\partial_\theta \bar{P} - f_3 \partial_{\bar{r}}\bar{P})_{groove} = (-\bar{h}^3 \partial_{\bar{r}}\bar{P})_{land} \tag{4.7}$$

The non-linear modified Reynolds equation is discretized using a finite difference scheme following section 2.3. The field of local clearance is updated based on the previously computed pressure.

Because it limits the wider application of the technology, the static performance is of primary importance in the design of gas thrust bearings. It appears more relevant than the dynamic behavior in a first study. Therefore, the performance metrics compare the investigated grooved and smooth layouts are the non-dimensional load capacity $\overline{W}$ and the non-dimensional drag torque $\overline{T}$:

$$\overline{W} = \int_{r_i}^{1}\int_{0}^{\theta_B} (\bar{P}-1)\bar{r}\mathrm{d}\theta\mathrm{d}\bar{r} \tag{4.8}$$

$$\overline{T} = \int_{r_i}^{1}\int_{0}^{\theta_B} \left(\frac{\alpha\bar{h}_g + (1-\alpha)\bar{h}_r}{2}\bar{r}\partial_\theta\bar{P} + \frac{\Lambda}{6}\bar{r}^3\left(\frac{\alpha}{\bar{h}_g} + \frac{1-\alpha}{\bar{h}_r}\right)\right)\mathrm{d}\theta\mathrm{d}\bar{r} \tag{4.9}$$

They are linked to their dimensional counterparts as follows:

$$W = P_a R_o^2 \overline{W} \tag{4.10}$$

$$T = P_a h_0 R_o^2 \overline{T} \tag{4.11}$$

It is useful to define the load capacity and drag torque of the grooved design normalized by the plain GFTB:

$$W_r = \frac{\overline{W}_{grooved}}{\overline{W}_{plain}} \tag{4.12}$$

$$T_r = \frac{\overline{T}_{grooved}}{\overline{T}_{plain}} \tag{4.13}$$

The outputs of the implemented model are compared to the results of Heshmat [1] as a sanity check for $\bar{h}_R = 1$, $\alpha = 1$, $\theta_B = 45°$ and $\theta_R/\theta_B = 0.5$, $R_o/R_i = 2$, suggesting a good agreement with the experimentally validated model (Figure 4.3). The largest relative deviation between the two models occurs at $\Lambda = 40$ and reaches 1.9%.

4.1.3 Numerical computations and results

The main geometrical parameters of the studied bearings follow the conclusion of Heshmat who identified the layout maximizing the load capacity for GFTB as being $R_o/R_i = 2$, $\theta_B = 45°$ and $\theta_R/\theta_B = 0.5$. The relative ramp height $\bar{h}_R$ is varied from low values

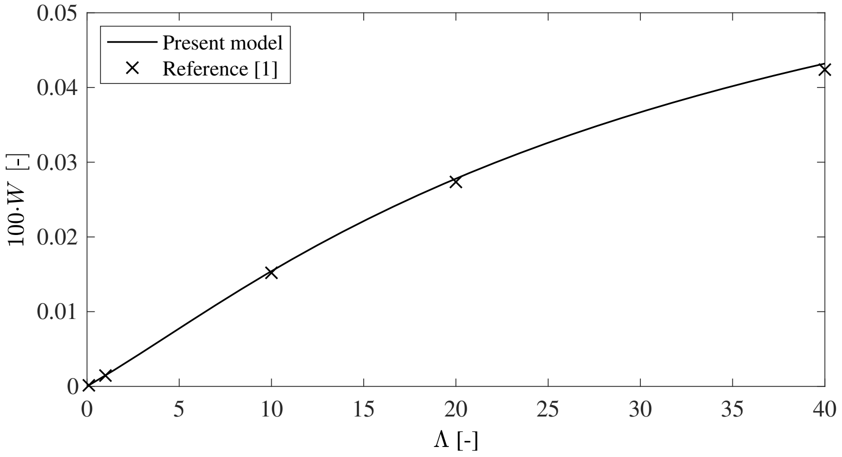

Figure 4.3 – Comparison of the present model with reference [1]

($\bar{h}_R = 1$) to values in the range recommended by Heshmat for maximum load capacity ($\bar{h}_R > 10$). Unless specified differently, the compliance is set to $\alpha_F = 1$ and the eccentricity ratio ϵ to 0.

4.1.3.1 Effect of logarithmic grooves on the bearing performance

In order to investigate the effect of grooved top foils on the defined performance indicators and to identify the optimum groove geometries, multi-objective optimizations were performed for different bearing geometries ($\bar{h}_R$) and operating conditions (Λ) simultaneously maximizing the load capacity and minimizing the drag torque. The decision variables are the 4 geometrical parameters describing the grooved region, namely:

$$\bar{h}_g \qquad \in [1,4] \tag{4.14}$$

$$\alpha = \frac{a}{a+b} \qquad \in [0.3, 0.7] \tag{4.15}$$

$$\beta \qquad \in [0, \pi] \tag{4.16}$$

$$\gamma = \frac{R_g - R_i}{R_o - R_i} \qquad \in [0.1, 0.9] \tag{4.17}$$

The optimizations were performed using a genetic algorithm [17] with 10^4 evaluations to obtain a satisfying convergence. The outputs of the optimization are Pareto fronts representing the optimal trade-offs between load capacity and drag torque. An example is given in Figure 4.4, for the case $\Lambda = 0.1$ and four different values of $\bar{h}_R$. The results clearly suggest the existence of regions with a positive effect of the spiral grooves on the drag torque and on the load capacity compared to plain GFTB. Depending on the constraints of a particular design problem, designers may either choose a solution favoring a high load capacity ratio or a low drag torque ratio. The Pareto fronts obtained for large ranges of h_R and Λ are processed to highlight two metrics of practical interest: (1) the

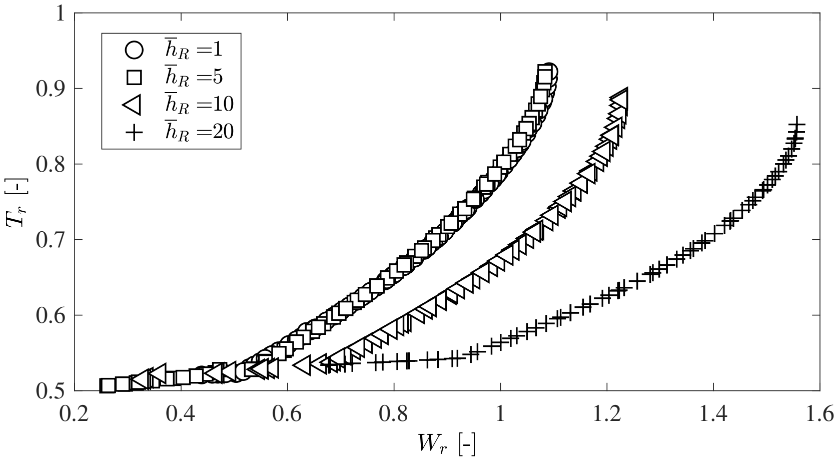

Figure 4.4 – Pareto fronts for $\Lambda = 0.1$ and different ramp depth ratios.

maximum value of W_r and (2) the value of T_r corresponding to the point where $W_r = 1$, which corresponds to (1) maximizing gain in load capacity without considering the drag and (2) minimizing the drag torque without losing load capacity compared to the plain GFTB design, respectively.

Figure 5 represents the maximum W_r as a function of the compressibility number for various ramp depth ratios and a constant compliance $\alpha_F = 1$. There is a strong influence of the relative ramp depth $\bar{h}_R$ on the potential performance gain. Low values exhibit stronger improvements at high values of Λ, with a relative gain of 70%, and inversely for large $\bar{h}_R$. This behavior can be explained by the absence of a limiting solution for $\Lambda \to \infty$ for rigid grooved bearings modeled with the NGT [18], which limits the performance of the smooth thrust bearings [19]. Ultimately, the results suggest that the maximum W_r for grooved thrust bearings is well above 1 for all values of $\bar{h}_R$. Although not captured by the NGT, a limiting solution does exist at very high compressibility in the case of grooved bearings. However, it is shifted to higher compressibility numbers [18], which maintains the interest of using the NGT even at such high values of Λ. For every investigated value of $\bar{h}_R$, a minimum in W_r is observed at intermediate values of Λ, where the optimal grooved case is close to the performance of a smooth design. The location of this minimum is shifted toward higher compressibility numbers as $\bar{h}_R$ increases. This is a consequence of the limiting solution at high compressibility numbers: a larger value of $\bar{h}_R$ leads to a limiting solution in pressure rise, which becomes more difficult to overcome by the pumping effect of grooves.

Figure 6 represents the drag loss ratio T_r as a function of the compressibility and for various ramp depth ratios at $W_r = 1$. The curves show that at equal load capacity, the grooved design can reduce the losses significantly depending on the geometry and the operating conditions. The most promising solutions maximizing the load capacity ratio in Figure 4.5 are also the most interesting ones regarding the drag reduction in drag torque in Figure 4.6. In these cases, the whole Pareto front happens to be partially or totally shifted in the domain $W_r > 1$, allowing a significant performance in the two metrics. Depending on the case, the reduction of drag torque can exceed 40%. In addition, two optimizations performed at high compressibility numbers (500 and 1000), both with $\bar{h}_R = 1$, only provide Pareto fronts with $W_r > 1$. As a consequence, the point of lowest W_r (and therefore lowest T_r) was displayed and the actual value of the load capacity ratio indicated.

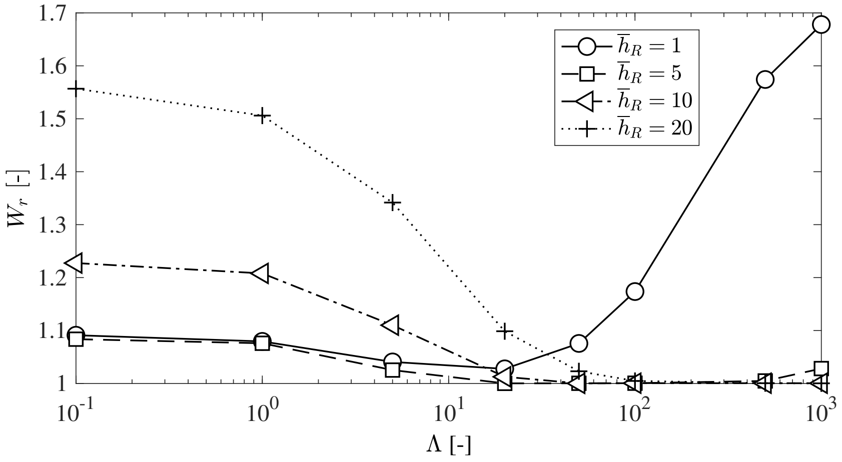

Figure 4.5 – Solutions of maximum W_r for a compliance $\alpha_F = 1$

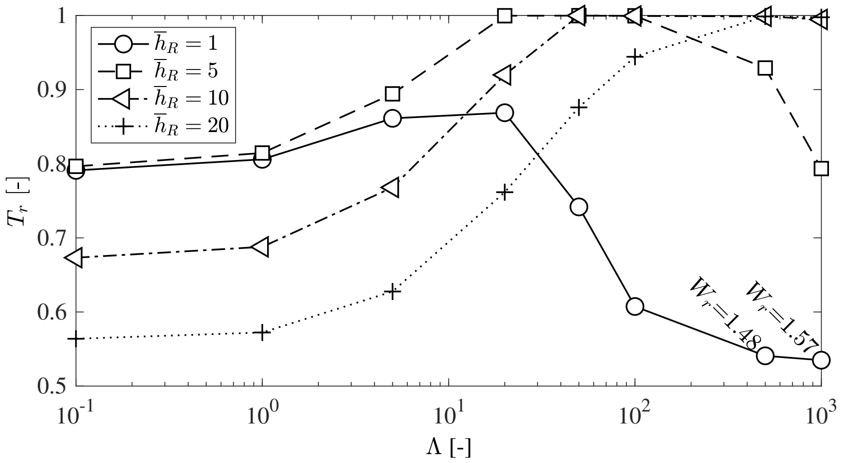

Figure 4.6 – Values of T_r for solutions with $W_r = 1$ for a compliance $\alpha_F = 1$

The groove parameters of the solutions for maximum load capacity shown in Figure 4.5 are displayed in Figure 4.7. Increasing the value of the ramp depth $\bar{h}_R$ tends to increase the optimum values of $\bar{h}_g$ and α, and decrease β and γ. At very high compressibility numbers Λ, the grooves tend to be deeper and occupy a larger area (higher α and lower γ), in particular for the cases $\bar{h}_R = 1$ and 5. It is important to note that for some cases the optimal design yield $\bar{h}_g = 1$, which corresponds to a plain design, where the other parameter have no influence on the bearing performance, thus explaining their swinging values for these particular cases. The optimal groove geometry does not evolve significantly for $\Lambda < 10$, which is a indicator for good off-design performance, as it will be shown below.

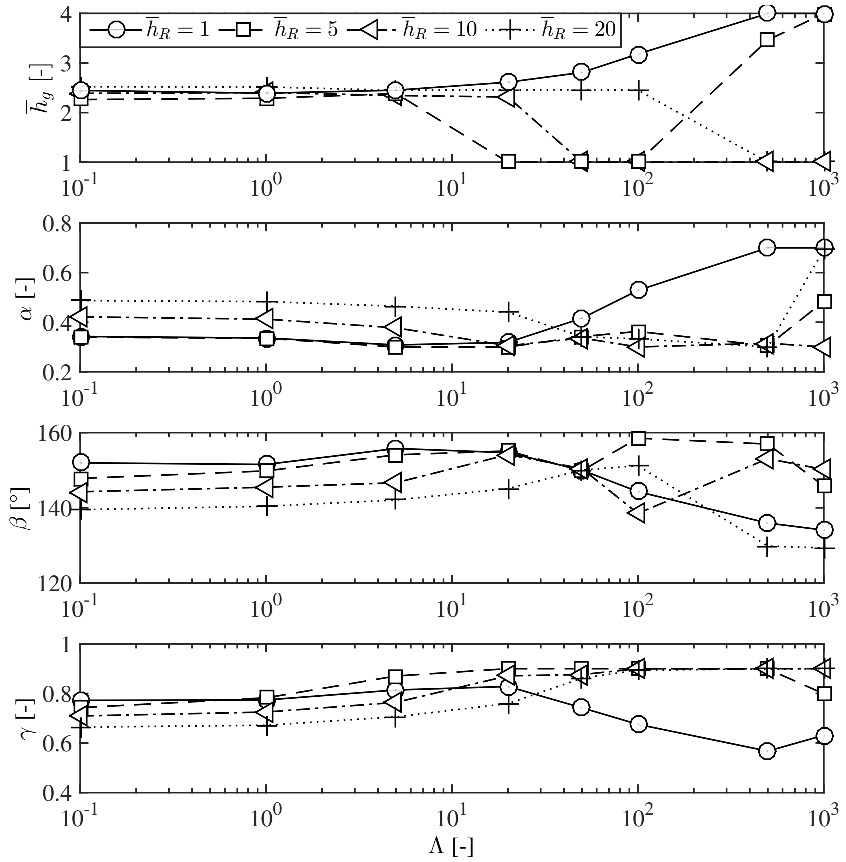

Figure 4.7 – Groove parameters corresponding to solutions in Figure 4.5

The points corresponding to $\Lambda = 5$ in Figure 4.5 have their pressure field represented in Figure 4.8. The pressure gradient in the radial direction is much stronger in the grooved zone for $\bar{r}_g < \bar{r} < 1$ than in the smooth zone, because of the pumping action of the grooved pattern. As the relative ramp depth increases, the zone of maximum pressure shifts from the center of the bearing toward the plateau, with a zone of maximum pressure bordered by the groove zone. In the ramp zone, the grooves tend to loose their pumping effect and become locally ineffective at building pressure or acting as a radial seal.

Since the presented results correspond to cases with a compliance $\alpha_F = 1$, the influence of this choice on the results is investigated. Figure 4.9 shows the influence of the foil compliance on the maximum load capacity ratio at a high compressibility number, resulting from an optimization performed at discrete values of α_F. Because of the low pressure build-up in the bearing at low values of Λ, the compliance has little effect on the performance metric because the resulting deflection of the top foil is not significant. W_r

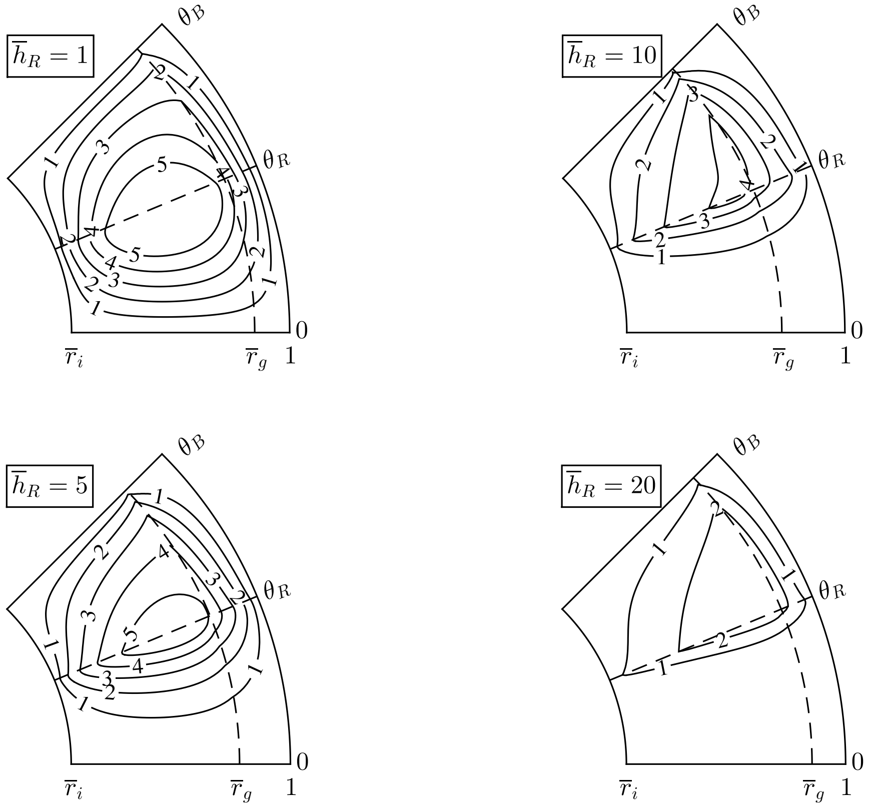

Figure 4.8 – Contour of $100 \cdot (\overline{P} - 1)$ for the geometries maximizing the load capacity at $\Lambda = 5$ and different ramp depths

exhibits a minimum at $\alpha_F \approx 0.35$ and increases approximately linearly at high compliance. However, the relative variation of W_r over the considered domain is low. It is therefore suggested that the compliance has little influence on the potential of the GFSGTB over the plain GFTB.

4.1.3.2 Off-design operation

Figure 4.10 represents the off-design performance in terms of compressibility number of two geometries with $\bar{h}_R = 20$ maximizing W_r at $\Lambda = 0.1$ and 50 respectively, for a compliance $\alpha_F = 1$. Since the optimal groove geometry does not evolve much for the case $\Lambda = 0.1$, the performance remains close to the optimum at low compressibility number, until $\Lambda \approx 20$. W_r drops below 1 for higher compressibility numbers. The design optimized for $\Lambda = 50$ maintains its performance close to 1 at high values of Λ with an appreciable gain at low compressibility, although it performs significantly lower than the local optimal geometry.

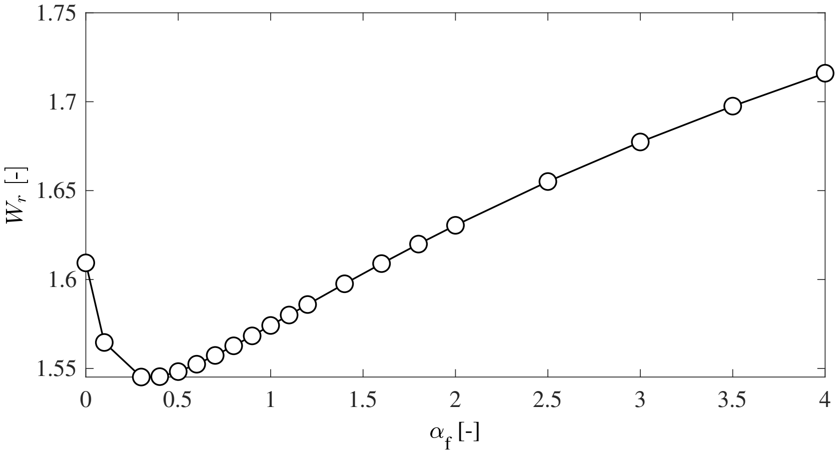

Figure 4.9 – Evolution of the load capacity ratio against the bearing compliance at $\Lambda = 500$ and $\bar{h}_R = 1$

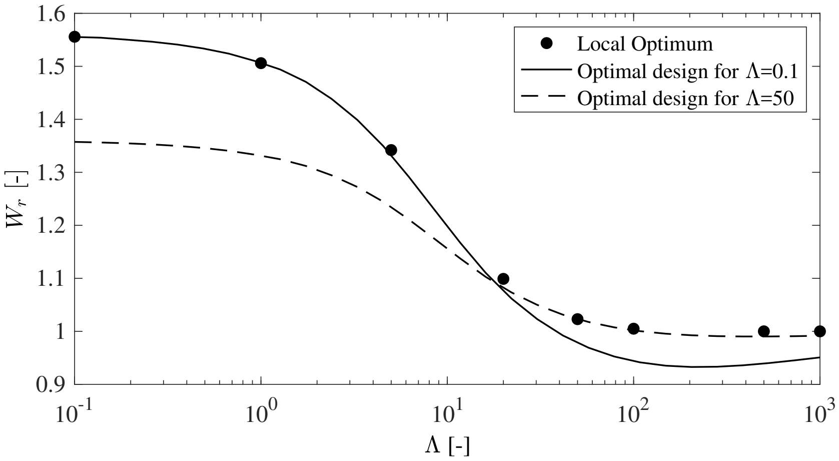

Figure 4.10 – Off-design performance ($\bar{h}_R = 20$) in terms of W_r of geometries optimized for $\Lambda = 0.1$ and 50

Figures 4.11 and 4.12 extend this analysis with $\bar{h}_R$ as a second variable, exploring the performance of the geometry optimized for $\Lambda = 0.1$ and $\Lambda = 50$ respectively, with $\bar{h}_R = 20$. The domain of interest with $W_r > 1$ is narrowed further in Λ as $\bar{h}_R$ departs from the design value. A local minimum in W_r is visible, however with a reduction of less than 15% compared to the design value. The performance increases sharply for low operating $\bar{h}_R$ at high compressibility, which corroborates with the results in Figure 4.5. It is important to note that for a given off-design value of $\bar{h}_R$, the performance passes through a minimum before increasing again. It supports the mentioned conjecture that an optimal groove design with $W_r > 1$ exists at very high values of compressibility number Λ for any value of ramp depth ratio $\bar{h}_R$, as long as the local incompressibility assumption of the NGT is verified [18]. A qualitatively similar observation can be made for the performance along the variable $\bar{h}_R$ at constant Λ. In both investigated cases, W_r passes through a minimum at $\bar{h}_R \approx 2$ for $\Lambda < 10$. The value of relative ramp height associated with this minimum increases at higher compressibility numbers. Note that cases close to $\bar{h}_R = 0$ represent two parallel surfaces, which are unable to build-up pressure if grooves are absent. Therefore, W_r becomes asymptotically large in these cases.

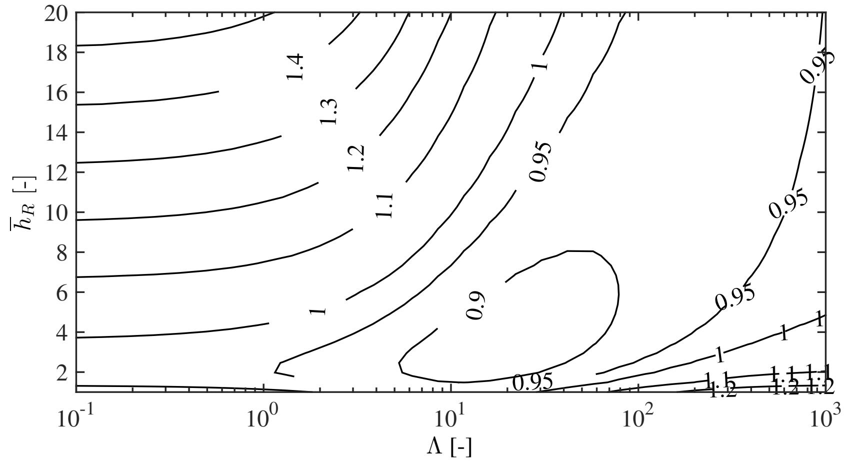

Figure 4.11 – Off-design performance in terms of W_r of the geometry optimized for $\Lambda = 0.1$ and $\bar{h}_R = 20$

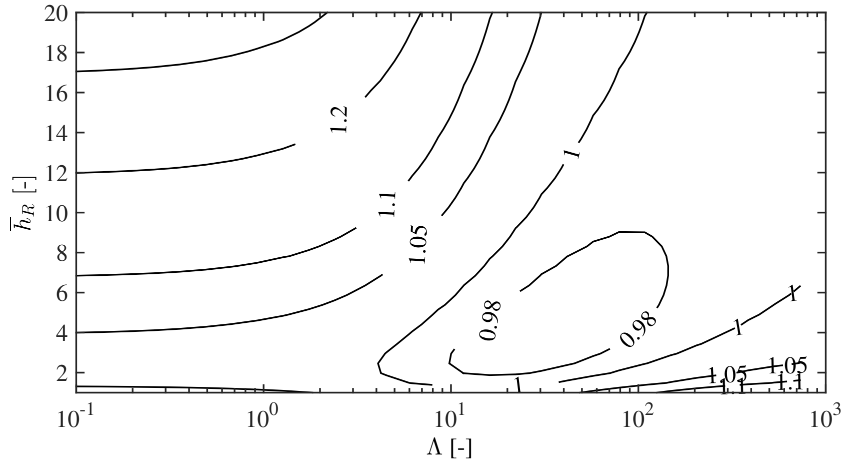

Figure 4.12 – Off-design performance in terms of W_r of the geometry optimized for $\Lambda = 50$ and $\bar{h}_R = 20$

The evolution of W_r with the eccentricity ratio ϵ, defined as the ratio between the actual minimum clearance over the nominal clearance, is shown in Figure 4.13. It is piratically equivalent to bearing operating in nominal conditions on which load is progressively added, having as consequence a decreased minimum clearance. The geometry of the five represented cases maximizes W_r at $\epsilon = 0$ and a nominal compliance $\alpha_F = 1$ evaluated at zero eccentricity. They initially operate at the compressibility number corresponding indicated in the legend. Note that in order to obtain these results, the stiffness of the elastic foundation is kept constant, which, according to Eq.4.4, leads to a compliance that evolves with eccentricity. All grooved geometries show an improved load capacity in nominal conditions but four of them exhibit a lower performance than the plain GFTB design at high eccentricity ratios, with a loss of nearly 25%. These cases correspond to the optimal geometries at $\Lambda = 1$. For them, W_r reaches a local maximum a high values of $\bar{h}_R$, which is not present for $\bar{h}_R$=1, where it decreases steadily with an increasing eccentricity ratio. The optimal geometry for $h_R = 1$ and $\Lambda = 100$ exhibits a comparatively smaller sensitivity toward the increase in eccentricity and achieves a ratio of load capacity slightly above 1 at high eccentricites. Theses results suggest that GFSGTB optimized for low compressibility numbers do not provide a higher ultimate load capacity compared to the plain design.

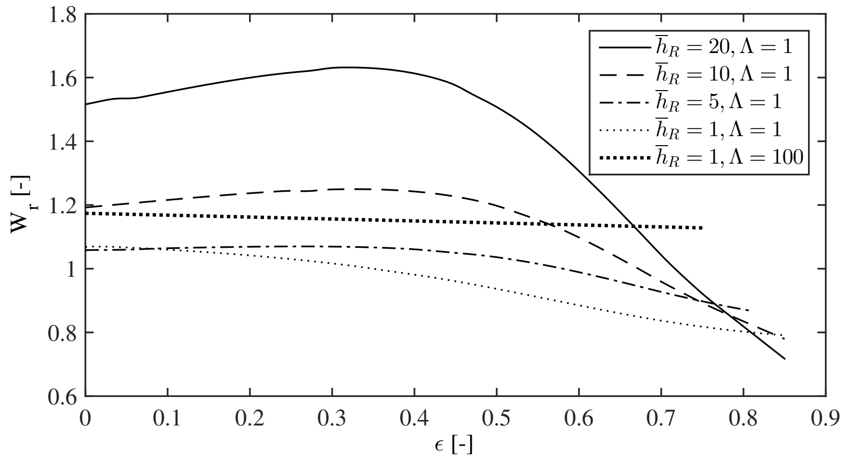

Figure 4.13 – Off-design performance in terms of W_r of the geometry optimized for $\Lambda = 1$ and $\Lambda = 100$

4.1.4 Conclusions

Based on Heshmat's work [1], a model of gas foil thrust bearing enhanced with logarithmic spiral grooves is developed using the Narrow Groove Theory. The improvement potential is evaluated in terms of load capacity and drag torque for a large range of compressibility numbers, relative ramp depth and bearing compliance. A multi-objective optimization for identifying the optimal groove geometries to maximize the load capacity while minimizing the drag torque leads to the following observations:

- The improvement potential of a grooved bearing compared to a plain one is the highest at low compressibility numbers and large relative ramp depth or inversely at high compressibility numbers and low ramp depths.
- Optimum groove geometries allow to improve the load capacity of a plain gas foil thrust bearing by nearly 70%.
- Optimum groove geometries allow to decrease the drag torque (losses) of the thrust

bearing by up to 40% compared to a plain Gas Foil Thrust Bearing, in cases where the specific load capacity between the two bearing types is the same.

- An assessment on off-design operation suggests that groove geometries optimized for low compressibility numbers negatively impact the load capacity at higher values (i.e. higher rotor speed and smaller clearance). However, a design optimized for high compressibility numbers still present a significant gain at lower compressibility numbers compared to plain gas foil thrust bearing.
- The presence of grooves optimized for low compressibility numbers negatively impacts the ultimate load capacity of the thrust bearings compared to the plain GFTB.

It follows that the addition of spiral grooves on the GFTB's top foil can be an interesting solution to improve the load capacity and/or relieve the thermal management of plain gas foil thrust bearings. Due to the simplicity of the added manufacturing step, the proposed bearing layout is applicable to both new and commissioned bearings (retrofit).

Bibliography

[1] H. Heshmat, J. A. Walowit, O. Pinkus, Analysis of Gas Lubricated Compliant Thrust Bearings, Journal of Lubrication Technology 105 (4) (1983) 638–646. `doi:10.1115/1.3254696`.

[2] T. M. Conboy, Real-Gas Effects in Foil Thrust Bearings Operating in the Turbulent Regime, Journal of Tribology 135 (3) (2013) 031703–031703–12. `doi:10.1115/1.4024048`.

[3] L. San Andrés, K. Ryu, P. Diemer, Prediction of Gas Thrust Foil Bearing Performance for Oil-Free Automotive Turbochargers, Journal of Engineering for Gas Turbines and Power 137 (3) (2014) 032502–032502–10. `doi:10.1115/1.4028389`.

[4] T. H. Kim, M. Park, T. W. Lee, Design Optimization of Gas Foil Thrust Bearings for Maximum Load Capacity1, Journal of Tribology 139 (3) (2017) 031705–031705–11. `doi:10.1115/1.4034616`.

[5] K. Ryu, L. San Andrés, On the Failure of a Gas Foil Bearing: High Temperature Operation Without Cooling Flow, Journal of Engineering for Gas Turbines and Power 135 (11) (2013) 112506–112506–10. `doi:10.1115/1.4025079`.

[6] S. H. Prasad, D. Kim, Scaling Laws for Radial Clearance and Support Structure Stiffness of Radial Foil Bearings, Journal of Engineering for Gas Turbines and Power 139 (4) (2016) 042502. `doi:10.1115/1.4034648`.

[7] C. DellaCorte, R. J. Bruckner, Remaining Technical Challenges and Future Plans for Oil-Free Turbomachinery, Journal of Engineering for Gas Turbines and Power 133 (4) (2011) 042502. `doi:10.1115/1.4002271`.

[8] A. Lehn, Air foil thrust bearings: A thermo-elasto-hydrodynamic analysis, Ph.D. thesis, Technische Universität, Darmstadt (2017).

[9] D. Lee, D. Kim, Design and Performance Prediction of Hybrid Air Foil Thrust Bearings, Journal of Engineering for Gas Turbines and Power 133 (4) (2010) 042501–042501–13. `doi:10.1115/1.4002249`.

[10] H. Heshmat, H. M. Chen, I. Walton, J. F., On the Performance of Hybrid Foil-Magnetic Bearings, Journal of Engineering for Gas Turbines and Power 122 (1) (1999) 73–81. `doi:10.1115/1.483178`.

[11] S. B. Malanoski, C. H. T. Pan, The Static and Dynamic Characteristics of the Spiral-Grooved Thrust Bearing, Journal of Basic Engineering 87 (3) (1965) 547–555. `doi:10.1115/1.3650603`.

[12] H. Hashimoto, M. Ochiai, Optimization of Groove Geometry for Thrust Air Bearing to Maximize Bearing Stiffness, Journal of Tribology 130 (3) (2008) 031101–031101–11. `doi:10.1115/1.2913546`.

[13] J. Schiffmann, Enhanced Groove Geometry for Herringbone Grooved Journal Bearings, Journal of Engineering for Gas Turbines and Power 135 (10) (2013) 102501. `doi:10.1115/1.4025035`.

[14] L. Licht, W. J. Anderson, S. W. Doroff, Design and Performance of Compliant Thrust Bearings With Spiral-Groove Membranes on Resilient Supports, Journal of Lubrication Technology 103 (3) (1981) 373–384. `doi:10.1115/1.3251681`.

[15] N. Zirkelback, L. San Andrés, Effect of Frequency Excitation on Force Coefficients of Spiral Groove Gas Seals, Journal of Tribology 121 (4) (1999) 853–861. `doi:10.1115/1.2834145`.

[16] J. Schiffmann, Integrated design, optimization and experimental investigation of a direct driven turbocompressor for domestic heat pumps, Ph.D. thesis, École Polytechnique Fédérale de Lausanne, Lausanne (2008). `doi:10.5075/epfl-thesis-4126`.

[17] G. B. Leyland, Multi-objective optimisation applied to industrial energy problems, Ph.D. thesis, École Polytechnique Fédérale de Lausanne (2002). `doi:10.5075/epfl-thesis-2572`.

[18] V. N. Constantinescu, V. Castelli, On the Local Compressibility Effect in Spiral-Groove Bearings, Journal of Lubrication Technology 91 (1) (1969) 79–86. `doi:10.1115/1.3554902`.

[19] T. H. Kim, L. San Andrés, Limits for high-speed operation of gas foil bearings, Journal of tribology 128 (3) (2006) 670–673. `doi:10.1115/1.2197851`.

4.2 Improvement of manufacturing through optimal tolerancing of HGJB

A significant proportion of the material presented in this section has been published in the following journal article:

Guenat, E., Schiffmann, J., 2019. Multi-Objective Optimization of Grooved Gas Journal Bearings for Robustness in Manufacturing Tolerances, Tribology Transactions. DOI:10.1080/10402004.2019.1642547

4.2.1 Introduction

Recent years have seen a strong development of high-speed turbomachinery supported on gas bearings, for example for heat pumping [1; 2] or fuel cell air supplies or recirculation devices [3]. Among the gas bearing technologies accompanying this development, HGJBs have the advantage of being reliably modelled and repeatable regarding manufacturing, characteristics still missing for compliant foil gas bearings [4]. However, the manufacturing tolerances necessary to achieve stable operation on rigid bearings represent a serious economic bottleneck limiting the large-scale marketability of HGJB-supported machines. Although several authors have investigated the sensitivity of stability in gas bearings to manufacturing errors [5–7], the literature lacks systematic design strategies to maximize the stability robustness. The optimization and integrated design of turbomachinery supported on HGJB is typically adopting a mono or multi-objective strategy comprising the maximization of the gas bearing stability, either in terms of critical mass [8], or logarithmic decrement [2]. Following the development of the Narrow-Groove Theory [9], HGJBs were first optimized to maximize the load capacity [9; 10]. Later, the optimization of HGJB was oriented toward a maximization of the stability based on the critical mass criterion [8; 11]. More recent years have seen the emergence of multi-objective, integrated optimal design of entire rotor-HGJB systems [12], also including the spiral groove thrust bearing in the optimization. Typical competing objectives are the minimization of losses and the maximization of a stability criterion. The underlying assumption is that a high nominal stability of the HGJB supported rotor will also allow a large deviation of the bearing parameters from their design point, while keeping the system dynamically stable. However, achieving an accurate bearing clearance through lapping or grinding is a challenging and expensive task. The manufacturing of the grooves through laser or chemical etching, grinding or even additive manufacturing [13], generally yields accurate groove width, length and angle. The groove depth, however, usually exhibits a large relative uncertainty [14; 15]. Since manufacturing deviation of the bearing clearance and groove depth can easily achieve ±15%, the effect of this wide dimensional range can have a significant impact on stability and load capacity. As a consequence, rather than simply maximizing the stability, the maximization of tolerances, might lead to a more manufacturing-oriented design procedure for HGJB, thus improving their cost effectiveness. Meanwhile, design tools and concepts such as multi-objective optimizations and Pareto fronts have already proven their suitability in the tolerancing of mechanical systems [16; 17] and might be of interest for the tolerancing of aerodynamic bearings.

The present work aims to 1) propose a multi-objective optimization procedure for maximizing the range of selected design parameters while minimizing their effect on selected performance metrics, 2) apply the methodology to the design of a gas bearing supported rotor and 3) use the results to devise design guidelines for the maximization of the manufacturing tolerances for HGJB.

4.2.2 Theory

The strategy to perform an optimization maximizing the manufacturing tolerances on design variables of HGJB consist in computing a stability criteria within a large non-dimensional design space, where each dimension of this space is a key variable of the gas bearing. Typically, the geometry of a classical HGJB (as illustrated in Figure 2.11) can be described by 6 non-dimensional variables: the groove aspect ratio α, the groove angle $\hat{\hat{\beta}}$, the relative land length γ, the relative groove depth $\bar{\delta}$, the bearing length-diameter ratio L/D and the compressibility number Λ. The 6-D space is discretized and and the non-dimensional stability is computed for each node using the critical mass criteria. This multi-dimensional matrix is the base that serves as a look-up table to investigate the performance of any HGJB. To study a particular rotor-bearing system undergoing an acceleration from rest to full speed, the stability is evaluated at discrete speeds in this range and the minimum stability achieved along this path of a given bearing geometry is retained. This step requires the dimensionalization of the hyperspace previously computed, using characteristics of the rotor (radius, mass, clearance, groove depth), the ambient conditions (pressure, viscosity) and the operating conditions (angular velocity). This transformation into the dimensional space allows to introduce clearance distortion effects related to the rotor speed (thermal and centrifugal) and the absolute manufacturing deviations. For each of the n speed steps along the acceleration path, a dimensional hyperspace is created from the generic non-dimensional one (Figure 4.14). The n hyperspaces are combined to retain the minimum critical mass at each node, leading to one single rotor-specific hyperspace used to express the minimum critical mass. Two of its design dimensions are kept dimensional: the bearing ridge clearance h_0 and the groove depth δ, since these are the critical variables for the manufacturing process. The 4 other dimensions are still non-dimensional: α, $\hat{\beta}$, γ and L/D.

The next step consists in slicing the specific dimensional hyperspace to extract planes along the bearing clearance and the groove depth. On each slice (constant α, $\hat{\beta}$, γ and L/D), a Monte Carlo method is used to generate a large number of rectangles aligned

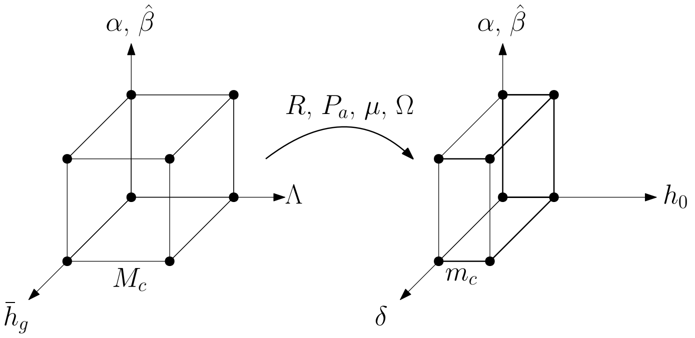
$\alpha,\,\hat{\beta}$
$\alpha,\,\hat{\beta}$
$R,\,P_a,\,\mu,\,\Omega$
Λ
h_0
M_c
m_c
$\bar{h}_g$
δ

a) Dimensionalization

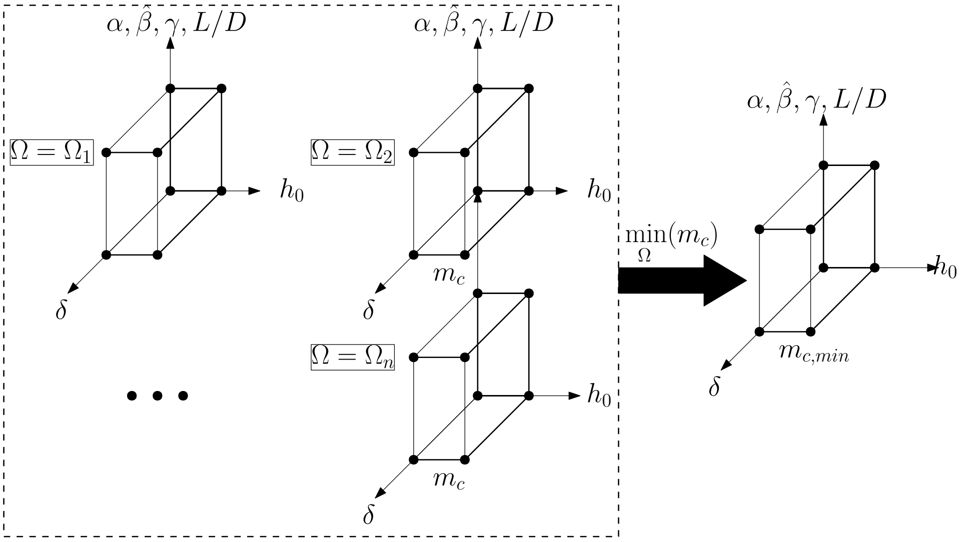
$\alpha,\hat{\beta},\gamma,L/D$
$\alpha,\hat{\beta},\gamma,L/D$
$\alpha,\hat{\beta},\gamma,L/D$
$\Omega=\Omega_1$
$\Omega=\Omega_2$
$\Omega=\Omega_n$
h_0
h_0
h_0
h_0
m_c
m_c
$\min_{\Omega}(m_c)$
$m_{c,min}$
δ
δ
δ
δ
• • •

b) Point-wise selection of the minimum critical mass

Figure 4.14 – Case-specific dimensionalization of the universal stability look-up table

on the axis of nominal clearance and groove depth, whose geometrical center is in the stable domain. Each rectangle is defined by 4 parameters: the position of its center along the clearance and groove depth ($h_{0,\square}$ and $\delta_\square$ respectively) and its half length along each axis (Δh_0 and $\Delta\delta$). Each rectangle undergoes a verification to ensure it satisfies the performance criterion ($m_{rotor} < m_{crit,min}$), the outliers being discarded. The validation algorithm checks 12 points on a grid centred on the rectangle and 8 points randomly scattered in the rectangle (Figure 4.15). Valid rectangles are represented in a 2D space defined by their length along the two directions, which represents the viable sets of manufacturing tolerances to obtain a stable operation of the specific rotor-bearing system:

$$h_0 = h_{0,\square} \pm \Delta h_0 \tag{4.18}$$

$$\delta = \delta_\square \pm \Delta\delta \tag{4.19}$$

The collection of all these feasible tolerance windows in a given dimensional slice allows to

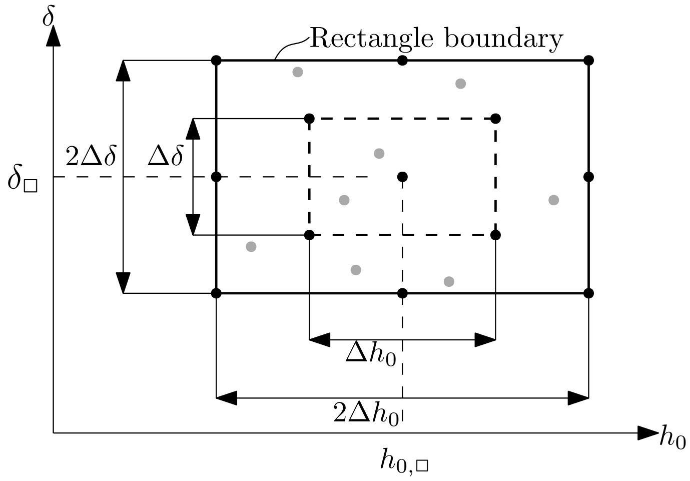

Figure 4.15 – Location of the rectangle stability check points to verify that the rectangle covers no unstable points. Check points are either on a grid (black points) or randomly positioned (grey points).

identify a Pareto front of optimum solutions in terms of maximal dimensional deviation and its constitutive points are stored. This procedure, depicted in Figure 4.16, is repeated for each dimensional slice of the discrete hypervolume. Finally, all the particular fronts are combined to obtain the global Pareto front for the particular system, as illustrated in Figure 4.17.

The global front represents the best feasible manufacturing tolerances regarding the nominal clearance and the groove depth for a particular rotor, while ensuring stable operation (i.e. satisfaction of a minimal performance metric). Depending on the accuracy of the considered manufacturing techniques, designers can then select a solution along the Pareto front suiting best their needs and possibilities, depending on the actual context.

The bearing is modeled using the NGT and the theory introduced in section 2.1, under the following assumptions:

- Ideal gas, isothermal and isoviscous lubricant

- Centered and axially symmetric bearing

The critical mass of HGJB is not necessarily decreasing with the compressibility number. Therefore, the minimum value of the critical mass between rest and maximum compressibility number has to be evaluated.

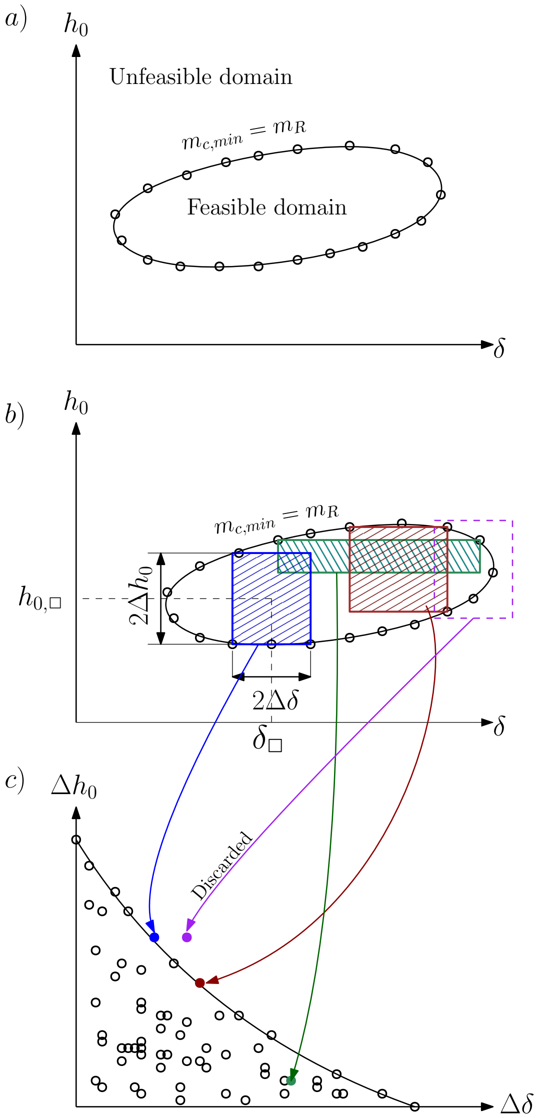
a)
h_0
Unfeasible domain
$m_{c,min} = m_R$
Feasible domain
δ
b)
h_0
$m_{c,min} = m_R$
$h_{0,\square}$
$2\Delta h_0$
$2\Delta\delta$
δ
$\delta_\square$
c)
Δh_0
Discarded
$\Delta\delta$

Figure 4.16 – Simplified representation of a stable domain on a slice (a), random generation rectangles in the stable domain (b) and determination of the particular Pareto front (c). The purple rectangle, falling outside of the feasibility domain, is discarded

4.2.3 Numerical computations and results

4.2.3.1 Computation of the non-dimensional design space

The computation of the universal non-dimensional 6D stability matrix is computationally expensive, since it can easily exceed 10^{10} evaluation points to obtain a sufficiently tight grid. In order to reduce this amount, the present analysis excludes the parameters γ and L/D, which are both set to 1 to maximize the stability of a bearing with the grooved member rotating [8]. The matrix is constituted of $3.2 \cdot 10^7$ elements in the following ranges of parameters:

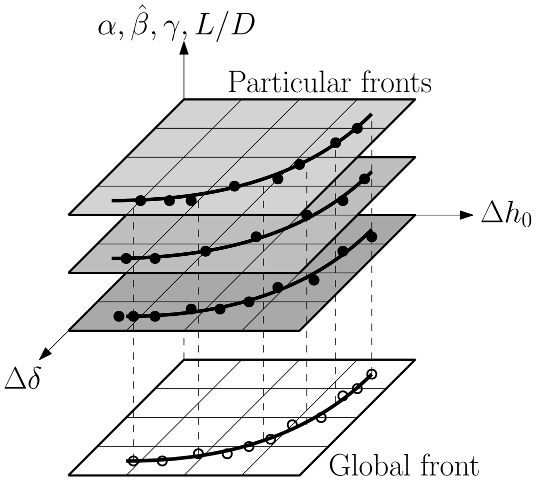

Figure 4.17 – Particular Pareto fronts projected to obtain the global front

Table 4.1 – Parameters of the studied rotor

Name	Symbol	Value
Bearing radius	R	5 mm
Rotor mass	m_R	0.075 kg
Maximum speed	N_{max}	200 krpm
Ambient pressure	P_a	10^5 Pa
Ambient gas viscosity	μ_a	18.5 µPa s

$$\Lambda \in [0, 200] \qquad \text{450 steps} \tag{4.20}$$

$$\alpha \in [0.4, 0.6] \qquad \text{10 steps} \tag{4.21}$$

$$\hat{\beta} \in [110^\circ, 170^\circ] \qquad \text{70 steps} \tag{4.22}$$

$$\bar{\delta} \in [0, 8] \qquad \text{100 steps} \tag{4.23}$$

4.2.3.2 Case study of the gas bearing supported rotor

A case rotor is defined for the dimensionalization of the pre-computed 4-D stability matrix and the determination of the optimal manufacturing tolerances. The rotor is taken as symmetric in order to have half the mass supported by each of the two journal bearings. Its main characteristics are listed in Table 4.1.

In a first approach, the centrifugal growth of the rotor is neglected. The critical mass is evaluated for 10 speeds between standstill and the maximum regime, in the following range of parameters:

$$h_0 \in [4\,\mathrm{\mu m}, 13\,\mathrm{\mu m}] \qquad \text{80 steps} \tag{4.24}$$

$$\delta \in [2\,\mathrm{\mu m}, 28\,\mathrm{\mu m}] \qquad \text{65 steps} \tag{4.25}$$

$$\alpha \in [0.4, 0.6] \qquad \text{10 steps} \tag{4.26}$$

$$\hat{\beta} \in [110^\circ, 170^\circ] \qquad \text{70 steps} \tag{4.27}$$

The lower bound of the clearance was chosen as a limit beyond which rarefied gas effects should have been considered. A groove depth of 0 µm was not investigated, since it corresponds to a plain bearing, which is unstable at concentric position. In each slice of the final stability matrix, $3 \cdot 10^5$ random tolerance windows are generated, whose centers are located in the stable domain of the slice, if any. An example of the stability limit for three values of groove angle is shown in the groove depth-clearance domain in Figure 4.18, for $\alpha = 0.6$. The arrows along the curves indicate the orientation towards the stable domain. It is interesting to note that for angles below 25° the stable region is fully contained between the corresponding contour. However, for an angle of 28° the topology of the feasible region changes. The stable region is a more complex one, since it is delimited by two concentric contours, yielding an unstable region centered around the considered range of clearance and groove depth. The advantage of the implemented methodology is that it can easily handle such changes in topology of the mathematical response surface.

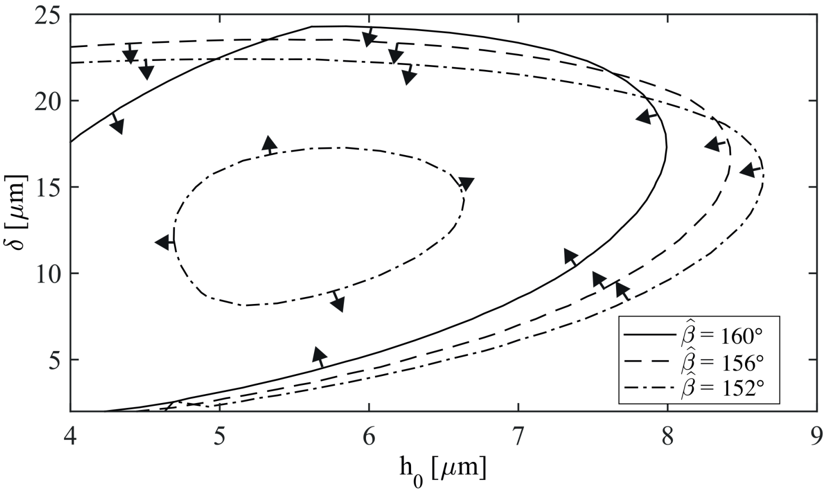

Figure 4.18 – Examples of stability limits for the considered rotor and α=0.6. The arrows indicate the orientation of the stable domain.

4.2.3.3 Nominal case

While the computation of the unique non-dimensional matrix demands 6 weeks of computation for a single-processor computer, the tolerancing algorithm, including the dimensionalization of the matrix, yields to the Pareto curve shown in Figure 4.19 within one minute with the same hardware. The Pareto curve indicates clearly that the two tolerances are competing: they can not be maximized both simultaneously. The maximum tolerance on the groove depth is roughly 5 times larger than the tolerance on the bearing clearance, indicating a lower sensitivity of the stability on this parameter. The extremities of the front are not particularly interesting from a manufacturing point of view, since a small concession on the maximized variable allows a large gain on the other. In this particular case, if one targets a large clearance tolerance, a reduction of 0.25 µm on Δh_0 from its maximum value, allows to increase the tolerance of delta-groove depth from nearly 0 to 4.5 µm on $\Delta\delta$.

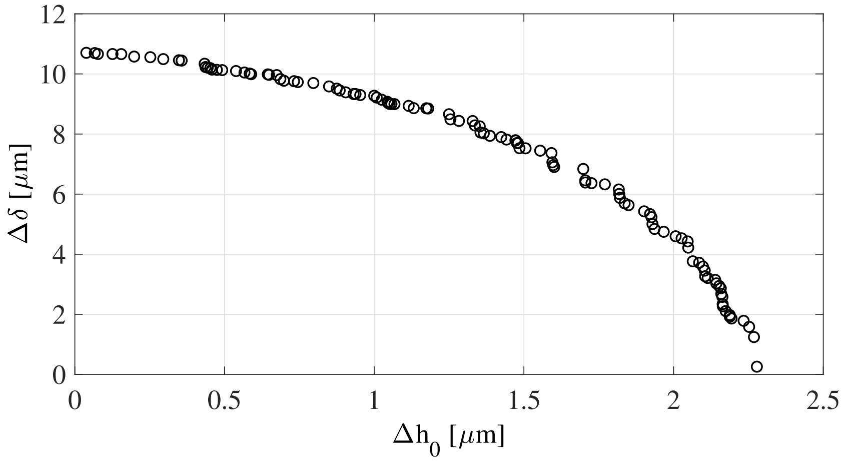

Figure 4.19 – Global Pareto front for the nominal rotor-bearing system

The parameters α and $\hat{\beta}$ of the points in the Pareto front are shown in Figure 4.20. A rising trend for $\hat{\beta}$ is visible as the tolerance on the clearance increases, ranging from 22° to 27°. No specific trend is visible for α, as optimal solutions are found over the entire range of this parameter. This suggests that although important when considering the maximum stability point, α is not as significant when considering the stability tolerance. The nominal clearance and groove depth values corresponding to the Pareto front are shown in Figure 4.21. The trend is rising on both values as the tolerance on the clearance increases. Past a value for Δh_0 of 0.5 µm, the trend for $h_{0,\square}$ follow a linear trend roughly expressed as follows: $h_{0,\square} = \Delta h_0 +$ 4 µm, meaning that the optimal tolerancing window is bounded by the lower limit for the bearing clearance set for this particular study. Interestingly, for Δh_0 <0.5 µm, this limit is not bounding the rectangles in the h_0 direction.

4.2.3.4 Comparison with stability maximization

For comparison purpose, the results of the optimization of the bearing parameters for the maximization of the stability without considering the effect of tolerancing is performed. In this case, the bearing nominal clearance is varied from 4 to 10 µm and the set of α,

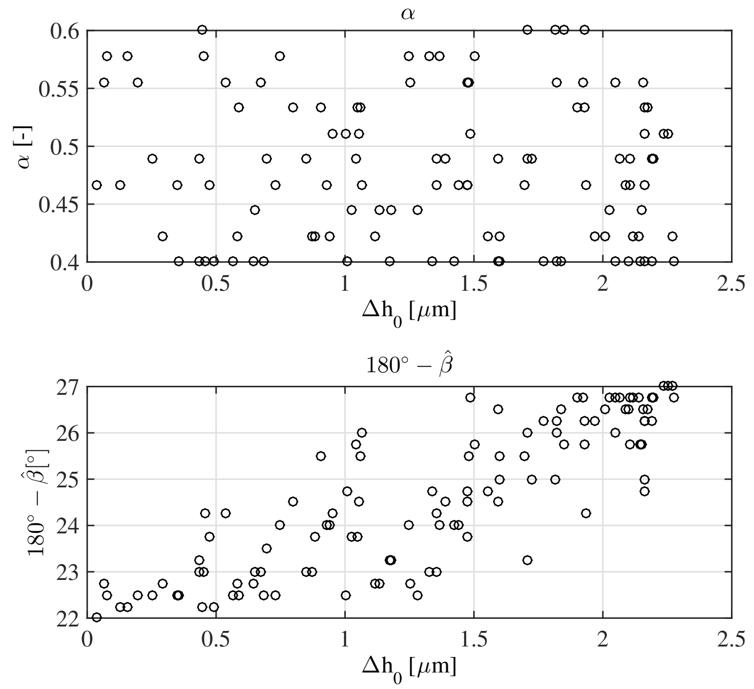

Figure 4.20 – Values of α and $\hat{\beta}$ resulting in the points shown in the Pareto front of Figure 4.19.

$\hat{\beta}$ and δ maximizing the minimum critical mass along the speed range is found in the dimensional look-up table. The results are shown in Figure 4.22. The parameters clearly deviate from the one shown in Figures 4.20 and 4.21. At equal bearing clearance, the groove angle tend to be higher and the grooves deeper when maximizing the tolerance windows and not the stability. This highlights the fact that a pure optimization for the maximization of the critical mass does not yield the same bearing parameters as an optimization maximizing the tolerances along h_0 and δ under the constraint of stable operation, therefore justifying a dedicated optimization procedure.

4.2.3.5 Sensitivity analysis

Starting from the studied rotor, the influence of the dimensionalization parameters on the manufacturing tolerances are studied. These parameters are the ambient pressure and viscosity, the rotor radius, mass and speed. Each parameter is varied of ±20% and the resulting global Pareto fronts are computed. Results are visible in Figure 4.23 to 4.27. The variations on the maximum achievable tolerances on the bearing clearance and groove depth are summarized in Figures 4.28 and 4.29 respectively. A variation on the radius has the largest effect on the tolerance windows with a relative variation on the maximum tolerances more than twice the radius relative variation. For the other

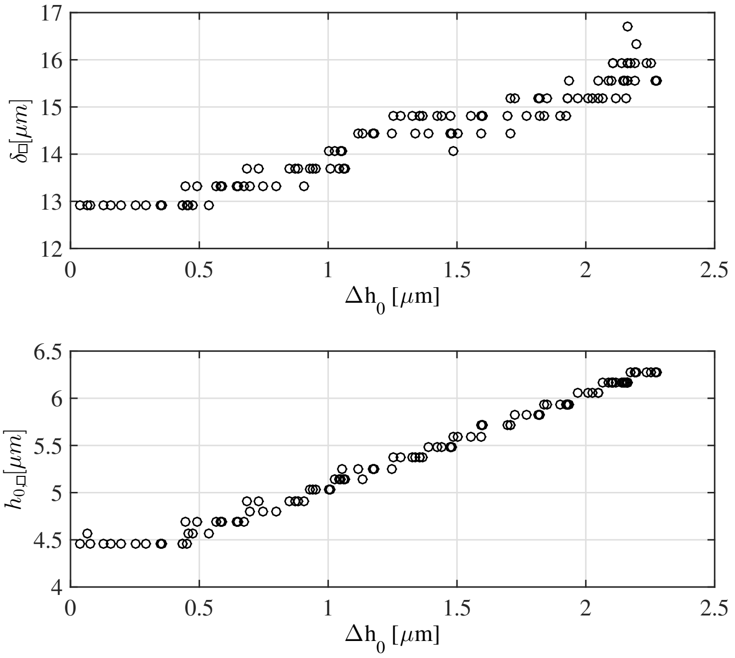

Figure 4.21 – Values of $h_{0,\square}$ and $\delta_\square$ resulting in the points shown in the Pareto front of Figure 4.19.

parameters have an influence smaller than their own variation. For the specific rotor studied here, the maximum rotor speed exhibits a negligible effect on the tolerances, meaning that the stability bottleneck is not located at the maximum speed, but at a lower rotor speed. Considering that the presented strategy is based on the minimum critical speed encountered from rest to maximum speed, increasing the target speed can either have a negative effect or no effect at all, but cannot improve the manufacturing tolerances.

In relative proportions, the tolerance on the bearing clearance is systematically more sensitive to parametric variations than the groove depth tolerance, suggesting that the designers should wisely select the rotor parameters if the goal is to ensure a possibly large tolerance on the bearing clearance. As design guidelines, the results indicate that lighter rotors with a larger diameter at bearing locations, operating at lower ambient pressures and higher temperatures (associated with higher gas viscosities) allow to achieve a broader manufacturing tolerance.

4.2.3.6 Effect of centrifugal growth

Typical high-speed rotors undergo a centrifugal growth leading to a significant reduction of the bearing clearance. The centrifugal growth is proportional to Ω^2, R^3 and to ρ/E.

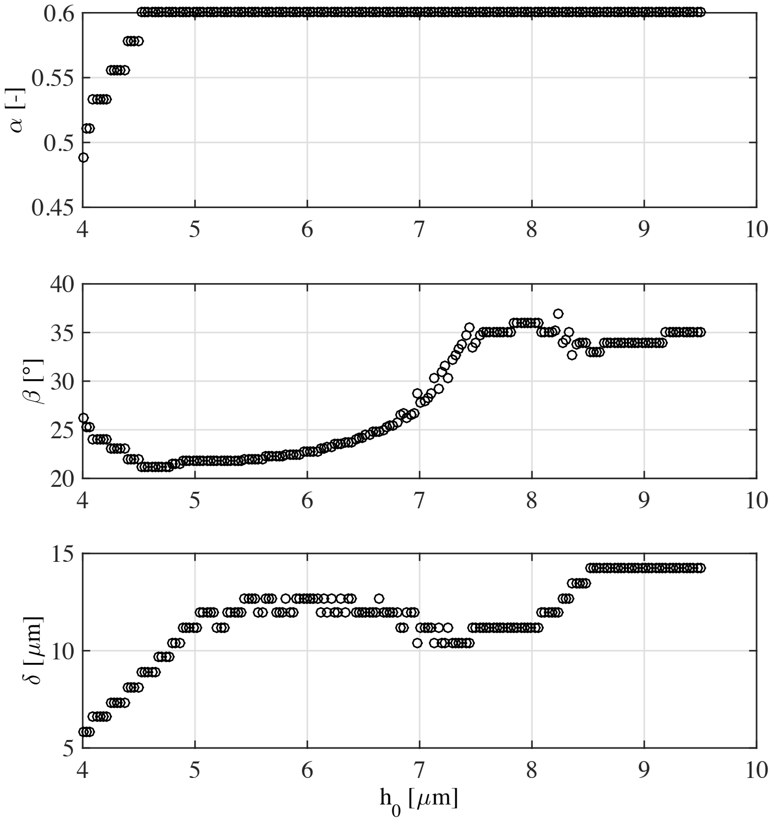

Figure 4.22 – Output parameters from the optimization maximizing the critical mass for different values of h_0.

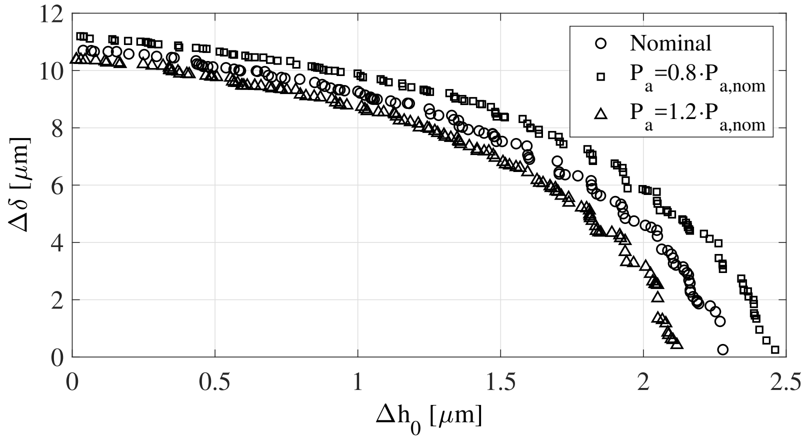

Figure 4.23 – Effect of the ambient pressure on the global Pareto front

The effect of the centrifugal growth is investigated here by setting the absolute radial growth of the rotor at maximum speed and to scale it for the different speeds from rest

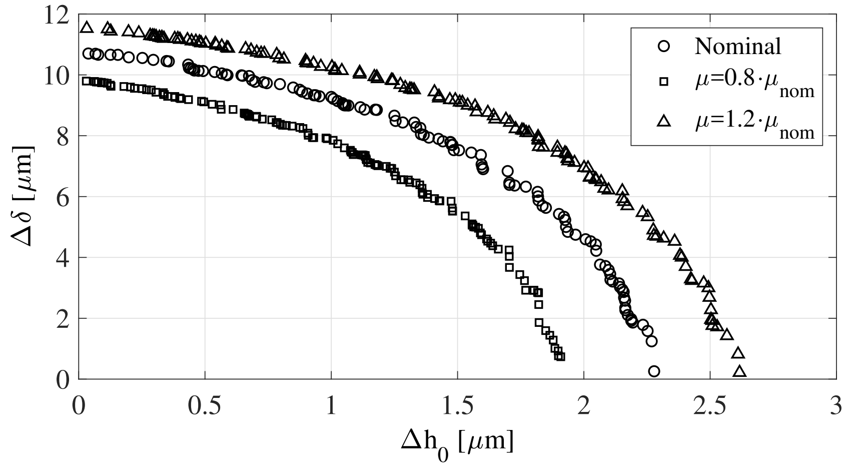

Figure 4.24 – Effect of the gas viscosity on the global Pareto front

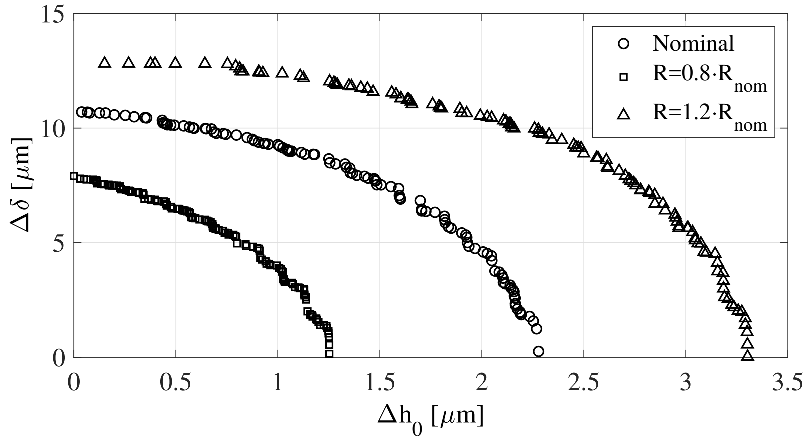

Figure 4.25 – Effect of the rotor radius on the global Pareto front

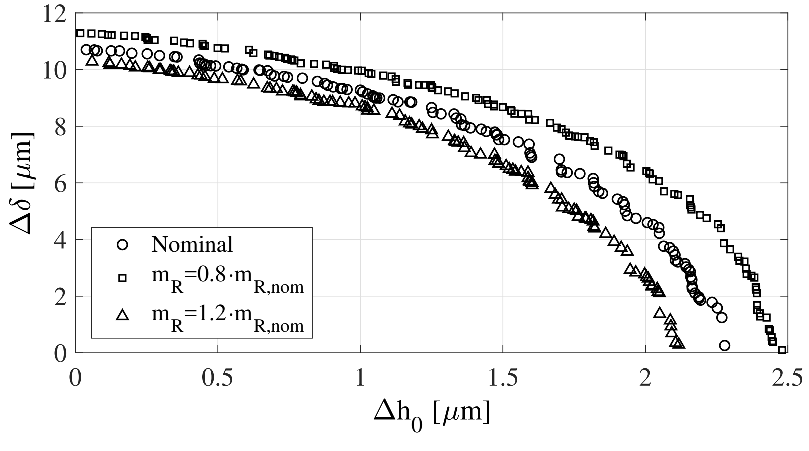

Figure 4.26 – Effect of the rotor mass on the global Pareto front

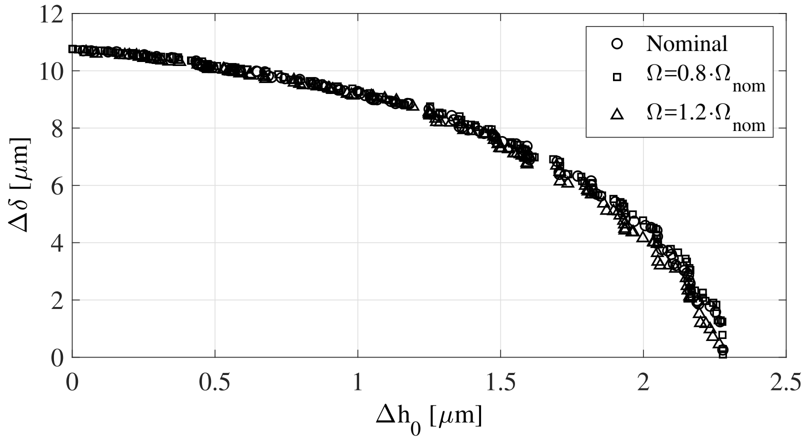

Figure 4.27 – Effect of the rotor maximum speed on the global Pareto front

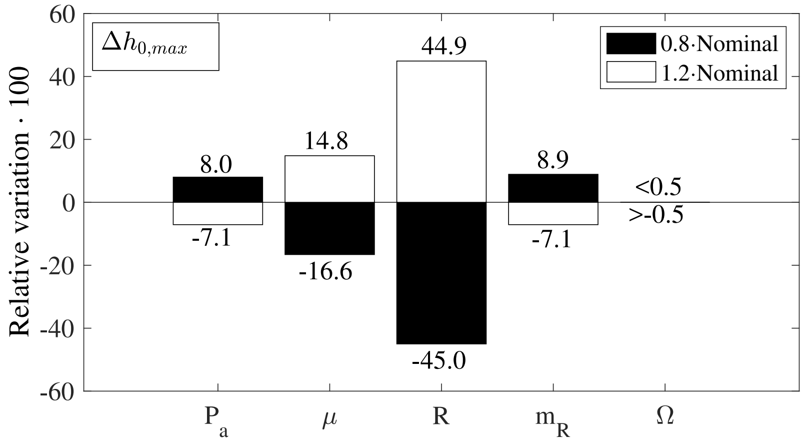

Figure 4.28 – Effect of parametric variation on the maximum clearance tolerance

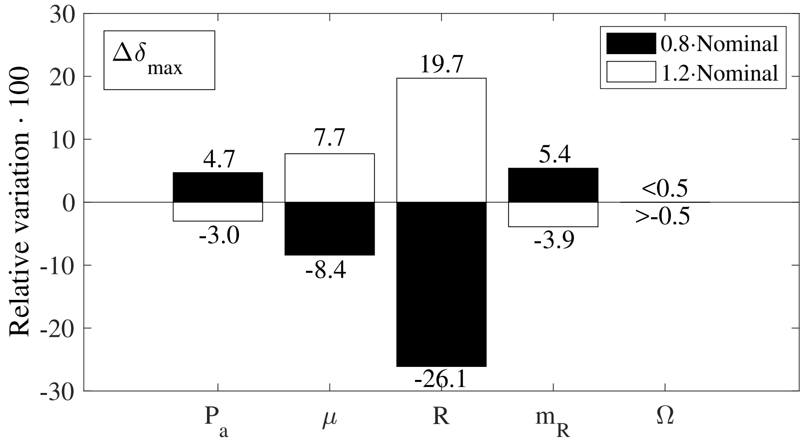

Figure 4.29 – Effect of parametric variation on the maximum groove depth tolerance

to the target rotor speed as follows [1]:

$$\Delta h_{growth} = \Delta h_{growth,max} \frac{\Omega^2}{\Omega_{max}^2} \tag{4.28}$$

which is used to compute the actual clearance:

$$h_r = h_0 - \Delta h_{growth} \tag{4.29}$$

The maximum expansion is set from 0 to 3 µm with a1 µm interval. Results in form of Pareto fronts are represented in Figure 4.30. Centrifugal growth has a slight positive effect of the maximum clearance tolerance. At a radial expansion of 3 µm, the maximum tolerance field is 10.0% higher than the nominal case without centrifugal growth. Interestingly, the maximum groove depth tolerance remains unaffected. The centrifugal growth appears to have a stabilizing effect by reducing the effective clearance. However, as the stability bottleneck happens at a lower speed than the target speed and considering the quadratic dependency of the expansion with the angular velocity, the overall effect is modest.

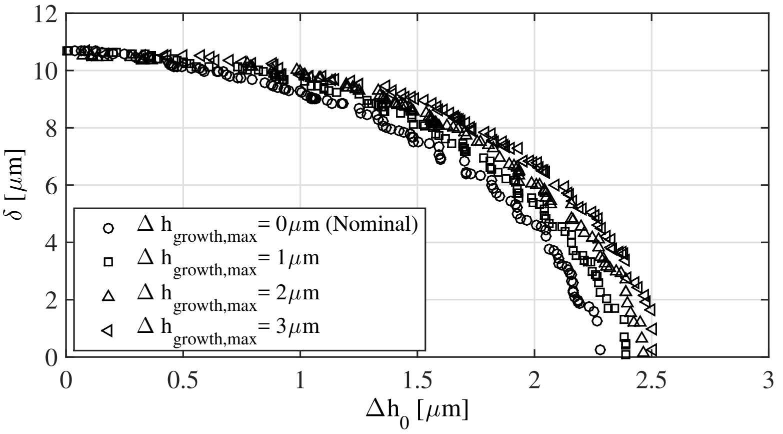

Figure 4.30 – Effect of the centrifugal rotor radial growth on the tolerance Pareto Front

4.2.4 Conclusions

A generalized method to perform a multi-objective optimization of a mechanical system for maximizing the manufacturing tolerances was presented. A computationally-intensive dimensionless look-up table of a feasibility criteria, covering all the design space is computed only once. This matrix is then converted into a dimensional, system-specific matrix at a very low computational cost. From this matrix, the Pareto front of competing manufacturing tolerances is found, allowing the designers to select the appropriate trade-off depending on the available resources. This data-driven methodology to identify the robustness limits with regards to dimensional deviation can be applied to any design problem that can be represented in a non-dimensional form. The method was applied to the problem of rotors supported on herringbone grooved journal bearings, where the critical mass is the feasibility criteria, and the clearance and groove depth the design parameter whose tolerance has to be maximized. A case rotor is investigated, and the influence of multiple rotor parameters on the manufacturing tolerances was analyzed.

The conclusive remarks for this particular design problem are:

- The determination of the manufacturing tolerances on the clearance is competing with the tolerance on the groove depth
- The groove depth tolerance field is significantly larger than the tolerance range on the bearing clearance
- The classical maximization of critical mass does not yield the bearing parameters corresponding to an optimal manufacturing tolerances.
- Low ambient pressures, high gas viscosities, large rotor diameters and low rotor masses allow a larger manufacturing tolerance of the HGJB in both groove depth and bearing clearance
- The centrifugal growth of the rotor has a slight positive influence on the manufacturing tolerance of the bearing clearance but not on the groove depth

The presented method allows to progress toward a cost-oriented design of high-speed gas bearing supported rotors, improving the marketability of such machines. The proposed method can also be generalized to any performance criterion other than the critical mass, not only constrained to stability nor to gas journal bearing. Any design of systems subject to deviations from design point might benefit from the present approach, as long as it can be modeled in a non-dimensional formulation.

4.3 Chapter conclusion

In order to extend the manufacturability and the field of application of aerodynamic bearings, the chapter explored two pathways. A hybrid foil bearing enhanced with spiral groove was proposed and investigated as a mean to improve the load capacity and reduce the drag torque. A multi-objective optimization of the groove parameters identified the improvement potential of this technology over the classical foil thrust bearing design for various configurations and compressibility numbers. The grooved pattern allows an increase of load capacity by 70% or the reduction of the drag torque by 40% while achieving equal or higher load capacity than the original design. However, the presence of spiral grooves designed for low speed appears affect negatively the ultimate load capacity of a foil bearing.

A robust design method maximizing the manufacturing tolerances on multiple bearing design parameters simultaneously was then introduced. The method is based on a large non-dimensional database covering a large portion of the design space, dimensional this space for a specific design case and explores the space for the Pareto-optimal windows of manufacturing tolerances. It was shown that this method yield different results than the sole maximization of the stability of a bearing, thus confirming that maximizing the stability does not maximize the robustness simultaneously. Beyond the scope of aerodynamic bearings, this method can be generalized to any mechanical system that can be modelled in a non-dimensional formulation.

The chapter provides a modelling approach for compliant grooved bearings that can be extended to other bearing types, such as foil journal bearings, which are prompt to dynamic instabilities and detachment of the top foil when sub-ambient pressures are reached in the gas film. The inexpensive addition of spiral grooves on the bearing top foil could be a mean to delay or relief these issues by manipulating the pressure in the gas film. Further research efforts should therefore investigate grooved foil journal bearings with additional objective functions suited for this type of bearing. Maximization of the the critical mass (stability) and minimization of the portion of the bearing encountering sub-atmospheric pressures could be explored. The presented tolerancing optimization method represents an attempt of robust design applied to aerodynamic bearings. In order to extend the practical viability of this method, the stability criterion should be extended to account for the dynamics of a complex rotor with four -or more- degrees of freedom.

Bibliography

[1] J. Schiffmann, D. Favrat, Integrated design and optimization of gas bearing supported rotors, Journal of Mechanical Design 132 (5) (2010) 051007. `doi:10.1115/1.4001381`.

[2] J. Schiffmann, Integrated design and multi-objective optimization of a single stage heat-pump turbocompressor, Journal of Turbomachinery 137 (7) (2015) 071002. `doi:10.1115/1.4029123`.

[3] P. H. Wagner, Z. Wuillemin, S. Diethelm, J. Van herle, J. Schiffmann, Modeling and designing of a radial anode off-gas recirculation fan for solid oxide fuel cell systems, Journal of Electrochemical Energy Conversion and Storage 14 (1) (2017) 011005. `doi:10.1115/1.4036401`.

[4] K. Shalash, J. Schiffmann, On the manufacturing of compliant foil bearings, Journal of Manufacturing Processes 25 (2017) 357–368. `doi:10.1016/j.jmapro.2016.12.021`.

[5] M. Song, S. Azam, J. Jang, S.-S. Park, Effect of shape errors on the stability of externally pressurized air journal bearings using semi-implicit scheme, Tribology International 115 (2017) 580–590. `doi:10.1016/j.triboint.2017.06.037`.

[6] H. Cui, Y. Wang, X. Yue, M. Huang, W. Wang, Effects of manufacturing errors on the static characteristics of aerostatic journal bearings with porous restrictor, Tribology International 115 (2017) 246–260. `doi:10.1016/j.triboint.2017.05.008`.

[7] Y.-B. P. Kwan, J. B. Post, A tolerancing procedure for inherently compensated, rectangular aerostatic thrust bearings, Tribology International 33 (8) (2000) 581–585. `doi:10.1016/S0301-679X(00)00109-2`.

[8] D. P. Fleming, B. J. Hamrock, Optimization of self-acting herringbone journal bearing for maximum stability, in: Proceedings of the fifth international gas bearing symposium, 1974.

[9] J. H. Vohr, C. Y. Chow, Characteristics of herringbone-grooved, gas-lubricated journal bearings, Journal of Basic Engineering 87 (3) (1965) 568–576. `doi:10.1115/1.3650607`.

[10] V. Castelli, J. H. Vohr, Performance characteristics of herringbone- grooved journal bearings operating at high eccentricity ratios and with misalignment, Gas Bearing Symposium (14) (1967) 1–17.

[11] J. W. Lund, Calculation of stiffness and damping properties of gas bearings, Journal of Lubrication Technology 90 (4) (1968) 793–803. `doi:10.1115/1.3601723`.

[12] J. Schiffmann, Integrated design, optimization and experimental investigation of a direct driven turbocompressor for domestic heat pumps, Ph.D. thesis, École Polytechnique Fédérale de Lausanne, Lausanne (2008). `doi:10.5075/epfl-thesis-4126`.

[13] E. Rasmussen, P. Rudolph, A. Mamishev, An experimental study of 3d printed herringbone grooved journal bearings, in: ASME 2017 International Mechanical Engineering Congress and Exposition, 2017. `doi:10.1115/IMECE2017-73502`.

[14] I. Ognjanovic, Experimental contribution to the mechanics of herringbone grooved journal air bearings, Ph.D. thesis, École Polytechnique Fédérale de Lausanne, Lausanne (2011). `doi:10.5075/epfl-thesis-4879`.

[15] M. Ochiai, N. Kato, H. Hashimoto, Groove shape optimization of thrust air bearing for small size spindle considering the processing errors, in: Proceedings of the ASME-JSME 2018, 2018, p. 3.

[16] N. Jawahar, R. Sivasankaran, M. Ramesh, Optimal pareto front for manufacturing tolerance allocation model, Vol. 231, 2017, pp. 1190–1203. `doi:10.1177/0954405415586548`.

[17] J. Natarajan, R. Sivasankaran, G. Kanagaraj, Bi-objective optimization for tolerance allocation in an interchangeable assembly under diverse manufacturing environment, The International Journal of Advanced Manufacturing Technology 95 (5) (2018) 1571–1595. `doi:10.1007/s00170-017-1232-y`.

5 Epilogue

5.1 Summary

The ability of the Narrow Groove Theory (NGT) to predict the dynamic coefficients of Herringbone Groove Journal Bearing (HGJB) was tested against experimental data. A test rig was built and employed in air to dynamically excite the bearing bushings of a 16 mm diameter rotor running at 100 krpm and retrieve the dynamic stiffness and damping coefficients from the displacement measurements, following a novel technique. The dynamic force coefficients were evaluated at different rotor speeds, excitation frequencies, excitation amplitudes and test rig orientation with regard to gravity. The NGT was found to provide qualitatively valid predictions although it tends to overestimate the bearing properties. The prediction based on the largest measured bearing clearance fitted best the experimental data. Of the 8 bearing dynamic coefficients, only the direct damping exhibited a significant non-linear behavior regarding the excitation amplitude. The rotor weight had a negligible effect on the identified force coefficients. This work fills a gap in the literature and further assess the validity of the NGT as a design and simulation tool.

Once experimentally validated, the NGT and the Reynolds equation were adapted to capture real-gas and humid air effects. Multiple bearing geometries were investigated (Rayleigh step slider bearing, plain journal bearing and herringbone groove journal bearing) in a non-dimensional framework in order to keep the observations as scalable as possible. When expressed in terms of reduced temperature and pressure (normalized by their respective value at the critical point) real-gas effects were found to be mostly fluid-independent. The increase of compressibility induced by the real-gas effects have a negative influence on the load capacity of investigated bearings. The effect on stability is either positive or negative depending on the reduced ambient condition and the compressibility number. Since the validity of the NGT depends on the assumption of incompressibility between each groove-ridge pair, a compressibility number threshold accounting for the real-gas effects was suggested, beyond which the NGT might deviate significantly due to local incompressibility. The humid air effects were found to have negligible effects on the load capacity of journal bearings. However, in very hot and humid ambient environments, the partial condensation of water in the air film can lead to a drop in the minimum critical mass of 25%, which is significant enough to be taken into account in the design process of a airborne turbomachinery operating in uncontrolled environments.

A model based on the Reynolds equation was developed and implemented to account for condensation in pure fluid gas lubricant. This model is based on the development in liquid-lubricated bearing and was used to study three 1-D slider bearings in near-saturation conditions. Because it limits the maximum pressure in the film to the saturation pressure corresponding to the ambient temperature, condensation was found to generally reduce the load capacity of such bearings. However, small gains in reaction force were predicted in particular conditions, due to the extension of a high-pressure zone toward the end of the bearing leading to an overall gain in load capacity. An original test rig was built to validate the model. The apparatus consists of a short 20 mm three-pocket Rayleigh step journal bearing driven by a high-speed DC motor via a flexible coupling, inspired by the very first gas bearing apparatus presented by Kingsbury in 1897. The test rig was enclosed in a pressure chamber filled with R245fa brought in near-saturation conditions and running at 30 krpm. Five pressure taps allowed to measure the gas film pressure along one of the bearing pockets. Both saturated and non-saturated tests were in very good agreement with the model. Condensation-induced touch-downs were experienced, however without any sub-synchronous frequency in the radial motion associated with a typical whirl instability. This indicates that achieving condensation within a thin gas film is possible but should be avoided for the sake of mechanical integrity. Furthermore, this work brings an additional evidence supporting the isothermal assumption in the compression occurring in a gas bearing.

In an attempt to explore the combination of foil and grooved bearings, a layout of Foil Thrust Bearing enhanced with spiral grooves was proposed and numerically investigated with a NGT-based model. Multi-objective optimization was performed on the groove geometry in order to identify promising geometries and assess the potential of the technology in terms of load capacity and drag torque. Results indicate that the load capacity can be increased by nearly 70% or a drag torque decreased by 40% compared to the ungrooved foil thrust bearing. However, the performance of the grooved bearing in very thin gas height was found to be systematically poorer than the smooth version, indicating that spiral grooves do not improve the ultimate load capacity of such bearings.

Finally, a novel optimization technique to maximize the robustness of HGJBs on key design parameters such as the nominal clearance and the groove depth was presented. The method explores a large normalized design space composed of millions of HGJB geometries evaluated in term of critical mass. The method employs a Monte-Carlo method to look for the region of this hyperspace offering an Pareto-optimal trade-off between the robustness on the key parameters, finally yielding a Pareto curve showing all optimal possibilities of robust design for a specific airborne rotor. The designer is then free to chose an optimal point based on the manufacturing resources available. The optimally robust designs deviate significantly from the design maximizing the critical mass alone, highlighting that maximizing the robustness and maximizing the stability are not equivalent. The method was applied on an example rotor and a sensitivity analysis could identify the bearing diameter and the lubricant viscosity as the parameters having the most influence on the robustness. The presented procedure is generalizable to any multi-variable system subjected to uncertainties.

5.2 Future work

The present work opens new ways in high-pressure gas lubricated bearings and design procedure for airborne rotating machinery. The suggestions are as follows:

- A research effort should be spent on experimentally validating the real-gas modelling of herringbone grooved journal bearings. The experimental procedure presented in Chapter 2.4 should be repeated in high-pressure refrigerant for this purpose, with the difference that a direct drive should be used instead of the impulse turbine, unsuited for confined environments.
- The test rig developed in Chapter 3.3 should be used in pressure chambers to validate the prediction of static pressure fields including 1) real-gas effects, 2) turbulence and 3) rarefied gas effects. This test rig is sufficiently small and simple to keep the cost and time requirements of such researches reasonable.
- The gas bearing model including isothermal condensation should be extended to become a practical design tool. In particular, it should 1) be extended for a bearing of finite axial length, 2) include the evaluation of dynamic effects, either using the perturbation method or a time-domain integration, and 3) be applied on HGJBs. The latter will require to resolve the grooves with the help of the Reynolds equation, since the assumption of local incompressibility necessary to the NGT is not met under isothermal condensation (equivalent to an infinite compressibility).
- Effect of condensation on a HGJB-supported rotor should be experimentally observed with a dedicated test rig to address the influence of saturation on the stability of the system
- An experimental investigation of the performance of Foil Thrust Bearings enhanced with spiral grooves should be performed to validate the model introduced in Chapter 4.1. Other layouts of such bearings should be investigated, such as a full 360° foil spiral groove bearing similar to Licht's bearing.
- The numerical analysis of grooved Foil Journal Bearings should be performed to assess its potential performance, in terms of load capacity, drag torque an stability.

More advanced grooving patterns should be investigated, for example with groove parameters varying along the axial and the circumferential direction.

- The design procedure for robustness maximization should be extended using more complete stability metrics beyond the critical mass (logarithmic decay of multi-DOF rotor-bearing systems). Because of the tremendous computation cost of the presented technique when not using the simple yet scalable critical mass, reduction methods such as surrogate models should be considered. The integration of enhanced groove geometries, with non-constant groove parameters evolving along the axial direction of the bearing, should be explored with this method. A research effort in this direction could lead to a strong reduction of the sensitivity of HGJBs against manufacturing errors and reduce strongly the production costs.
- The effect of shape errors such as cylindricity and circularity on the stability of rotor-bearing systems should be studied both numerically and experimentally. The NGT-based model presented in Chapter 2 can be used for this purpose, since it can model a non-circular bushing. It should also be used to study the influence of side pressurization, where the two axial ends of a journal bearing at not at the same pressure level, which is often the case in airborne turbomachinery.

A Reynolds equation

Two surfaces, A and B, are in relative motion in 3 directions within a lubricant fluid, as illustrated in Figure A.1. Surface B has the velocity ($\vec{u}$,$\vec{w}$,$\vec{v}$) in the directions ($\vec{x}$,$\vec{y}$,$\vec{z}$) respectively, while A is static. The film thickness h between the two surfaces is very small compared to the lengths in directions $\vec{x}$ and $\vec{z}$. The following assumptions are made:

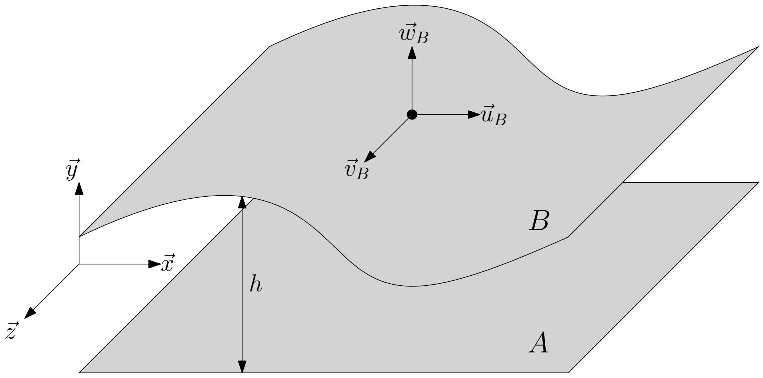

Figure A.1 – Surfaces in motion in a lubricant

- The lubricant is a Newtonian fluid
- The film thickness is much smaller than the two other orthogonal directions
- The fluid characteristics (viscosity, pressure, density) are constant across the film thickness
- Viscous forces dominate the inertia and the flow is laminar

Under such conditions, the Navier-Stokes equations boil down to the following expressions in $\vec{x}$ and $\vec{z}$:

$$\begin{aligned} \frac{\partial p}{\partial x} &= \frac{\partial}{\partial y}\left(\mu \frac{\partial u}{\partial y}\right) \\ \frac{\partial p}{\partial z} &= \frac{\partial}{\partial y}\left(\mu \frac{\partial v}{\partial y}\right) \end{aligned} \qquad \text{A.1}$$

These equations are integrated once:

$$\begin{aligned} \frac{\partial u}{\partial y} &= \frac{y}{\mu}\frac{\partial p}{\partial x} + \frac{A}{\mu} \\ \frac{\partial v}{\partial y} &= \frac{y}{\mu}\frac{\partial p}{\partial z} + \frac{B}{\mu} \end{aligned} \qquad \text{A.2}$$

and twice, to obtain an expression of the velocity in the two directions $\vec{x}$ and $\vec{z}$

$$\begin{aligned} u &= \frac{y^2}{2\mu}\frac{\partial p}{\partial x} + A\frac{y}{\mu} + B \\ v &= \frac{y^2}{2\mu}\frac{\partial p}{\partial z} + C\frac{y}{\mu} + D \end{aligned} \qquad \text{A.3}$$

The boundary conditions are applied as follows :

$$\begin{aligned} & y = 0, u = 0, v = 0 \\ & y = h, u = u_B, v = v_B \end{aligned} \qquad \text{A.4}$$

Which allows to express the four integration constants of equation A.3:

$$\begin{aligned} u &= -y\left(\frac{h-y}{2\mu}\right)\frac{\partial p}{\partial x} + u_B\frac{y}{h} \\ v &= -y\left(\frac{h-y}{2\mu}\right)\frac{\partial p}{\partial z} + v_B\frac{y}{h} \end{aligned} \qquad \text{A.5}$$

The mass flow rate per unit length is expressed by integrating the velocity over the thickness of the film times the average density across the film:

$$\begin{aligned} \psi_x = \rho\int_0^h u\mathrm{d}y \quad &= \rho\left(-\frac{h^3}{12\mu}\frac{\partial p}{\partial x} + \frac{u_b}{2}h\right) \\ \psi_y = \rho\int_0^h v\mathrm{d}y \quad &= \rho\left(-\frac{h^3}{12\mu}\frac{\partial p}{\partial y} + \frac{v_b}{2}h\right) \end{aligned} \qquad \text{A.6}$$

The continuity equation is integrated over the film thickness:

$$\int_0^h \left(\frac{\partial \rho}{\partial t} + \frac{\partial}{\partial x}(\rho u) + \frac{\partial}{\partial z}(\rho v) + \frac{\partial}{\partial y}(\rho w)\right) \mathrm{d}y = 0 \tag{A.7}$$

It is convenient to use the following general integration rule to express the continuity equation:

$$\int_0^h \frac{\partial}{\partial \gamma}[f(\gamma, y)]dy = \frac{\partial}{\partial \gamma}\left(\int_0^h f(\gamma y)\mathrm{d}y\right) - f(\gamma, h)\frac{\partial h}{\partial \gamma} \tag{A.8}$$

The second term of Eq.A.7 is developed as follows:

$$\int_0^h \frac{\partial}{\partial x}(\rho u)\mathrm{d}y = -\rho u_b \frac{\partial h}{\partial x} + \frac{\partial}{\partial x}\left(\rho \int_0^h u\mathrm{d}y\right) \tag{A.9}$$

Similarly, for the third term:

$$\int_0^h \frac{\partial}{\partial z}(\rho v)\mathrm{d}y = -\rho v_b \frac{\partial h}{\partial y} + \frac{\partial}{\partial y}\left(\rho \int_0^h v\mathrm{d}y\right) \tag{A.10}$$

The fourth term of the continuity equation is simply integrated:

$$\int_0^h \frac{\partial}{\partial y}(\rho w)\mathrm{d}y = \rho w_b \tag{A.11}$$

Finally, the continuity equation leads to the following expression, where one can identify the mass flow rate per unit length ψ_x and ψ_z, in $\vec{x}$ and $\vec{z}$ respectively:

$$\frac{\partial}{\partial x}\underbrace{\left(\rho \int_0^h u\mathrm{d}y\right)}_{\psi_x} + \frac{\partial}{\partial z}\underbrace{\left(\rho \int_0^h v\mathrm{d}y\right)}_{\psi_z} + h\frac{\partial \rho}{\partial t} + \rho \underbrace{\left(-u_b\frac{\partial h}{\partial x} - v_b\frac{\partial h}{\partial z} + w_b\right)}_{\frac{\partial h}{\partial t}} = 0 \tag{A.12}$$

The last three terms of Equation A.12 can be grouped in $\frac{\partial h}{\partial t}$, following the development of the material derivative. It is expressed as follows:

$$\frac{\mathrm{D}h}{\mathrm{D}t} = \frac{\partial h}{\partial t} + \frac{\partial h}{\partial x}\frac{\mathrm{d}x}{\mathrm{d}t} + \frac{\partial h}{\partial z}\frac{\mathrm{d}z}{\mathrm{d}t} \tag{A.13}$$

The derivative terms can be substituted:

$$\frac{\mathrm{d}x}{\mathrm{d}t} = u_b \quad \frac{\mathrm{d}y}{\mathrm{d}t} = v_b \qquad \frac{\mathrm{D}h}{\mathrm{D}t} = w_b \tag{A.14}$$

Leading to the partial derivative of h in time:

$$\frac{\partial h}{\partial t} = \left(-u_b \frac{\partial h}{\partial x} - v_b \frac{\partial h}{\partial z} + w_b\right) \qquad \text{A.15}$$

Finally, using Eq.A.6, the Reynolds equation is obtained:

$$0 = \frac{\partial}{\partial x}\left(-\frac{\rho h^3}{12\mu}\frac{\partial p}{\partial x}\right) + \frac{\partial}{\partial z}\left(-\frac{\rho h^3}{12\mu}\frac{\partial p}{\partial z}\right) + \frac{\partial}{\partial x}\left(\frac{\rho h u_B}{2}\right) + \frac{\partial}{\partial z}\left(\frac{\rho h v_B}{2}\right) + \frac{\partial(\rho h)}{\partial t} \qquad \text{A.16}$$

B Matrix coefficient of bearing impedance identification

$$\mathbf{A} = \begin{bmatrix} a_1 & a_2 & 0 & 0 & a_3 & a_4 & 0 & 0 \\ 0 & 0 & a_5 & a_6 & 0 & 0 & a_7 & a_8 \\ a_9 & a_{10} & 0 & 0 & a_{11} & a_{12} & 0 & 0 \\ 0 & 0 & a_{13} & a_{14} & 0 & 0 & a_{15} & a_{16} \end{bmatrix} \tag{B.1}$$

$$a_1 = x + L_A\alpha - x_A \tag{B.2}$$
$$a_2 = y - L_A\beta - y_A \tag{B.3}$$
$$a_3 = x - L_B\alpha - x_B \tag{B.4}$$
$$a_4 = y + L_B\beta - y_B \tag{B.5}$$
$$a_5 = y - L_A\beta - y_A \tag{B.6}$$
$$a_6 = x + L_A\alpha - x_A \tag{B.7}$$
$$a_7 = y + L_B\beta - y_B \tag{B.8}$$
$$a_8 = x - L_B\alpha - x_B \tag{B.9}$$
$$a_9 = L_A(x + L_A\alpha - x_A) \tag{B.10}$$
$$a_{10} = L_A(y - L_A\beta - y_A) \tag{B.11}$$
$$a_{11} = -L_B(x - L_B\alpha - x_B) \tag{B.12}$$
$$a_{12} = -L_B(y + L_B\beta - y_B) \tag{B.13}$$
$$a_{13} = -L_A(y - L_A\beta - y_A) \tag{B.14}$$
$$a_{14} = -L_A(x + L_A\alpha - x_A) \tag{B.15}$$
$$a_{15} = L_B(y + L_B\beta - y_B) \tag{B.16}$$
$$a_{16} = L_B(x - L_B\alpha - x_B) \tag{B.17}$$

C HGJB groove parameters measurements

The assessment method of the groove parameters for the HGJBs presented in Chapter 2 is presented here.

Groove angle and aspect ratio

The groove angle $\hat{\beta}$ and the groove aspect ratio α are controlled optically using a computer-controlled microscope and numerical measurement tools. Figure C.2 show the measurement of the groove angle $\pi - \hat{\beta}$, estimated to be $20.041° \pm 0.05°$, close to the nominal value of 20° ($\hat{\beta}$=160°).

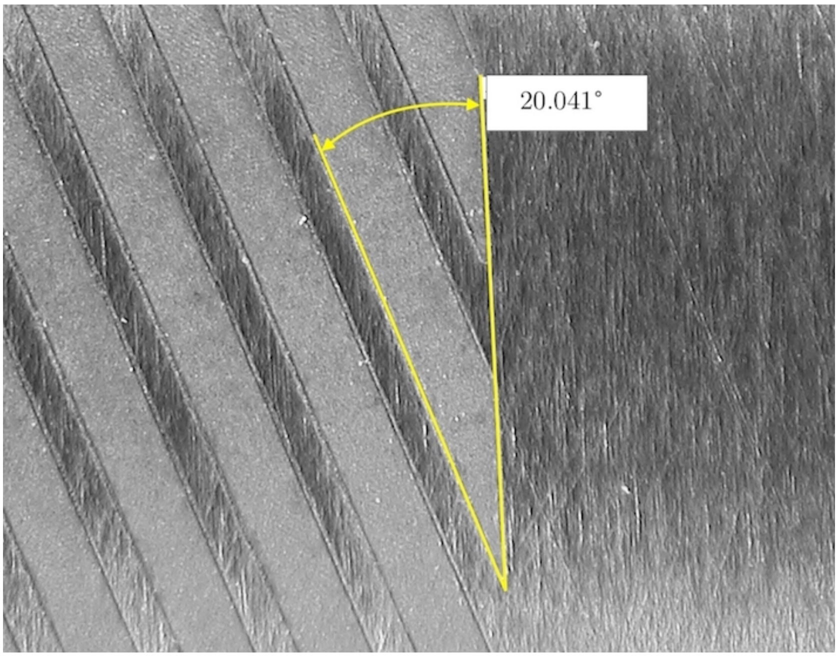

Figure C.1 – Optical measurement of the groove angle using a digital microscope

The groove aspect ratio is determined by the measurement of the groove width and of the ridge width, using the same tool as for the groove angle. The results gives an estimation of $\alpha = 0.6509 \pm 0.005$, close to the nominal value of 0.65.

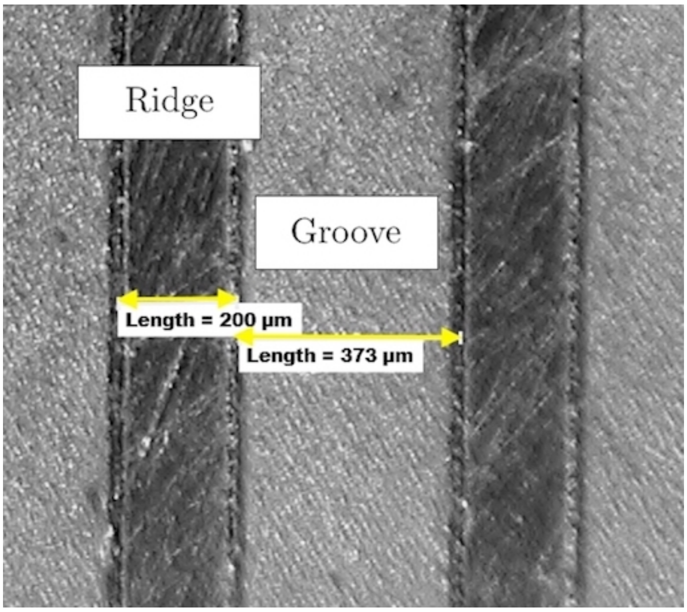

Figure C.2 – Optical measurement of the groove aspect ratio using a digital microscope

Groove depth

The groove depth is measured using a rugosimeter *TESA Rugosurf 90G* measuring the bearings along the axial direction over a ridge-groove pair. The measurement setup is shown in Figure C.3 and an example of measured profile is showed in Figure 2.38. The groove depth was measured between 15 and 17 µm.

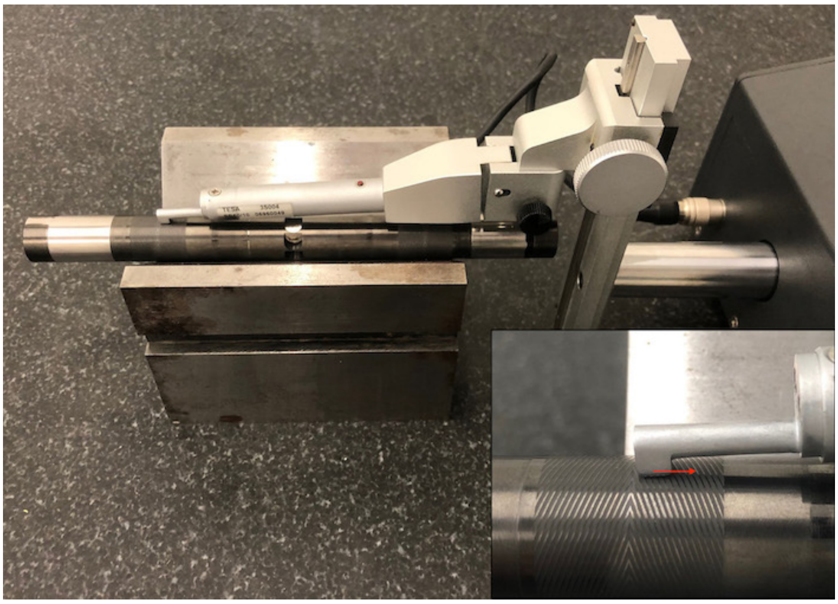

Figure C.3 – Measurement of the groove depth using a rugosimeter

D Parameters and displacement uncertainties

D.1 Rotor mass

The rotor mass was measured on a precision scale with 10 measurements, leading to an overall uncertainty of 3 mg.

D.2 Rotor transverse inertia

The nominal value on the rotor transverse inertia $I_{T,0}$ is given using a 3D model of the shaft, given its nominal density and geometry. The uncertainty on this value is assumed to come from the balancing planes, because they lay at the extremities of the shaft, the furthest from the center of mass. To estimate the effect of balancing on the inertia, a worst case scenario is investigated, consisting of a annular removal of matter on the axial faces of the rotor (Figure D.1). A ring of matter has a transverse rotational inertia of I_Δ. The nominal case would consist in the rings half-removed, therefore of depth 1 mm. The uncertainty would then reside on the depth of the rings: ±1 mm, leading to the final value for the inertia:

$$I_T = I_{T,0} - I_\Delta \pm I_{T,\Delta} \tag{D.1}$$

$$I_{T,\Delta} \approx m_\Delta l_\Delta^2 \tag{D.2}$$

Where m_Δ and l_Δ are respectively the mass of a ring and its mean distance from the center of mass. Applying the dimensions of Figure D.1 and $\rho = 7700\,\mathrm{kg\,m^{-3}}$, this leads to :

$$I_T = 7.01 \cdot 10^{-4}\,\mathrm{kg\,m^2} \pm 1.12 \cdot 10^{-5}\,\mathrm{kg\,m^2} \tag{D.3}$$

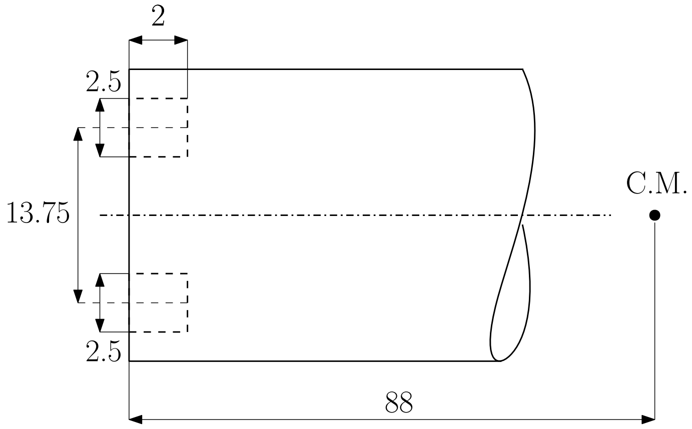

Figure D.1 – Close view of the annular mass removal scenario for estimation of the uncertainty on transverse inertia

D.3 Rotor axial inertia

The uncertainty on the polar inertia is estimated following the same approach as for the transverse inertia. Assuming a ring of removed mass as described in Figure D.1, the nominal value on the rotor transverse inertia $I_{P,0}$ is given using a 3D model of the shaft, given its nominal density and geometry. It is then corrected by the removal of two half rings, with un uncertainty of two half rings:

$$I_P = I_{P,0} - I_\Delta \pm I_{P,\Delta} \tag{D.4}$$

$$I_{P,\Delta} \approx \frac{1}{2} m_\Delta (r_o^2 - r_i^2) \tag{D.5}$$

where r_o and r_i are the outer and inner radius of the ring, respectively. It leads to the following inertia:

$$I_P = 8.83 \cdot 10^{-6}\,\mathrm{kg\,m^2} \pm 2.50 \cdot 10^{-7}\,\mathrm{kg\,m^2} \tag{D.6}$$

D.4 Center of mass position

Following the approach with the two rings of removed mass, the uncertainty on the axial position of the center of mass Δx_{CM} is :

$$\Delta x_{CM} = \frac{m_\Delta \cdot L}{M_r} = 0.2\,\mathrm{mm} \tag{D.7}$$

where L is the distance between the geometrical center (corresponding to the center of mass of the perfect rotor) and the axial center of the ring. This value is taken as the dominant uncertainty on the the parameters L_W and L_B of Table 2.9, respectively the distance of the probes $\mathrm{W}_{2,4,6,8}$ to the center of mass and the distance of the bearing center to the center of mass. The geometrical uncertainty σ_{geom} affecting these two values are estimated to be 0.15 mm, corresponding to the manufacturing tolerance ISO 2768f to these scales of length. Therefore, the uncertainty on these parameters is:

$$\sigma = \sqrt{\Delta x_{CM}^2 + \sigma_{geom}^2} = 0.25\,\mathrm{mm} \qquad \text{D.8}$$

D.5 Displacement probes

D.5.1 Random error

The random error from the displacement probes is assessed by capturing 1 s of data at the nominal sampling rate (50 kHz) at rest, and computing the standard deviation of the recorded data. Figure D.2 depicts the histogram of the recorded data for channel W_1, exhibiting the normal nature of its distribution.

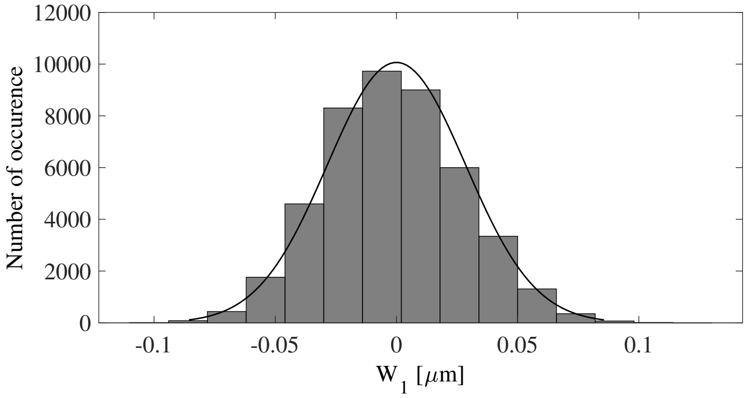

Figure D.2 – Distribution of the recorded data from W_1 in static conditions around its mean value

The standard deviation of the 8 channels is shown in Figure D.3. These values are used to evaluate the uncertainty on the amplitude and phase of the sine function fitted on the data by the least square method, namely:

$$\sigma_A = \frac{\sigma}{\sqrt{\frac{N}{2}}} \qquad \text{D.9}$$

$$\sigma_\phi = \frac{\sigma}{A\sqrt{\frac{N}{2}}} \qquad \text{D.10}$$

Where N is the number of points in the data, typically $2 \cdot 10^5$ for a 4 second excitation run, and A the amplitude of the fitted sine. Figure D.4 and D.5 present the resulting uncertainties for amplitude and phase, applying a guess amplitude A of 0.2 µm for the sake of example.

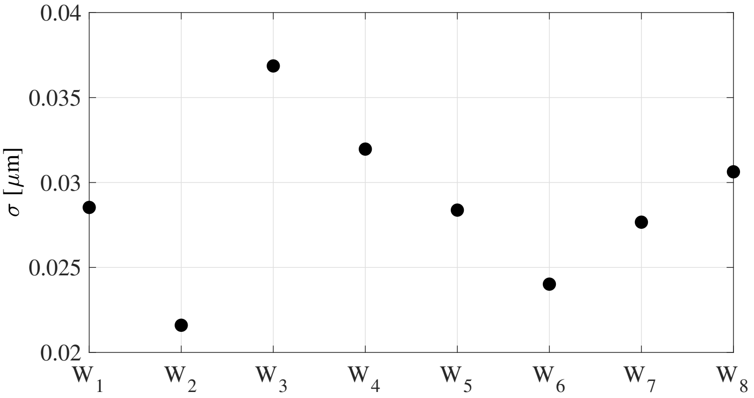

Figure D.3 – Standard deviation due to random error of each of the 8 displacement channels

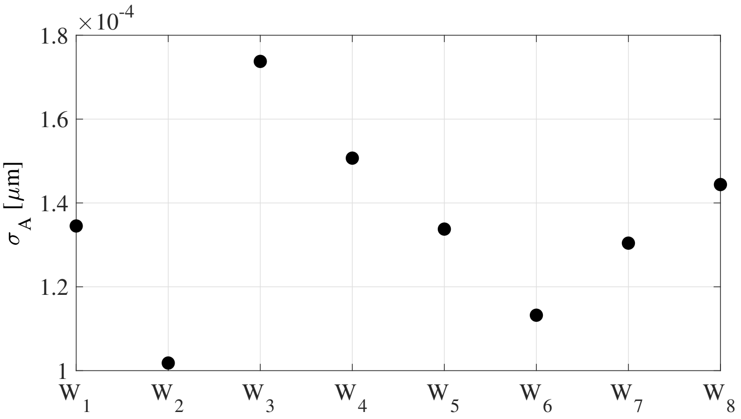

Figure D.4 – Uncertainty on the amplitude of the fitted sine from $2 \cdot 10^5$ data points

D.5.2 Linearity error

The proximity probes manufacturer guarantee a maximum linearity error of 0.026% of the full measurement range, here 500 µm, resulting in a absolute deviation of 0.13 µm. However, this value is not the uncertainty on the amplitude of a small relative displacement where the absolute position is meaningless. The significant metric to know is the deviation of the sensor sensitivity from linearity. In order to address it, the manufacturer provided the author with a calibration report of such a device, showing the relative deviation on voltage in function of the absolute position. The data were digitized and fitted with a polynomial, to be then scaled up to reach a maximum relative deviation of 0.026%,

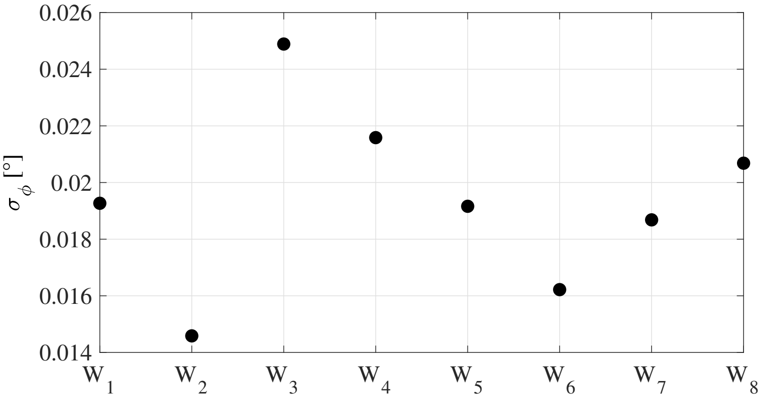

Figure D.5 – Uncertainty on the phase of the fitted sine from $2 \cdot 10^5$ data points, assuming a sine amplitude of 0.2 µm

representing a conservative case (Figure D.6) .

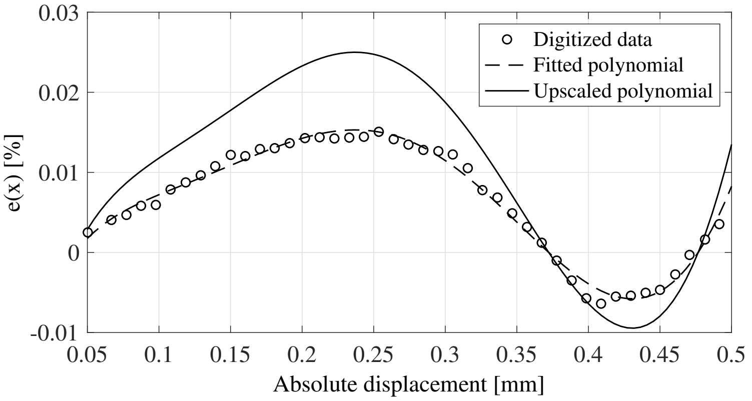

Figure D.6 – Relative linearity error on the voltage, scaled on the full scale range of the sensor

$$e(x) = \frac{V(x) - V_{lin}(x)}{V_{max}} \tag{D.11}$$

$$V(x) = V_{max} e(x) + V_{lin}(x) \tag{D.12}$$

Defining the sensitivity α:

$$\alpha = \frac{\mathrm{d}V(x)}{\mathrm{d}x} = V_{max} \frac{\mathrm{d}e(x)}{\mathrm{d}x} + \frac{\mathrm{d}V_{lin}(x)}{\mathrm{d}x} = V_{max} \frac{\mathrm{d}e(x)}{\mathrm{d}x} + \alpha_{lin} \tag{D.13}$$

And the error on the amplitude of a relative displacement:

$$Err = \frac{\Delta x_{lin} - \Delta x}{\Delta x_{lin}} = \frac{\alpha - \alpha_{lin}}{\alpha} \qquad \text{D.14}$$

$$Err = 1 - \frac{\alpha_{lin}}{V_{max}\frac{\mathrm{d}e(x)}{\mathrm{d}x} + \alpha_{lin}} \qquad \text{D.15}$$

The result of this equation is shown in Figure D.7 for different absolute positions. The upper bound for the linearity error of the local measurement of small amplitude displacement is 0.4 %. This conservative value is used in the uncertainty computations.

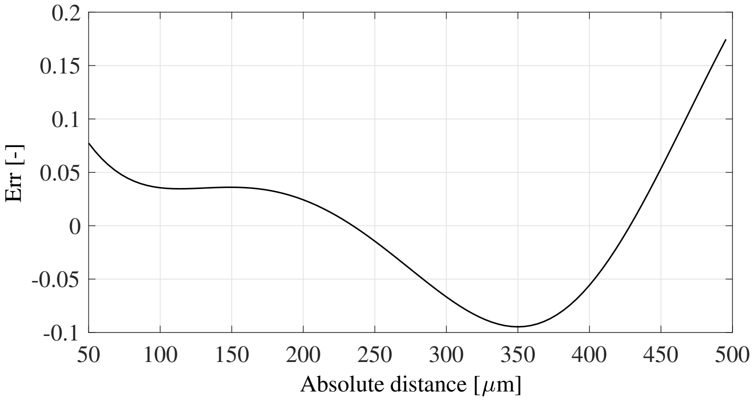

Figure D.7 – Relative error on small relative displacements against the absolute position

D.5.3 Roundness error

The displacement capacitive sensors are provided with a default calibration for a flat surface. However, the target of 4 of the 8 probes bearing a rotor, the curvature of the target has an influence of the measurements, especially when the measurement distance is small. In order to quantify the measurement error of small amplitude displacements caused by the curvature, a test rotor of diameter 16 is installed on a calibration rig (Figure D.8) consisting of a micrometric screw moving a slider where the target is attached, whose position is measured by a reference displacement probe. In front of the target is fixed the test probe. The micrometric screw is slowly actuated to push the target toward the probe while both displacements are being recorded.

The absolute error against position is shown in Figure D.9, with a logarithmic curve fitted on the data points. The capacitive sensor reports a distance systematically higher than the output of the reference probe. The error is maximum when the distance is maximum, with an offset of the 0 point (physical contact between the probe head and the target surface) of approximately 26 µm. However, as only relative displacements are of importance for the identification of bearing impedances, the error on the sensitivity of

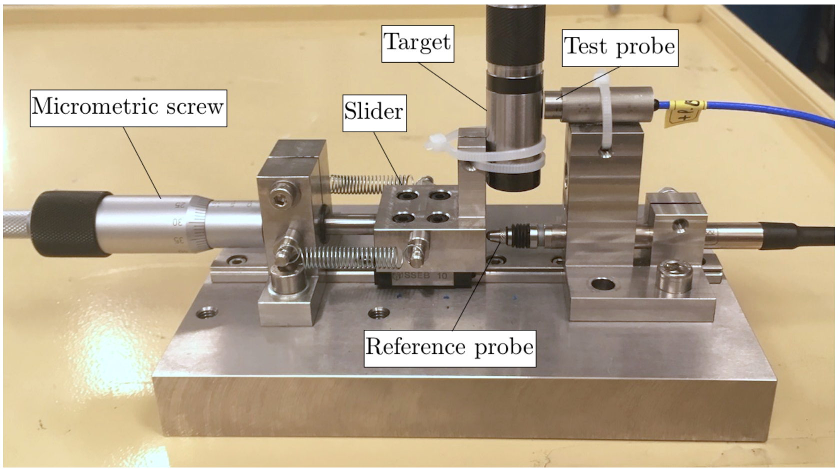

Figure D.8 – Calibration apparatus assessing the measurement error due to curvature of the target

the probe is the relevant metric to assess. The relative sensitivity error, i.e. the derivative of the error over the displacement based on the fitted curve, is shown in Figure D.10. The relative error is maximum when the target and probe head are in physical contact, and decreases monotonically as the two element are moved apart. The threshold of 5% error on the sensitivity is reached at a approximately 0.3 mm, therefore the sensors are employed beyond this limit in order to keep the sensitivity error to acceptable values.

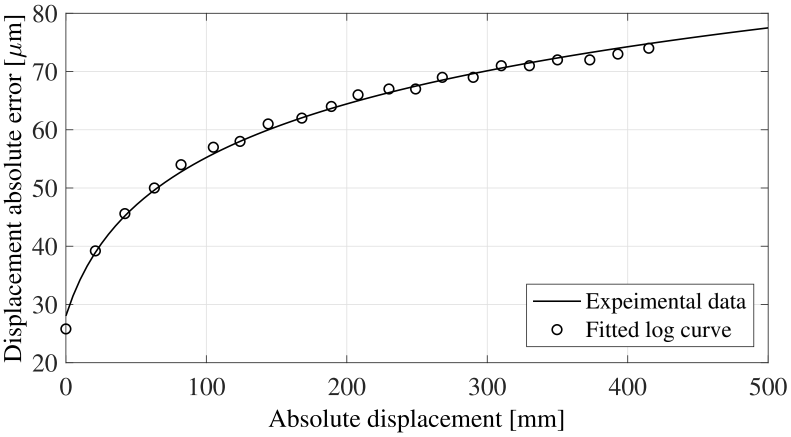

Figure D.9 – Absolute error on the position against target distance

The roundness relative error, affecting displacement channels W_2, W_4, W_6 and W_8, is put at the conservative value of 5%:

$$|\frac{\sigma_i}{x_i}| = 0.05 \tag{D.16}$$

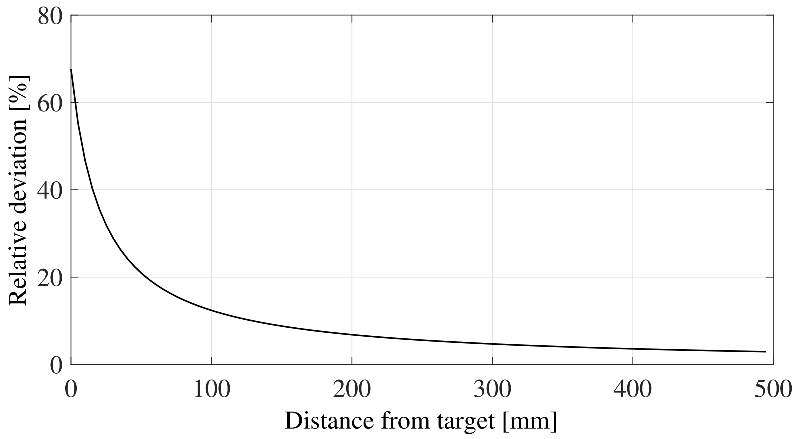

Figure D.10 – Error on the local sensitivity of the probe

D.5.4 Filter and fit error

In order to extract motion at a particular frequency, a time-domain method is used. the time domain raw data are band-filtered around a guess frequency and fitted with a sine, outputting amplitude, phase and signal frequency. In order to estimate the uncertainty on these parameters due to the filtering and fitting steps, a simulation is put in places with the conditions actually used to process the raw data. A signal composed of one known single sine wave is polluted with a Gaussian noise of known amplitude.

$$y_i = \sin(\omega_{ex} t_i) + N_r n \tag{D.17}$$

where n is a random variable following a normal law:

$$n \sim \mathcal{N}(0,\, 1) \tag{D.18}$$

The noise ratio N_r is varied between 0 and 10. The band-pass filter is applied around $\omega_e x$ and the time-domain sine fit is performed to extract the amplitude and the phase. For each noise ratio, the identification exercise was repeated 285 times to extract statistical information out of the process. The signal is of the same duration and sampling rate as in experimental conditions.

An example of error distribution on the amplitude and phase made on the signal to isolate is shown for a noise ratio of 5 in Figures D.11 and D.12 respectively.

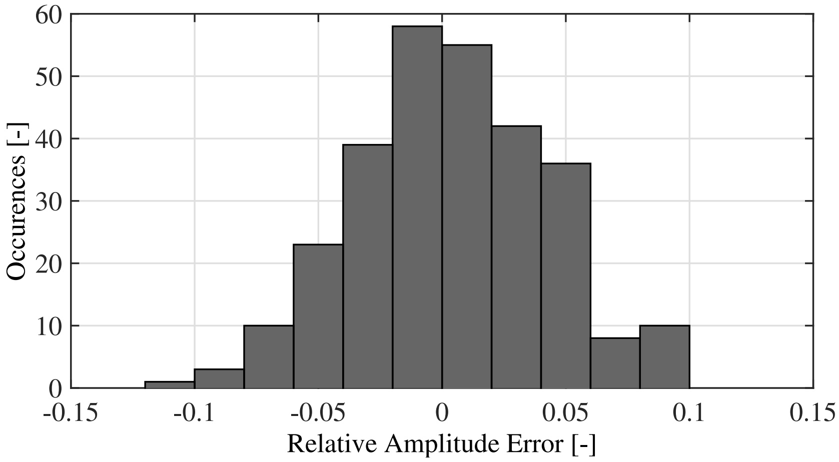

Figure D.11 – Distribution of relative amplitude error on the isolated signal for a noise ratio of 5

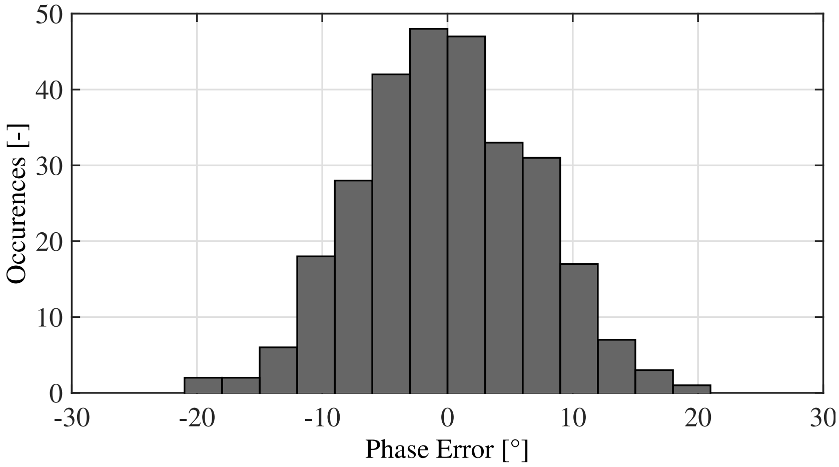

Figure D.12 – Distribution of absolute phase error on the isolated signal for a noise ratio of 5

Obtaining the distribution of errors over a spectrum of noise ratio and extracting their standard deviation, a link can be established between the noise ratio and a signal processing uncertainty. The standard deviation over noise ratio are shown for amplitude and phase in Figure D.13 and D.14 respectively.

In practice, a reference data sample where no shakers are activated is first used to evaluate the level of background noise in the vicinity of the excited frequencies, and determine a equivalent noise ratio of each excited data sample and finally conclude to signal processing uncertainties based on these simulations.

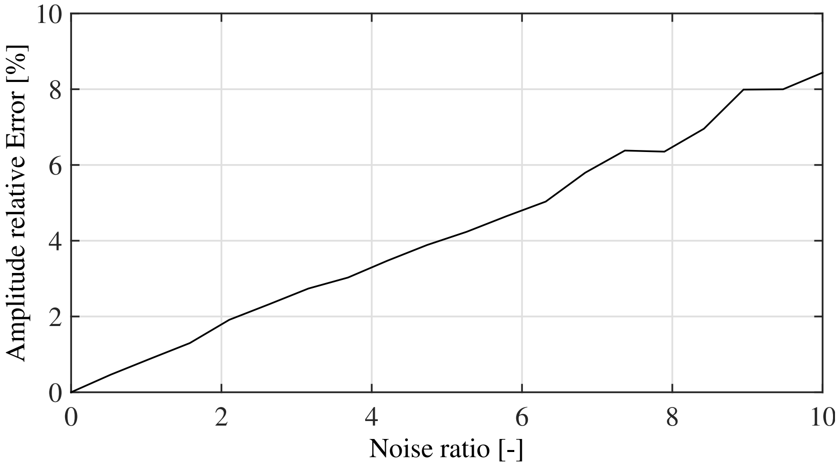

Figure D.13 – Standard deviation of relative amplitude error on the isolated signal for different noise ratio

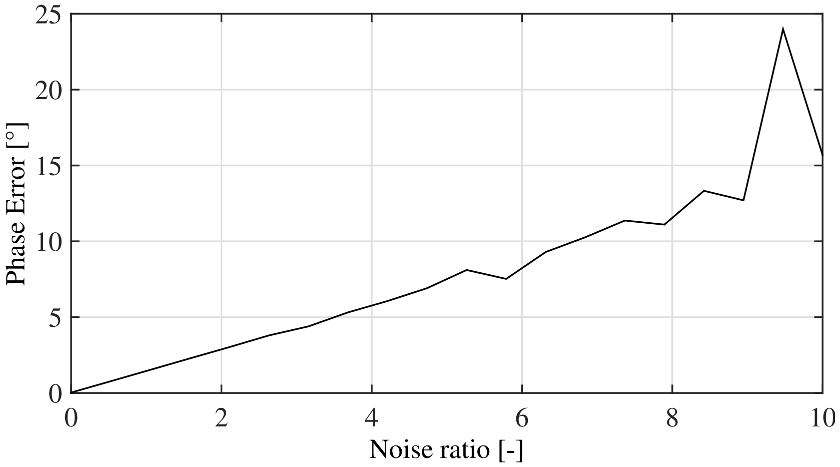

Figure D.14 – Standard deviation of absolute phase error on the isolated signal for different noise ratio

D.6 Temperature measurements

D.6.1 Infra-red temperature sensors

The two IR temperature sensors are calibrated for the particular rotor and tilted configuration using a setup as described in Figure D.15. The rotor is inserted in a heating bed in one end while the other end has its surface temperature measured with the test two probes, maintained in position and angle with a 3D-printed support mounted on the shaft itself. A reference PT100 probe measures the shaft temperature at the same axial position as the IR-probes. The setup is insulated and the heating bed temperature is progressively increased in steps, with 2 hours hours settling time between each measurement point. A linear regression is performed on the data of each of two sensors to establish a calibration curve between the output of the sensors and the measures of the reference probe. Results are shown in Figure D.16.

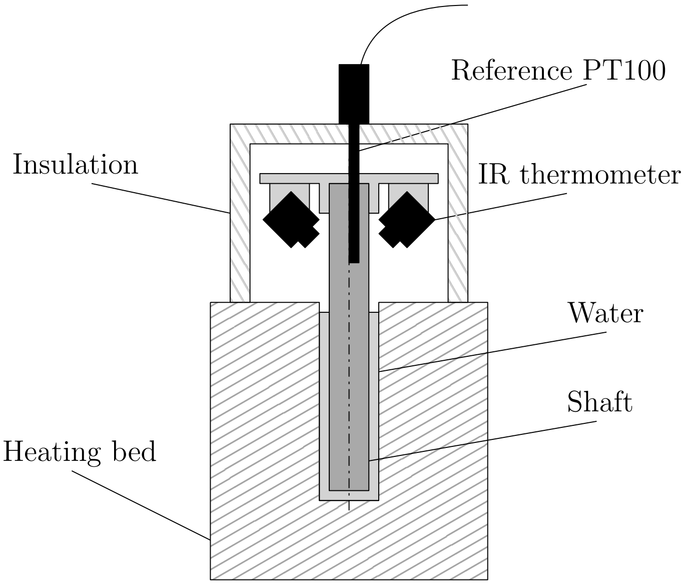

Figure D.15 – Setup for the calibration of the two IR probes

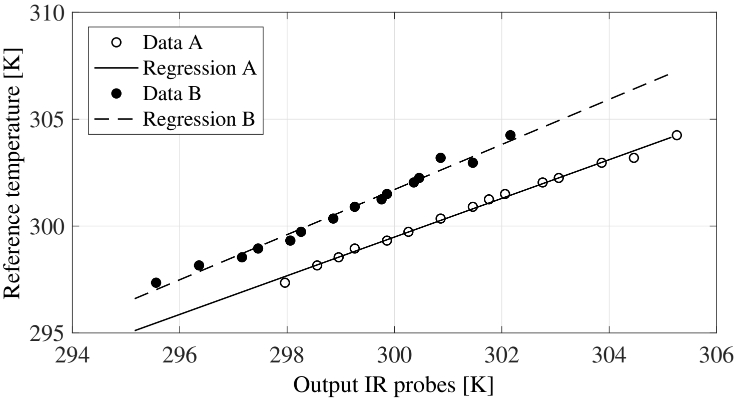

Figure D.16 – Results of the calibration, with the two sets of data and the corresponding regression

D.6.2 PT100 temperature sensors

The PT100 inserted in the bushings flexible supports are calibrated following a similar procedure. The setup, described in Figure D.17, consist of a heating bed, a reference PT100 probe and the two test probes.The heating bed is heated in steps, with two hours between each measures. Results are shown in Figure D.18.

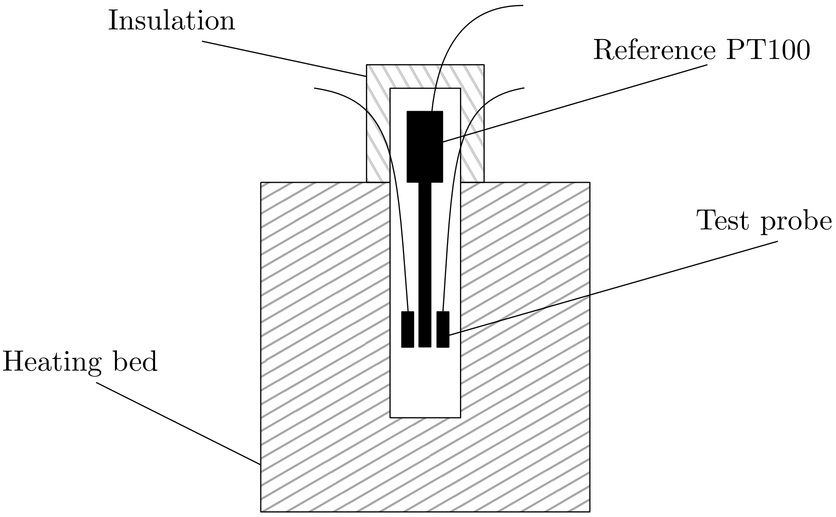
Insulation
Reference PT100
Test probe
Heating bed

Figure D.17 – Setup for the calibration of the PT100 probes

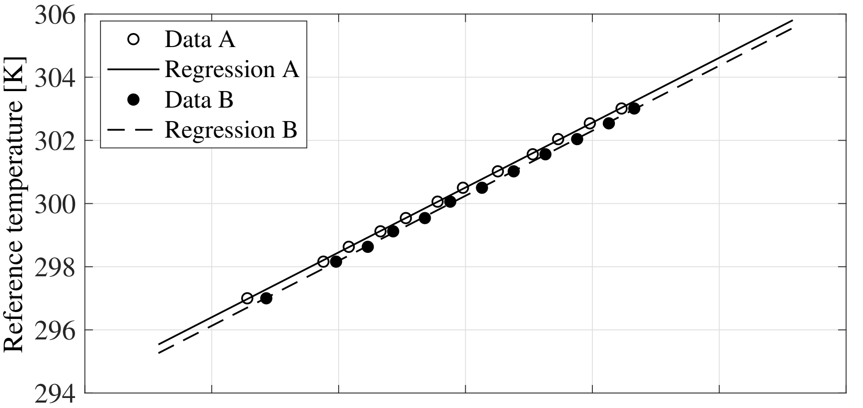

Figure D.18 – Results of the PT100 calibration, with the two sets of data and the corresponding regression

E Results of force coefficients identification is ambient air

Results of the identification of bearing force coefficients are presented for different rotational speeds.

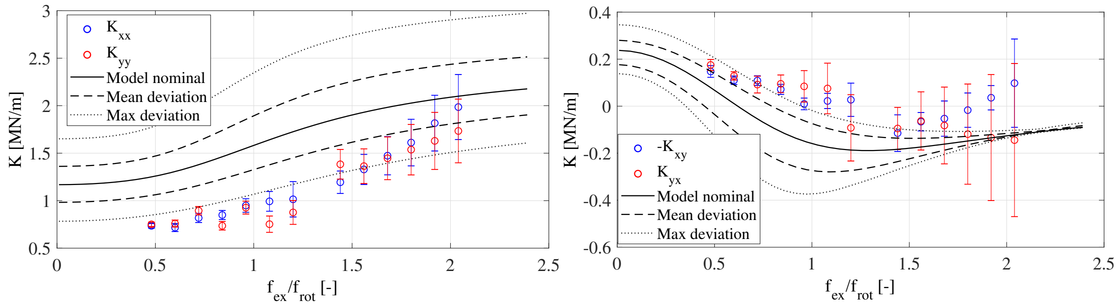

Bearing A, Direct stiffness

Bearing A, Cross-coupled stiffness

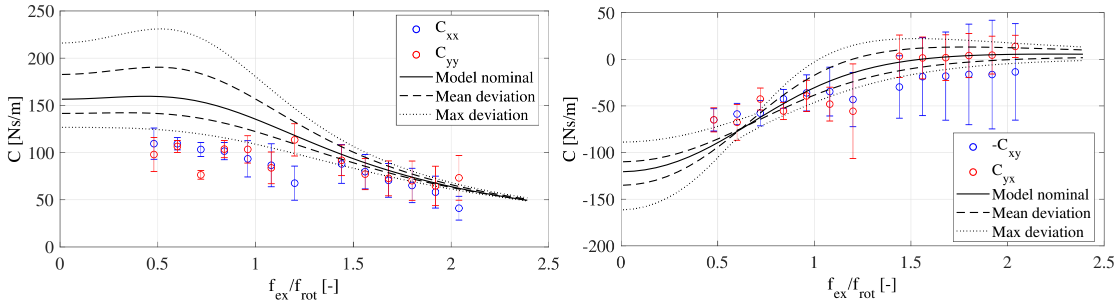

Bearing A, Direct damping

Bearing A, Cross-coupled damping

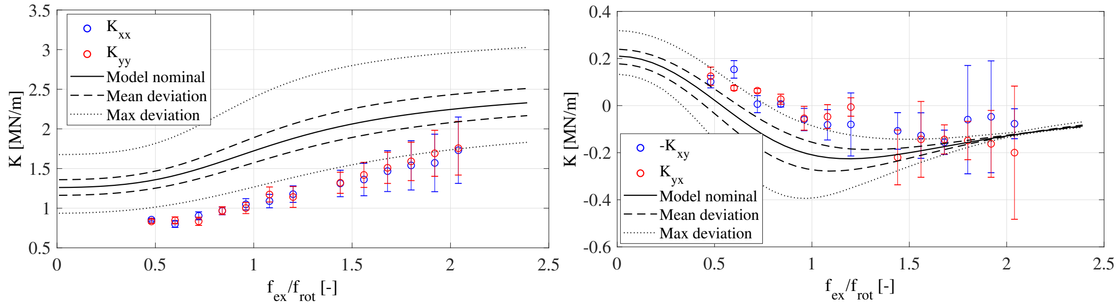

Bearing B, Direct stiffness

Bearing B, Cross-coupled stiffness

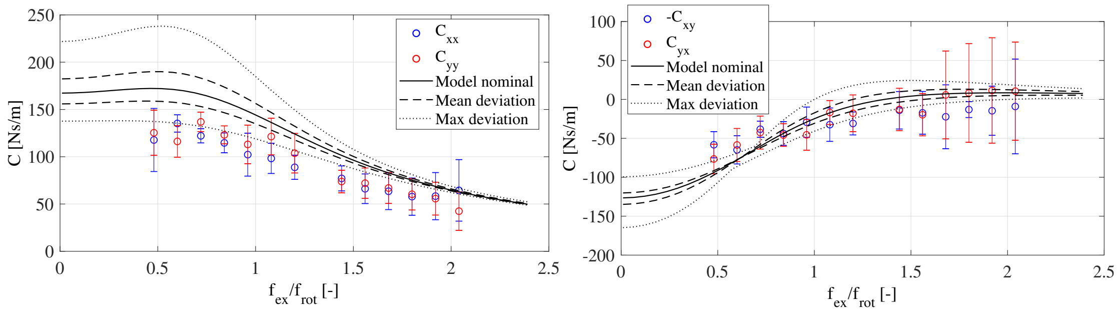

Bearing B, Direct damping

Bearing B, Cross-coupled damping

Figure E.3 – Results of identified force coefficient for 50 krpm in ambient air

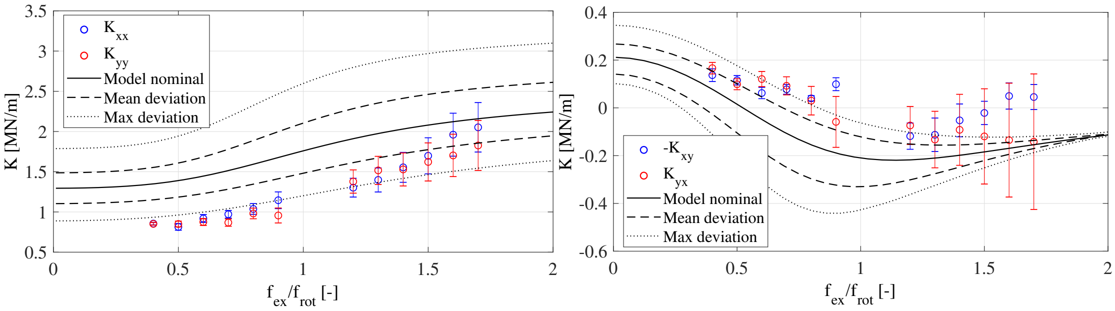

Bearing A, Direct stiffness

Bearing A, Cross-coupled stiffness

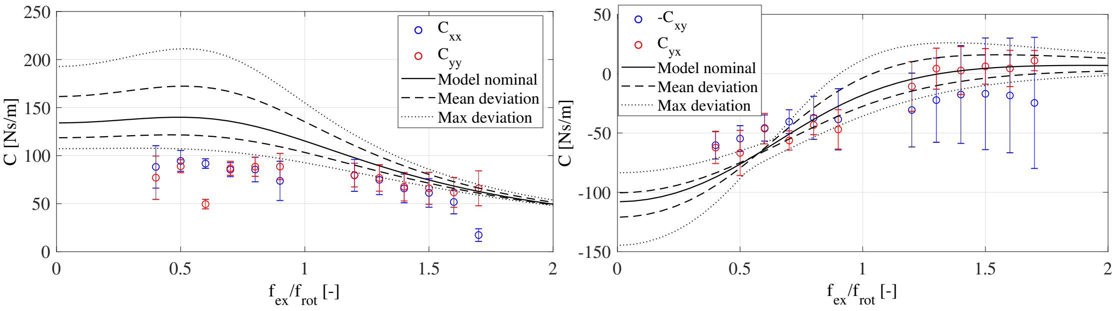

Bearing A, Direct damping

Bearing A, Cross-coupled damping

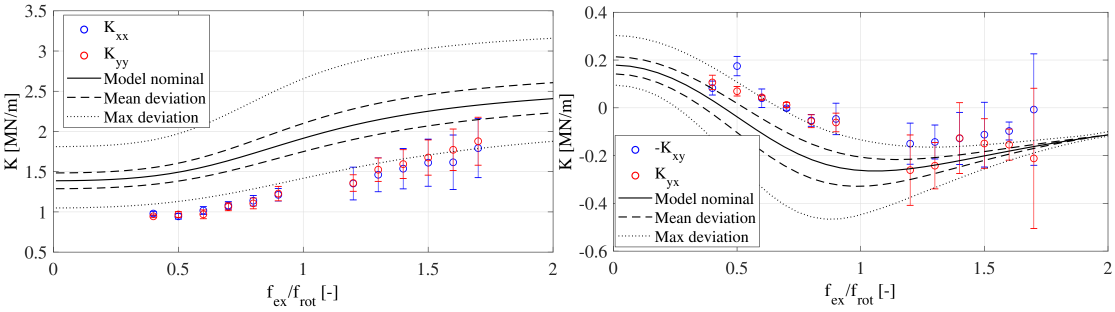

Bearing B, Direct stiffness

Bearing B, Cross-coupled stiffness

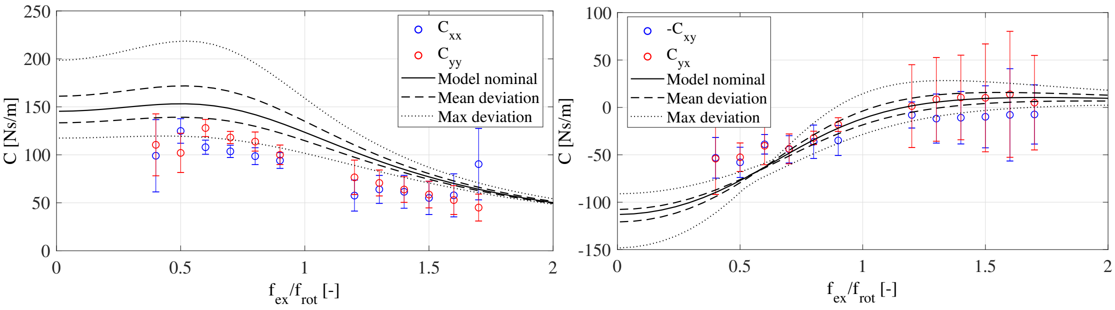

Bearing B, Direct damping

Bearing B, Cross-coupled damping

Figure E.4 – Results of identified force coefficient for 60 krpm in ambient air

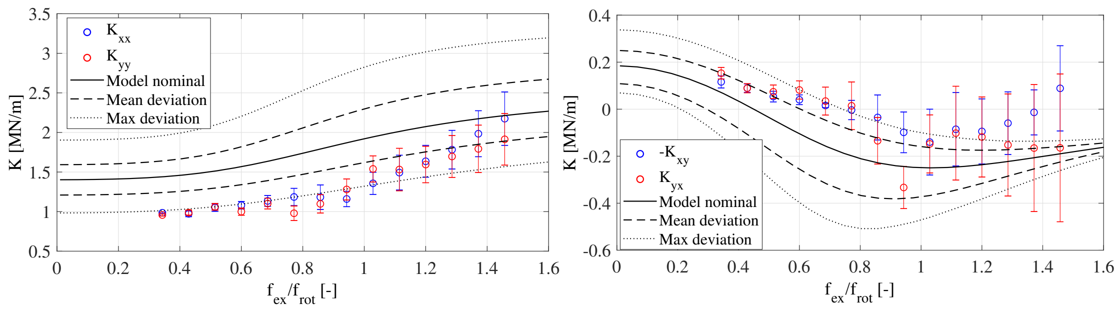

Bearing A, Direct stiffness

Bearing A, Cross-coupled stiffness

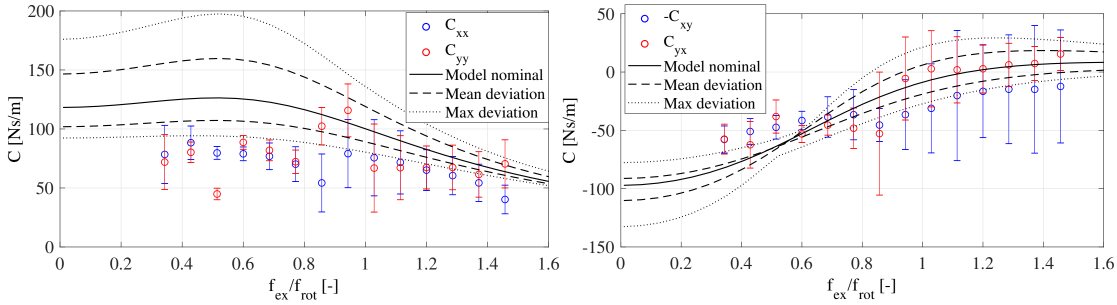

Bearing A, Direct damping

Bearing A, Cross-coupled damping

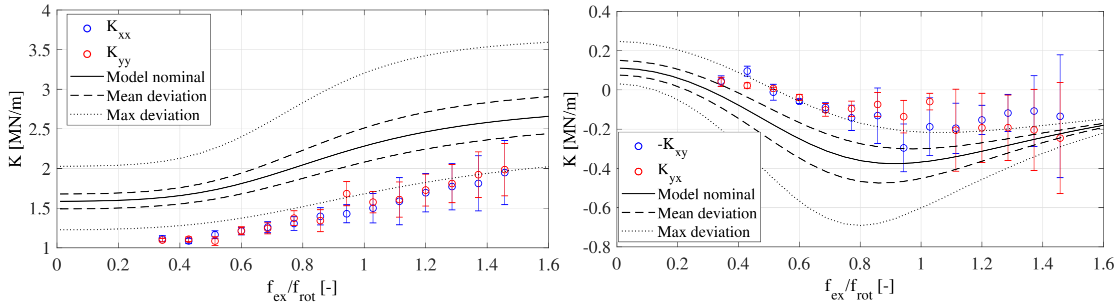

Bearing B, Direct stiffness

Bearing B, Cross-coupled stiffness

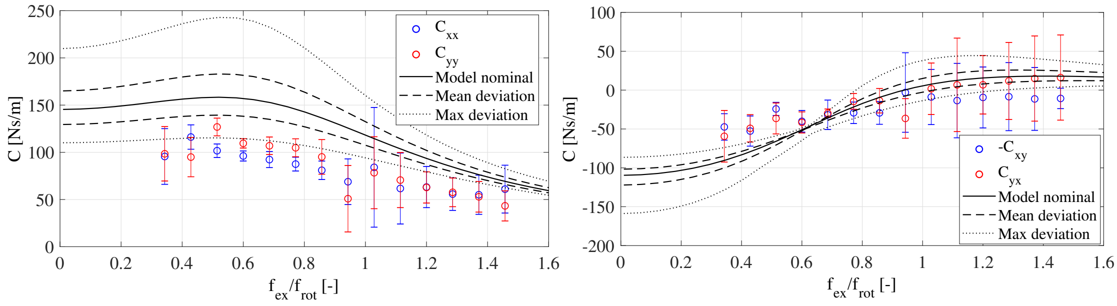

Bearing B, Direct damping

Bearing B, Cross-coupled damping

Figure E.5 – Results of identified force coefficient for 70 krpm in ambient air

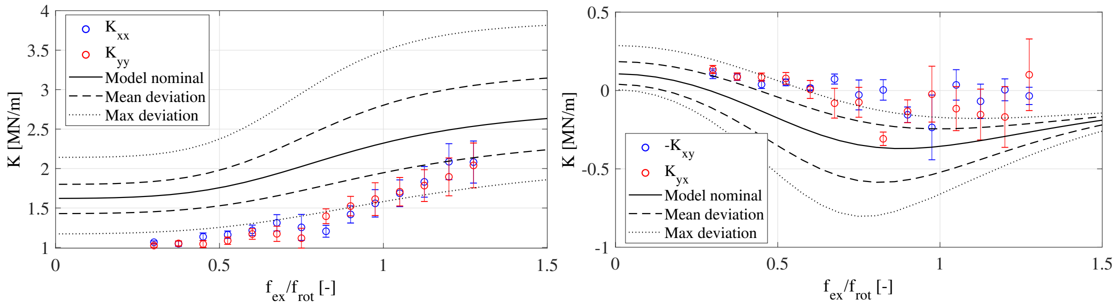

Bearing A, Direct stiffness

Bearing A, Cross-coupled stiffness

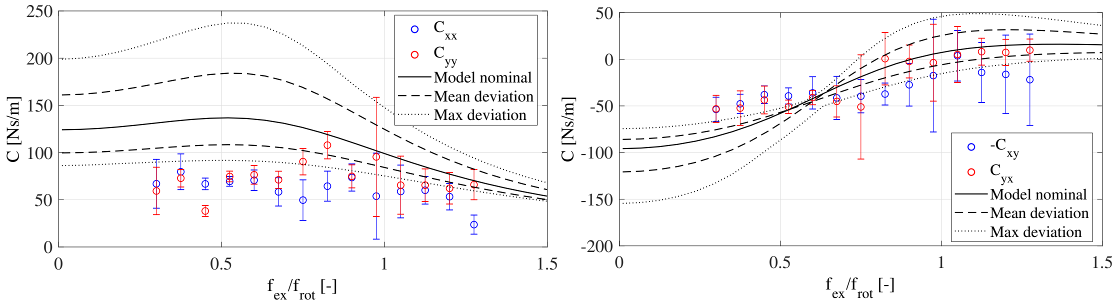

Bearing A, Direct damping

Bearing A, Cross-coupled damping

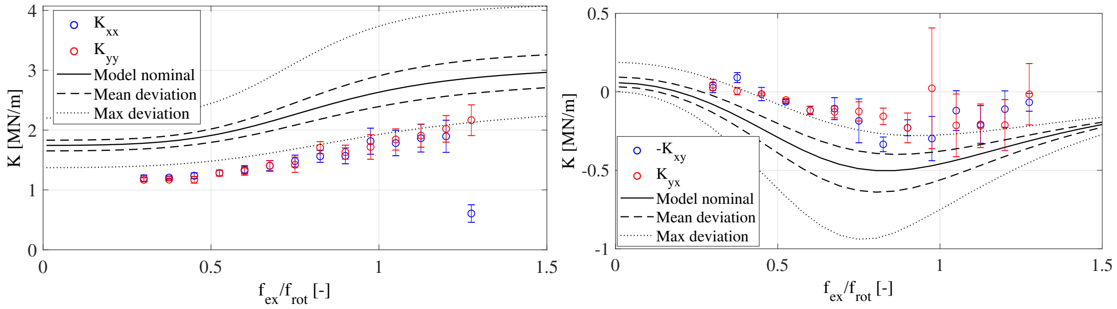

Bearing B, Direct stiffness

Bearing B, Cross-coupled stiffness

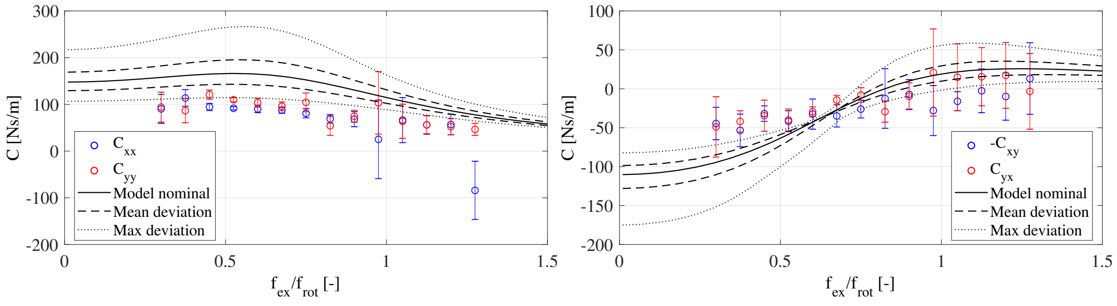

Bearing B, Direct damping

Bearing B, Cross-coupled damping

Figure E.6 – Results of identified force coefficient for 80 krpm in ambient air

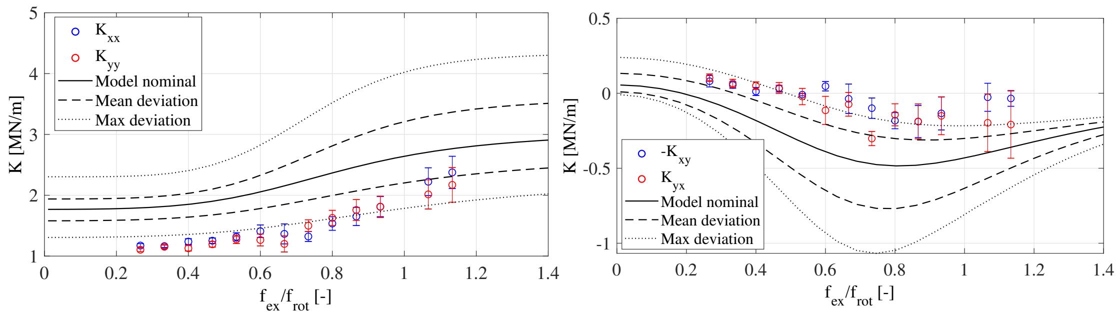

Bearing A, Direct stiffness

Bearing A, Cross-coupled stiffness

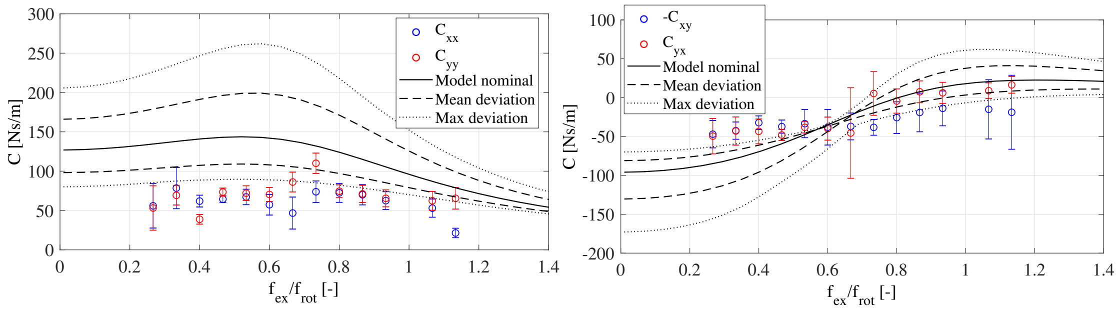

Bearing A, Direct damping

Bearing A, Cross-coupled damping

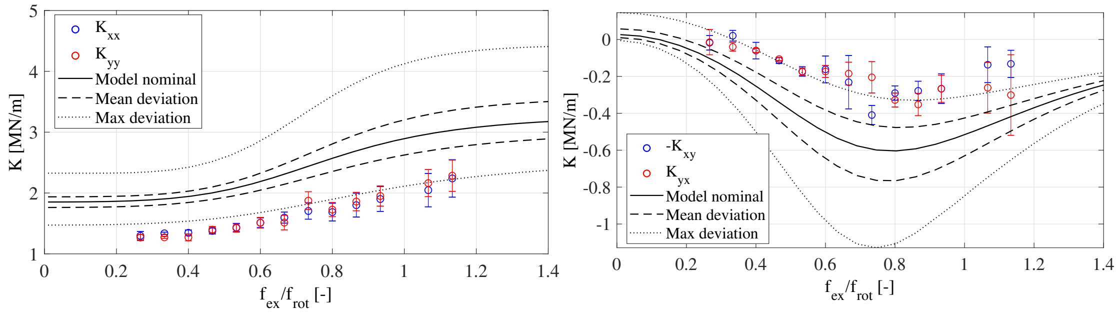

Bearing B, Direct stiffness

Bearing B, Cross-coupled stiffness

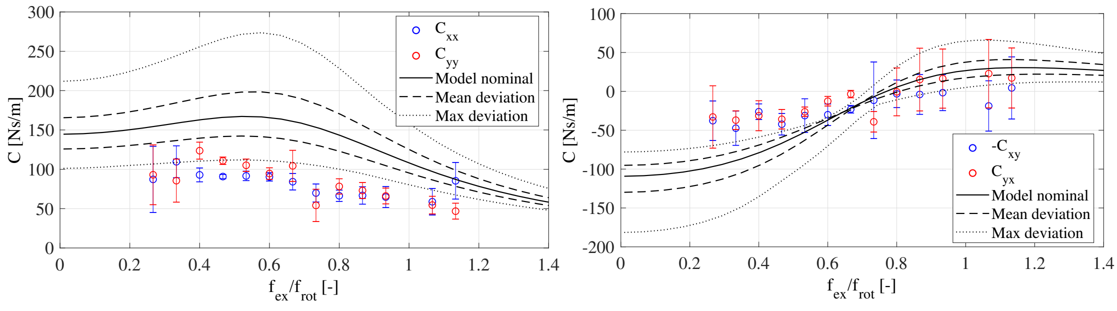

Bearing B, Direct damping

Bearing B, Cross-coupled damping

Figure E.7 – Results of identified force coefficient of bearing A for 90 krpm in ambient air

F Nucleation in saturated thin gas films

The time required for condensation to actually happen, considering the nucleation time required to form stable liquid droplets, estimated. If the pressure excursion in the saturated domain is not sufficient or if the residence time of the fluid at saturated conditions is too short, formation of a liquid phase within the gas phase might not happen and the study of saturated-gas bearings would be reduced to the evaluation of super-saturated gas properties (non-equilibrium state). A strategy applied by Lettieri [1] and Baltadjiev [2] in the problem of condensation in a CO_2 compressor wheel is applied to the present problem, which consists of the evaluation of the time in the saturated region required to have the first stable nucleus of liquid and compare it to the residence time of the gas in this region. If the ratio is well below 1, condensation will occur and the state is assumed to be at thermodynamic equilibrium. In the inverse case, condensation will not occur and the fluid remains single-phase in super-saturated conditions.

Unlike Lettieri who neglected heterogeneous nucleation (nucleation occurring on the walls or on foreign particulates serving as nucleation sites) to consider the homogeneous nucleation only (the gas molecules serve as nucleation site themselves), it is believed that the particular aspect ratio in thin-fluid lubrication will bring the influence of the walls to a non-negligible order of magnitude compared to the homogeneous nucleation. From the classical nucleation theory [3], the rate of homogeneous nucleation is defined as follows

$$J_{homo} = \underbrace{\left(\sqrt{\frac{2\sigma}{\pi m^3}}\frac{\rho_v^2}{\rho_l}\right)}_{1}\underbrace{\exp\left(\frac{-\Delta G_{homo}}{kT}\right)}_{2} \qquad \text{F.1}$$

The prefactor (noted 1) corresponds to the rate of nuclei formation while the term noted 2 is the probability for a nucleus to reach a stable radius. ΔG_{homo} is the Gibbs free energy barrier between the saturated and super-saturated states to form a spherical nuclei

$$\Delta G_{homos} = \frac{16\pi\sigma^3}{3\rho_l^2[g(P_v,T) - g(P_s,T)]^2} \qquad \text{F.2}$$

The presence of walls in the heterogeneous nucleation problem reduces the Gibbs free energy required to form a nuclei of stable size

$$\Delta G_{hetero} = \Delta G_{homo} \frac{2 - 3\cos\theta + \cos^3\theta}{4} \qquad \text{F.3}$$

Where θ is the contact angle between a liquid-phase drop and the wall. Heterogeneous and homogeneous nucleation time constant are considered separately as follows

$$t_{homo} = \frac{1}{J_{homo,max} V_{homo}} \qquad t_{hetero} = \frac{1}{J_{hetero,max} V_{hetero}} \qquad \text{F.4}$$

V_{homo} and V_{hetero} are the volumes of the fluid subjected to homogeneous and heterogeneous saturation respectively

$$V_{homo} = S_{sat} h_0 \qquad V_{hetero} = 2 S_{sat} \delta \qquad \text{F.5}$$

Where S_{sat} is the saturated area of the thin film and δ is the mean free path of the gas molecules, representing the thickness of the gas layer subjected to interact with the wall. Figure F.1 presents the result of the ratio nucleation time over residence time for CO_2 at two reduced pressure against the saturated pressure ratio. The considered geometry is a infinitely long journal bearing ($10mm$ diameter, $5\mu m$ clearance, running at 100 kRPM with a saturated region covering a angle of 20°). The contact angle is 30°, the same value as chosen in the work of Letieri [1]. Two observations can be made : High reduced temperature decreases the nucleation time and the heterogeneous nucleation dominates the nucleation process. A ratio of time constant of 1 is reached at $T_r = 0.85$ at a pressure ratio of 1.05, meaning that the particular bearing configuration will not induce condensation with lower saturated pressure ratios.

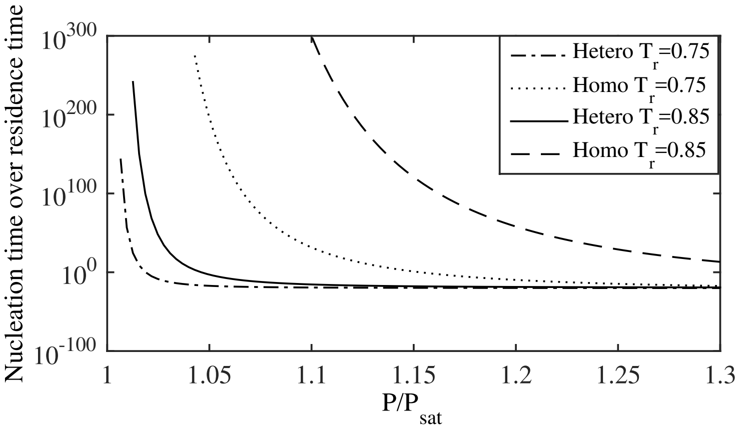

Figure F.1 – Ratio of nucleation time over residence time against saturation pressure ratio for CO_2

Literature on contact angle measurements for artificial refrigerants is meager. A value of

5 ° between R134a and aluminum and steel plates is taken as reference [4], although these two materials are not commonly used for the manufacturing of gas bearings. With such a contact angle value and under the same conditions as previously applied, condensation occur virtually at $P/P_{sat} = 1$ because of the extremely reduced heterogeneous Gibbs free energy , which makes the residence time to overcome the heterogeneous nucleation time by 20 orders of magnitude, as shown in Figure F.2. This ratio is large enough to discard the influence of the particular bearing geometry and operating conditions on the results. Even very close to the triple point temperature, the heterogeneous condensation time dominates for pressure ratios very close to unity. Lack of data regarding contact angle measurements of refrigerant and construction material for aerodynamic bearing (coated steel, carbides) is compensated by the extremely low values of contact angle reported in the literature, values so close to 0 degree that the assumption of thermodynamic equilibrium in the condensation process is legitimated in most practical cases.

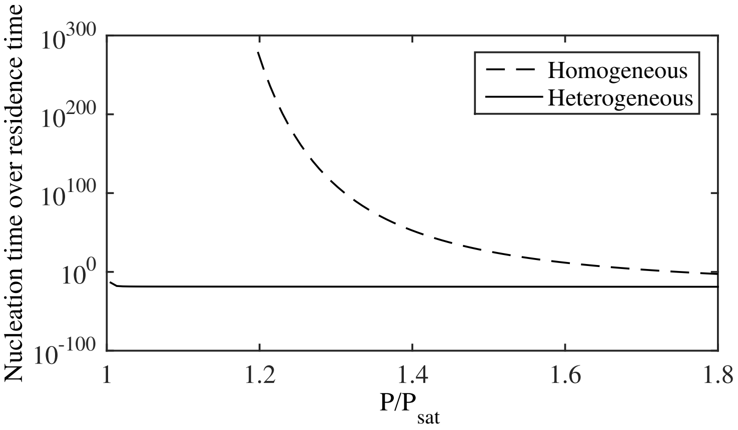

Figure F.2 – Ratio of nucleation time over residence time against saturation pressure ratio for R134a, $T_r = 0.85$

Bibliography

[1] C. Lettieri, D. Yang, Z. Spakovszky, An investigation of condensation effects in supercritical carbon dioxide compressors, Journal of Engineering for Gas Turbines and Power 137 (8) (2015) 082602.

[2] N. D. Baltadjiev, C. Lettieri, Z. S. Spakovszky, An investigation of real gas effects in supercritical CO2 centrifugal compressors, Journal of Turbomachinery 137 (9) (2015) 091003.

[3] J. E. McDonald, Homogeneous nucleation of vapor condensation. I. Thermodynamic aspects, American Journal of Physics 30 (12) (1962) 870–877.

[4] X. Lu, J. Liu, X. Xu, Contact angle measurements of pure refrigerants, International Journal of Heat and Mass Transfer 102 (2016) 877–883.

Eliott Guenat

1991, Swiss citizen

Rue des Sabons 2
Neuchâtel
Switzerland
✉ *eliott@guenat.org*

Education

2016–2020	**PhD**, *Ecole Polytechnique Fédérale de Lausanne*, Lausanne - Switzerland, *Energy*.
2019	**Certificate of Avanced Studies**, *Ecole Polytechnique Fédérale de Lausanne*, Lausanne - Switzerland, *Governing the Energy Transition*.
2018	**Certificate**, *PRINCE2 Foundation Certificate in Project Management*, Lausanne - Switzerland.
2013–2016	**Master of Science**, *Ecole Polytechnique Fédérale de Lausanne*, Lausanne - Switzerland, *Mechanical Engineering*.
2013–2016	**Minor**, *Ecole Polytechnique Fédérale de Lausanne*, Lausanne - Switzerland, *Energy*.
2010–2013	**Bachelor of Science**, *Ecole Polytechnique Fédérale de Lausanne*, Lausanne - Switzerland, *Mechanical Engineering*.

Professional experience

2016–2020	**Doctoral assistant**, *Laboratory for Applied Mechanical Design, EPFL*, Neuchâtel - Switzerland. Working on a PhD thesis on aerodynamic bearing for energy applications in conditions of non-ideal gas and advanced design methodologies.
2015	**Intern**, *Celeroton*, Zürich, Switzerland. 6-month intership in the field of high-speed electric machines
2012	**Intern**, *Rolex*, Geneva, Switzerland. 6-week Internship in the Quality department

Extra-curriculum actvities

since 2018	Board member, Dark-Sky Switzerland
2017-2020	PhD students representative, Doctoral program for Energy, EPFL
2013-2016	Students delegate, Section of Mechanical Engineering, EPFL

Languages

French	Native
English	C2
German	C1
Spanish	B1